Metal trap development and formation mechanisms of clastic-dominated Zn-Pb±Ag mineralization in Paleozoic strata of the Macmillan Pass (Selwyn Basin, Canada)

Dissertation
zur Erlangung des Grades eines
Doktors der Naturwissenschaften (doctor rerum naturalium)
am Fachbereich Geowissenschaften
der Freien Universität Berlin

vorgelegt von:
Haruna Muhammed Grema

Berlin, 2024

FREIE
UNIVERSITÄT
BERLIN

GFZ
Helmholtz-Zentrum
POTSDAM

First reviewer (Erstgutachterin):
Prof. Dr. Sarah A. Gleeson
Institute of Geological Sciences, Freie Universität Berlin, Berlin, Germany
Section 3.1: Inorganic and Isotope Geochemistry, GFZ German Research Centre of Geosciences, Potsdam, Germany

Second reviewer (Zweitgutachter):
Prof. Dr. Jamie J. Wilkinson
Department of Earth Sciences, Natural History Museum, London, United Kingdom
Department of Earth Science and Engineering, Imperial College London, London, United Kingdom

Doctoral Committee (Promotionsausschuss):
Prof. Dr. Friedhelm von Blanckenburg (Vorsitz)
Institute of Geological Sciences, Freie Universität Berlin, Berlin, Germany

Prof. Dr. Timm John
Institute of Geological Sciences, Freie Universität Berlin, Berlin, Germany

Prof. Dr. Sarah A. Gleeson
Institute of Geological Sciences, Freie Universität Berlin, Berlin, Germany
Section 3.1: Inorganic and Isotope Geochemistry, GFZ German Research Centre of Geosciences, Potsdam, Germany

Prof. Dr. Jamie J. Wilkinson
Department of Earth Sciences, Natural History Museum, London, United Kingdom
Department of Earth Science and Engineering, Imperial College London, London, United Kingdom

Priv.-Doz. Dr. Jörg E. Hoffmann
Institute of Geological Sciences, Freie Universität Berlin, Berlin, Germany

Dr. Joseph M. Magnall
Section 3.1: Inorganic and Isotope Geochemistry, GFZ German Research Centre of Geosciences, Potsdam, Germany

Day of defense (Tag der Disputation):
08.11.2024

Declaration / Eidesstattliche Erklärung

I hereby affirm on oath that this thesis was not written by anyone other than myself. All resources used, such as reports, books, websites, or similar, are listed in the bibliography. The thesis has not been submitted to any other examination board in the same or a similar form. The parts of the thesis that have already been published, in review, or to be submitted to a journal are indicated in the preface.

Haruna Muhammed Grema

Berlin, 11.07.2024

Summary

The growing global demand for metals needed for the green energy transition has led to renewed exploration efforts. Ancient sedimentary basins contain a number of important resources such as zinc (Zn) and lead (Pb), and sometimes germanium (Ge), gallium (Ga), and indium (In). Some of the largest Zn deposits are called clastic-dominant (CD-type) deposits because they are hosted in clastic rocks like mudstones and siltstones. These deposits are thought to have formed when metal-rich fluids from deep in the Earth's crust were expelled towards the surface along faults. However, many aspects of this overall model are not well understood. For example, the composition of the ancient metal-rich fluids is largely unknown, along with the mechanisms by which metals are deposited to form economic enrichments in certain locations.

The Selwyn Basin (Canada) contains a number of important CD-type deposits that formed hundreds of millions of years ago. The rocks hosting these deposits are now incorporated into the Canadian Cordillera, meaning they have been uplifted and deformed. This can make it challenging to interpret the rocks and understand how the deposit formation (mineralization) occurred. As a result, it is crucial to carefully examine samples that preserve some of the key primary features of the host rocks and the deposits.

This project evaluates aspects of the CD-type deposit model using various approaches that utilize two sample sets. 1) Barite- and pyrite-rich samples from the Late Devonian Canol Formation in Canada, which contain no Zn, Pb sulfides and formed at the same time as those rocks containing the deposits at other locations, were used to determine how the ancient environment was before the deposits formed. 2) Mineralized rock samples from a newly discovered CD-type deposit (Boundary Zone, Canada) were utilized to evaluate i) how these deposits formed, ii) the physicochemical properties of the metal-rich fluids, and iii) what essential metals are present. To answer some of the abovementioned questions, these two sample groups were used to make petrographic, mineralogical, and geochemical observations across various scales, from hand specimen to microscopic levels.

Data obtained through detailed petrographic and isotopic analyses indicate that the barite and pyrite in the Canol Formation formed during early diagenesis and that biological activity was critical for converting sulfate to sulfide. Similar mineral phases are observed in the samples from the Boundary Zone, where sulfide formed during early diagenesis likely reacted with metal-bearing hydrothermal fluids during an initial stage of ore formation. The first stage is dominated by fine-grained sphalerite formed as layers due to the replacement of quartz (and barite) components of the rocks. A second ore stage consists of several sphalerite types forming in cracks within the same rocks after fracturing. Critical metals, including Ge and deleterious components like Hg, occur in high amounts in the sphalerite from both the mineralized stages. Furthermore, experiments conducted on tiny droplets of fluids trapped within sphalerite and quartz indicate that the mineralizing fluids consist of variable salinity and homogenization temperature ranging from low (around 120 °C) during the early ore-forming stages to high (around 260 °C) at a later period. This suggests that the Boundary Zone deposit formed due to mixing of these fluids at some point.

Altogether, this thesis provides significant insights into components of the CD-type deposit model. It shows how vital microbial activities were during the formation of rocks that later host these deposits and also highlights prolonged hydrothermal fluid flow that could form multiple mineralization types. These findings are valuable for exploration strategies in the Macmillan Pass district and similar geological settings.

Zusammenfassung

Die weltweit steigende Nachfrage nach Metallen, die für die Energiewende benötigt werden, hat zu einem Aufleben der Explorationsbemühungen für diese Metalle geführt. Alte Sedimentbecken enthalten eine Reihe wichtiger Metallressourcen wie Zink (Zn) und Blei (Pb), manchmal auch Germanium (Ge), Gallium (Ga) und Indium (In). Einige der größten Zn-Lagerstätten werden als klastisch dominierte Lagerstätten (CD-Typ) bezeichnet, da sie in siliziklastischen Gesteinen wie Ton- und Siltsteinen vorkommen. Es wird angenommen, dass sich diese Lagerstätten gebildet haben, als metallreiche Flüssigkeiten aus den Tiefen der Erdkruste entlang von Verwerfungen an die Oberfläche aufgestiegen sind. Viele Aspekte dieses Entstehungsmodells sind jedoch noch nicht gut verstanden. So ist zum Beispiel die Zusammensetzung der metallreichen Fluide weitgehend unbekannt, ebenso wie die Mechanismen, durch die Metalle abgelagert werden, um an bestimmten Orten wirtschaftlich relevante Anreicherungen zu bilden.

Das Selwyn-Becken (Kanada) enthält eine Reihe bedeutender Lagerstätten des CD-Typs, die vor Hunderten von Millionen Jahren entstanden sind. Das Gestein, in dem sich diese Lagerstätten befinden, ist heute Teil der kanadischen Kordilleren, d. h., die stratigraphischen Einheiten des Beckens wurden angehoben und verformt. Diese Veränderungen erschweren es, die Gesteinszusammensetzung zu interpretieren und die Lagerstättenbildung (Mineralisierung) zu verstehen. Es ist daher von entscheidender Bedeutung, Gesteinsproben sorgfältig zu untersuchen, die einige der wichtigsten primären Merkmale des Ursprungsgesteins und der Lagerstätten enthalten.

In diesem Projekt werden verschiedene Aspekte des Entstehungsmodells für CD-Lagerstätten anhand verschiedener Ansätze betrachtet. Hierfür werden zwei verschiedene Probensätze verglichen. Um festzustellen, wie die Umgebungsbedingungen vor der Entstehung der Lagerstätten aussahen, wurden zunächst baryt- und pyrithaltige Proben aus der spätdevonischen Canol Formation in Kanada untersucht, die keine essenzielle Metallanreicherung zeigen und zur gleichen Zeit entstanden sind wie die Gesteine, in denen sich die Lagerstätten an anderen Orten gebildet haben. Im zweiten Fall wurden mineralisierte Gesteinsproben aus einer neu entdeckten Lagerstätte des CD-Typs (Boundary Zone, Kanada) verwendet, um zu klären i) wie diese Lagerstätten entstanden sind, ii) die physikalisch-chemischen Eigenschaften der metallreichen Fluide waren und iii) welche essenziellen Metalle vorhanden sind. Um einige der oben genannten Fragen zu beantworten, wurden diese beiden

Probengruppen für petrographische, mineralogische und geochemische Beobachtungen auf verschiedenen Skalen (von Handstück bis hin zu mikroskopischen Größen) untersucht.

Die durch detaillierte petrographische und isotopische Analysen gewonnenen Daten zeigen, dass sich Baryt und Pyrit in der Canol-Formation während der frühen Diagenese gebildet haben und dass biologische Prozesse für die Umwandlung von Sulfat in Sulfid entscheidend waren. Ähnliche Mineralphasen werden in den Proben aus der mineralisierten Boundary Zone beobachtet, wo das während der frühen Diagenese gebildete Sulfid wahrscheinlich während einer ersten Phase der Erzbildung mit metallhaltigen hydrothermalen Fluiden reagiert hat. Das erste Vererzungsstadium wird von feinkörnigem Sphalerit dominiert, welches sich durch die Verdrängung von Quarz- (und Baryt-) Bestandteilen des Gesteins als Schichten gebildet hat. Ein weiteres zweites Erzstadium ist durch verschiedene Sphalerittypen gekennzeichnet, die sich in Rissen innerhalb desselben Gesteins gebildet haben. Kritische Metalle, darunter Ge, aber auch Bestandteile wie Hg, kommen im Sphalerit beider Mineralisierungsstufen in großen Mengen vor. Darüber hinaus deuten Resultate aus winzigen Flüssigkeitseinschlüssen, die in Sphalerit und Quarz vorkommen, darauf hin, dass die mineralisierenden Fluide einen variablen Salzgehalt und eine variable Temperatur hatten. Diese reichen von niedrig (um 120°C) in den frühen Erzbildungsphasen bis hoch (um 260°C) in einer späteren Phase. Die neuen Resultate deutet darauf hin, dass die Lagerstätte in der Boundary Zone entstand, als sich die verschiedenen Flüssigkeiten vermischt haben.

Insgesamt liefert diese Arbeit wichtige Erkenntnisse über einzelne Komponenten des CD-Lagerstättenmodells. Sie zeigt, wie wichtig mikrobielle Aktivität während der Bildung der Gesteine war, die später diese Lagerstätten beherbergen. Darüber hinaus belegen die neuen Ergebnisse auch einen anhaltenden hydrothermalen Flüssigkeitsstrom, durch den sich mehrere Mineralisierungstypen bilden konnten. Diese Erkenntnisse sind für Explorationsstrategien im Macmillan-Pass-Distrikt und in ähnlichen geologischen Gebieten von großem Wert.

Acknowledgments

This is the last part of the thesis I wrote, mainly because of the immense gratitude I owe to so many people who contributed in various ways to the success of this PhD project.

First, my deepest gratitude goes to Sarah for the opportunity to undertake my PhD with you and for providing every opportunity to succeed. I immensely appreciate your dedication, patience, consideration, thorough reviews, and the research freedom you allowed me. Your unwavering support is boundless, and I am eternally grateful.

To my co-supervisor and mentor, Joe: you exemplify positivity and mentorship. Your timely responses, critical feedback, and persistence in improving my skills daily have profoundly shaped my scientific understanding, presentation, and writing abilities. I have cherished your friendship, guidance, and understanding throughout this journey.

To my co-supervisor Hans-Martin, my sincere appreciation for always being available for discussions, irrespective of the topic. Thank you for all the proofreading and encouragement. I am grateful for your untiring support and for always checking on me and ensuring my mental well-being.

My sincere appreciation to the Petroleum Technology Development Fund (PTDF), the Deutscher Akademischer Austauschdienst (DAAD), the Helmholtz Recruitment Initiative, and the Society of Economic Geologists Foundation (SEG) Spora's Explorers Fund for their financial support for this project through scholarships, research, conference, and publication funding. I also appreciate the Usmanu Danfodiyo University (UDUS), Nigeria, for providing the platform to launch my academic career.

My profound appreciation to my current and former colleagues from Sections 3.1 and 3.2 at the GFZ. You contributed tremendously to the success of this project through countless exciting discussions, laboratory analyses, and guidance. Thank you for all the friendly chats and cheerful moments that provided refreshing avenues to keep me going. Thank you, Alicja, Andrea, Anja, Anne, Bob, Candice, Christian, Christof, Claudia, Dilara, Franzi, Frederic, Hartmut, Jakob, Jessica, Johannes, Julia, Juliane, Lisa, Marcus, Maria, Marie, Marta, Marta, Martin, Michael, Mohammed, Moustapha, Peter, Phil, Phillip, Rebecca, Rolf, Uwe, Valby, Vitor, Volker, Wei, YuFu, and Yulia.

To the numerous other wonderful colleagues, collaborators, and friends I have met at the Telegrafenberg, FU Berlin, conferences, workshops, and seminars: thank you for all the ideas we shared and the exciting discussions, both scientific and otherwise. Your companionship during both the happiest and most challenging moments in the past few years has been invaluable. To name a few, thank you, Alex-Selene, Anke, Ebuka, Franca, Franziska, Halleluya, Ilona, Jana, Johannes, Jon, Lydia, Martin, Mubarak, Oona, Pia, and Ruth. I am also grateful for the assistance from Martin Whitehouse of the Swedish Museum of Natural History in performing our isotopic analysis despite the pandemic restrictions.

My appreciation to the Fireweed Metal Corporation team for providing unrestricted access to their database and samples from the Macmillan Pass project, without which this project would not have been completed. Specifically, Jack, the Vice President Geology, whose insights and discussions on the Boundary Zone I deeply appreciated. Thanks also to Moira Cruickshanks, Kaitie Purdue, and Quinton Willms for their assistance in packaging and shipping my samples despite the pandemic restraints.

To Gabriele, I offer my sincere appreciation. Thank you for your friendship over the past four and a half years, especially during the pandemic lockdown. Thank you for all the cups of coffee and tea during my initial literature review sessions and for the bike rides and trips that always allowed me to recharge. To the rest of the Markarian family: Ulli, Josefine, Nepo, Dina, and Marisela, thank you all for easing me into the German culture, language, and traditions.

My sincere gratitude to the geoscientists who have shaped our understanding of sediment-hosted base metal mineral systems. Their foundational contributions to the field provided the platform upon which this thesis stands.

I am thankful for my family and friends back home in Nigeria, the new ones I met in Germany, and others all across the globe for their ceaseless support during my PhD studies. I very much appreciate you all.

Finally, to my wife Zainab and kids, Ammar and Hauwa: you are formidable. I would not choose any other team to go through the PhD journey with. You made countless sacrifices that I can never repay. I would like to say so much, but above all, thank you for the unconditional love and support and for always giving me a reason to come home every day.

Preface

This doctoral thesis consists of five chapters (1-5). Chapter 1 introduces the scope of the study, and Chapters 2, 3, and 4 comprise individual studies on different aspects of the thesis that have either been published, under revision or are to be submitted to a peer-reviewed journal for publication. Chapter 5 consists of the thesis conclusions and future outlook. The contributions of the author (H. M. Grema), co-authors, and other colleagues and collaborators to each of the chapters are provided below. The Petroleum Technology Development Fund (PTDF) and Deutscher Akademischer Austauschdienst (DAAD) doctoral scholarship to the author, Helmholtz recruitment initiative grant to S. A. Gleeson, and Society of Economic Geologists Foundation (SEG) Student Research Grant-Spora's Explorers Fund to the author provided funding for this doctoral project.

Chapter 1 introduces and summarizes important aspects of CD-type sulfide deposits. The author wrote the chapter with inputs from J. M. Magnall, S. A. Gleeson, and H.-M. Schulz.

Chapter 2 has been published in Frontiers of Earth Science journal. The co-authors of the article include J. M. Magnall, M. J Whitehouse, S. A. Gleeson, and H.-M. Schulz. https://doi.org/10.3389/feart.2021.784824.

Barite and pyrite hosted in mudstones from different stratigraphic sections and depths were sampled and analyzed using petrographic and *in-situ* secondary ion mass spectrometry (SIMS). Earlier collected in-house samples were resampled and described in detail by the author following discussion and planning with S. A. Gleeson and J. M. Magnall. The author conducted multiple-scale petrographic examinations using binocular, transmitted, and reflected light microscopy. Sample pucks were microdrilled by the author, guided by J. M. Magnall, and these were cast in epoxy mounts by U. Dittmann. The author performed electron probe microanalysis (EPMA), backscatter electron imaging (BSE), energy dispersive X-ray spectroscopy (EDS), guided by F. Wilke and O. Appelt. F. Wilke conducted element mapping and wavelength-dispersive X-ray spectrometry on regions of interest selected by the author. Scanning electron microscopy (SEM) was conducted by I. Schapän. The author selected *in-situ* SIMS analysis spots with guidance from J. M. Magnall and S. A. Gleeson. M. J. Whitehouse performed the isotope analysis and initial data processing. The author conducted data processing, interpretation, and presentation in collaboration with J. M. Magnall and S. A. Gleeson. The author combined all datasets and wrote the manuscript with input from all co-authors.

Chapter 3 is under revision in the journal Economic Geology and two expert reviewers have already provided positive reviews. The chapter provides the first description of CD-type sulfide mineralization occurring in both Late-Ordovician to Early Silurian and Middle to Late Devonian rocks in a single location in the Selwyn Basin, Canada. The chapter further discusses constraints for the replacement of pre-ore barite and pyrite and the formation of ore-stage sulfides in the deposit. The co-authors of the manuscript include J. M. Magnall, S. A. Gleeson, J. E. Milton, A. Wudarska, A. M. Schleicher, and H.-M. Schulz.

J. E. Milton provided drill core samples from the study location, with the selection guided by J. M. Magnall, S. A. Gleeson, and the author. The author conducted a detailed hand specimen examination and selected regions of interest for sample preparation with guidance from J. M. Magnall. The author conducted thin section, XRD, and U-Pb fluorapatite geochronology sample preparations, guided by H. Liep, A. M. Schleicher, A. Gottsche, and aided by D. Topal. Thin sections were prepared by U. Dittmann and C. Fischer at the GFZ Potsdam and University of Potsdam, aided by the author. XRD analysis was conducted by A. M. Schleicher, and the author processed the data with guidance from A. M. Schleicher. The author performed EPMA guided by F. Wilke, while F. Wilke conducted element mapping and wavelength-dispersive X-ray spectrometry on regions of interest selected by the author. SEM was conducted by I. Schapän under the author's guidance. *In-situ* SIMS measurements were conducted by F. Couffignal and the author, and data processing was carried out by A. Wudarska and M. Wiedenbeck. The author interpreted the data and wrote the manuscript with input from the co-authors.

Chapter 4 is in an advanced stage of preparation and is planned to be submitted to a peer-reviewed journal. The chapter provides the first sphalerite mineral chemistry and microthermometry characteristics of sphalerite-hosted fluid inclusions of CD-type deposits in the Selwyn Basin. Co-authors of the manuscript include J. M. Magnall, S. A. Gleeson, M. Sośnicka, J. E. Milton, V. Barrote, and H.-M. Schulz.

The author selected samples for the analysis with J. M. Magnall and S. A. Gleeson. Thick sections were prepared by U. Dittmann. V. Barrote, and the author conducted LA-ICP-MS analysis on the sphalerite. The author conducted data reduction, processing, and interpretation with oversight from V. Barrote. Fluid inclusion wafers were prepared by the author with guidance from M. Sośnicka. The author conducted Raman spectroscopy and microthermometry with supervision by M. Sośnicka. Data interpretation was conducted by the author with a discussion from M. Sośnicka. The author conducted all data integration and interpretation with inputs from J. M. Magnall and S. A. Gleeson. The manuscript was written by the author with input from all the co-authors.

Chapter 5 provides a conclusion for the doctoral study and highlights important broader implications for our understanding of the ore-forming processes in CD-type mineral system in Paleozoic-hosted strata. Future research outlook is also provided at the end of the chapter. The author wrote the chapter with guidance from J. M. Magnall, S. A. Gleeson, and H.-M. Schulz.

Additionally, several parts of this thesis have been presented at the following conferences:

- **Grema H. M.**, Magnall J. M., Gleeson S. A., Milton J. E., Barrote V. R., Sośnicka M., & Schulz H.-M. (2023): *Mineralogy & paragenesis of the Boundary Zone clastic-dominated Zn deposit (Macmillan Pass, Yukon).* Society of Economic Geologists SEG2023 Conference, London, United Kingdom, 26-29 August 2023. Oral presentation.
- **Grema H. M.**, Magnall J. M., Gleeson S. A., Milton J. E., Barrote V. R., Sośnicka M., & Schulz H.-M. (2023): *Fluid & chemical constraints on sphalerite precipitation in the Boundary Zone Zn-Pb deposit, Yukon, Canada*. GeoBerlin 2023 150th PGLA (BGR) Anniversary & 175th DGGV Anniversary Conference, Berlin, Germany, 3 – 7 September 2023. Oral presentation.
- **Grema H. M.**, Magnall J. M., Whitehouse M. J., Gleeson S. A., & Schulz H.-M. (2022*): Sulfur cycling in the Late Devonian: microscale analysis of pyrite ($\delta^{34}S$) & barite ($\delta^{34}S$, $\delta^{18}O$) in the Canol Formation mudstones (Selwyn Basin, Canada)*. Gordon Research Conference (Geochemistry of Mineral Deposits), Barcelona, Spain, 22-27 May 2022. Poster presentation.
- **Grema H. M.**, Magnall J. M., Whitehouse M. J., Gleeson S. A., & Schulz H.-M. (2022): *Diagenetic constraints on the formation & replacement of bedded barite in the Selwyn Basin, Canada*. In: Christie A.B. (ed.) Proceedings of the 16th SGA Biennial Meeting, Rotorua, New Zealand (online), 28-31 March 2022. Oral presentation.
- **Grema H. M.**, Magnall J. M., Whitehouse M. J., Gleeson S. A., & Schulz H.-M. (2021): *The origin of barite & formation of 'Superheavy Pyrite' in the Late Devonian Canol Formation, Selwyn basin, Canada: Insight from pyrite ($\delta^{34}S$) & barite ($\delta^{34}S$; $\delta^{18}O$) in-situ stable isotope analyses*. 49th Annual Yellowknife Geoscience Forum, Northwest Territories, Canada, (online), 24-26 November 2021. Oral presentation.

Table of Contents

CHAPTER 1

CHAPTER 2

CHAPTER 3

CHAPTER 4

CHAPTER 5

List of Figures

CHAPTER 1

CHAPTER 2

CHAPTER 3

CHAPTER 4

List of Tables

CHAPTER 1

Introduction

1.1. Raw material demand for low a carbon society

The demand for raw materials due to decarbonization, together with population growth and increasing standards of living, will require a significant increase in metal production in the coming decades. In the next 20 years, for instance, the consumption of bulk commodities such as copper (Cu), nickel (Ni), zinc (Zn), and lead (Pb) is set to exceed the total amount ever produced in human history (Ali *et al.*, 2017; Mudd *et al.*, 2017; Schodde, 2017). Zinc is an essential metal for the green transition and globally is the fourth most commonly used metal after iron (Fe), aluminium (Al), and Cu (United States Geological Survey, 2024). Over 60% of Zn is used in galvanizing Fe and steel, essential for solar panels, wind turbines, electric transmission, and electric vehicles (International Zinc Association, 2022). Other important uses include alloying, die casting, fertilizer and paint production, and pharmaceuticals, meaning that Zn is important for transportation, infrastructure, construction, manufacturing, agriculture, and the health industries (International Zinc Association, 2022). Primary Zn resources account for ~70% of production, with recycling and other secondary sources amounting to 30% (Redmond, 2023); however, the Zn in many of these products will be incorporated into multi-decadal infrastructure, meaning that high-quality primary Zn resources and exploration for new deposits will be needed to meet projected demand (Wojcik, 2023).

Additionally, critical metals such as germanium (Ge), gallium (Ga), and indium (In) can be produced as by-products from Zn, Pb, silver (Ag), and Cu ores, where they occur in trace amounts (Cook *et al.*, 2009; Frenzel *et al.*, 2014; Belissont *et al.*, 2016). These elements, together with barite ($BaSO_4$), which can also be found associated with Zn deposits, have been classified as critical and strategic raw materials necessary for modern society and economic security (Schulz *et al.*, 2017) by the European Union (Fig. 1-1; European Commission, 2023), United States (United States Geological Survey, 2024), and China (Ge and Ga; Jiang *et al.*, 2023). Germanium, Ga, and In are primarily used in infrared, fiber optics, and solar and electronic device manufacturing. Barite has found increasing applications in plastic, rubber, and paint production as an extender, filler, or weighting agent, as well as in shielding X-ray and gamma-ray emissions (United States Geological Survey, 2024).

1.2. Global distribution of Zn, Pb, and barite

The majority of Zn (54%) and Pb (68%) resources are located in ancient sedimentary basins, primarily of Proterozoic and Paleozoic age (Huston *et al.*, 2006; Leach *et al.*, 2010; Huston *et al.*, 2022). There are two main types of sediment-hosted Zn-Pb deposits, which can be subdivided according to host rock composition and the timing of mineralization relative to rock deposition: Mississippi-Valley type (MVT) and clastic-dominated (CD-type) deposits (Leach *et al.*, 2005b; Leach *et al.*, 2010; Wilkinson, 2014). The MVT deposits are epigenetic and hosted in dolostone and limestone units. In contrast, CD-type deposits are hosted in siliciclastic or mixed siliciclastic-carbonate units, and considerable debate has been focused on whether mineralization is formed via synsedimentary or epigenetic processes (Leach *et al.*, 2010). Irish-type deposits represent a subclass comprising certain aspects of the MVT and CD-type deposits and are formed during diagenesis in carbonate units (Hitzman & Large, 1986; Wilkinson, 2014).

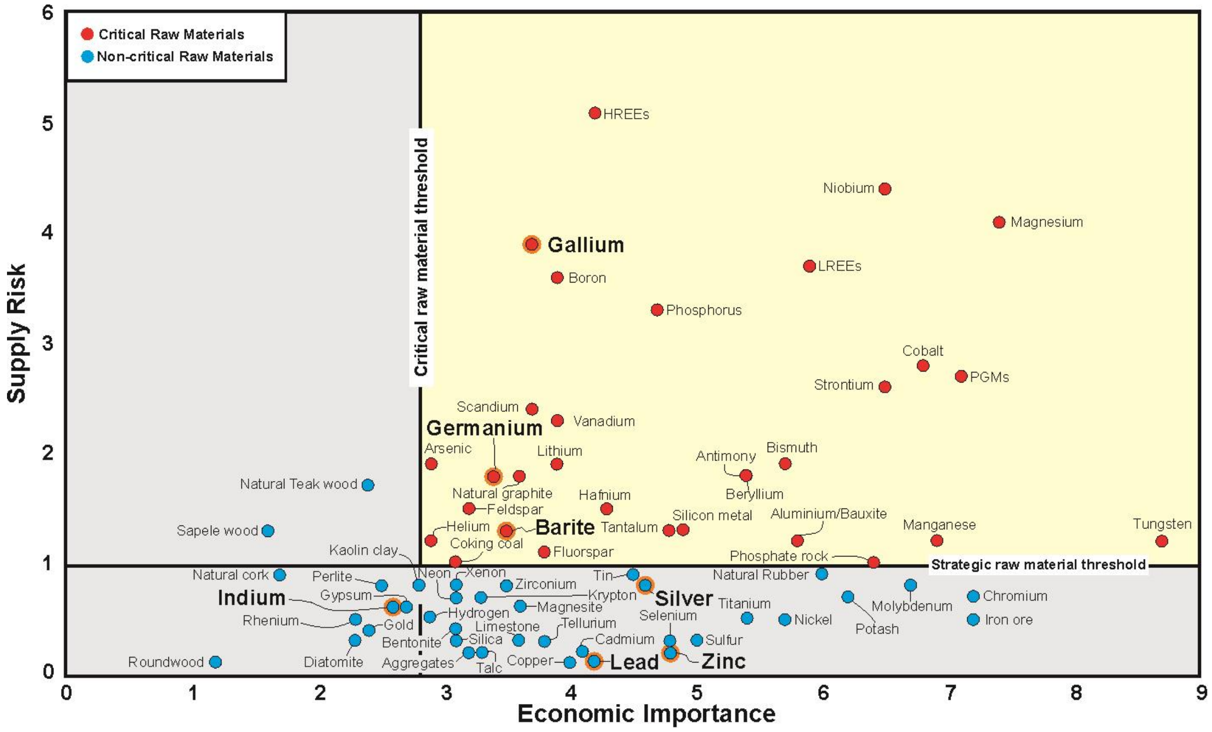

Fig. 1- 1: The European Union critical and strategic raw material 2023 plot highlighting economic importance and associated supply risk factors. Modified from Grohol and Veeh (2023).

The majority of the global Zn and Pb are hosted by CD-type deposits concentrated in supergiant and giant districts, including Mount Isa and Broken Hill (Australia), Rampura Agucha (India), Rammelsberg (Germany), Red Dog (United States), and Howard's Pass and Sullivan in Canada (Fig. 1-2). Barite occurrences are a common feature in a number of Paleozoic CD-type districts; and some basins host over ~1 Gt barite, for instance, the Kuna Basin, Alaska, which also hosts the giant Red Dog district deposits (Johnson *et al.*, 2004; Kelley *et al.*, 2004; Leach *et al.*, 2004). Barite occurs throughout the geologic record, from the Early Archean and the Paleozoic, and in sedimentary basins as stratiform or stratabound units, commonly at passive margins (Maynard & Okita, 1991; Jewell, 2000).

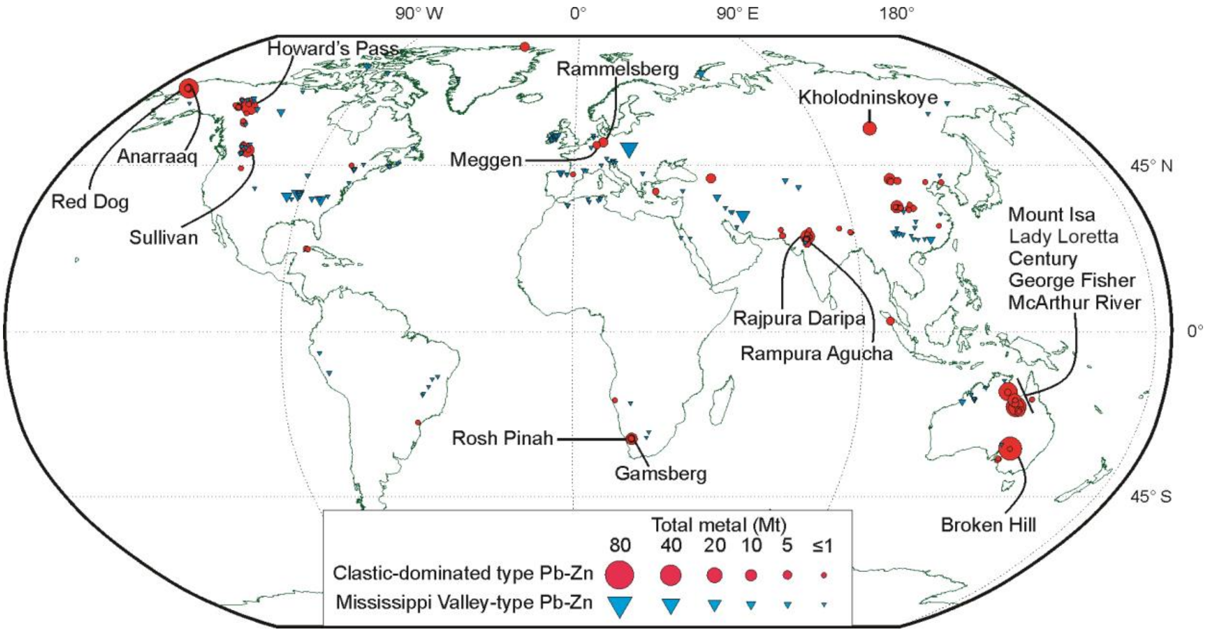

Fig. 1- 2: Global distribution of sediment-hosted Pb and Zn deposits. Sizes of the circle and triangle correspond to contained Pb+Zn. Modified from Taylor *et al.* (2009).

Recently, the discovery of new significant CD-type deposits has been largely limited. In the past two decades, only two new deposits have been identified despite a significant increase in exploration activities and investment. The Teena deposit is the most recent discovery of CD-type occurrence in the Proterozoic Carpentaria Zn Province, Australia (Taylor *et al.*, 2017), which already hosts the most significant such Zn resources in the world (30% of global Zn resources; Huston *et al.*, 2006). Recent studies on the Teena deposit have focused on characterizing the deposit model, mineralization style, and ore assemblages of the deposit (Taylor *et al.*, 2017; Hayward *et al.*, 2021; Magnall *et al.*, 2021; Magnall *et al.*, 2023) to further enhance our understanding of the CD-type mineral systems. In the Selwyn Basin, the Boundary Zone Zn-Pb±Ag deposit in the Macmillan Pass district represents the other significant recent Zn discovery, which is investigated in this thesis.

1.3. The clastic-dominated Zn-Pb mineral system

1.3.1. Tectonic setting

Clastic-dominated deposits are formed in continental and back-arc rifts, sag basins, and passive margin tectonic settings (Leach *et al.*, 2005b). The deposits are commonly restricted to fault-bound subbasins (Betts *et al.*, 2003; Hayward *et al.*, 2021) developed from long-lived regional fault systems (Leach *et al.*, 2005b; Emsbo *et al.*, 2016). The subbasins are characterized by graben structures, abrupt changes in sedimentary facies, and, in places, the presence of breccias and fault scarp debris flows (Leach *et al.*, 2005b; Goodfellow & Lydon, 2007). These deposits show no apparent relationship with intrusive rocks and are generally regarded as unrelated to magmatic processes (Wilkinson, 2014).

1.3.2. Metal source(s)

A clear understanding on the source of the metals that form CD-type deposits has yet to be achieved, as typically, the potential source areas are not exposed. Crustal metal sources for the mineralization have been suggested based on Pb isotope geochemistry and numerical modeling (Godwin *et al.*, 1982; Ayuso *et al.*, 2004; Leach *et al.*, 2005b; Nelson & Colpron, 2007; Ootes *et al.*, 2013; Rodríguez *et al.*, 2021). Leach *et al.* (2010) highlighted the importance of continental and volcanic rocks. For example, the Zn and Pb in the Carpentaria Zn Province are thought to be sourced from underlying mafic volcanic units (Cooke *et al.*, 1998; Cooke *et al.*, 2000; Huston *et al.*, 2023), whereas synrift clastic sedimentary rocks are indicated as likely metal sources in the Selwyn Basin (Leach *et al.*, 2005b; Wilkinson, 2014; Rodríguez *et al.*, 2021).

1.3.3. Fluids and fluid pathway(s)

There are limited examples of CD-type systems with fluid inclusion data; consequently, the nature of the mineralizing fluids is not clear. The lack of fluid inclusion microthermometry data is largely due to the fine-grained nature of the sulfides and associated gangue minerals and tectonic overprinting that complicate fluid inclusion characterization and mineral paragenesis reconstruction. As such, few ore-forming fluid constraints have been obtained from fluid inclusions hosted in sulfides and coeval gangue minerals phases in CD-type deposits (e.g., Gardner & Hutcheon, 1985; Ansdell *et al.*, 1989; Leach *et al.*, 2004; Polito *et al.*, 2006; Rajabi *et al.*, 2015b; Magnall *et al.*, 2016b). A number of these studies suggested that the mineralizing fluids are saline in nature, with fluids from the Red Dog district suggested to have originated from evaporated seawater (Leach *et al.*, 2004). The deposits are reported to have temperatures ranging from 70 to 300 °C and salinities of 10 to 30 wt.% NaCl equiv. (Wilkinson, 2014 and references therein).

At elevated temperatures (>100 °C), evaporated seawater is capable of leaching metals from clastic units and basement rocks (Leach *et al.*, 2004; Polito *et al.*, 2006; Leach *et al.*, 2010). Metals are suggested to have been transported mainly as Cl complexes in hydrothermal fluids that range from neutral to acidic (Cooke *et al.*, 1998; Cooke *et al.*, 2000). Notably, almost all significant CD-type deposits occur proximal to large fault systems (Huston *et al.*, 2023, and references therein), which are considered as conduits for hydrothermal fluid flow in several CD-type mineral systems (Wilkinson, 2014; Rodríguez *et al.*, 2021). Fluids in CD-type systems are thought to have been circulated by a number of different flow regimes, including sediment compaction, gravity, compressional tectonics, and heat from the underlying basement (Solomon & Heinrich, 1992; Burnham, 1997; Cooke *et al.*, 1998).

1.3.4. Metal trap

There are many different models on the timing of CD-type deposits in a given basin. The formation of the deposits has been suggested to be synsedimentary (Carne & Cathro, 1982; Goodfellow *et al.*, 1993; Large *et al.*, 2005), to diagenetic (Kelley *et al.*, 2004; Gadd *et al.*, 2016a, b; Slack *et al.*, 2017; Johnson *et al.*, 2018; Magnall *et al.*, 2020a), or to having formed during basin inversion periods (Gibson *et al.*, 2017). The generation of reduced sulfur (H_2S) provides the metal trap, which may be derived from i) stratified water column with anoxic to euxinic bottom water (e.g., Goodfellow, 1987), ii) reducing pore fluids in organic-rich sediments (Ohmoto & Goldhaber, 1997; Borowski *et al.*, 2013; Huston *et al.*, 2023), and iii) hydrothermal fluids (e.g., Cooke *et al.*, 2000).

In the Macmillan Pass district, Selwyn Basin, for example, ore-forming processes are generally suggested to involve hot (up to 300 °C) metalliferous fluids mixing with reduced aqueous sulfur species (Goodfellow & Jonasson, 1984; Goodfellow, 1987; Magnall *et al.*, 2016b). The H_2S is generally implied to be generated *in situ* via the reduction of seawater sulfate (SO_4^{2-}) or from sulfate reduction after the dissolution of sulfate-bearing mineral phases, e.g., barite (equation 1; Goodfellow, 1987; Cooke *et al.*, 2000; Huston & Gutzmer, 2023). The diagenetic environment in the host rock to CD-type deposits can be a critical factor in the generation of H_2S and ground preparation for the metal trap. The diagenetic pre-ore stage in CD-type settings is often dominated by sulfate reduction processes, primarily microbial sulfate reduction (MSR) and sulfate reduction coupled to anaerobic oxidation of methane (SR-AOM; Canfield, 2001a;

Machel, 2001; Jørgensen & Kasten, 2006). These processes generate various sulfide species that dissolve in hydrothermal fluids, forming effective complexes for the precipitation and, thus, metal traps in the host rocks (Hemley & Hunt, 1992; Leach *et al.*, 2010; Wilkinson, 2014).

1.3.5. Sulfur cycling and ground preparation in CD-type systems

In organic matter-rich sediments, sulfate is first metabolized during MSR (equation 2). When aqueous sulfate concentrations are diminished, typically at greater sediment depths, labile organic matter is metabolized further during methanogenesis, generating biogenic methane and carbon dioxide (equation 3). Methane-rich pore fluids may then diffuse or be advected (seep) upwards, and the interaction between this upward flux of methane and downward-diffusing sulfate results in SR-AOM (equation 4; Boetius *et al.*, 2000). This sulfate-methane transition zone (SMTZ) is a major diagenetic redox boundary, where reactions are mediated by a consortium of methanotrophic bacteria and archaea (Leloup *et al.*, 2007; Borowski *et al.*, 2013). Both MSR and SR-AOM processes produce H_2S, which can react with ferrous Fe to form pyrite (FeS_2) (Canfield, 2001a; Jørgensen & Kasten, 2006).

$$BaSO_4 \rightarrow Ba^{2+} + SO_4^{2-} \tag{1}$$

$$SO_4^{2-} + 2CH_2O \rightarrow H_2S + 2HCO_3^- \tag{2}$$

$$2CH_2O \rightarrow CO_2 + CH_4 \tag{3}$$

$$SO_4^{2-} + CH_4 \rightarrow HS^- + HCO_3^- + H_2O \tag{4}$$

Barium is also soluble in the strongly reducing methane-rich pore fluids. The Ba in organic-rich sediments is most commonly derived from biogenic barite, which precipitated from seawater in microenvironments associated with sinking particulate matter (Paytan *et al.*, 2002; Paytan & Griffith, 2007). Below the SMTZ, where sulfate-limited conditions develop, the dissolution of biogenic barite increases the content of dissolved Ba^{2+} species in diagenetic pore fluids. The upward diffusion of Ba can then result in the precipitation of authigenic barite at the SMTZ via reaction with dissolved sulfate from above. This model of diagenetic barite formation has been used to explain the formation of stratiform and stratabound barite beds along continental margins and rift settings that are commonly spatially and temporally associated with CD-type deposits (Torres *et al.*, 1996; Hein *et al.*, 2007; Zhou *et al.*, 2015; Magnall *et al.*, 2016a; Fernandes *et al.*, 2017; Reynolds *et al.*, 2021). In contrast, barite that shares a direct genetic link with CD-type deposits has also been suggested to have formed via hydrothermal processes where dissolved Ba was delivered together with Zn, Pb, and Fe in the hydrothermal fluid (Goodfellow & Lydon, 2007).

The MSR and SR-AOM sulfate reduction pathways are the primary microbial pathways of sulfate consumption at low temperatures (<150 °C; Stetter *et al.*, 1990; Parkes *et al.*, 1994); importantly, microbes preferentially utilize lighter sulfur isotopes (^{32}S) during both reactions (Berner, 1984; Ohmoto & Goldhaber, 1997). During MSR and SR-AOM, microbially induced sulfur isotope fractionation results in ^{34}S-depleted sulfide in porewaters within marine sediments, which may then be incorporated into pyrite (e.g., Magnall *et al.*, 2016a). In comparison, subsequent pyrite generations often preserve more positive $\delta^{34}S$ values linked to sulfate limitation and closed system Rayleigh fractionation effects, which may be sensitive to sedimentation rates (Pasquier *et al.*, 2017; Pasquier *et al.*, 2021), and concentration of dissolved sulfate (Johnston, 2011; Algeo *et al.*, 2015) or methane (Deusner *et al.*, 2014). Additionally, thermochemical sulfate reduction (TSR) also results in positive $\delta^{34}S_{pyrite}$ values and commonly occurs at relatively higher temperatures (>100 °C) during late diagenesis deeper in the sediments (Ries *et al.*, 2009; Cui *et al.*, 2018; Yan *et al.*, 2020; Huston & Gutzmer, 2023).

Sulfate-limited conditions in marine sediments develop where sulfate supply<<sulfate depletion, resulting in the development of anoxic or euxinic conditions, and this can be linked to global events (e.g., Frasnian-Famennian Kellwasser crisis; Buggisch, 1991) or localized changes in depositional environments (Fike *et al.*, 2015; Liu *et al.*, 2019; Yan *et al.*, 2020). In this regard, pyrite has been used for paleoenvironmental reconstructions and tracking global and local sulfur cycles throughout the geologic record utilizing the offset between $\delta^{34}S$ values in pyrite and those in coeval seawater sulfate and sulfate-bearing phases, e.g., barite (Claypool *et al.*, 1980; Bottrell & Newton, 2006; Fike *et al.*, 2015). The sulfur isotope composition of pyrite and barite both provide an important archive for reconstructing pre-ore redox conditions in host rocks to CD-type deposits in a number of basins (Magnall *et al.*, 2016a; Gadd *et al.*, 2017; Rieger *et al.*, 2020; Leighton *et al.*, 2021a; Reynolds *et al.*, 2021).

1.4. Clastic-dominated type deposits in the Selwyn Basin

The Selwyn Basin is located in Canada (Fig. 1-3a) and hosts several polymetallic deposits essential for the country's economic security and decarbonization drive, as well as for trading partners, including the European Union states (NRCan, 2021). For example, Canada is estimated to have ~12.5% of global unexploited Zn resources (Mudd *et al.*, 2017) primarily hosted in CD-type deposits. The CD-type deposits in the Selwyn Basin have been studied in detail, and some of the pioneering genetic models were developed from studies in the basin (e.g., Goodfellow & Jonasson, 1984; Goodfellow, 1987). Sulfide mineralization mainly occurs in carbonaceous and siliciclastic units and is spatially associated with barite in certain locations. The largest deposits are hosted in three stratigraphic intervals (Fig. 1-3a), which include Cambrian rocks in the Anvil district (Pigage, 1991), Late-Ordovician to Early Silurian strata in the Howard's Pass district (Fig. 1-3b; Morganti, 1979), and Middle to Late Devonian units in the Macmillan Pass district (Carne, 1979; Gardner & Hutcheon, 1985).

1.4.1. Genetic models for CD-type systems in the Selwyn Basin

In the Selwyn Basin, the formation of CD-type sulfide mineralization was long attributed to sedimentary exhalative (SEDEX) processes (Carne & Cathro, 1982). This was due mainly to the previous understanding that laminated sulfides that often characterize these deposits formed as a result of the exhalation of mineralizing fluids into stratified seawater (Goodfellow & Jonasson, 1984; Goodfellow & Rhodes, 1990; Goodfellow *et al.*, 1993). Importantly, deposit formation was ascribed to basin stagnation and the development of anoxic to euxinic conditions in the Selwyn Basin (Goodfellow, 1987). Ore precipitation was then suggested due to interaction between the hydrothermal fluid and reduced sulfur-bearing seawater (Goodfellow *et al.*, 1993). However, more recent research on the Selwyn Basin CD-type mineralization has suggested a subseafloor replacement model for ore formation (Magnall *et al.*, 2016a; Magnall *et al.*, 2020c).

In the Howard Pass district, the bulk of the ore sulfides are hosted in the calcareous, siliceous, and carbonaceous mudstones of the Active Member of the Late Ordovician to Early Silurian Duo Lake Formation (Morganti, 1979; Gadd *et al.*, 2016b). Mineralization is suggested to result from the diagenetic reaction of carbonaceous sediments containing reduced sulfur derived from TSR or partly by SR-AOM with dense hydrothermal fluids (Gadd *et al.*, 2017; Johnson *et al.*, 2018). Subseafloor replacement of diagenetic barite has been suggested as the dominant mechanism of Zn-Pb mineralization hosted in the Late Devonian strata in the Macmillan Pass district (Magnall *et al.*, 2020c). In the Macmillan Pass district (Fig. 1-4), CD-type sulfide mineralization overprints an early diagenetic barite and pyrite assemblage (Magnall *et al.*, 2016a). Stratiform barite formed during diagenesis and preserves evidence of open system MSR and SR-AOM processes at the SMTZ (Magnall *et al.*, 2016a). The stratiform mineralization later formed via the replacement of the diagenetic barite. Fluid inclusion microthermometric studies on coeval gangue minerals reveal that a relatively low salinity (~6 wt.% NaCl equiv.) and high temperature (270 – 300 °C) hydrothermal fluid was responsible for the formation of vein sulfide mineralization at the Tom and Jason deposits (Gardner & Hutcheon, 1985; Ansdell *et al.*, 1989; Magnall *et al.*, 2016b). Reduced sulfur generated via TSR was considered for the vein-hosted sulfide formation (Gardner & Hutcheon, 1985), with the generation of carbonic acid facilitating further porosity development through host rock dissolution (Magnall *et al.*, 2020c).

1.4.2. Discovery of the Boundary Zone Zn-Pb±Ag mineralization

The sulfide mineralization at the Boundary Zone occurs in an area where vein- and breccia-hosted Zn-Pb mineralization was earlier reported by Turner and Rhodes (1990). However, a recent exploration program starting in 2018 by Fireweed Metals Corporation (formerly Fireweed Zinc Limited) identified extensive mineralization that includes bedding parallel sulfides in broad stratigraphic intervals. These stratigraphic intervals comprise the Late Ordovician–Early Silurian Duo Lake Formation and Middle-Late Devonian Portrait Lake Formation strata, which is the first time that mineralization has been found in the two stratigraphic intervals in one location. This mineralization style at the Boundary Zone is unique among Zn-Pb deposits in the basin and provides an important natural laboratory to study the nature of sulfide mineralization hosted in multiple stratigraphic units.

1.5. Motivation for the current study and objectives

1.5.1. Paleoenvironmental reconstruction of premineralization diagenetic stages

One of the enigmatic features of CD-type metallogenesis during the Late Devonian in the Selwyn Basin is the spatial association between sulfide and stratiform barite deposits. Up until recently, the accepted paradigm has been that stratiform barite formed via hydrothermal processes, therefore sharing a genetic relationship with the sulfide deposits (e.g., Goodfellow, 1987). However, studies have since shown that barite at the Tom and Jason deposits, for example, likely formed via pre-ore diagenetic processes (Magnall *et al.*, 2016a), which suggests that despite being co-spatial, the barite and sulfides may not be co-genetic (Magnall *et al.*, 2020c).

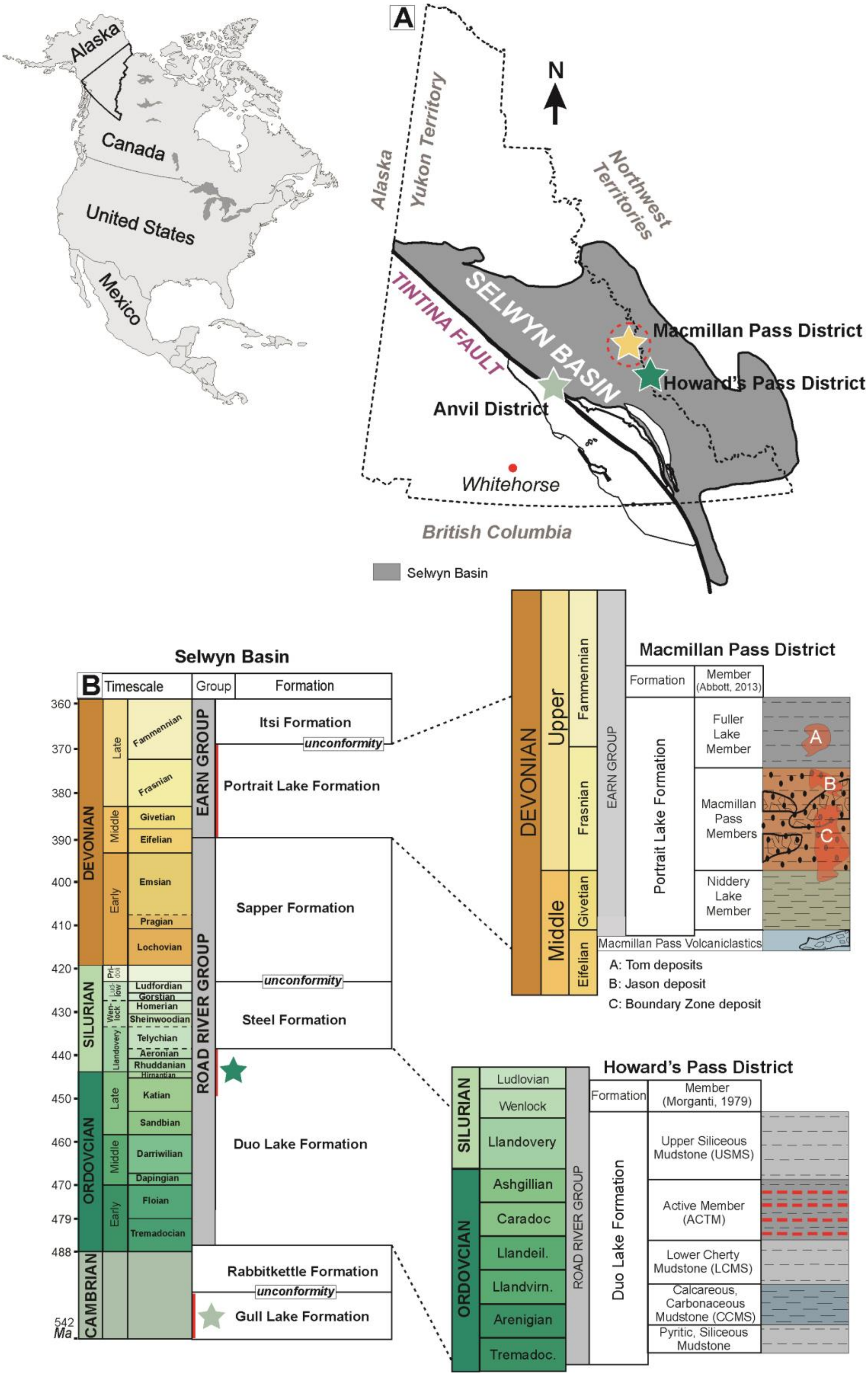

Fig. 1- 3: General overview of the geology and stratigraphy of the Selwyn Basin with details of the Macmillan Pass area: A) Location and simplified geological map of the Selwyn Basin in

the Yukon Territory, Canada. The three major Zn districts of the basin are denoted by stars, with that of the Macmillan Pass district highlighted in a red circle. Modified from Goodfellow (2007). B) Chronostratigraphic sequence through Cambrian to Devonian rocks of the Selwyn Basin. The Zn-Pb mineralized strata in the Howard's Pass and Macmillan Pass districts are further detailed in the blow out sequences. Modified from Nelson and Colpron (2007) and Fraser *et al.* (2020).

Fernandes *et al.* (2017) explored the formation mechanisms of the stratiform barite in unmineralized mudstones using $\delta^{34}S$ and $\delta^{18}O$ values from samples of bulk mineral separates. The authors suggested that barite formed during diagenesis around the SMTZ. However, bulk mineral separate techniques often do not resolve microscale heterogeneities (e.g., zonation resulting from overgrowths) that are almost always present as a result of multiple precipitation stages (Nabhan *et al.*, 2020; Yan *et al.*, 2020; Wang *et al.*, 2021). Furthermore, to develop a more complete understanding of diagenetic sulfur cycling, it is necessary to analyze $\delta^{34}S$ values in both oxidized (e.g., anhydrite, carbonate-associated sulfate, and barite) and reduced (e.g., pyrite) sulfur-bearing mineral phases (Fike *et al.*, 2015; Gomes & Hurtgen, 2015; Niu *et al.*, 2016; Jiang *et al.*, 2020).

Premineralization diagenetic processes are critical for ground preparation in host rocks of a number of CD-type deposits. The preservation of diagenetic barite and pyrite in regional stratiform barite deposits provides a valuable opportunity to investigate the origin of barite and dynamics of the diagenetic sulfur cycle in the host rocks to CD-type deposits in the Macmillan Pass district. *In-situ* microanalytical techniques such as secondary ion mass spectrometry (SIMS) mean it is possible to analyze individual grains of different sulfur-bearing phases (e.g., barite and pyrite) while retaining important petrographic information. This enables much more accurate models for the diagenetic sulfur cycle in the Selwyn Basin, which was particularly important for the development of the metal trap in nearby CD-type deposits (Magnall *et al.*, 2016a; Gadd *et al.*, 2017; Leighton *et al.*, 2021a).

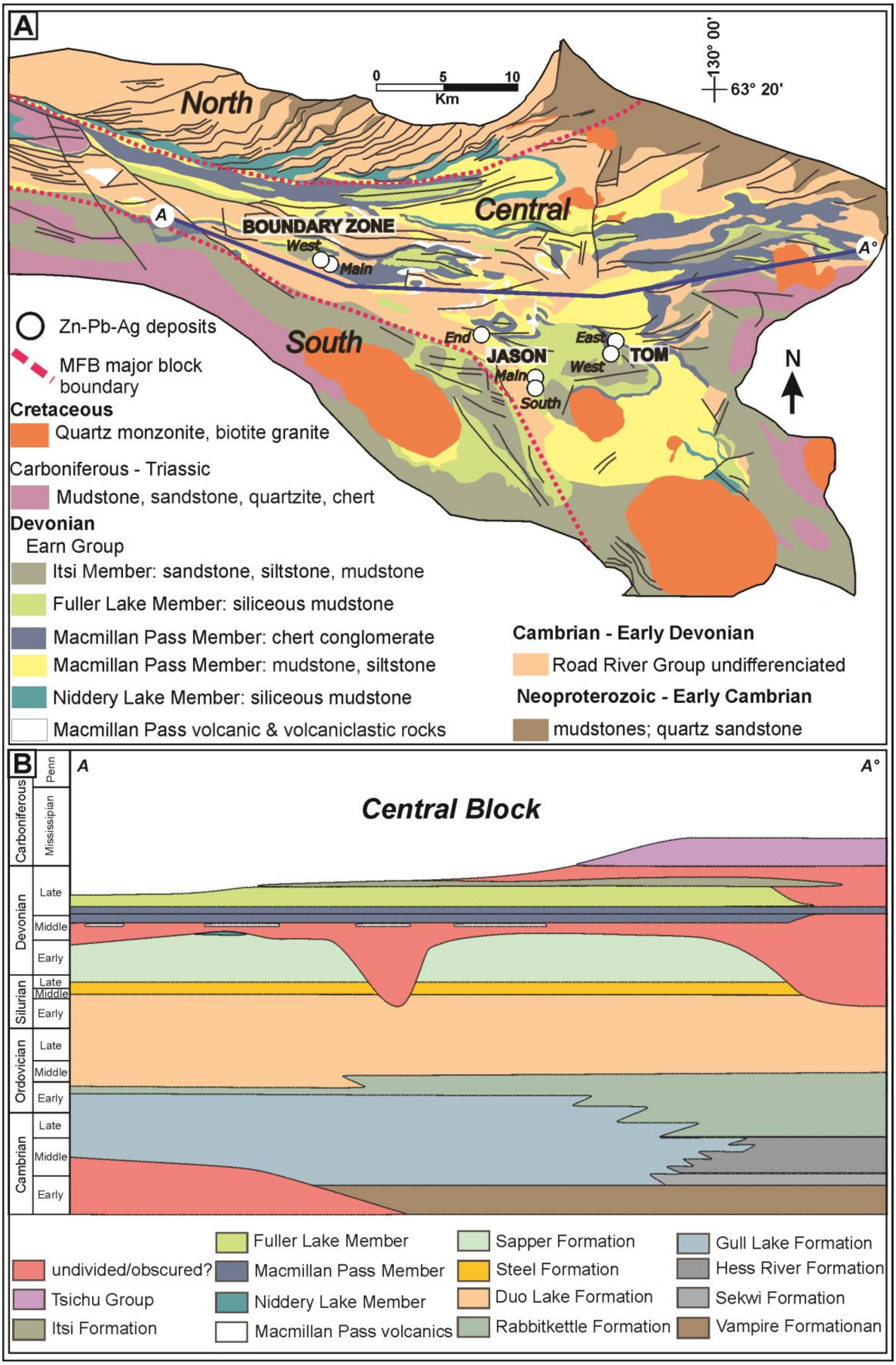

Fig. 1- 4: A) Geologic map of the Macmillan Fold Belt (MFB) region. Modified from Turner and Rhodes (1990) and Abbott (2013). B) Cross section through A to A° in A.

1.5.2. Timing of Zn-Pb±Ag mineralization in Selwyn Basin CD-type deposits and ore-forming fluid characteristics

The CD-type deposits in the Selwyn Basin are hosted by different stratigraphic units that were deposited during the Cambrian (Jennings & Jilson, 1986; Maynard & Okita, 1991), Late-Ordovician to Early Silurian (Morganti, 1979; Norford & Orchard, 1985; Johnson *et al.*, 2014), and Middle to Late Devonian (Carne, 1979; McClay, 1984; Bailes *et al.*, 1986; Turner, 1986; Goodfellow & Rhodes, 1990). Drilling at the Boundary Zone deposit has intersected sulfide mineralization in both the Late-Ordovician to Early Silurian Duo Lake Formation and the Middle to Late Devonian Portrait Lake Formation, which is the first time that mineralized rocks have been discovered at two stratigraphic levels in a single location; this provides a unique opportunity to investigate the timing of the ore formation in relation to host rock deposition and diagenesis.

Understanding the mineralogy, paragenetic sequence(s), and alteration assemblages of the host rocks is critical for interpreting the exact mechanisms and processes during sulfide mineralization. Moreover, our knowledge of the characteristics of ore-forming fluids in CD-type sulfide mineralization is limited by the small number of fluid inclusion studies on these deposits. The majority of the published microthermometry data have been generated on gangue mineral phases that give wide salinity and temperature ranges, and even this is limited to a few CD-type deposit locations. For example, fluid temperature constraints are mainly derived from fluid inclusion microthermometry of coeval quartz and carbonate mineral phases (Gardner & Hutcheon, 1985; Ansdell *et al.*, 1989; Leitch & Lydon, 2000; Rajabi *et al.*, 2015b; Magnall *et al.*, 2016b), with a very few obtained directly from sphalerite hosted fluid inclusions (Leach *et al.*, 2004; Polito *et al.*, 2006; Yarmohammadi *et al.*, 2016; Mahmoodi *et al.*, 2018).

Other geothermometric approaches that can provide indirect constraints include isotopic and thermodynamic modeling (Rye & Williams, 1981; Cooke *et al.*, 2000; Ireland *et al.*, 2004) and trace element geothermometry (Mladenova & Valchev, 1998). Recently, a sphalerite trace element geothermometer (GGIMFis) was developed based on the correlation of Ge, Ga, In, Mn, and Fe concentrations with temperatures of ore formation obtained directly from sphalerite-hosted fluid inclusion microthermometry (Frenzel *et al.*, 2016). The GGIMFis geothermometer has since been used to constrain ore-forming temperatures of Zn-Pb deposits that do not preserve measurable fluid inclusions (Bauer *et al.*, 2019; Schaarschmidt *et al.*, 2021; Luo *et al.*, 2022; Torró *et al.*, 2023; Yu *et al.*, 2024). Furthermore, the major, minor, and trace element composition of sphalerite constrains the element enrichment processes during sulfide precipitation and the nature of the chemistry of ore formation (Roberts, 1982; Graham *et al.*, 2009; Bauer *et al.*, 2019).

During the course of this thesis research, some of the fundamental questions around host rock diagenesis and hydrothermal processes involved in CD-type metallogenesis have been investigated using a variety of petrographic and geochemical datasets. In particular, the following questions form the primary focus of the doctoral thesis research:

- *How did the diagenetic sulfur cycle influence the isotopic composition of barite ($\delta^{34}S_{barite}$, $\delta^{18}O_{barite}$) and pyrite ($\delta^{34}S_{pyrite}$) in unmineralized Late Devonian strata? Following on, how does this paragenetically constrained isotopic data compare with equivalent datasets from regionally correlative mineralized samples at Macmillan Pass?*
- *What is the paragenesis and mineralogy of the recently discovered Boundary Zone Zn-Pb±Ag deposit, and how does it compare to other deposits in the Howard's Pass and Macmillan Pass districts that are hosted by the Duo Lake and Portrait Lake Formations?*
- *What fundamental physicochemical constraints (e.g., temperature and salinity) can be derived from fluid inclusions hosted by ore and gangue stage minerals at the Boundary Zone?*

1.6. Outline of the thesis

This thesis comprises five chapters that aim to answer the aforementioned questions. The chapters include a published article, a manuscript under review, and another manuscript that is in the advanced preparation stage.

Chapter 1 comprehensively introduces the need for Zn and critical raw materials, including Ge, Ga, In, and barite, for decarbonization and a low-carbon society. The introduction segues into the global distribution and mineral systems of CD-type Zn-Pb deposits. The development of different genetic models for the deposits is explored with particular focus on the Selwyn Basin, where the early understanding of these systems was developed, and the discovery of the Boundary Zone Zn-Pb±Ag deposit was made. The motivation for conducting this research is discussed in the chapter and provides the basis for establishing the critical research questions answered by the thesis.

Chapter 2 was published in the journal Frontiers in Earth Science in 2022 with the title "The Formation of Highly Positive $\delta^{34}S$ Values in Late Devonian Mudstones: Microscale Analysis of Pyrite ($\delta^{34}S$) and Barite ($\delta^{34}S$, $\delta^{18}O$) in the Canol Formation (Selwyn Basin, Canada)" by Haruna M. Grema, Joseph M. Magnall, Martin J. Whitehouse, Sarah A. Gleeson, and Hans-Martin Schulz (https://doi.org/10.3389/feart.2021.784824). A supplementary data publication is available online in the GFZ data repository with the title "Isotopic data of pyrite ($\delta^{34}S$) and barite ($\delta^{34}S$, $\delta^{18}O$) in the Canol Formation (Selwyn Basin, Canada)" by Haruna M. Grema, Joseph M. Magnall, Martin J. Whitehouse, Sarah A. Gleeson, and Hans-Martin Schulz. GFZ Data Services. https://doi.org/10.5880/GFZ.3.1.2021.006.

This chapter answers the first research question in the form of a study conducted on barite and pyrite from sixty-five (65) unmineralized mudstone samples obtained from nine (9) barite-bearing sections in the Mackenzie Mountains of the Selwyn Basin, Canada. High-resolution petrography and *in-situ* SIMS (sulfur and oxygen) isotopic analyses of barite and pyrite hosted in these samples were conducted to evaluate the nature of sulfur cycling in Late Devonian mudstones of the Selwyn Basin. This represents the first microscale paired barite and pyrite isotopic study on unmineralized mudstones away from CD-type mineralized locations in the Selwyn Basin. The study allows for an understanding of the nature of reduced and oxidized sulfur and the complete picture of the nature of diagenetic sulfur cycling and different sulfate reduction mechanisms.

Chapter 3 is under revision in the journal Economic Geology with the title "Mineralogy and paragenesis of the Boundary Zone Zn-Pb±Ag deposit, Yukon, Canada" by Haruna M. Grema, Joseph M. Magnall, Sarah A. Gleeson, Jack E. Milton, Alicja Wudarska, Anja M. Schleicher, and Hans-Martin Schulz. A data publication accompanies this manuscript and is available in the GFZ data repository titled "Petrography, quantitative mineralogy, and U-Pb geochronology of the Boundary Zone Zn-Pb±Ag deposit, Yukon, Canada" by Grema, H. M., Wudarska, A., Wilke, F. D. H., Schleicher, A. M., Milton, J. E., Magnall, J. M., Gleeson, S. A., and Schulz, H.-M. GFZ Data Services. https://doi.org/10.5880/GFZ.3.1.2024.007.

Please access via https://dataservices.gfz-potsdam.de/panmetaworks/review/4d977202cbc26dabe4526cfbbe177869faff51af98518d4411dadc5e14d71768/.

The chapter answers the second research question and provides the first description of the stratabound and vein- and breccia-hosted Zn-Pb±Ag occurrence at the newly discovered

Boundary Zone deposit in the Macmillan Pass district. Seventy-three (73) drill core samples were collected from nine (9) drill holes that are spatially distributed in the deposit location. These samples were studied using multiple petrographic (binocular, reflected, and transmitted light microscopy, n=80), mineralogical (whole rock and clay fraction X-ray diffractometry, n=73), and U-Pb geochronological (n=6) techniques.

The Boundary Zone mineralization was observed to have formed in two contrasting ore-forming stages that are preceded by a premineralization stage dominated by the early diagenetic formation of quartz, barite, pyrite, fluorapatite, and phyllosilicates. The first ore stage comprises stratabound sulfides formed via subseafloor replacement of radiolarian tests and barite and via nucleation on pre-ore pyrite. The second ore stage crosscuts the early mineralization and constitutes the high-grade volumetrically major mineralization in veins and breccias. A prolonged mineralization period is suggested for the Boundary Zone ore formation, spanning from diagenesis periods of the mudstones to possibly the deformation episodes associated with the Cordilleran orogeny in the Selwyn Basin. The findings from this study have significant implications for exploration strategies in the Macmillan Pass district and similar CD-type geological settings.

Chapter 4 addresses the third research question concerning the fundamental physicochemical properties of the mineralizing fluids preserved in fluid inclusions at the Boundary Zone. The chapter will be submitted to a journal with the title "Microthermometry and trace element chemistry of sphalerite in the Boundary Zone clastic-dominated type Zn-Pb system, Yukon, Canada" by Haruna M. Grema, Joseph M. Magnall, Sarah A. Gleeson, Marta Sośnicka, Jack E. Milton, Vitor R. Barrote, and Hans-Martin Schulz. A data publication is deposited in the GFZ data repository with the title "Sphalerite major, trace element chemistry and fluid inclusion microthermometry data from the Zn-Pb±Ag Boundary Zone deposit, Yukon, Canada" by Haruna M. Grema, Marta Sośnicka, Vitor R. Barrote, Joseph M. Magnall, Sarah A. Gleeson, Jack E. Milton, and Hans-Martin Schulz. GFZ Data Services. https://doi.org/10.5880/GFZ.3.1.2024.008.

Please access via https://dataservices.gfz-potsdam.de/panmetaworks/review/66434e4a4731d6ada2a01378e4fbfa88375c14b81a0168c15b7140db3540ee3f/.

Microthermometry and Raman spectroscopy (on fluid inclusions hosted in sphalerite and quartz) were combined with sphalerite major, minor, and trace element chemistry obtained from electron probe microanalysis (EPMA) and *in-situ* laser ablation-inductively coupled plasma mass spectrometry (LA-ICP-MS). The study demonstrates how critical metal enrichments in sphalerite vary across the generations and are incorporated into the crystal lattice via direct and couple substitutions. The study also provides the first direct sphalerite fluid inclusion microthermometric measurements from CD-type mineralization in the Selwyn Basin and has been successfully coupled with sphalerite trace element geothermometry, enabling temperature constraints to be derived from the different stages of the paragenesis. It also provides important salinity constraints and evidence of fluid mixing between a high salinity – low-temperature fluid and a low salinity – high-temperature fluid.

Chapter 5 comprises the concluding remarks for the thesis and studies conducted herein. Potential directions for future research are also highlighted.

CHAPTER 2

The formation of highly positive δ^{34}S values in Late Devonian mudstones: microscale analysis of pyrite (δ^{34}S) and barite (δ^{34}S, δ^{18}O) in the Canol Formation (Selwyn Basin, Canada)

Haruna M. Grema[1,2,], Joseph M. Magnall[1], Martin J. Whitehouse[3], Sarah A. Gleeson[1,2], Hans-Martin Schulz[1]*

[1]GFZ German Research Centre for Geosciences, Potsdam, Germany
[2]Institute of Geological Sciences, Freie Universität Berlin, Berlin, Germany
[3]Department of Geosciences, Swedish Museum of Natural History, Stockholm, Sweden
[*]Corresponding author: Haruna M. Grema. Email address: hgrema@gfz-potsdam.de

Keywords: *sulfur isotopes, microscale SIMS analyses, anaerobic oxidation of methane, microbial sulfate reduction, sulfur cycling, Late Devonian*

The Chapter is published in Frontiers in Earth Science (https://doi.org/10.3389/feart.2021.784824) under the terms of the CC BY license (https://creativecommons.org/licenses/by/4.0/.

A supplementary data publication is available online in the GFZ Data Repository (https://doi.org/10.5880/GFZ.3.1.2021.006).

2.1. Abstract

The sulfur isotope composition of pyrite in marine sedimentary rocks is often difficult to interpret due to a lack of precise isotopic constraints for coeval sulfate. This study examines pyrite and barite in the Late Devonian Canol Formation (Selwyn Basin, Canada), which provides an archive of $\delta^{34}S$ and $\delta^{18}O$ values during diagenesis. Scanning electron microscopy (SEM) has been combined with microscale secondary ion mass spectrometry (SIMS) analysis (n= 1032) of pyrite ($\delta^{34}S$) and barite ($\delta^{34}S$ and $\delta^{18}O$) on samples collected from nine stratigraphic sections of the Canol Formation. Two paragenetic stages of pyrite and barite formation have been distinguished, both replaced by barium carbonate and feldspar. The $\delta^{34}S_{barite}$ and $\delta^{18}O_{barite}$ values from all sections overlap, between +37.1‰ to +67.9‰ (median = +45.7‰) and +8.8‰ and +23.9‰ (median = +20.0‰), respectively. Barite morphologies and isotopic values are consistent with precipitation from diagenetically modified porewater sulfate (sulfate resupply << sulfate depletion) during early diagenesis. The two pyrite generations (Py-1 and Py-2) preserve distinct textures and end-member isotopic records. There is a large offset from coeval Late Devonian seawater sulfate in the $\delta^{34}S_{pyrite}$ values of framboidal pyrite (-29.4‰ to -9.3‰), consistent with dissimilatory MSR during early diagenesis. The Py-2 is in textural equilibrium with barite generation 2 (Brt-2) and records a broad range of more positive $\delta^{34}S_{Py-2}$ values (+9.4‰ to +44.5‰). The distinctive highly positive $\delta^{34}S_{pyrite}$ values developed from sulfate-limited conditions around the sulfate methane transition zone (SMTZ). We propose that a combination of factors, including low sulfate concentrations, MSR, and sulfate reduction coupled to anaerobic oxidation of methane (SR-AOM), led to the formation of highly positive $\delta^{34}S_{pyrite}$ and $\delta^{34}S_{barite}$ values in the Canol Formation. The presence of highly positive $\delta^{34}S_{pyrite}$ values in other Late Devonian sedimentary units indicates that diagenetic pyrite formation at the SMTZ may be a more general feature of other Lower Paleozoic basins.

2.2. Introduction

Methane is a powerful greenhouse gas that is produced during all stages of organic matter maturation (Knittel & Boetius, 2009). Changes in the flux of methane (from sediment to oceans) have been linked with major climatic impacts at particular stages of Earth history (e.g., Dickens *et al.*, 1995). In modern ocean sediments, sulfate reduction coupled with the anaerobic oxidation of methane (SR-AOM) accounts for approximately 80% of methane oxidation, thereby regulating the release of methane into the atmosphere (Egger *et al.*, 2018). Authigenic pyrite (FeS_2) and barite ($BaSO_4$) can both form as by-products of SR-AOM, meaning these phases provide a potential archive of methane oxidation (e.g., Borowski *et al.*, 2013; Wood *et al.*, 2021)

Pyrite and barite also provide an important archive for sulfur isotopes in marine environments, which can be used to reconstruct biogeochemical processes that link the sulfur, carbon, and iron cycles (Bottrell & Newton, 2006; Fike *et al.*, 2015). For example, pyrite forms as a by-product of microbial sulfate reduction (MSR) and SR-AOM. There is a large isotopic fractionation associated with MSR due to the differential reaction rates of the sulfate isotopologues ($^{32}S^{16}O_4 > {}^{34}S^{18}O_4$; Kaplan & Rittenberg, 1964; Seal *et al.*, 2000; Canfield, 2001a). As a result, pyrite often preserves $\delta^{34}S$ values that are offset relative to coeval seawater sulfate ($\delta^{34}S_{pyrite} << \delta^{34}S_{seawater}$; Fike *et al.*, 2015). Stratigraphic variability in $\delta^{34}S$ values has been used to infer regional to global-scale changes in the sulfur cycle that reflect enhanced pyrite burial (e.g., Goodfellow & Jonasson, 1984) and the size of the marine sulfate reservoir (e.g., Kah *et al.*, 2004).

More recently, studies have shown how sulfur isotope variability may instead be controlled by sedimentary facies and diagenetic processes (Magnall *et al.*, 2016a; Pasquier *et al.*, 2017; Marin-Carbonne *et al.*, 2018; Bryant *et al.*, 2019; Richardson *et al.*, 2019; Bryant *et al.*, 2020; Pasquier *et al.*, 2021). For example, the progressive modification of pore fluid sulfate by MSR during diagenesis can result in strong isotopic gradients and a range of $\delta^{34}S_{pyrite}$ values, depending on the location of pyrite formation in the sediment (Canfield, 2001b; Canfield *et al.*, 2010). In particular, studies have benefited from the generation of isotopic data using microscale techniques (e.g., secondary ion mass spectrometry; SIMS), which enable the determination of paragenetically constrained phase specific $\delta^{34}S$ values. However, there are relatively few examples where $\delta^{34}S_{pyrite}$ and proxies for coeval $\delta^{34}S_{sulfate}$ values have been paired at high spatial resolutions (e.g., Magnall *et al.*, 2016a). As a result, the origin of highly positive or 'superheavy' $\delta^{34}S_{pyrite}$ values ($\delta^{34}S_{pyrite} > \delta^{34}S_{SO4}$; Ries *et al.*, 2009) can be particularly difficult to constrain. For example, highly positive $\delta^{34}S$ values in pyrite in sedimentary units from the Late Devonian period have been linked with MSR in low sulfate water/sediment columns (Goodfellow & Jonasson, 1984; Sim *et al.*, 2015; Zhang *et al.*, 2020) or formation through hydrothermal or thermochemical sulfate reduction (TSR; Yan *et al.*, 2020).

The Late Devonian was one of the major periods of organic carbon burial in Earth history (Klemme & Ulmishek, 1991). In the Selwyn Basin, Canada, clastic-dominated type (CD-type)

Zn-Pb ± Ba mineralization is hosted by Late Devonian mudstones (Goodfellow & Jonasson, 1984; Goodfellow, 1987; Hanor, 2000; Johnson *et al.*, 2009; Farquhar *et al.*, 2010; Magnall *et al.*, 2020c). Bedded barite is hosted by unmineralized Late Devonian mudstones in the Selwyn Basin (Fernandes *et al.*, 2017), although the spatial association with the CD-type massive sulfide deposits meant the barite was considered to be a distal expression of sedimentary exhalative (SEDEX) hydrothermal activity (Large *et al.*, 2005; Leach *et al.*, 2005a; Goodfellow & Lydon, 2007; Leach *et al.*, 2010). In this SEDEX model, highly enriched δ^{34}S values in pyrite and barite have been interpreted to indicate nearly complete sulfate reduction during MSR in a stagnant and stratified anoxic water column (Goodfellow & Jonasson, 1984).

Recent studies, however, have highlighted how barite may have been formed by diagenetic processes before being subsequently replaced during hydrothermal sulfide mineralization (Johnson *et al.*, 2009; Magnall *et al.*, 2016a; Johnson *et al.*, 2018; Magnall *et al.*, 2020b; Reynolds *et al.*, 2021). In the diagenetic model, it is proposed that the barite formed in a setting analogous to cold seep environments where methane is oxidized by sulfate through microbial metabolic processes (Greinert *et al.*, 2002; Paytan *et al.*, 2002; Torres *et al.*, 2003; Canet *et al.*, 2014). The sulfate methane transition zone (SMTZ) is a diagenetic redox boundary in organic carbon-bearing sediments that is an important habitat for a consortium of sulfate-reducing and methanotrophic microorganisms (Torres *et al.*, 1996; Machel, 2001; Arning *et al.*, 2015). Organic matter is converted during early diagenesis in such sediments, and the water-soluble products (e.g., acetic acid, CO_2, and CH_4) change the porewater composition (e.g., pH), resulting in a series of hydrogeochemical reactions of dissolution (e.g., feldspar) or precipitation (e.g., barite). Diverse $\delta^{34}S_{barite}$ values have been recorded at modern cold seeps (up to ~ 40‰; Greinert *et al.*, 2002; Wood *et al.*, 2021) that are correspondingly similar to highly positive δ^{34}S values in Paleozoic bedded barite (Johnson *et al.*, 2009; Canet *et al.*, 2014). Such highly positive $\delta^{34}S_{barite}$ values are interpreted to result from the residual sulfate pool at the SMTZ (Canet *et al.*, 2014; Clark *et al.*, 2015). When methane oxidation is coupled to sulfate reduction at the SMTZ and in the presence of an iron source, pyrite is formed at the SMTZ, and this pyrite can have positive $\delta^{34}S_{pyrite}$ values (e.g., Borowski *et al.*, 2013).

This study integrates high-resolution scanning electron microscopy petrography of barite (+ associated barium phases) and pyrite, together with microscale isotopic microanalyses of $\delta^{34}S_{pyrite}$, $\delta^{34}S_{barite}$, and $\delta^{18}O_{barite}$ of selected samples from the Late Devonian Canol Formation of the Selwyn Basin. We have targeted samples containing both barite and pyrite to develop paired isotopic constraints on the evolution of sulfur during diagenesis. In particular, we have focused on the precise mechanism by which highly positive $\delta^{34}S_{pyrite}$ developed in the Canol Formation and discussed the implications for interpreting sulfur isotopes in similar settings.

2.3. Regional geology

The Selwyn Basin (Fig. 2-1a) is primarily made up of Neoproterozoic to Mississippian, deep to shallow marine siliciclastics, and platform carbonate strata, deposited on the margin of the ancestral North American continent (Mair *et al.*, 2006).

Formation of the basin stems from widespread protracted extensional tectonics of the Rodinian supercontinent that led to the re-emergence of the Laurentian craton between 825 to 740 Ma (Martel *et al.*, 2011) with resulting development of the epicontinental margin and Selwyn Basin during the Ediacaran – Cambrian periods (Gordey & Anderson, 1993). The oldest strata in the basin consist of the syn-rift Neoproterozoic-Terreneuvian Windermere Supergroup overlain by basinal post-rift Paleozoic sedimentary rocks with a combined total thickness of around 7,500 m (Ootes *et al.*, 2013). Abrupt episodic extension and volcanism during the Early Cambrian, Middle Ordovician, and Devonian are characterized by mafic volcanics within the platform carbonate and the basinal strata (Goodfellow & Lydon, 2007). Collision with an island arc during the Late Devonian is suggested to have led to deformation and subsequent incorporation of the Selwyn Basin strata into the fold and thrust belt of the North American Cordillera (Mair *et al.*, 2006). A sudden change in depositional regime during the Late Devonian led to the deposition of siliciclastic sediments that spread from the margin of Laurentia toward the interior of the craton (Martel *et al.*, 2011). Together with an overlying turbidite unit, the siliciclastic sediments are collectively known as the Earn Group (Fig. 2-1b; Gordey, 2013; Ootes *et al.*, 2013).

The Earn Group is subdivided into an upper unit of coarse-grained siliciclastic turbidites and sandstones of the Imperial Formation and a lower Canol Formation (Martel *et al.*, 2011). The Canol Formation is of Upper-Devonian (Frasnian – early Famennian) age and consists primarily of dark grey to black mudstones locally calcareous or siliceous with occasional carbonate concretions of variable sizes (Mair *et al.*, 2006; Martel *et al.*, 2011). The formation is extensively widespread in the Mackenzie Mountains region, with variable thickness that reaches 400 m (Cecile *et al.*, 1983; Martel *et al.*, 2011; Gadd *et al.*, 2016a). The depositional setting of the Canol Formation has been interpreted to be deep-water marine, formed during the early stages of foredeep basin development (Cecile *et al.*, 1983).

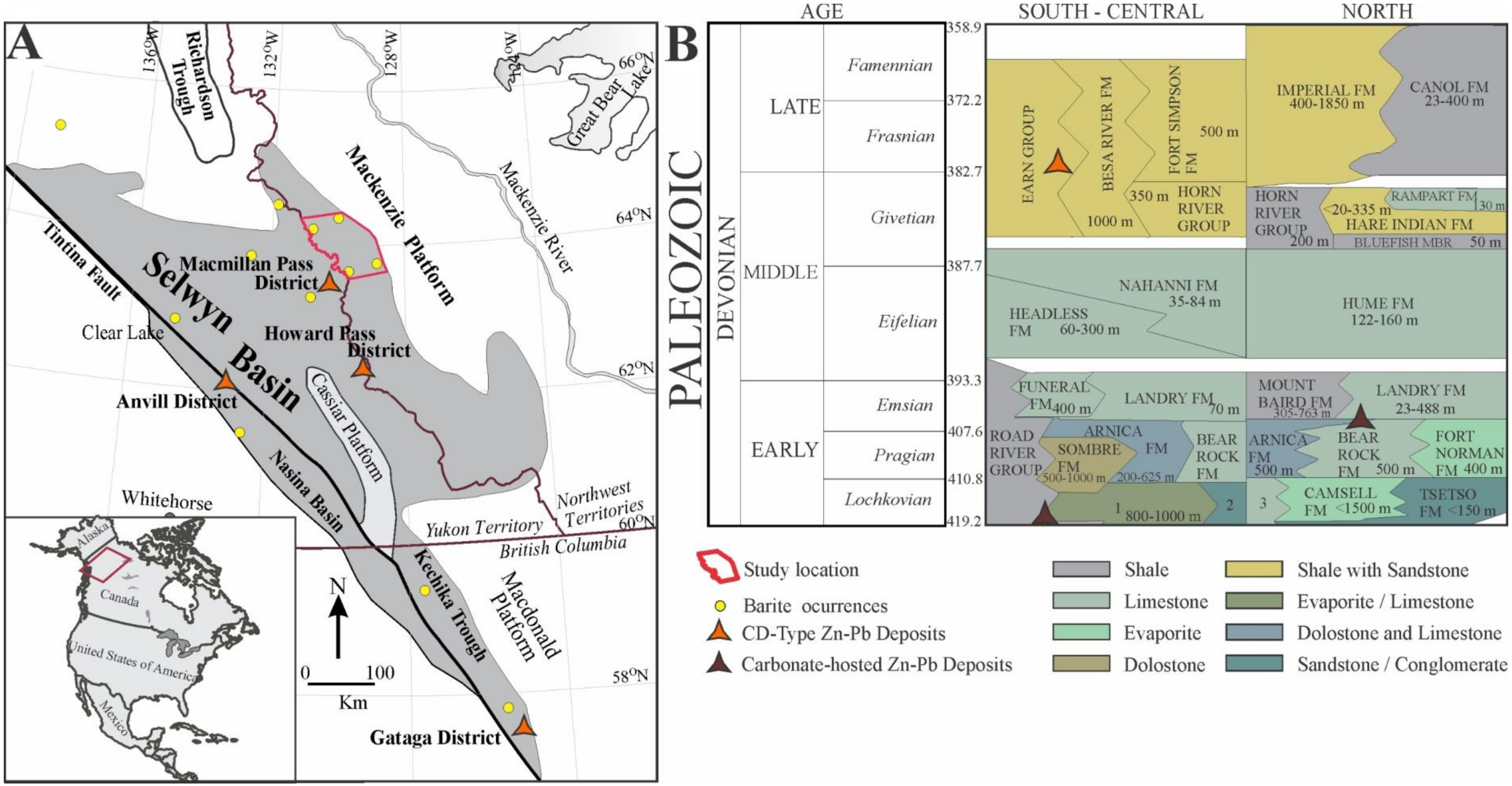

Fig. 2- 1: Regional geology and stratigraphy of the Selwyn Basin within the North American continent, with red rectangle indicating map A. A) Simplified geologic map of Paleozoic sedimentary units in the Selwyn Basin bounded by the Tintina Fault in the west and the Mackenzie carbonate platform in the east (modified from Goodfellow & Lydon, 2007). Major barite and clastic-dominated (CD-type) Zn-Pb deposits are indicated by the yellow cycle and red triangle, respectively. The green area in B depicts the current study location. B) Devonian stratigraphic sequence of the Selwyn Basin from south to north (modified from Martel *et al.*, 2011; Ootes *et al.*, 2013; Morrow, 2018). 1 = Camsel – Cadillac Delorme Formation. 2 = Tsetso Formation. 3 = Unnamed formation.

2.4. Local geology

This study builds on an earlier study by Fernandes *et al.* (2017) located northeast of the Macmillan Pass district (Fig. 2-1a). The sedimentary rocks of the Canol Formation in the study area consist of gently open-folded, bedded coarser-grained siliciclastics and organic-rich mudstones that are moderate to steeply dipping and weathering to silver color (Fernandes, 2011; Fernandes *et al.*, 2017). These lithologic units host several stratiform barite beds that form barite horizons in equivalent Devonian stratigraphic intervals on a regional scale (e.g., Goodfellow & Jonasson, 1984; Smith *et al.*, 1993; Magnall *et al.*, 2016a; Fernandes *et al.*, 2017).

In the Northwest Territories part of the Selwyn Basin, 22 to 72 m thick barite sequences occur within stratigraphic sections at Bunk-1, Bunk-2, Cowan, NAFCAC-1, NAFCAC-2, Anita, Axe, Harp, and Wise locations (Fig. 2-2, 2-3; Fernandes *et al.*, 2017). These barite-bearing sections occur as topographic highs in a broad 200 km long NW-SE trend, are all confined to the upper parts of the Canol Formation, below the unconformity with the fine-grained siliciclastics of the Imperial Formation, and are considered to be Frasnian in age (Martel *et al.*, 2011; Fernandes *et al.*, 2017).

Mineralogically, the mudstones consist of varying amounts of clay minerals, quartz, and organic matter, with barite, pyrite, and Ba-bearing feldspar (hyalophane (K, Ba) [Al (Si, Al)$_3$O$_8$] and cymrite $BaAl_2Si_2(O, OH)_8 \cdot H_2O$) constituting the major accessory minerals (Fernandes, 2011). Fernandes *et al.* (2017) further describe the intricate relationship between barite and Ba-bearing carbonates and silicates; witherite ($BaCO_3$) forms a textural association with barite, replacing both laminated and nodular barite grains, while hyalophane and cymrite are 0.5 to 2 mm crystals found replacing barite and witherite in both the laminae and nodules (Fernandes *et al.*, 2017).

2.5. Bedded barite mineralization style in the Canol Formation

There are two types of barite (laminated and nodular) identified in the upper Canol Formation that occur interlaminated together; nodular barite is dominant over the laminated form (Fig. 2-3; Fernandes *et al.*, 2017). Brief descriptions of the barite forms from Fernandes *et al.* (2017) are highlighted below and shown in Fig. 2-4.

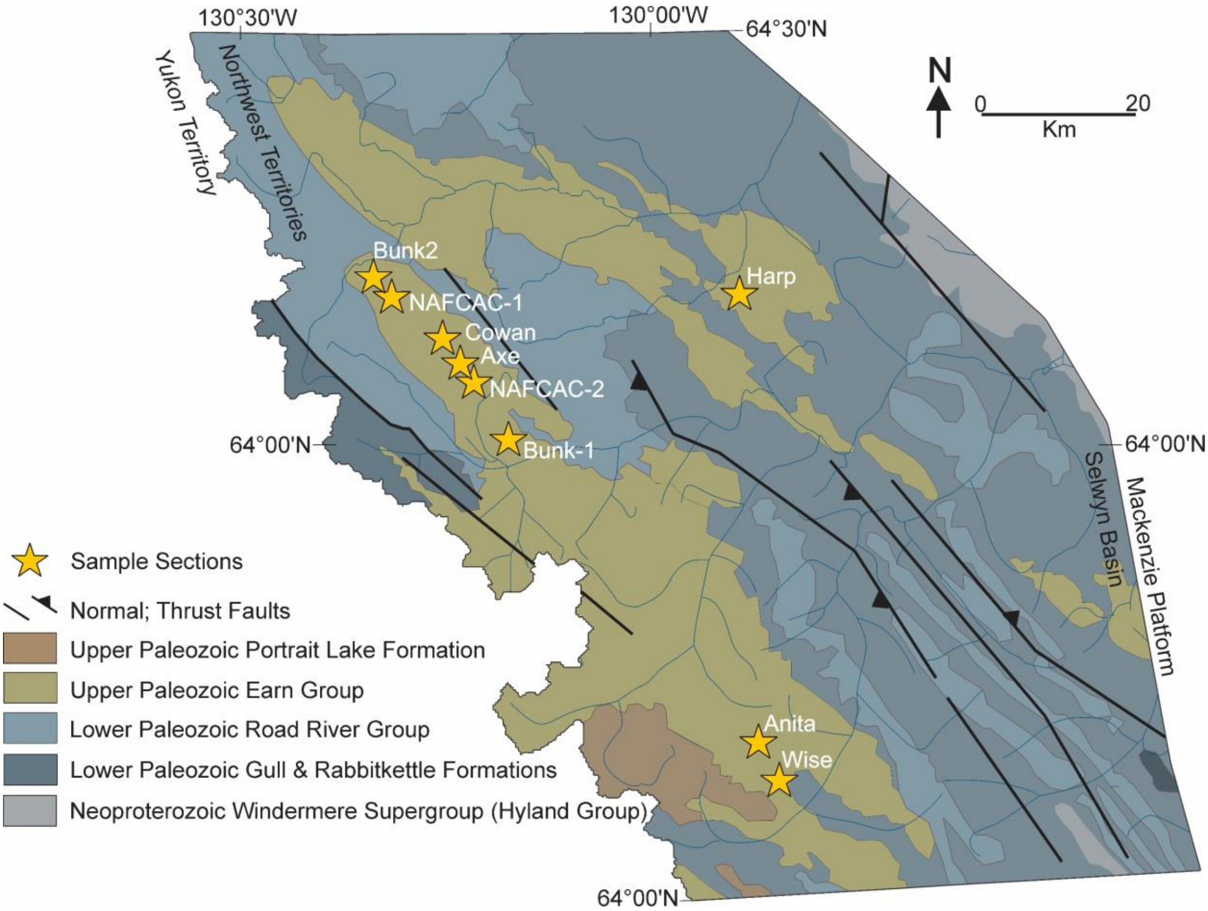

Fig. 2- 2: Geologic map of the study area showing the sampled stratigraphic sections. Modified from Ootes *et al.* (2013) and Fernandes *et al.* (2017).

The barite nodules in mudstones are spherical, ellipsoidal, or irregular (Fig. 2-4a-c). The nodules often contain barite crystals that are rosette or tabular with a size range from less than 100 µm to 1.2 cm (Fig. 2-4e). Witherite, hyalophane, cymrite, and quartz are associated primarily with the barite crystals (Fig. 2-4g, h). The laminated barite has been described to primarily occur as clusters of intergrown anhedral crystals within 50 -100 µm laminae (e.g., Fig. 2-4d). Associated minerals include pyrite, cymrite, quartz, and hyalophane with intercalated clay-rich laminae (Fig. 2-4h). Grey mudstone with about a meter of laminated and nodular barite occurs in the Bunk-2 section between dark grey siltstone hosting nodular barite (Fig. 2-4i). The barite crystals range from <10 µm to 70 µm, either concordant with the lamina or irregular with no specific direction.

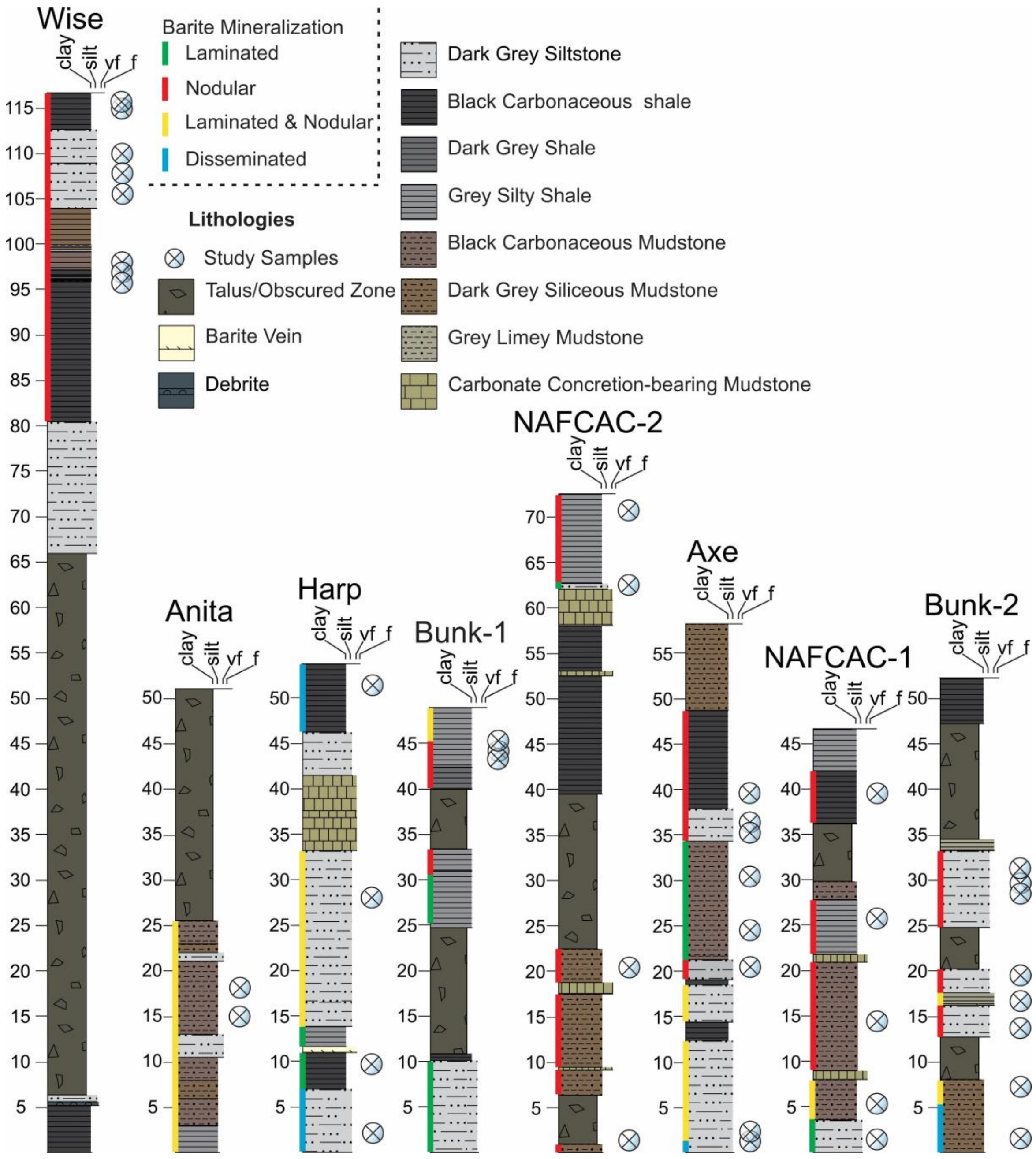

Fig. 2- 3: Lithostratigraphic profiles of barite-bearing upper sections of the Canol Formation. Modified from Fernandes *et al.* (2017).

2.6. Methodology

2.6.1. Sampling

Sixty-five (65) mudstone samples from the nine barite-bearing sections from the suite of samples investigated by Fernandes (2011) were resampled. Samples containing pyrite and barite were targeted, and their mineralogical and paragenetic relationships were examined using binocular microscopy as a first step.

2.6.2. Petrography

Detailed petrographic examination of the mineralogical and textural relationships was carried out on thin sections using an Olympus BX51 microscope, equipped with a Sc50 camera, in transmitted and reflected light settings. Polished thin sections were additionally prepared and carbon-coated to a thickness of 20 nm for further examination and imaging using an electron probe microanalyzer (EPMA) and scanning electron microscope (SEM). Backscatter electron images (BSE) were obtained using Japan Electron Optics Limited (JEOL) JXA-8530F Hyperprobe, equipped with a wavelength and energy dispersive spectrometry combined system. The EPMA was operated using a beam diameter between 1 to 3 µm, beam current of 15 nA, and accelerating potential of 15 kV, in secondary electron (SE) and BSE modes. Organic petrography using a standard reflection microscope showed that randomly distributed organoclasts occur as < 2µm sized particles. Due to the thermal overmaturity, the particles are inertinite and prevent a broader reconstruction of organic matter type.

2.6.3. Secondary ion mass spectrometry analyses of sulfur and oxygen isotopes

Microdrills of regions of interest (n= 54) were made on polished sections to obtain suitable subsamples, using a 4 mm diameter diamond core drill, from the whole sample suite in Fernandes (2011). Several representative subsamples were cast into 25 mm epoxy pucks, together with reference materials (RMs) of pyrite S0302A ($\delta^{34}S_{\text{V-CDT}} = 0.0 \pm 0.2$‰; Liseroudi *et al.*, 2021) and barite S0327 ($\delta^{34}S_{\text{V-CDT}} = 11.0 \pm 0.5$ ‰; $\delta^{18}O_{\text{V-SMOW}} = 21.3 \pm 0.2$ ‰; Magnall *et al.*, 2016a).

Re-examination and further BSE imaging were carried out with EPMA after carbon-coating, with subsequent 30 nm gold coating added to the mounts before isotope measurement. Microscale isotopic analyses were carried out using a Cameca IMS1280 large-geometry secondary ion mass spectrometer (SIMS) operated in multi-collector mode at the NordSIMS laboratory, Stockholm, Sweden. For the measurements, a $^{133}Cs^{+}$, 20 kV impact energy primary beam was utilized. The beam current was 1 nA for all barite analyses, and the larger pyrite targets, yielding a ca. 10 µm spot; a 400 – 500 pA beam was used for smaller pyrite targets yielding a ca. 6 µm spot. A normal incidence low-energy electron flooding gun was utilized for charge compensation. Sulfur and oxygen isotopes were determined in separate analytical sessions in which secondary ion signals of ^{32}S and ^{34}S or ^{16}O and ^{18}O were measured simultaneously in two Faraday cups.

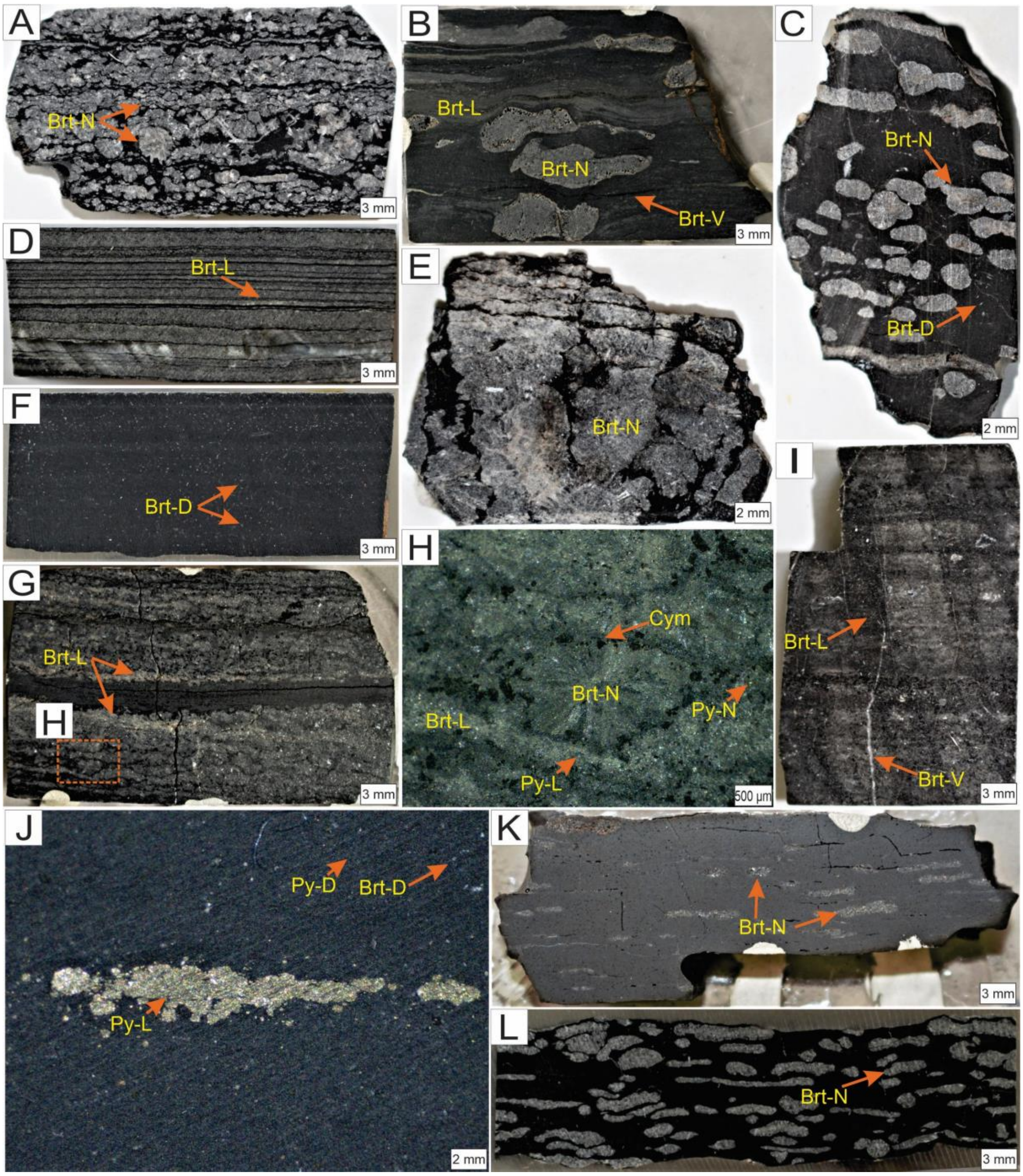

Fig. 2- 4: Representative hand specimen and binocular photographs of mudrocks showing different forms of barite mineralization. A) Black carbonaceous mudstone with nodular barite grains (Brt-N). B) Dark grey shale with thin barite laminations (Brt-L) and nodular (Brt-N) irregular barite grains. Dark grey barite veins (Brt-V) are observed to have formed parallel to the bedding. C) Dark grey siliceous mudstone showing nodular barite. D) Grey siliceous shale with thinly laminated barite. E) Large barite nodules within dark grey siltstone. F) Black carbonaceous mudstone. Disseminated barite (Brt-D) is commonly associated with anhedral quartz grains. G) Laminated and rosette nodular barite with stratiform pyrite and barite are intergrown with cymrite (cym) in H. I) Rare lime dark grey mudstone with discordant barite vein. J) Binocular microscope photograph of black mudstone with disseminated pyrite (Py-D) and aggregates of stratiform pyrite (Py-L). K) Dark grey siliceous shale showing ellipsoidal barite nodules parallel to the bedding. L) Highly irregular barite nodules in black carbonaceous shale.

A total of 1032 sulfur and oxygen isotope measurements ($\delta^{34}S_{pyrite}$ = 200; $\delta^{34}S_{barite}$ = 485, $\delta^{18}O_{barite}$ = 338) on pyrite and barite grains were obtained using automated analytical sequences; with every 6 to 7 measurements followed by 1 to 2 RM analyses. The $\delta^{34}S_{barite}$ and $\delta^{18}O_{barite}$ values measurements were carried out on the same barite grains to capture the covariation between the sulfur and oxygen isotopic systems. Within-session drift and instrumental mass fractionation (IMF) were corrected using the regularly interspersed analyses of the RMs in each session. The IMF-corrected $^{34}S/^{32}S$ ratios are reported relative to Vienna Canyon Diablo Troilite (V-CDT) and $^{18}O/^{16}O$ ratios relative to Vienna Standard Mean Ocean Water (V-SMOW), using conventional delta notation:

$$\delta^{34}\mathrm{S}\ (‰, \mathrm{V-CDT}) = \left[\left(\frac{(^{34}\mathrm{S}/^{32}\mathrm{S})\ \mathrm{sample}}{(^{34}\mathrm{S}/^{32}\mathrm{S})\ \mathrm{V{-}CDT}}\right) - 1\right] \times 1000$$

$$\delta^{18}\mathrm{O}\ (‰, \mathrm{V-SMOW}) = \left[\left(\frac{(^{18}\mathrm{O}/^{16}\mathrm{O})\ \mathrm{sample}}{(^{18}\mathrm{O}/^{16}\mathrm{O})\ \mathrm{V{-}SMOW}}\right) - 1\right] \times 1000$$

External analytical reproducibility (1 σ) was typically ± 0.04‰ $\delta^{34}S$ for pyrite, ± 0.15‰ $\delta^{34}S$, and ± 0.12‰ $\delta^{18}O$ for barite. The reproducibility for each session is the standard deviation of the reference material measurements in that session. For any individual measurement, the external uncertainty is propagated together with the within-run uncertainty for an overall value. Post SIMS SEM imaging was carried out on each barite and pyrite spot for confirmation of target integrity; measurements on pyrite-barite grain boundaries were discarded (n= 14).

2.7. Results

2.7.1. Mineralogy and paragenesis

Different pyrite and barite formation stages have been defined in terms of shape, size, and distribution, broadly comparable across the different stratigraphic intervals (Fig. 2-5). The different stages of pyrite and barite are described in terms of their relative timing of formation (paragenesis). Detailed descriptions are given below.

Stage 1: The earliest stage of pyrite (Py-1) comprises framboids present in all the sections (apart from NAFCAC-2 and Anita). Framboidal pyrite is particularly enriched in the mudstones of the Harp and Axe sections. Py-1 is commonly located in the inter-and intra-granular pore space of the mudstone laminae and nodules (Fig. 2-6a, b). The framboids have a broad size distribution, mostly <45 µm (Fig. 2-6c), although spherical to irregular clusters of polyframboids reach up to 80 µm in diameter (Fig. 2-6d). The individual framboid nanocrystals are <5 µm, mostly equant, cubic, or pyritohedral (Fig. 2-6c). The first stage of barite (Brt-1) is microcrystalline, <35 µm with subhedral to euhedral disseminated grains, and is found in mudstones in all sections. The Brt-1 is intergrown with quartz and cymrite in clay-rich or quartz-dominated matrices (Fig. 2-7a - d). The Brt-1 and Py-1 grains rarely occur together, and establishing their paragenetic relationship was consequently difficult.

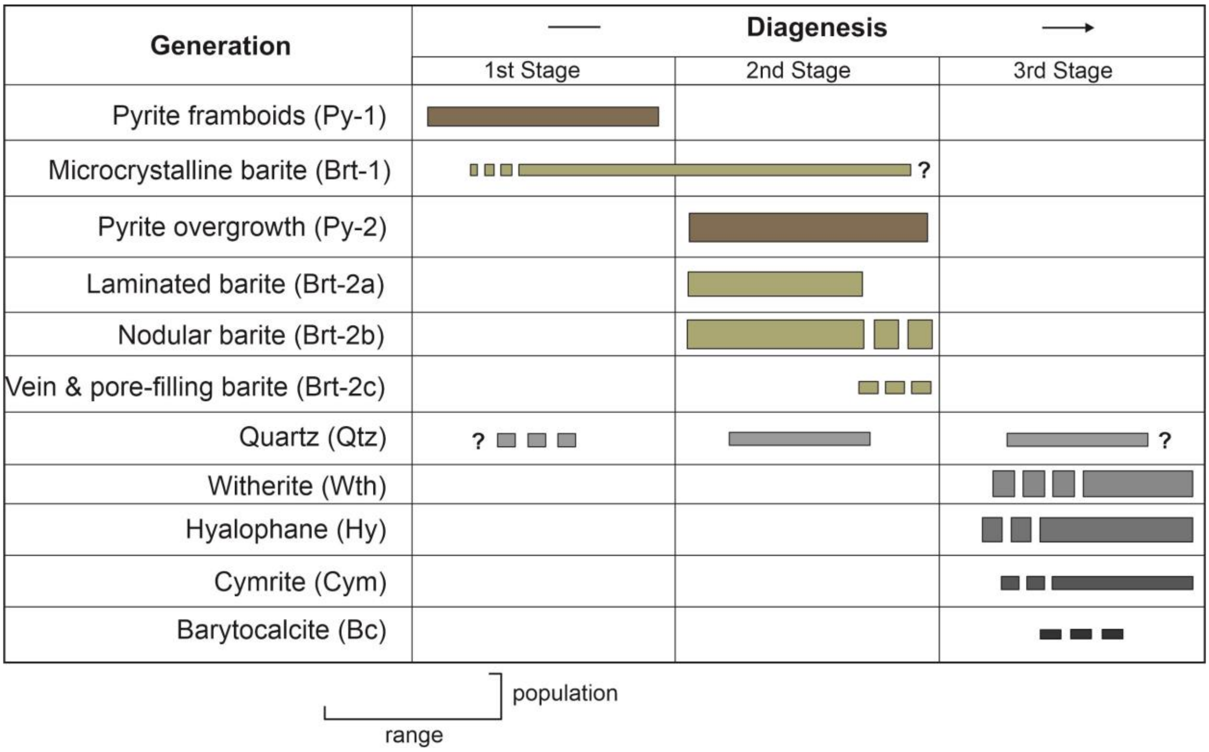

Fig. 2- 5: Simplified paragenetic succession of main pyrite and barite generations.

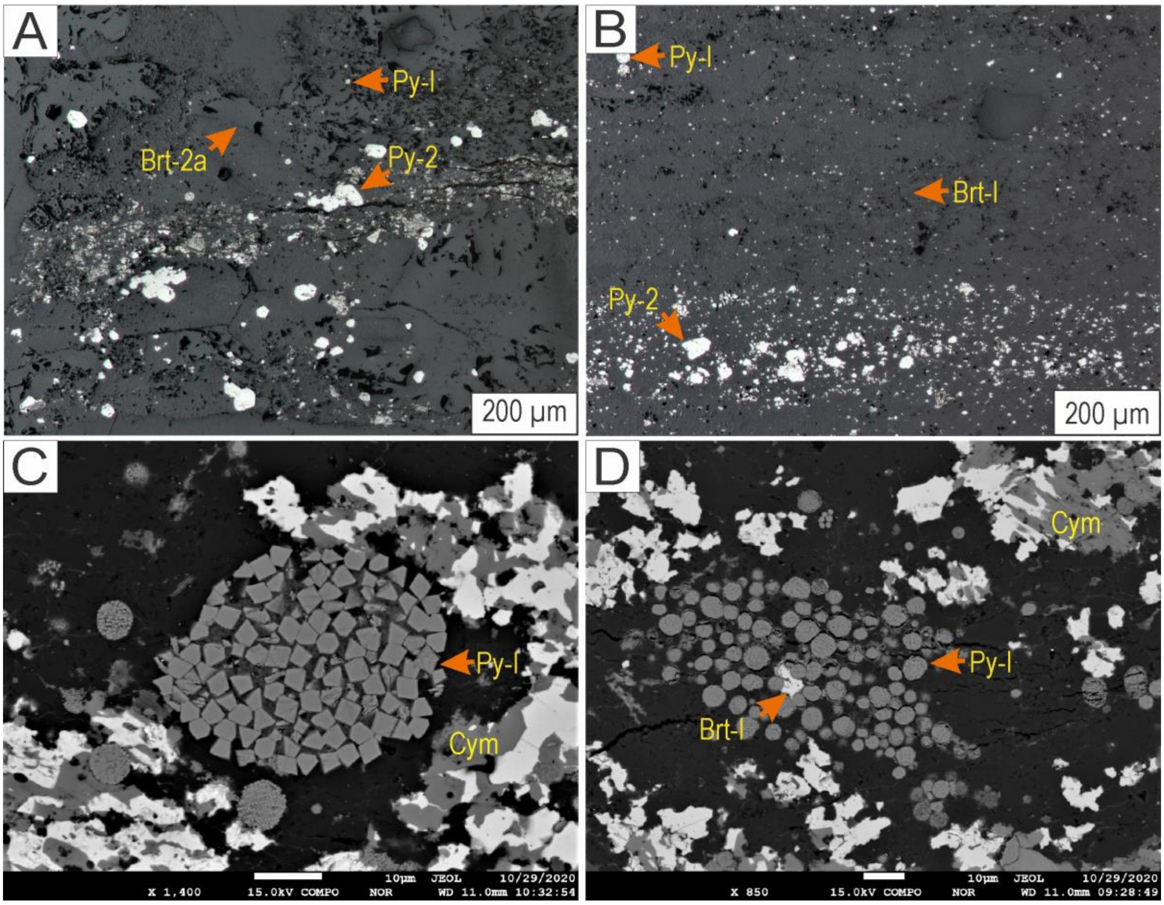

Fig. 2- 6: Reflected light and backscatter electron (BSE) images of pyrite and barite generations. A) Reflected light image showing pyrite framboids (Py-1) in intra- and intergranular pores spaces of barite (Brt-2a) and clay matrix. Pyrite (Py-2) is observed to be disseminated within the matrix and in and around interlocking grains of laminated barite (Brt-2a). B) Reflected light image of stratiform pyrite (Py-2) in clay lamination with microcrystalline barite (Brt-1) and pyrite framboids (Py-1). C) BSE image of pyrite framboids (Py-1) of variable sizes and nanocrystal morphologies within carbonaceous mudrock matrix. D) BSE image of Py-1 framboids and polyframboids with disseminated microcrystalline barite (Brt-1) and replaced mainly by witherite (Wth) and cymrite (Cym).

Stage 2: The second stage, pyrite (Py-2), forms porous, subhedral to idiomorphic grains, primarily concentrated in laminae and nodules of the mudstones (Fig. 2-8a, b). In the lower part of the Harp section, where the mudstones contain no barite laminae or nodules, Py-2 either occurs as disseminated crystals (<70 µm) or forms aggregates that are up to 2.7 mm (Fig. 2-4j). The Py-2 grains sometimes form overgrowths on Py-1 and may contain inclusions of framboids, quartz, and barite (Fig. 2-8c, d). Barite (Brt-2) forms subhedral to anhedral stratiform barite crystals (Brt-2a, Fig. 2-9a) and spherical to irregular barite nodules (Brt-2b, Fig. 2-9b). Together with other barium phases, this barite replaces the earlier formed Brt-1 (Figs. 2-6d, 2-7b).

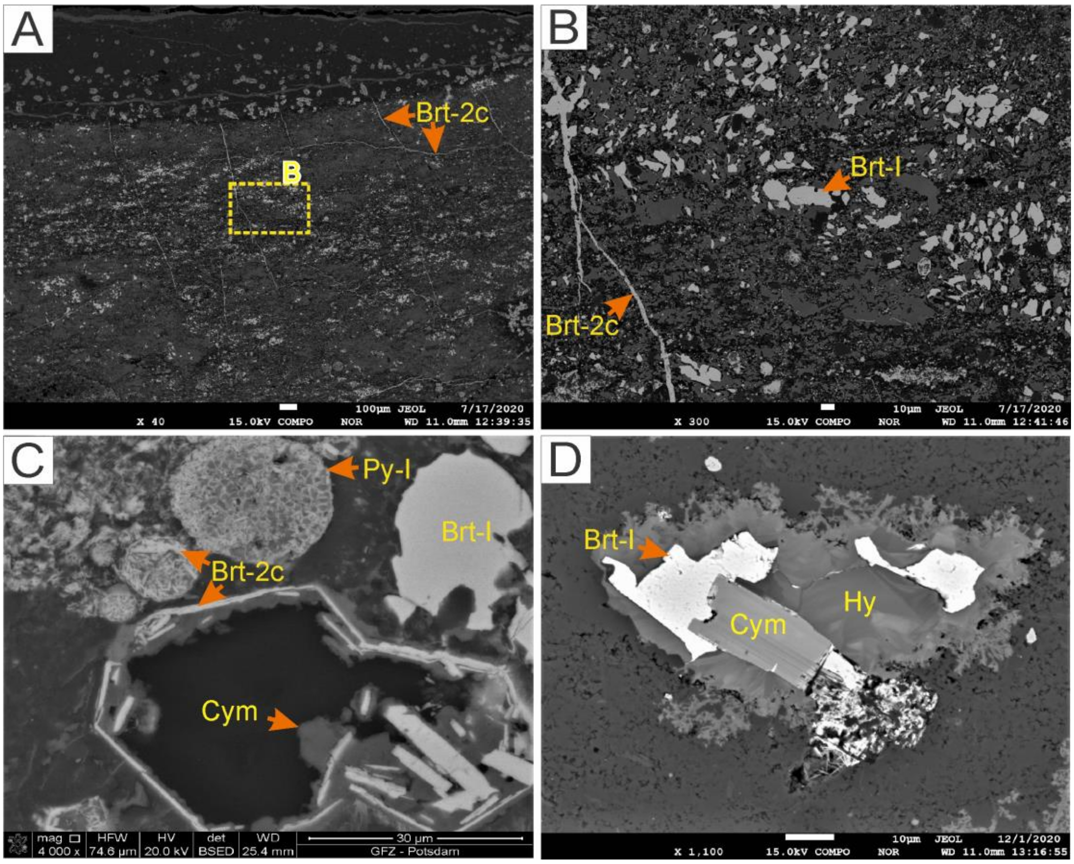

Fig. 2- 7: A) BSE image of barite crystals with barite veins (Brt-2c). The orange box depicts BSE image B. B) BSE image of barite vein (Brt-2c) crosscutting earlier formed barite grains, including microcrystalline barite (Brt-1). C) Scanning electron microscope (SEM) BSE image of barite replacement of framboidal pyrite (Py-I) by Brt-2c. Cymrite (Cym) grows in the pore spaces left by the dissolution of pyrite (Py-2) grains. D) BSE image of Brt-I intergrowth with cymrite (Cym) and within subhedral and dendritic hyalophane (Hy).

The Brt-2a mainly occurs as well-formed horizontal (Fig. 2-4d) and wavy to irregular laminae with intercalations of clay-rich laminae (Fig. 2-9a); nodular Brt-2b is the dominant form of barite in the samples (Fig. 2-9c). The Brt-2a laminae tend to wrap around rosette and nodules of Brt-2b when they occur together, associated with witherite, quartz, hyalophane, and cymrite (Fig. 2-9d, e, f). Importantly, Brt-2b is intergrown with Py-2 with clear planar crystal boundaries, suggesting coprecipitation (e.g., Fig. 2-8b, d). Notably, Brt-2 and Brt-1 are replaced by witherite, mainly in the dark grey mudstones of the Harp, Cowan, and Axe sections. The vein and pore-filling barite (Brt-2c) comprises precipitation in the pore, intergranular spaces and fractures, and is most commonly observed in the Axe, NAFCAC-1, and Harp sections. Barite-2c tends to form replacement and feeder (conduits) textures, including veins, veinlets, lensoids, and idiomorphic barite crystals overgrowing or replacing earlier formed barite and pyrite and cymrite grains (Figs. 2-7b, 2-10).

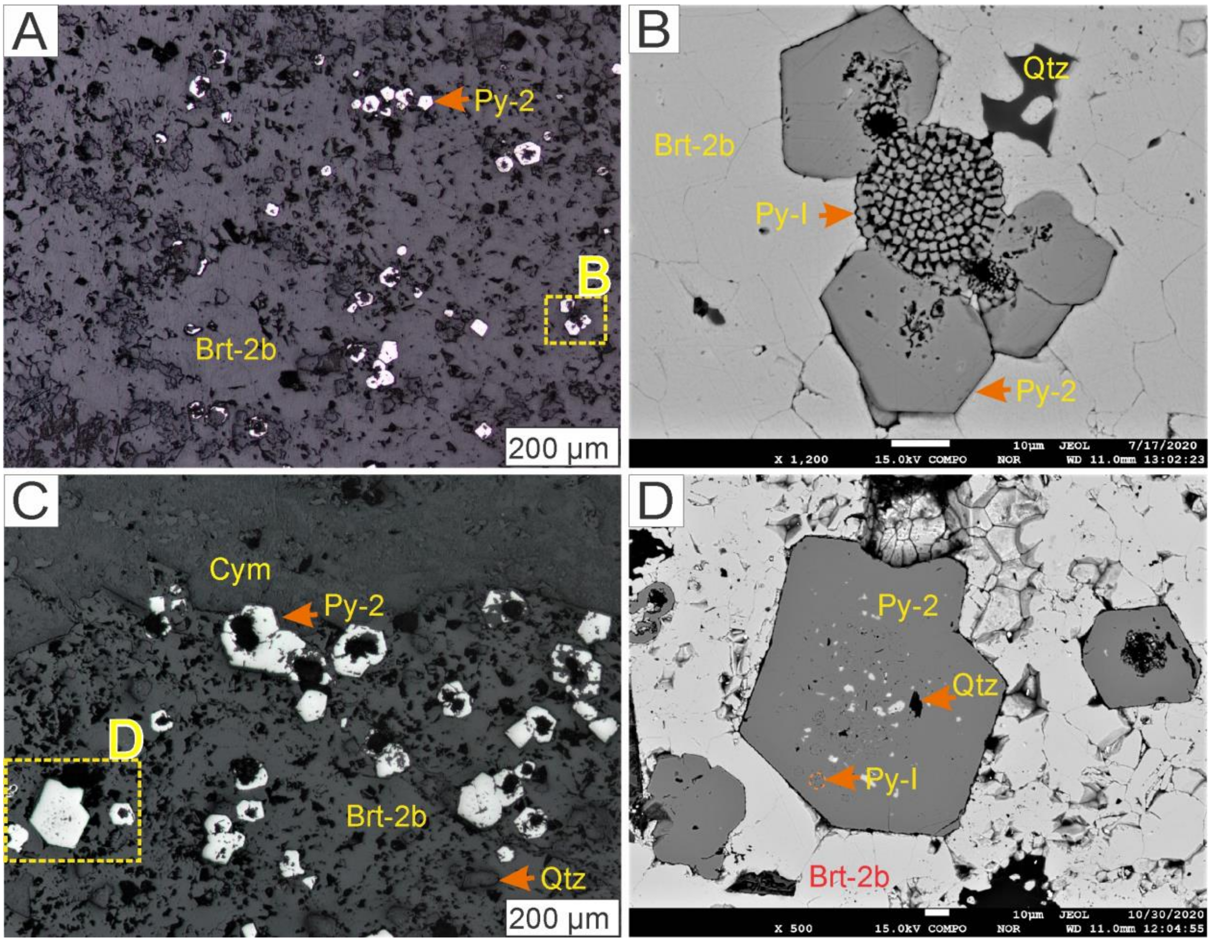

Fig. 2- 8: A) Reflected light photomicrograph of nodular barite (Brt-2b) with interlocking grains and intergrowing subhedral to euhedral pyrite (Py-2). B) BSE image of the highlighted region in A showing the intergrowth relationship between Py-2 and Brt-2b. C) Reflected light photomicrograph of Py-2 with porous cores that contain Py-1, barite, and quartz (quartz) inclusions, better highlighted in BSE image D.

Stage 3: The third stage in the paragenesis comprises Ba-bearing minerals, including cymrite and hyalophane, precipitating as pseudomorphs of earlier formed mineral phases (Fig. 2-7c). In essence, the formation of cymrite and hyalophane, together with witherite and quartz, continues after the precipitation of Py-2 and Brt-2 (Fig. 2-10c).

2.7.2. Sulfur and oxygen isotopes in pyrite and barite

The results of the SIMS analyses of the isotopic compositions of pyrite and barite are provided in Appendix Tables A-1 and A-2 and presented in Figs. 2-11 and 2-12. Pyrite has a large range of $\delta^{34}S$ values (Figs. 2-11, 2-13). Framboidal pyrite (Py-1) preserves mostly negative $\delta^{34}S$ values, between -29.4‰ and -9.4‰, with a mean $\delta^{34}S$ value of -21.0‰ ± 6.3‰ (1σ, n= 23). Pyrite-2 preserves more positive $\delta^{34}S$ values between +9.4‰ and +44.5‰ and the mean is +31.0 ± 7.7‰ (1σ, n= 177).

The $\delta^{34}S_{barite}$ values in the barite in this study overlap (Fig. 2-12a) and range between +37.1‰ to +67.9‰ (+51.1‰ ± 7.7‰, 1σ) with an outlier of +15.3‰ from the mudstones of the NAFCAC-2 section. Measured $\delta^{18}O_{barite}$ values from the sections also overlap and are between +8.8‰ to +23.9‰ (+21.0‰ ± 1.7‰, 1σ). The Brt-2a $\delta^{34}S$ values are between +37.1‰ and +60.1‰ with a mean $\delta^{34}S$ value of +49.2‰ ± 4.7‰ (1σ, n=63). Corresponding $\delta^{18}O$ values of +19.5‰ to +23.7‰ with a mean $\delta^{18}O$ value of +21.8‰ ± 1.5‰ (1σ, n=24) are preserved in the Brt-2a barite (Fig. 2-12a). The $\delta^{34}S$ and $\delta^{18}O$ values of Brt-2b (+51.4‰ ± 8.1‰, 1σ) are between +38.8‰ and +67.9‰ (n=391) and +8.8‰ to +23.9‰ (+21.0‰ ± 1.7‰, 1σ, n=284) respectively, with an outlier $\delta^{18}O$ value of -5.5‰ (corresponding $\delta^{34}S$ value of +40.1‰). The Brt-2b barite from the Cowan and NAFCAC-2 sections record the highest $\delta^{34}S$ values between +60.8‰ and +67.9‰, with corresponding $\delta^{18}O$ values between +18.4‰ and +23.5‰ (Fig. 2-12a). Analyses of barite veins produced $\delta^{34}S$ values between +44.4 and +51.1‰ (+48.5‰ ± 3.6‰, 1σ) and $\delta^{18}O$ values between +16.6‰ and +21.5‰ (+19.5‰ ± 2.6‰, 1σ) respectively. Overall, there is observed covariation between $\delta^{34}S_{barite}$ and $\delta^{18}O_{barite}$ values, as indicated by the coefficient of determination ($r^2 = 0.52$; Fig. 2-12a).

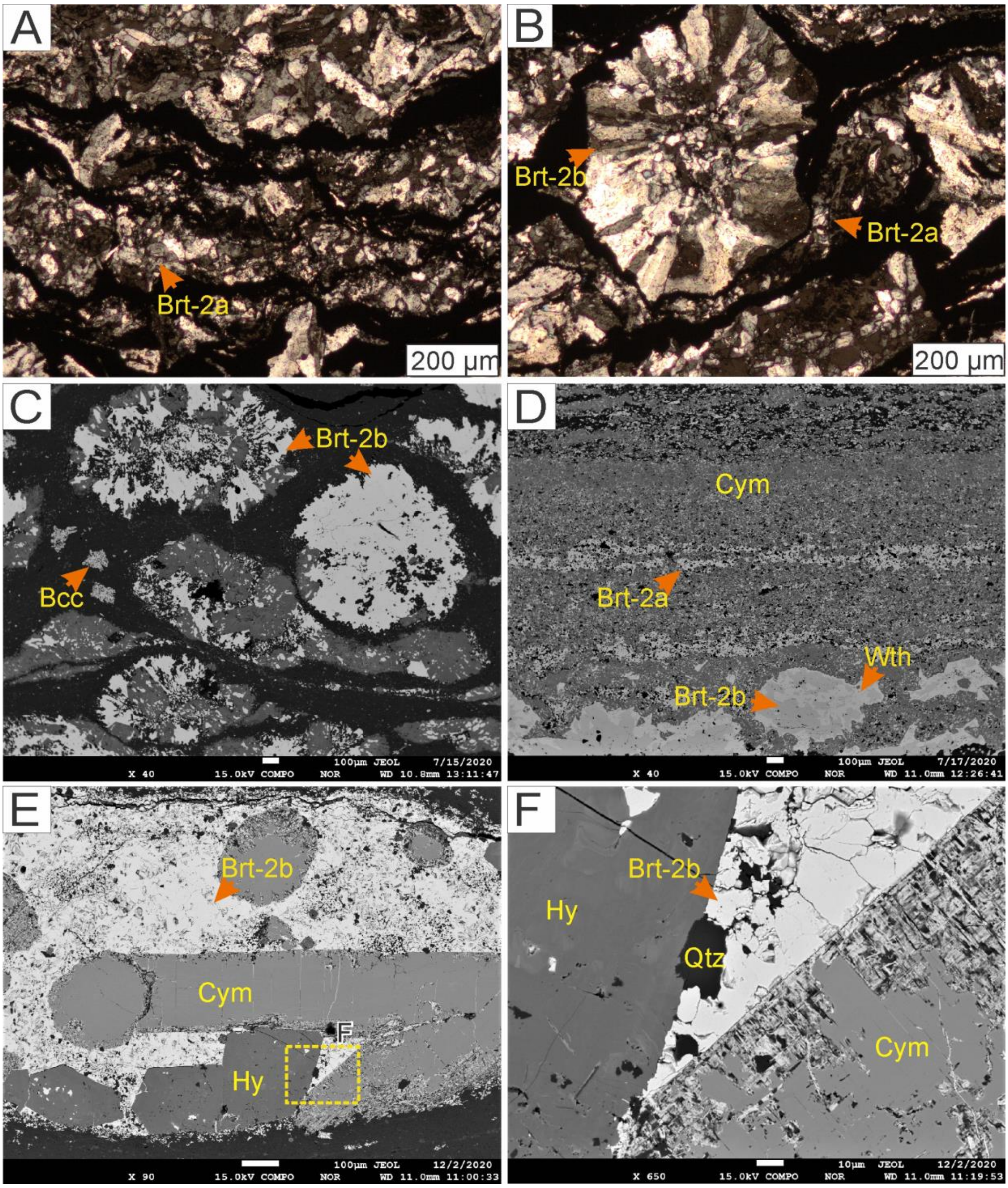

Fig. 2- 9: A) Transmitted light photomicrograph of kinked laminations of stratiform barite (Brt-2a) intercalated with clay-rich laminae. B) Transmitted light photomicrograph in cross-polarized light of laminated barite (Brt-2a) wrapping around nodular barite (Brt-2b) grain. C) BSE image of spherical and ellipsoidal Brt-2b with quartz intergrowth replaced by cymrite (Cym). Minor barytocalcite (Bcc) crystals are observed as spongy crystals within the matrix. D) BSE image of laminated barite (Brt-2a) and nodular barite (Brt-2b). Brt-2b are replaced mainly by witherite, similar to the Ba-carbonate replacement of Brt-2a observable in the laminations. E) BSE image of a nodule with subhedral to idiomorphic cymrite (Cym) and hyalophane (Hy) crystals in barite (Brt-2b). F) BSE image of the area highlighted in image E showing the boundary relationship between the minerals present. The cymrite is seen being replaced from the margins by acicular barite and nanocrystals of quartz.

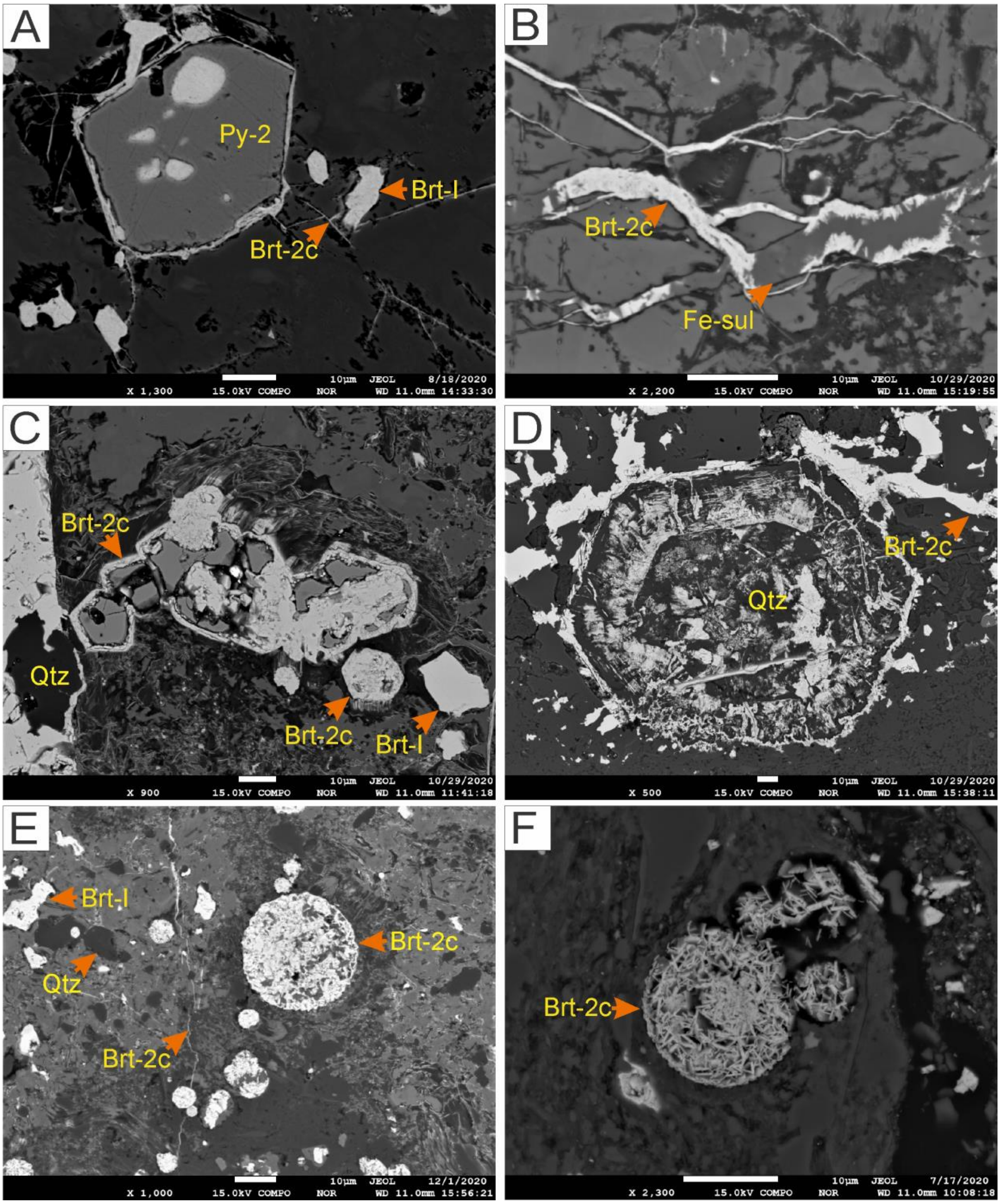

Fig. 2- 10: A) BSE image of Py-2 pyrite crystal with pores filled by barite. Barite veins (Brt-2c) are observed to rim the crystal. B) Barite and iron-sulfate vein that appear to rim earlier formed minerals, as seen in image A. C) BSE image of showing the progressive replacement of pyrite (Py-2) by barite (Brt-2c), that subsequently replace the pyrite grain but retaining the hexagonal shape of the mineral. D) acicular barite pseudomorph retaining the replaced euhedral quartz habit. E) BSE image showing barite vein (Brt-2c) crosscutting and replacing pyrite framboids (Py-1). F) Py-1 framboids completely replaced by euhedral microcrystals of barite, suggested to have progressed from the process observed in images C and E.

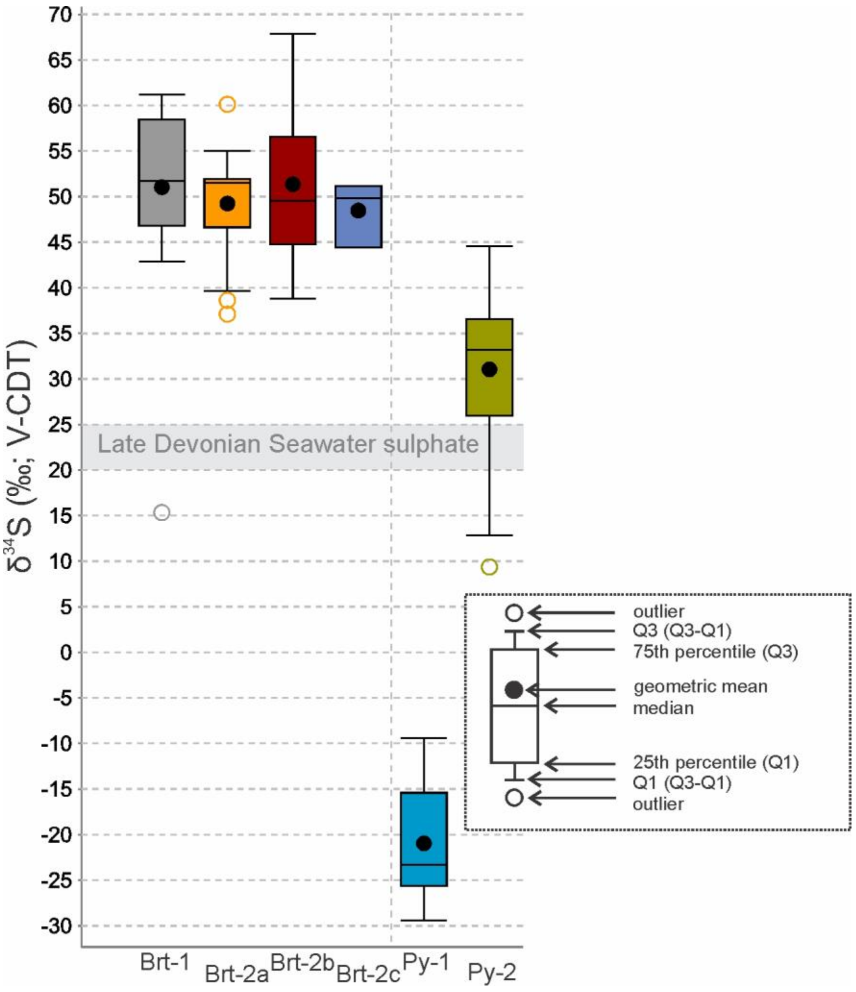

Fig. 2- 11: Box and whisker plot of barite and pyrite $\delta^{34}S$ values from this study. Grey area indicates the composition of Late Devonian seawater (John *et al.*, 2010). The colors are intended as visual aids, highlighting the barite and pyrite types.

2.8. Discussion

The mineralogical paragenesis and microscale isotopic constraints for pyrite and barite enable the reconstruction of the sulfur cycle during the deposition of the Canol Formation in the Late Devonian. The paired isotope data ($\delta^{34}S_{pyrite}$, $\delta^{34}S_{barite}$, and $\delta^{18}O_{barite}$) can be used to unravel the fate and behavior of the archived sulfate and to interpret the end-member $\delta^{34}S_{pyrite}$ values. In particular, the highly positive values occur in samples from several regionally correlative sections; this suggests the formation of these distinctive isotopic values could represent a regionally important (> 10s km) process during the Late Devonian Selwyn Basin.

2.8.1. Barite formation

The formation of pelagic barite in marine environments is initially associated with sinking particulate organic matter (Paytan *et al.*, 2002; Gonzalez-Muñoz *et al.*, 2012; Martinez-Ruiz *et* *al.*, 2020), which may then be recycled under reducing conditions during diagenesis (Torres *et al.*, 1996). Under open-system conditions, biogenic barite preserves $\delta^{34}S$ and $\delta^{18}O$ values that represent unmodified seawater sulfate (Paytan & Griffith, 2007; Griffith & Paytan, 2012).

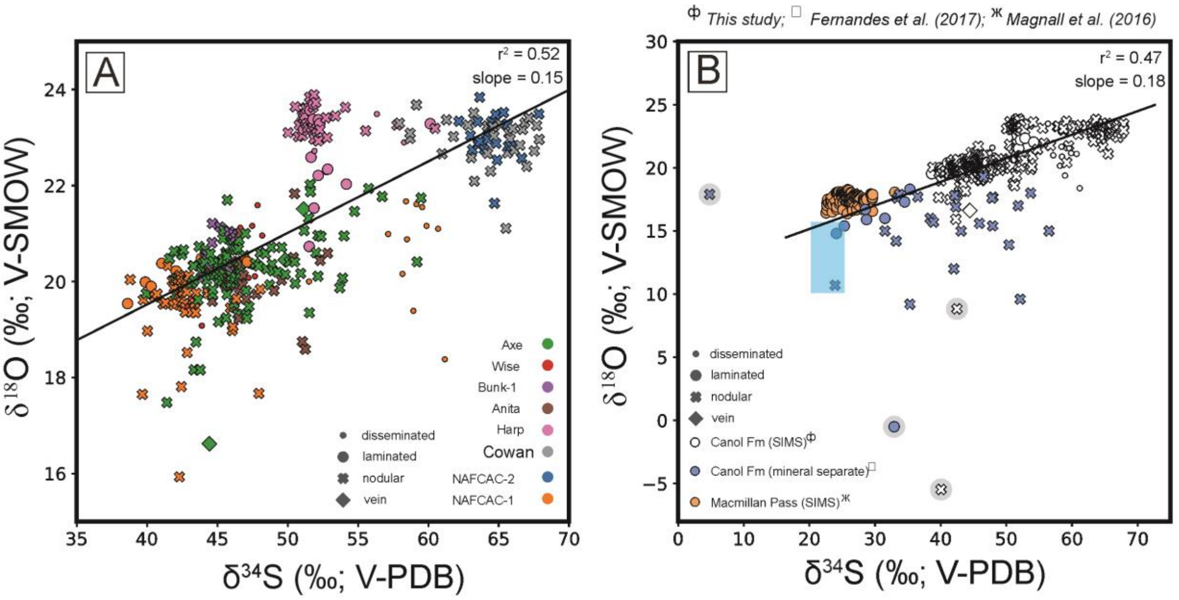

Fig. 2- 12: A) Bivariate plot showing $\delta^{34}S$ values vs. $\delta^{18}O$ values generated by SIMS analysis of barite from the Canol Formation. The regression analysis excludes the outliers that are highlighted in B. B) Bivariate plot showing $\delta^{34}S$ values vs. $\delta^{18}O$ values for a compilation of Late Devonian barite data, including mineral separate analyses of Canol Formation barite (Fernandes *et al.*, 2017) and SIMS analyses of barite from Macmillan Pass (Magnall *et al.*, 2016a). The regression analysis includes the SIMS and mineral separate data for Canol Formation barite but excludes the outliers from either dataset (highlighted by grey circles). The blue box represents the range of constraints for Late Devonian seawater (John *et al.*, 2010; Chen *et al.*, 2013).

The constraints for unmodified Late Devonian seawater sulfate ($\delta^{34}S$ values = 20‰ and 25‰; $\delta^{18}O$ values = 10‰ to 16‰) are provided by analyses of carbonate associated sulfate (CAS) from the Frasnian-Famennian boundary (John *et al.*, 2010; Chen *et al.*, 2013). However, the barite from all stratigraphic sections in this study preserves higher $\delta^{34}S_{barite}$ values (median = 45‰), representing a substantial offset from Late Devonian seawater sulfate (Fig. 2-11). Barite crystals with variable isotopic ratios are not restricted to a single section, depth, or lithology; the analyses reveal isotopic heterogeneity within and between grains of the same barite generation that are only a few microns apart (Fig. 2-13). This lack of isotopic distinction between the different barite types and the distribution of the isotopically heterogenous barite within the lithologies and sections may indicate a similar environment of formation across all stratigraphic sections (e.g., Magnall *et al.*, 2016a; Fig. 2-12b).

The size (>5 µm) and morphology of the barite crystals are also consistent with barite precipitation in diagenetic pore fluids (Paytan *et al.*, 2002; Paytan & Griffith, 2007). The two barite generations (Brt-1 and Brt-2) are isotopically indistinct (Fig. 2-12a), despite paragenetic relationships that suggest barite precipitation during two stages (Figs. 2-6 and 2-9). Both generations of barite are also surrounded by the siliciclastic and organic-rich host mudstones, suggesting formation in early diagenesis near the seafloor (Aplin & Macquaker, 2011). The formation of the barite nodules (Brt-2b) might have coincided with increased compaction of the sediments, with clay mineral and organic matter dehydration possibly causing the nodules to form into ellipsoidal and irregular shapes (e.g., Fig. 2-9c), parallel to the bedding plane (Goldberg *et al.*, 2006; Paytan & Griffith, 2007; Zan *et al.*, 2020).

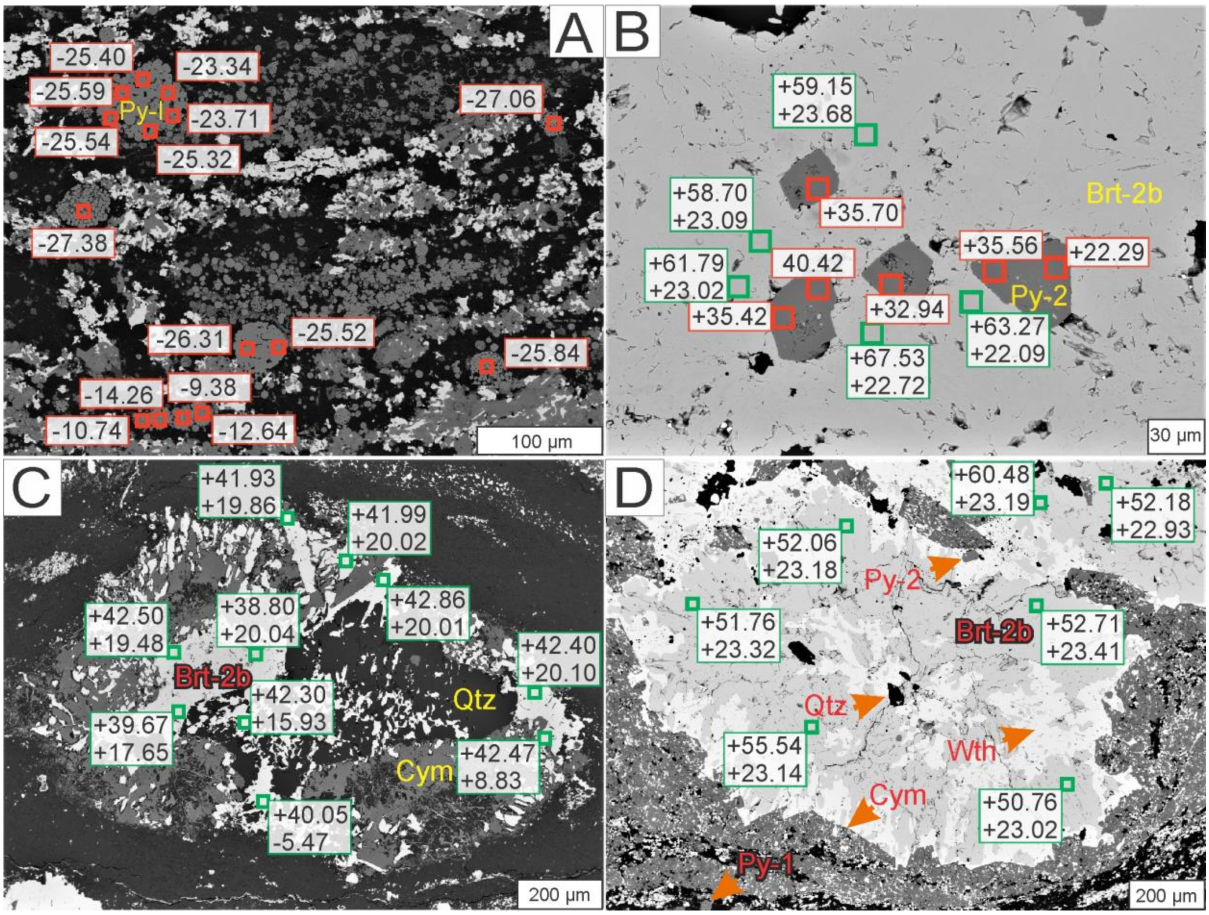

Fig. 2- 13: BSE images draped with pyrite (red squares) $\delta^{34}S$ values and barite (green squares) $\delta^{34}S$ and $\delta^{18}O$ values. $\delta^{34}S$ and $\delta^{18}O$ values are in per mil (‰).

Diagenetic barite formation is generally associated with the sulfate methane transition zone (SMTZ), where opposing diffusional fluxes of methane and sulfate interact (Barnes & Goldberg, 1976; Reeburgh, 1976; Jørgensen & Kasten, 2006). Barium is soluble in the strongly reducing CH_4-bearing fluids but will form diagenetic barite upon mixing with downward diffusing sulfate (Torres *et al.*, 1996; Dickens, 2001). The depth of diagenetic barite formation and the degree to which pore fluid sulfate has been modified via MSR will significantly influence $\delta^{34}S_{barite}$ and $\delta^{18}O_{barite}$ values (Bottrell & Newton, 2006; Goldberg *et al.*, 2006; Antler *et al.*, 2013). Compared to the mineral separate analyses from the previous study (Fernandes *et al.*, 2017), the microscale $\delta^{34}S_{barite}$ and $\delta^{18}O_{barite}$ values in this study lean towards an end member that represents strongly modified seawater (Fig. 2-12b). Samples containing both pyrite and barite were targeted in this study, meaning the barite only samples that contained lower $\delta^{34}S_{barite}$ and $\delta^{18}O_{barite}$ values are underrepresented in the microscale dataset. Nevertheless, when interpreted together, the bulk rock and microscale data plot along a consistent trend (Fig. 2-12b) that is typical of the progressive modification of seawater sulfate via MSR (e.g., Antler *et al.*, 2013; Pellerin *et al.*, 2019).

The overall trend between unmodified Late Devonian seawater and higher $\delta^{34}S_{barite}$ values indicates that barite formed under progressively sulfate-limited conditions in which the rate of sulfate depletion exceeded that of sulfate resupply (Torres *et al.*, 1996; Fike *et al.*, 2015). The $\delta^{34}S_{barite}$ values of Brt-2b represent the most evolved isotope signatures (Fig. 2-12a), consistent with precipitation under sulfate limitation during later stages of diagenesis (Turchyn & Schrag, 2006; Aller *et al.*, 2010; Gomes & Johnston, 2017). Later changes in the barite front may have resulted in the formation of the vein and pseudomorphic barite (Brt-2c), which formed within pore spaces of existing pyrite and barite (Figs. 2-7, 2-10) but appears to have precipitated from a similar sulfate pool (Fig. 2-11) during the second stage of the paragenesis.

Covariation between $\delta^{18}O$ and $\delta^{34}S$ values can provide further information on the diagenetic environment of barite formation. In sediment pore fluids, the slope of the apparent linear phase (SALP; Antler *et al.*, 2013), which describes covariation between $\delta^{18}O$ and $\delta^{34}S$ values, has been linked to sulfate reduction rate (SRR; Böttcher *et al.*, 1998; Böttcher *et al.*, 1999; Aharon & Fu, 2000; Brunner *et al.*, 2005). At low SRR, a high degree of reversibility in the enzymatic pathway of sulfate reduction is thought to promote oxygen isotope exchange between intermediate sulfur phases (e.g., sulfite) and H_2O (Fritz *et al.*, 1989; Brunner & Bernasconi, 2005), resulting in high SALP values. In contrast, where $\delta^{34}S$ values increase without a corresponding increase in $\delta^{18}O$ values (low SALP), it is thought that high SRR results in a lower degree of reversibility (Antler & Pellerin, 2018). At high SRR, kinetic isotope effects will provide the primary control on $\delta^{18}O$ values, resulting in a SALP value of ~0.25 that represents an oxygen fractionation factor that is approximately 25% that of sulfur (Mizutani & Rafter, 1973). Importantly, diagenetic mineral phases that contain sulfate (e.g., barite, celestine and carbonates) have the potential to preserve the SALP signature (Antler & Pellerin, 2018). There is a strong positive correlation between $\delta^{18}O$ and $\delta^{34}S$ values in barite from the Canol Formation (Fig. 2-12b), which corresponds with a low SALP value and high SRR. Similar low SALP values have been described in authigenic carbonate formed in ancient cold seep environments (e.g., Feng *et al.*, 2016).

2.8.2. Barite replacement

Barium concentrations in basinal waters are controlled by sulfate concentration and reduction (Torres *et al.*, 2003). The low solubility of barite means the stability field of $BaSO_4$ overlaps with conditions in which reduced sulfur is the dominant sulfur species rather than sulfate (Fig. 2-14). The dissolution and replacement of diagenetic barite may then proceed under conditions of extreme sulfate limitation that typically develop in carbonaceous sediments (Hanor, 2000). The diagenetic barite in the Canol Formation has been replaced by Ba-carbonates (witherite and barytocalcite), followed by Ba-feldspars (hyalophane and cymrite; Figs. 2-9, 2-13d).

The presence of replacive Ba-bearing phases may imply the progressive diagenetic replacement of barite arising from continuous depletion of the sulfate concentration (e.g., Hanor, 2000). High Ba concentrations (around six orders of magnitude relative to seawater) coupled with extreme sulfate depletion have been shown to result in witherite formation (Maynard and Okita (1991). Barium concentrations in modern seawater are between ~5 to 20 µg/L in the open ocean (Hanor, 2000) and up to 60 µg/L occurs in anoxic deep marine environments (Falkner *et al.*, 1993). Thus, Ba concentrations may increase with depth (Paytan & Griffith, 2007; Carter *et al.*, 2020), mediated by microbial activities in the presence of organic matter. Two conditions are suggested by Maynard and Okita (1991) as a prerequisite for witherite replacement of barite: a) a closed or restricted system with sulfate resupply << sulfate reduction or b) high organic matter contents for diagenetic barite conversion to witherite. However, barite dissolution and witherite formation have also been shown as a function of temperature, CO_2 dissolution (Busenberg & Plummer, 1986), and pH (Melero-García *et al.*, 2009; Hill *et al.*, 2014), with dissolved carbonate likely supplied from organic matter degradation (Maynard & Okita, 1991; Hanor, 2000).

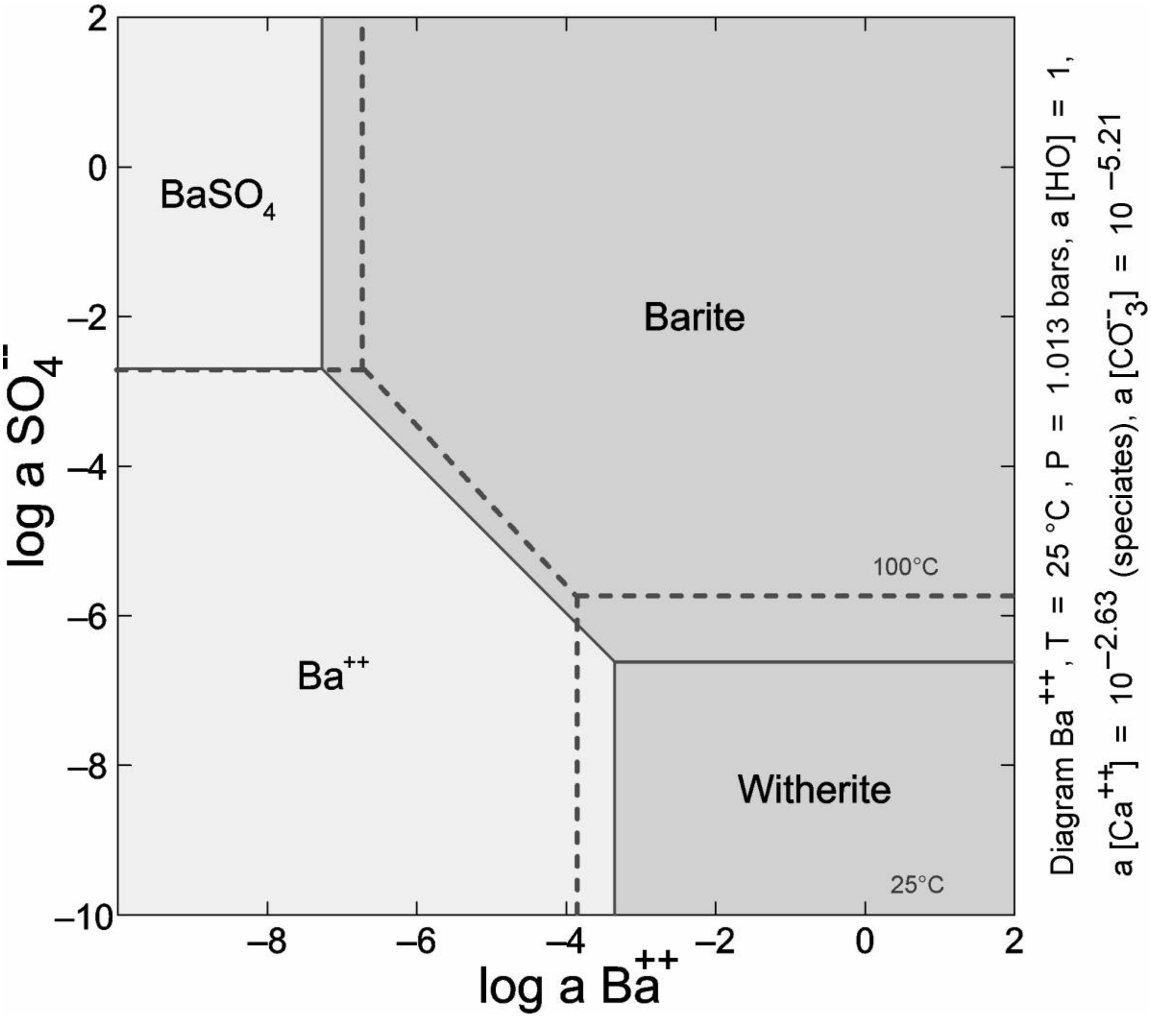

Fig. 2- 14: Phase diagram showing barite and witherite stability fields typical of modern seawater at 25 °C and 100°C with $a(Ca^{2+}) = 10^{-2.63}$ and $a(CO_3^{2-}) = 10^{-5.21}$. Parameters for phase diagram construction from Maynard and Okita (1991).

2.8.3. Pyrite formation

Pyrite in the Canol Formation samples preserves end-member $\delta^{34}S$ values (Fig. 2-11) that are associated with two morphologically distinct stages of pyrite formation (Fig. 2-13a, b). Framboidal pyrite (Py-1) in the Canol Formation preserves $\delta^{34}S$ values that are significantly lower than Late Devonian seawater (Fig. 2-11), which represents a large isotopic fractionation (≤75‰). The $\delta^{34}S_{py\text{-}2}$ values are more positive (mean= +31.0‰) than upper constraints for Late Devonian seawater (+25‰; John *et al.*, 2010; Chen *et al.*, 2013). The formation of highly positive $\delta^{34}S_{pyrite}$ values has been attributed to various processes that include MSR (Drake *et al.*, 2018), sulfide reoxidation (Kah *et al.*, 2016), TSR (Cui *et al.*, 2018; Yan *et al.*, 2020), rapid sedimentation (Pasquier *et al.*, 2017), and sulfate limitation (Ries *et al.*, 2009). Highly positive $\delta^{34}S$ values from mineral separate analyses of pyrite and barite in siliciclastic units from the

Selwyn Basin have been interpreted to have developed from water mass restriction and euxinic conditions in the Late Devonian (Goodfellow & Jonasson, 1984). However, the pyrite paragenesis indicates Py-2 precipitated below the SWI during diagenesis (e.g., Fig. 2-8) when sulfate limitation would have developed on a much smaller pore fluid scale. Importantly, there is no observable alteration relating to hydrothermal fluids (e.g., Cui *et al.*, 2018; Yan *et al.*, 2020), which rules out any high-temperature origin for Py-2. Highly positive $\delta^{34}S_{pyrite}$ values could have developed due to high sedimentation rates reducing the diffusional exchange between diagenetic pore fluids and overlying seawater (e.g., Pasquier *et al.*, 2017). However, there does not appear to be any lithological control on the development of highly positive $\delta^{34}S_{pyrite}$ values in the Canol Formation, which may imply that depositional environment was not the primary control on $\delta^{34}S_{pyrite}$ values.

The combination of highly positive $\delta^{34}S_{pyrite}$ values and evidence of barite solubility represents a trend of progressive sulfate depletion, which is typical of the diagenetic evolution of anoxic sediments (e.g., Torres *et al.*, 1996; Aloisi *et al.*, 2004). Importantly, there is evidence of textural equilibrium between Py-2 and Brt-2 (e.g., Fig. 2-8) and it is apparent that $\delta^{34}S_{pyrite}$ values do not exceed coeval $\delta^{34}S_{barite}$ values (Fig. 2-11), meaning they are not strictly 'superheavy' ($\delta^{34}S_{pyrite} > \delta^{34}S_{SO4}$; Ries *et al.*, 2009; Cui *et al.*, 2018). A similar pyrite paragenesis and assemblage between Py-2 and Brt-2 has also been described at Macmillan Pass, where it was linked with two separate stages of diagenetic pyrite formation associated with MSR and SR-AOM (Magnall *et al.*, 2016a). Compared to the offset between Py-1 and Late Devonian seawater ($\Delta^{34}S = 43.3‰$), the $\Delta^{34}S$ for Brt-2 and Py-2 is smaller (Fig. 2-11). This reduced $\Delta^{34}S$ value could represent a smaller isotopic fractionation ($\varepsilon^{34}S$), possibly linked with higher SRR that are typical of methane and gas seeps (Deusner *et al.*, 2014). Indeed, the low SALP value that is recorded in barite (Fig. 2-12a) would support this interpretation, although it is also possible that Py-2 and Brt-2 did not precipitate precisely at the same time from the same porewater fluids. Nevertheless, the overall evidence of high SRR and increasing sulfate depletion still provides the most plausible explanation for the development of highly positive $\delta^{34}S_{pyrite}$ values in the Canol Formation.

2.8.4. Implications

Previous studies on diagenetic pyrite and barite linked highly positive $\delta^{34}S$ values to sulfate limitation in a euxinic water column (Goodfellow & Jonasson, 1984). More recent studies have now shown that these isotopic values developed as part of a diagenetic assemblage associated with the SMTZ, where sulfate limitation occurred at the pore fluid scale (e.g., Magnall *et al.*, 2016a; Johnson *et al.*, 2018). Notably, the same 2-stage paragenesis comprising framboidal pyrite followed by an assemblage of euhedral pyrite and barite has been identified in Late Devonian strata that host CD-type deposits in the Macmillan Pass district (Magnall *et al.*, 2016a). Thus, the formation of highly positive $\delta^{34}S_{pyrite}$ values and bedded barite in the Canol Formation is evidence of a similar diagenetic assemblage that has been preserved in unmineralized Late Devonian stratigraphy. Moreover, the preservation of this assemblage in multiple stratigraphic sections in the Canol Formation implies periodical stability in the SMTZ on a large scale (> 10 km) in order to allow pyrite and barite to accumulate (e.g., Lin *et al.*, 2017; Liu *et al.*, 2019).

In the modern oceans, shallow SMTZ and high methane fluxes are located along productive continental margins with high sedimentation rates (Egger *et al.*, 2018). Other factors controlling the depth of the SMTZ include organic matter content and decomposition and sulfate concentrations (Torres *et al.*, 2003; Jørgensen *et al.*, 2004; Borowski *et al.*, 2013; Lin *et al.*, 2016b; Lin *et al.*, 2017; Liu *et al.*, 2019; Liu *et al.*, 2020). In the Canol Formation, high total organic carbon (1.5 to 9.2 wt.%; Kabanov & Gouwy, 2017) is associated with facies characterized by dynamic sedimentation and bioturbation that have been linked with partial oxygenation (Biddle *et al.*, 2021). The stabilization of the SMTZ is likely to require constant fluxes of methane and sulfate (Fig. 2-15) coupled with a hiatus in sedimentation, and changes to any of these parameters may potentially result in the alteration of authigenic mineral phases (Arning *et al.*, 2015).

The relatively minor replacement of Py-2 by veined Brt-2c (Fig. 2-10) may therefore suggest abrupt albeit short-lived fluctuation of the SMTZ due to changes in either methane or sulfate fluxes within the sediments. Barite solubility is drastically increased below the SMTZ, and where sulfate concentrations diminish, Ba diffuses upward and reacts with other available cations (Maynard & Okita, 1991; Hanor, 2000). Considering that SR-AOM in the SMTZ also leads to the generation of alkalinity, this may explain the origin of barium carbonate in these samples (e.g., Fig. 2-13d). The origin of carbonate in these samples could be evaluated using carbon isotopes, but this is beyond the scope of this study.

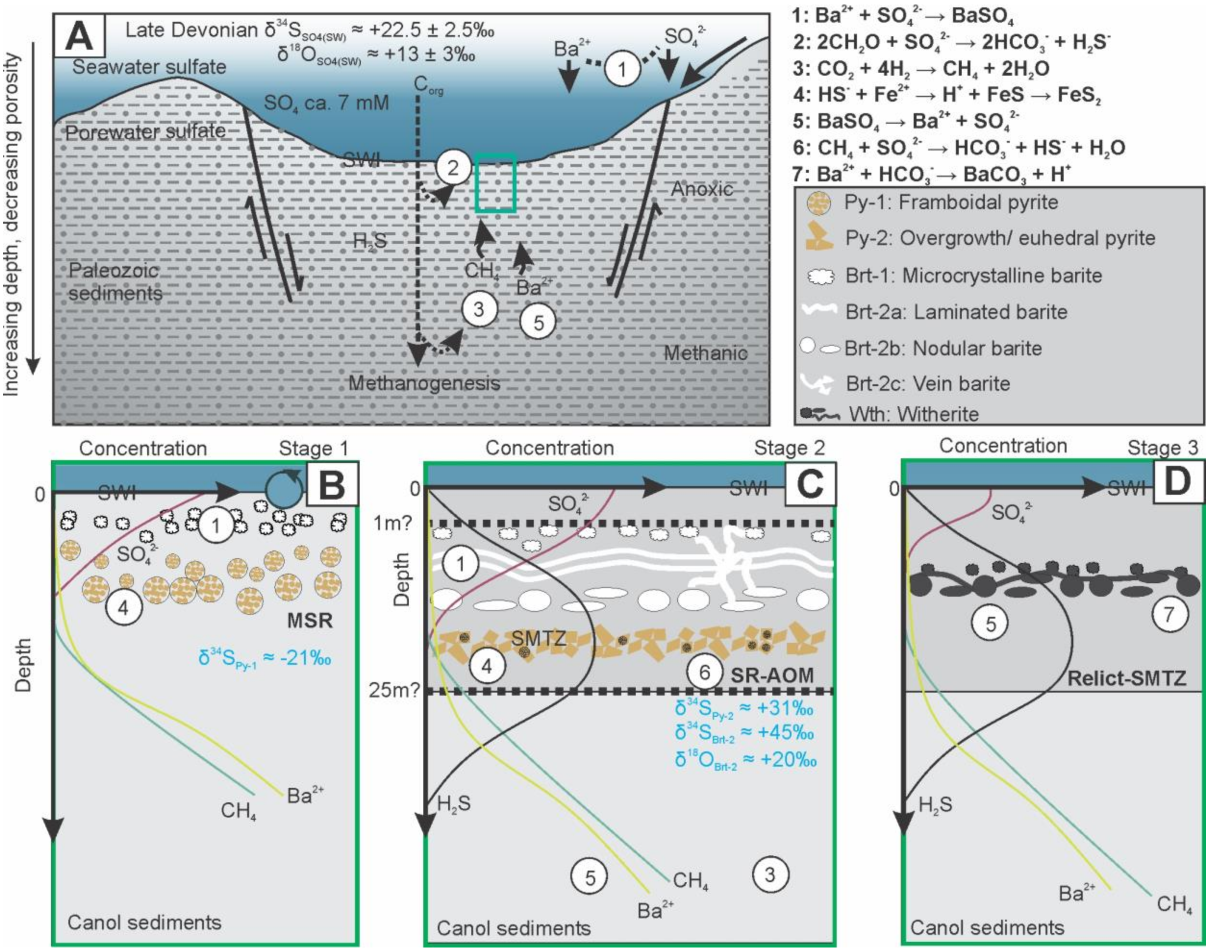

Fig. 2- 15: A schematic illustration of temporal Late Devonian diagenetic processes in the Canol Formation of the Selwyn Basin, depicting sulfur cycle and stages of the formation of the two sulfur sinks (barite and pyrite) and witherite (no scale implied; modified from Hanor, 2000; Magnall *et al.*, 2016a; Zan *et al.*, 2020). A) Cross-section showing a portion of the Selwyn Basin on the western North American continental margin in the Late Devonian (modified from Hanor, 2000). Sulfate (SO_4^{2-}) from the terrestrial environment is delivered to the marine environment. Biogenic barite (1) forms and is delivered to the seafloor via fecal pellets and marine showers, which get buried and inherit the Late Devonian seawater ($\delta^{34}S$ values = 20 to 25‰). Organic matter (C_{org}) is deposited together with sediment where degradation is continuous through (2) below the sediment-water interface (SWI) with SO_4^{2-} as oxidant and continuous deep down the sediment column via methanogenesis (3). B) Framboidal pyrite (Py-1) represents a sink for H_2S with negative $\delta^{34}S$ values produced during microbial sulfate reduction (MSR). Dissolution of the biogenic barite provides Ba to form authigenic (diagenetic) barite (Brt-1) under an apparent open system condition. C) Development of diagenetic redox front, the sulfate-methane transition zone (SMTZ), resulting from diffusion of methane and Ba-rich fluids from the depth and downward diffusing sulfate. The interaction allowed for the formation of ^{34}S-enriched laminated (Brt-2a), nodular (Brt-2b), and vein (Brt-2c) barite above the SMTZ and superheavy pyrite (Py-2) along this sulfate reduction coupled to anaerobic oxidation of methane (SR-AOM) zone under a restricted depositional setting. D) severe sulfate undersaturation allowed for large-scale barite dissolution and formation of Ba-bearing phases, e.g., witherite at the relict SMTZ. See the text for a detailed explanation.

Similar barite-pyrite-Ba-carbonate/silicate assemblages have also been reported in other Paleozoic strata (e.g., Maynard & Okita, 1991; Jewell, 2000; Koski & Hein, 2003), including Qinling-Daba, southern China (Wang & Li, 1991; Xu *et al.*, 2016). The low seawater concentrations in the Lower Paleozoic (ca. <1 to 10 mM; Horita *et al.*, 2002; Brennan *et al.*, 2004; Gill *et al.*, 2007), relative to modern ocean seawater sulfate that is about 28 mM (Rickard, 2012; Fike *et al.*, 2015; Jørgensen *et al.*, 2019), would have restricted the amount of sulfate resupply below the seafloor in organic-rich sediments (Greinert *et al.*, 2002; Paytan *et al.*, 2002). Continuous fractionation of the porewater sulfate through MSR and SR-AOM likely led to the formation of highly positive $\delta^{34}S_{pyrite}$ values in this study and other similar settings. We would suggest that highly positive $\delta^{34}S_{pyrite}$ values and barite formation, dissolution, and replacement by other Ba-bearing phases might have been a more general feature of methane diagenesis in the lower Paleozoic.

2.9. Conclusion

The diagenetic sulfur cycle in the Selwyn Basin has been reconstructed using microscale (SIMS) paired isotope constraints on pyrite and barite in samples from multiple stratigraphic sections of Late Devonian sedimentary rocks. Two distinct stages of pyrite formation formed via microbial sulfate reduction (MSR) under contrasting levels of sulfate availability. The initial stage of pyrite formation developed during early diagenesis under relatively open-system conditions, which resulted in the precipitation of the framboidal pyrite (Py-1) and preservation of negative $\delta^{34}S$ values. Deeper in the sediment profile, MSR resulted in progressive sulfate depletion and the development of the sulfate methane transition zone (SMTZ), where sulfate reduction was coupled with the anaerobic oxidation of methane (SR-AOM). Highly positive $\delta^{34}S$ values in pyrite developed as a result of high sulfate reduction rates and progressive depletion of sulfate. Sulfate-limited, methane-rich diagenetic fluids beneath the SMTZ provided conditions under which barium was soluble. Barite formed when opposing diffusional fluxes of barium and sulfate-bearing fluids mixed at the SMTZ. Importantly, the paragenetically constrained analyses indicate that highly positive $\delta^{34}S_{pyrite}$ values formed during diagenesis in multiple correlated stratigraphic sections from the Late Devonian in the Selwyn Basin, indicating this diagenetic assemblage was a regional feature. We propose that the formation of highly positive $\delta^{34}S$ values in pyrite, dissolution of barite, and replacement by other Ba-bearing phases, could have been a more general features of methane diagenesis in the lower Paleozoic.

2.10. Data availability statement

The dataset presented in this study can be found online at the data repository of the GFZ German Research Centre for Geosciences, Potsdam, Germany. GFZ Data Services. https://doi.org/10.5880/GFZ.3.1.2021.006.

2.11. Author contributions

SAG and JMM designed the study. HMG prepared the samples and performed the petrographic analysis (optical microscopy, EPMA-EDS, and SEM). MJW conducted the SIMS analyses in coordination with HMG and JMM. HMG interpreted the data and wrote the manuscript with contributions from JMM, SAG, HMS, and MJW

2.12. Funding

We gratefully acknowledge financial support from the Petroleum Technology Development Fund (PTDF) and German Academic Exchange Service (DAAD) through the co-financed Nigerian-German postgraduate training program 2019 (DAAD funding no. 57473408) to H. M. Grema and the Helmholtz Recruitment Initiative to S. A. Gleeson. The NordSIMS facility in Stockholm operates as a research infrastructure under Swedish Research Council grant 2017-00671.

2.13. Conflict of interest

The authors declare that the research was conducted in the absence of any commercial or financial relationships that could be construed as a potential conflict of interest

2.14. Publisher’s note

2.15. Acknowledgments

Uwe Dittmann (mount preparation), Franziska Wilke and Oona Appelt (EPMA), and Ilona Schäpan (SEM) are deeply appreciated for technical support during sample preparation and analyses. Christof Kusebauch, Marcus Oelze, and Philip Rieger are gratefully acknowledged for constructive discussions during the research. We also thank the Editor, Julia Ribeiro, and the two reviewers for providing constructive comments that greatly improve this manuscript.

CHAPTER 3

Mineralogy and paragenesis of the Boundary Zone Zn-Pb±Ag deposit, Yukon, Canada

Haruna M. Grema[1,2,], Joseph M. Magnall[1], Sarah A. Gleeson[1,2], Jack E. Milton[3], Alicja Wudarska[1,4], Anja M. Schleicher[1], Hans-Martin Schulz[1]*

[1]*GFZ German Research Centre for Geosciences, Germany*
[2]*Institute of Geological Sciences, Freie Universität Berlin, Germany*
[3]*Fireweed Metals Corporation, British Columbia, Canada*
[4]*Institute of Geological Sciences, Polish Academy of Sciences, Warsaw, Poland*
[*]*Corresponding author: Haruna M. Grema. Email address: hgrema@gfz-potsdam.de*

This chapter is under revision in Economic Geology.

The data for this chapter is available as data publication in the GFZ Data Repository and is cited as Grema *et al.* (2024a). Data can be accessed is via https://dataservices.gfz-potsdam.de/panmetaworks/review/4d977202cbc26dabe4526cfbbe177869faff51af98518d4411dadc5e14d71768/.

3.1. Abstract

Clastic-dominated (CD-type) Zn-Pb±Ag deposits account for significant global Zn and Pb resources, and the demand for metals for the green transition has increased exploration interest. Several CD-type deposits are interpreted to have formed by subseafloor replacement processes. However, our understanding of the nature of host rock replacement in these deposits remains limited due to the incomplete preservation of the deposit architecture and/or postmineralization overprinting events. In this contribution, we describe a new Zn-Pb±Ag deposit, Boundary Zone, which has been recently discovered in the Macmillan Pass district, Yukon, Canada. Nine drill holes were sampled and studied using petrography, mineralogy (whole rock and clay fraction X-ray diffractometry), and U-Pb fluorapatite geochronology approaches. These methods were used to develop a mineralogical paragenesis to constrain the timing of sulfide mineralization and controls on ore formation.

The mineralized rocks at the Boundary Zone are hosted by a broad stratigraphic interval spanning the Late Ordovician-Early Silurian Duo Lake Formation to the Middle-Late Devonian Portrait Lake Formation. The discovery of mineralized Ordovician-Silurian rocks at Boundary Zone is the first time that significant stratabound mineralization has been identified in rocks of this age within the Macmillan Pass district. The premineralization stage is dominated by early diagenetic phases, including quartz, barite, pyrite, fluorapatite, and phyllosilicates. Two genetically distinct ore-stages have been identified. Ore-stage I comprises the formation of stratabound fine-grained sphalerite, pyrite, galena, sulfosalts, and barian mica during later burial. This formed via barite replacement, nucleation on pre-ore pyrite, and primarily through porosity exploitation during early biogenic silica transformation of opal-A to cryptocrystalline ($Qz_{\text{-cryp}}$) and microquartz ($Qz_{\text{-mic}}$) in highly siliceous mudstones (< 85 wt.% quartz). The high-grade and volumetrically major ore-stage II mineralization formed following significant hydrothermal fluid-induced brecciation and veining of the host rocks and is accompanied by silicification and siderite formation.

In one sample from the Niddery Lake Member, a discordant vein crosscuts ore-stage I, but its paragenetic relationship with ore-stage II could not be determined. Fluorapatite in this vein records a U-Pb age of 169 ± 10 Ma. We suggest the multiple mineralizing events at the Boundary Zone formed during a prolonged period of fluid flow, spanning from diagenetic stages in the basin, possibly to periods of Cordilleran-related deformation in the Selwyn Basin. These findings have significant implications for exploration strategies in the Macmillan Pass

district and similar geological settings, where biosiliceous mudstone deposition, diagenetic barite formation, and multiple hydrothermal fluid pulses are evident.

3.2. Introduction

Clastic-dominated (CD-type) deposits are stratiform and stratabound massive sulfide deposits commonly hosted in fine-grained Proterozoic and Paleozoic siliciclastic-carbonate rocks (Leach *et al.*, 2005b). These deposits contain some of the largest Zn and Pb resources and associated critical metals (e.g., Ge, Ga, In), and increasing demand relating to the green transition has driven a new wave of exploration (Jowitt & McNulty, 2021; Valckx *et al.*, 2021). A small number of ancient sedimentary basins (North Australian Proterozoic and the North American Paleozoic basins) contain the largest CD-type deposits, and the most notable recent discoveries have been made during brownfield exploration programs in well-endowed, world-class provinces (e.g., Teena deposit, Carpentaria Province; Hayward *et al.*, 2021).

The Selwyn Basin (Canada; Fig. 3-1a) is one of the top three CD-type provinces in the world (Goodfellow & Lydon, 2007). Mineralized rocks are hosted across three broad stratigraphic intervals within the Paleozoic (Fig. 3-1b), which are all characterized by periods of carbonaceous mudstone deposition (Abbott & Turner, 1990). These comprised i) the Anvil district where sulfide mineralized rocks are hosted by Cambrian units that have been highly deformed and subjected to greenschist facies grade metamorphism (Jennings & Jilson, 1986; Pigage, 1991), ii) in the Howard's Pass district, sulfide mineralized rocks are hosted by Late Ordovician to Early Silurian units (Morganti, 1979), and iii) the Macmillan Pass district in which sulfide mineralized rocks are well-preserved in Middle to Late Devonian units (Turner, 1986; Goodfellow & Lydon, 2007; Magnall *et al.*, 2016a). Both the Howard's Pass and Macmillan Pass districts have been metamorphosed to low facies grade between the Jurassic to Cretaceous periods (Morganti, 1979; McClay, 1984; Martel, 2017).

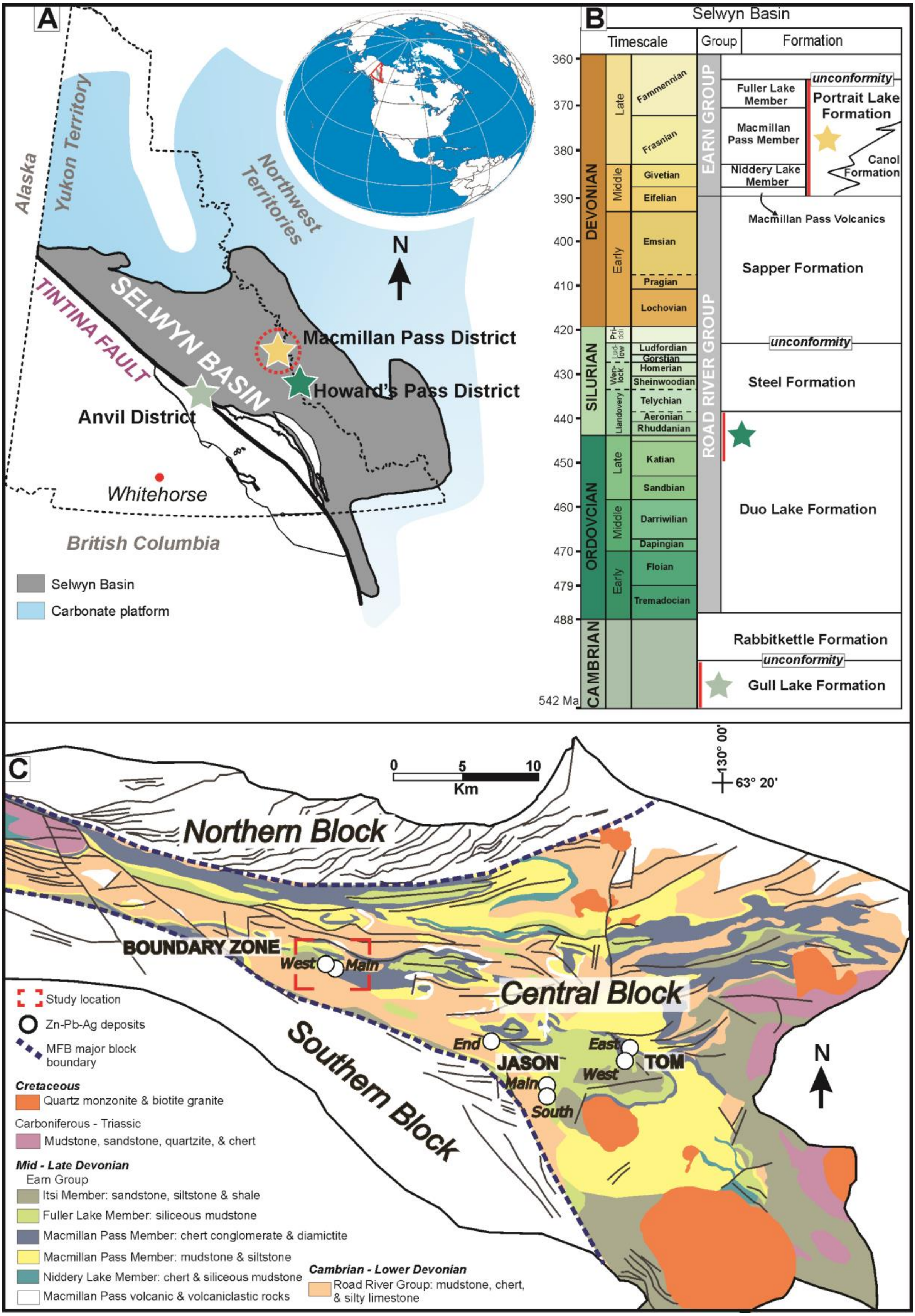

Fig. 3- 1: General overview of the geology and stratigraphy of the Selwyn Basin with details of the Macmillan Pass area: A) Location and simplified geological map of the Selwyn Basin in the Yukon Territory, Canada. The three major Zn districts of the basin are denoted by stars, with

that of the Macmillan Pass district highlighted in a red circle. Modified from Goodfellow (2007). B) Stratigraphy of the Selwyn Basin from the Cambrian to Devonian periods. The Portrait Lake Formation is further subdivided into individual members. Volcaniclastic rocks occur at the bottom of the Portrait Lake Formation and are interbedded with the Macmillan Pass Member. The Macmillan Pass Member comprises the mudstone, conglomerate, and diamictite units. Modified from Nelson and Colpron (2007). C) Geologic map of the Macmillan Fold Belt (MFB) region, highlighting the facies in the Central Block. The locations of the Tom and Jason deposits and the Boundary Zone deposit are shown. Modified from Turner and Rhodes (1990) and Abbott (2013).

In the Macmillan Pass district (Fig. 3-1c), the complete deposit architecture occurs in at least two localities (Tom and Jason); these have been particularly important for the development of genetic models (Fig. 3-2). Early studies on the Tom and Jason deposits led to the development of the sedimentary exhalative (SEDEX) model, which has since been more broadly applied to CD-type deposits in other districts (Carne & Cathro, 1982; Goodfellow, 1987; Goodfellow *et al.*, 1993). In the SEDEX model (Fig. 3-2a), ore-stage sulfides formed following the hydrothermal exhalation of Zn-Pb ± Ba-rich fluids into an H_2S-bearing (euxinic) water column (Goodfellow, 2007a). In many deposits, there is no direct evidence of a feeder zone preserved in the rock record (e.g., Howards Pass district); therefore, the exhalation of dense, bottom-hugging brines (Fig. 3-2b) has been invoked as a mechanism for sulfide precipitation in topographic depressions on the seafloor, away from sites of venting (Sangster, 2002). However, studies in the Selwyn and the McArthur Basins have described how sulfide mineralization may have formed during the early burial stages of diagenesis (e.g., Fig. 3-2c-d) via host rock replacement (Williams, 1978a, 1978b; Gadd *et al.*, 2017; Magnall *et al.*, 2020c). Magnall *et al.* (2020c) suggested that this two-stage model (Fig. 3-2c-d) comprises a barite and pyrite assemblage forming an early diagenetic assemblage at sulfate-methane transition zone (SMTZ). This assemblage is indicated to have been replaced by ore-stage sulfides that formed stratiform mineralization (Fig. 3-2d), for instance, at the Tom and Jason deposits (Magnall *et al.*, 2016a). Importantly, these new genetic models have the potential to fundamentally change exploration strategies.

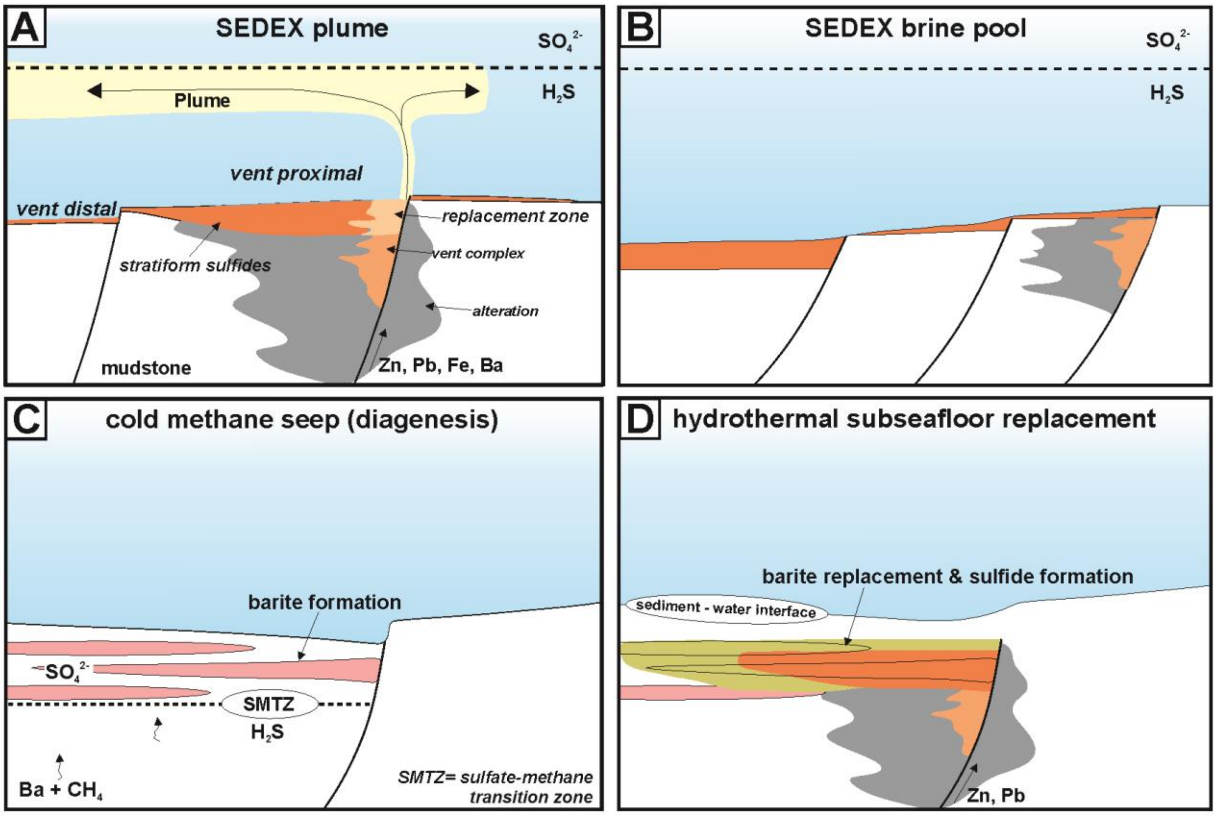

Fig. 3- 2: Schematic diagrams of the genetic models suggested for the formation of Zn-Pb±Ba deposits in the Selwyn Basin: A) The sedimentary exhalative (SEDEX) model comprises a stratified water column where metalliferous hydrothermal fluids are exhaled. Sulfide minerals precipitate in the reduced sulfur (H_2S-rich), anoxic to euxinic, bottom water. Barite forms in the sulfate (SO_4^{2-}) saturated zone of the water column and may be found with both the proximal and distal sulfide assemblages, modified from Goodfellow *et al.* (1993). B) The brine pool model is a modified version of the SEDEX model in which hydrothermal fluids are exhaled into the water column and migrate, as part of bottom water-hugging dense brines, to depressions on the seafloor where sulfides form, modified from Sangster (2002). C-D) Two-stage genetic model for the formation of Zn-Pb±Ba deposits. In the cold methane seep model, fluids rich in barium (Ba) and methane (CH_4) are delivered, for example, through diffusion, into a sulfate-saturated sediment column, resulting in diagenetic precipitation of barite (C), adapted from (Torres *et al.*, 2003). Hydrothermal fluids infiltrating the shallow sub-seafloor result in the dissolution of barite and the subsequent precipitation of sulfide minerals through subsurface diagenetic replacement (D), modified from Magnall *et al.* (2020c).

The recent discovery at Boundary Zone (Macmillan Pass district) provides an excellent example of successful exploration within a long-known district. The Boundary Zone deposit comprises sulfide mineralized rocks that are located west of the Tom and Jason deposits in the Macmillan Pass district (Fig. 3-1c). The Boundary Zone deposit is situated in an area historically known as Boundary Creek (Abbott & Turner, 1990), where stockwork-vein-style mineralization was drilled in the 1980s and was interpreted as being a feeder zone of a SEDEX deposit (Turner & Rhodes, 1990). Recent drilling programs by Fireweed Metals Corporation have discovered mineralization which is far more extensive than previously thought. The bedded mineralization at Boundary Zone has been intersected in two different stratigraphic units: the Late Ordovician to Early Silurian Duo Lake Formation (part of the Road River Group, which hosts the Howard's Pass district mineralization; Morganti (1979) and the Middle to Late Devonian Portrait Lake Formation (Earn Group), also host to the Tom and Jason deposits (Gardner & Hutcheon, 1985; Bailes *et al.*, 1986). The presence of multiple mineralized zones in different stratigraphic intervals is unique among CD-type deposits in the Selwyn Basin and could provide new perspectives on ore formation in the basin and CD-type deposits more broadly.

In this study, samples obtained from nine drill holes intersecting the Boundary Zone deposit have been investigated. This study has utilized: i) a combination of petrographic techniques, including reflected and transmitted light microscopy, cathodoluminescence (CL) imaging, electron probe microanalysis (EPMA), and scanning electron microscopy (SEM), ii) quantitative X-ray diffractometry (QXRD) of bulk rock powders and semi-quantitative analyses of clay-size fraction, and iii) fluorapatite U-Pb dating with secondary ion mass spectrometry (SIMS). The primary objectives of this study were to: i) characterize the mineralogy of the host rocks and diagenetic assemblages and ii) determine the timing of the sulfide mineralization and associated alteration assemblages.

3.3. Background geology

3.3.1. Selwyn Basin

The Selwyn Basin is bounded by the Mackenzie platform carbonate to the east and by accreted terranes and the Tintina fault to the west (Gabrielse, 1967). The formation of the basin followed protracted extensional tectonics and the breakup of the Rodinian supercontinent, which led to the re-emergence of the Laurentian craton between 775 and 720 Ma (Milton *et al.*, 2017). A 4-6 km thick sequence of Neoproterozoic – Terreneuvian syn-rift strata comprises the Windermere Supergroup, which represents the oldest stratigraphic unit in the Selwyn Basin (Gordey & Anderson, 1993). During the Paleozoic, a thick sequence of post-rift clastic sedimentary rocks was deposited over the basal strata as the depositional environment evolved into deeper water conditions (Gordey & Anderson, 1993).

The basal part of the Paleozoic sequence comprises the Early to Middle Cambrian Gull Lake Formation (Fig. 3-1b), which is overlain by the Late Cambrian to Early Ordovician limestones and siltstones of the Rabbitkettle Formation (Gordey & Anderson, 1993). The Road River Group, comprising Early Ordovician to Early Devonian strata, overlies the Rabbitkettle Formation and represents the last sequence before a drastic change in sedimentation style to deep basinal facies that formed the Earn Group (Gordey & Anderson, 1993). The overlying deep marine Middle to Late Devonian Earn Group consists of an abrupt change in facies development characterized by variable lithological thickness and unconformities (Abbott *et al.*, 1986; Mair *et al.*, 2006). The complex and dramatic lithological changes are suggested to represent the deposition of the Earn Group chert-rich and turbiditic clastic rocks during a period of transtensional and tensional rifting that led to the development of the fault-bound (sub-) basins (Abbott *et al.*, 1986).

Three phases of alkalic to ultra-potassic volcanic activity occurred during the Early Cambrian, Early to Middle Ordovician, and Middle to Late Devonian (Goodfellow, 1987; Abbott & Turner, 1990; Cobbett *et al.*, 2020). The volcanism has been interpreted to represent intermittent rifting and extension of the continental margin (Gordey & Anderson, 1993; Goodfellow *et al.*, 1995), concomitant with the melting of the heterogeneous lithospheric mantle (e.g., Scanlan, 2022).

In the Jurassic, island arc accretion resulted in the Selwyn Basin strata being incorporated into the fold and thrust belt of the North American Cordillera (Monger *et al.*, 1982; Nelson & Colpron, 2007). Regional deformation resulted in open to tight folds, axial planar slaty cleavage, and gently dipping thrust faults (Gordey *et al.*, 2010; Martel, 2017). The Cordilleran deformation terminated during the Late Cretaceous (~100 Ma) and was followed by post-orogenic plutonism and emplacement of intermediate to felsic granitoids with ages of ~110-90 Ma (Gordey & Anderson, 1993; Hart *et al.*, 2004; Gordey *et al.*, 2010).

The Selwyn Basin hosts three major Zn-Pb mineralized districts (Fig. 3-1b). In the Anvil district, five Zn-Pb massive sulfide deposits are hosted in phyllites and schists of the Mount Mye Formation, which is time-equivalent to the Gull Lake Formation (Pigage, 1991). These five deposits had a combined pre-mining mineral resource of 120 Mt at 5.6% Zn, 3.7% Pb, and 45-50 g/t Ag (Jennings & Jilson, 1986). The Howard's Pass district consists of fourteen deposits hosted in the Late Ordovician to Early Silurian Duo Lake Formation of the Road River Group (Morganti, 1979; Slack *et al.*, 2017). A combined estimated 400.7 Mt grading at 4.5% Zn and 1.5% Pb is reported for the Zn-Pb deposits in the district, including the XY, Don, and Anniv deposits (Kirkham *et al.*, 2012). Sulfide mineralization mainly occurs in carbonaceous, siliceous, and calcareous mudstones and cherts of the Active Member, with gangue mineral phases such as pyrite, quartz, calcite, and apatite (Jonasson *et al.*, 1986; Gadd *et al.*, 2017). The overlying siliceous mudstones of the Upper Siliceous Mudstone and Backside Siliceous Mudstone (Portrait Lake Formation) Members in the Howard's Pass district have also been shown to host relatively minor sulfide mineralization (Gadd *et al.*, 2016b; Slack *et al.*, 2017). The Zn-Pb±Ba mineralization in the Macmillan Pass district is hosted in carbonaceous and biosiliceous mudstones of the Middle to Late Devonian Portrait Lake Formation (Goodfellow, 2004; Magnall *et al.*, 2015). In the following section, the key features of the Macmillan Pass district are discussed in further detail.

3.3.2. Stratigraphy of the Macmillan Pass district

The Macmillan Pass district is located at the eastern margin of the Selwyn Basin, at the border between the Northwest Territories and Yukon (Fig. 3-1a). The district is within the Macmillan Fold Belt (MFB), which formed as a result of Mesozoic accretionary deformation and comprises west-trending tight folds that deformed the Paleozoic sequences of the Earn Group and sulfide mineralization (Abbott & Turner, 1991). Based on field mapping, Abbott (1982) defined three tectonostratigraphic domains in the MFB: the Northern, Central, and Southern Blocks that encompass the Macmillan Pass district (Fig. 3-1c). The Macmillan Pass district is located in the Central Block, which is distinguished from surrounding blocks by the presence of volcanic rocks, diamictites, and certain stratigraphic units that are absent elsewhere, implying the presence of syndepositional faults (Abbott & Turner, 1990; Turner & Rhodes, 1990). Stratiform barite deposits occur in both the Northern and Southern Blocks of the MFB, including the significant Walt barite deposit in the Northern Block (Abbott and Turner, 1991).

Road River Group: The Road River Group comprises Early Ordovician to Late Silurian, mudstone, chert, and limestone units overlying deep-water carbonates and shales of the Gull Lake Formation (Abbott & Turner, 1990; Abbott, 2013). The group is divided into the Duo Lake, Steel, and Sapper Formations (Fig. 3-1b). Graptolite biostratigraphy constrains the age of the Duo Lake Formation to the Late Tremadocian (Lower Ordovician) to Early Wenlock (Silurian; Cecile, 1982). It comprises bedded siliceous mudstones and chert that are overlain by black siliceous mudstone and chert (Abbott, 2013). Conformably overlying Duo Lake Formation is the Steel Formation, comprising dark grey mudstone that is wispy-laminated and bioturbated (Gordey & Anderson, 1993). The Road River Group's youngest strata comprise the Sapper Formation, consisting of recessive silty limestone and calcareous black mudstone (Abbott, 2013) and constrained to the Late Eifelian age (Fraser *et al.*, 2020).

Earn Group: The Earn Group overlies Road River Group and is divided into the Portrait Lake and Itsi Formations (Abbott *et al.*, 1986; Abbott, 2013). The age of the Portrait Lake Formation ranges from Givetian to Famennian, constrained by conodont biostratigraphy (Abbott, 2013), and is host to the Tom and Jason deposits at Macmillan Pass.

The Macmillan Pass area hosts the type section of the Portrait Lake Formation (Cecile, 2000; Martel *et al.*, 2011), which is broadly time-equivalent to the Canol Formation in the Mackenzie Mountains (Blusson, 1978; Carne, 1979; Abbott & Turner, 1990). The Portrait Lake Formation comprises the informal Niddery Lake, Macmillan Pass, and Fuller Lake Members, which are underlain by and interbedded with the Macmillan Pass volcaniclastics. The Macmillan Pass Volcaniclastics is an informal term that describes the carbonate-altered lapilli tuffs, tuffs, mafic flows, volcaniclastic breccias, sills, and dykes that are interbedded with the clastic rocks of the Earn Group (Turner & Rhodes, 1990; Ootes *et al.*, 2013; Fraser *et al.*, 2020). Turner and Rhodes (1990) constrained the age of volcanic rocks to Middle Devonian; however, interbedded volcanic layers are also observed in the underlying mudstones of the Duo Lake Formation.

The Niddery Lake Member comprises cherty and black siliceous radiolarian mudstones that occur with barite and limestone lenses that reach up to 30 m thick (Abbott, 2013). The overlying Macmillan Pass Member comprises three units (Gordey and Anderson (1993), and at Macmillan Pass, the lithofacies change laterally in thickness and lithofacies. The Macmillan Pass Member broadly consists of grey to black thinly laminated silty mudstone that is finely interbedded with sandstones. A thick chert pebble conglomerate forms a continuous sequence with minor sandstone (Abbott, 2013). The Fuller Lake Member, previously called the Tom sequence (Abbott & Turner, 1990), is sandwiched between the Itsi Formation and the Macmillan Pass Member. The member comprises a 200-1,500 m thick succession of carbonaceous mudstones that are commonly pyritic (Goodfellow & Rhodes, 1990). Pyritized radiolarian tests have been identified in the Portrait Lake Formation mudstones, and the abundance of cryptocrystalline quartz ($Qz_{\text{-cryp}}$) has been linked with biogenic silica sourced from high levels of primary productivity in the basin (Magnall *et al.*, 2015).

Structure: In the Macmillan Pass district, Jurassic to Early Cretaceous tectonic overprint has resulted in the formation of tight, west-trending folds where the most intense deformation is concentrated in the hinge zones (Abbott & Turner, 1990). The Portrait Lake Formation sequence at the Macmillan Pass area is considered to be of subgreenschist facies metamorphic grade, with most of the primary sedimentary and hydrothermal features well preserved within the limbs of folded strata (Magnall *et al.*, 2016b).

3.3.3. Sulfide mineralization in the Macmillan Pass district

In the Macmillan Pass district, Zn-Pb±Ba mineralized rocks follow a 25 km trend defined by the Hess fault system that runs across the MFB (Abbott & Turner, 1991). The Tom and Jason deposits are ~5 km apart and comprise stratiform and stratabound sulfide mineralization with a combined indicated resource estimated at 11.21 Mt at 6.59% Zn, 2.48% Pb, and 21.33 g/t Ag, with inferred resources of 39.47 Mt at 5.84% Zn, 3.14% Pb, and 38.15 g/t Ag (Fireweed Metals Corporation, 2018). Feeder zone mineralization and alteration are well-preserved at the Tom and Jason deposits, including stockwork, breccias, and veins with quartz and Fe-carbonate altered mudstones overlain by stratiform sulfide and barite mineralized mudstones (Goodfellow & Rhodes, 1990; Magnall *et al.*, 2016b).

The Tom deposit is hosted in the Fuller Lake Member and comprises the Tom East and Tom West mineralized zones (Fig. 3-1c; Carne, 1979; Goodfellow & Rhodes, 1990). The stratigraphy of the zones is debated with the suggestion that mineralized rocks either occur in equivalent stratigraphic intervals (McClay & Bidwell, 1986) or have formed in two distinct intervals (Large, 1981). The distribution of the mineralized Fuller Lake Member mudstones reflects the abrupt changes in sedimentary facies and bed thickness close to a nearby synsedimentary fault (Ansdell *et al.*, 1989). The ore minerals are mainly characterized by sphalerite, galena, and pyrite (Carne, 1979).

The Jason deposit is hosted by the Macmillan Pass Member, which is folded into tight west-trending and east-plunging folds that are disrupted by the nearby Hess Fault (Turner, 1991). The deposit comprises two sulfide mineralized zones, the Main Zone and the South Zone (Fig. 3-1c), which occur at separate levels within the Macmillan Pass Member (Gardner & Hutcheon, 1985). The End Zone represents another sulfide mineralized zone hosted in the Portrait Lake Formation, with a characteristic feeder zone mineralogical assemblage (mainly ankerite, siderite, pyrite, sphalerite, and galena) and zonation that is bounded by a syndepositional normal fault (Abbott & Turner, 1991).

An important mineralogical assemblage within the stratiform mineralization at the Tom and Jason deposits includes barium feldspars, carbonates, and pyrite. Barite replacement by ore-stage sulfides has been linked with the formation of barium feldspar and barium carbonate alteration (Magnall *et al.*, 2020c). Pyrite textures and chemistry have been used to highlight the evolution of the pre-ore, ore-stage, and postore in the Tom and Jason mineralized areas (Magnall *et al.*, 2016a; Magnall *et al.*, 2018; Leighton *et al.*, 2019). These studies trace mixing of diagenetic and hydrothermal fluids in the feeder zones and in distal unmineralized barite-rich regions (e.g., Canol Formation, Leighton *et al.*, 2021a; Leighton *et al.*, 2021b). Leighton *et al.* (2021a) also recognized postmineralization recrystallized pyrite that forms overgrowths on earlier pyrite generations and is interpreted to be metamorphic in origin. Similar metamorphic pyrite overgrowths are also recognized in the Howard's Pass district (Lianxing & McClay, 1992) and are suggested to have formed during the regional Mesozoic orogeny (Jonasson *et al.*, 1986).

3.3.4. Boundary Zone deposit

The Boundary Zone deposit is located 15 km northwest of the Jason deposit (Fig. 3-1c) on the Nidd property claims and was first staked by Cominco Limited in 1976. Fireweed Metals Corporation (formerly Fireweed Zinc Ltd.) acquired the claims in 2018 following the acquisition of the Tom and Jason deposits from HudBay Minerals Inc. in 2016. Subsequently, Fireweed Metal Corporation continues to conduct mapping, sampling, and drilling programs at the Tom and Jason deposits and Boundary Zone.

Previous work on Boundary Zone: The first description of Boundary Zone described the host rocks and the sulfide mineralization. The mineralization was suggested to have formed in a subbasin consisting of carbonaceous and siliceous mudstones, cherty conglomerates, diamictites, and volcaniclastics (Turner & Rhodes, 1990). Abbott and Turner (1990) suggested that the sulfide mineralization at the Boundary Zone may have formed synchronously with the stratiform mineralization at the Tom and Jason deposits and, therefore, represent the feeder zone facies of the SEDEX system. The mineralization was interpreted to be epigenetic, having formed below the seafloor due to fluid flow from syn-depositional faults developed during the Late Devonian (Turner & Rhodes, 1990). Furthermore, the Boundary Zone mineralization has been suggested to be genetically related to the regional alkaline volcanics (Turner & Rhodes, 1990; Abbott & Turner, 1991). A recent study by Scanlan (2022) on volcaniclastic rocks in the Selwyn Basin, including samples from the Boundary Zone, indicates that alkaline magmatism may have contributed to sulfide formation by increasing the crustal heat flow and fluid circulation.

3.4. Methods

3.4.1. Sampling

A total of seventy-nine (79) samples for this study were collected from nine drill holes of the Boundary Zone, comprising NB84-10, NB19-001, NB19-002, NB20-001, and NB20-002 drill holes in the eastern part and NB20-004, NB20-007, NB20-009, and NB21-001 drill holes (Fig. 3-3). The selected samples cover all the known mineralization and alteration styles and mineral assemblages. Seventy-three samples containing key mineral assemblages and paragenetic relationships were selected for petrographic and mineralogical investigation.

3.4.2. Petrography

Drill core samples were examined using a binocular microscope, and representative areas were selected for polished thin section (~25 µm) preparation (n=80). A dual reflected and transmitted light Olympus BX51 polarizing microscope was used for detailed petrographic, textural, and mineralogical examination. A hot-cathode optical CL petrographic system was used to observe luminescence and zonation in sphalerite, fluorapatite, barite, and quartz from selected samples.

3.4.3. Electron probe micro-analysis (EPMA) and scanning electron microscopy (SEM)

Selected samples were carbon coated (20 nm thick) and analyzed using a field emission Japan Electron Optics Limited (JEOL) JXA-8530F Hyperprobe EPMA at the GFZ Potsdam, Germany. Mineralogical, textural, and paragenetic relationships were examined using backscattered electron (BSE) imaging and electron dispersive spectroscopy (EDS) analysis. Mineral chemistry data by wavelength dispersive spectroscopy (WDS) were obtained using the EPMA equipped with a combined system of one energy dispersive spectrometer and five wavelength-dispersive spectrometers. Standard operating conditions were set using a beam diameter between 1 and 3 µm, a beam current of 15 nA, and an accelerating potential of 15 kV in secondary electron (SE) and backscatter electron (BSE) modes. Natural and synthetic materials were used to calibrate the microprobe for the determination of element contents. Element mapping and mineral chemistry were performed on selected samples to examine the textures and mineral assemblages in the different lithologies. For fluorapatite mineral chemistry determination, the following oxides and elements were measured: P_2O_5, SiO_2, SO_3, Y_2O_3, La_2O_3, Ce_2O_3, Pr_2O_3, Nd_2O_3, CaO, MnO, MgO, FeO, Na_2O, SrO, F, and Cl.

High-resolution BSE imaging and false color element distribution mapping of selected samples were performed using SEM. Carl Zeiss Microscopy GmbH Ultra Plus field emission SEM was used.

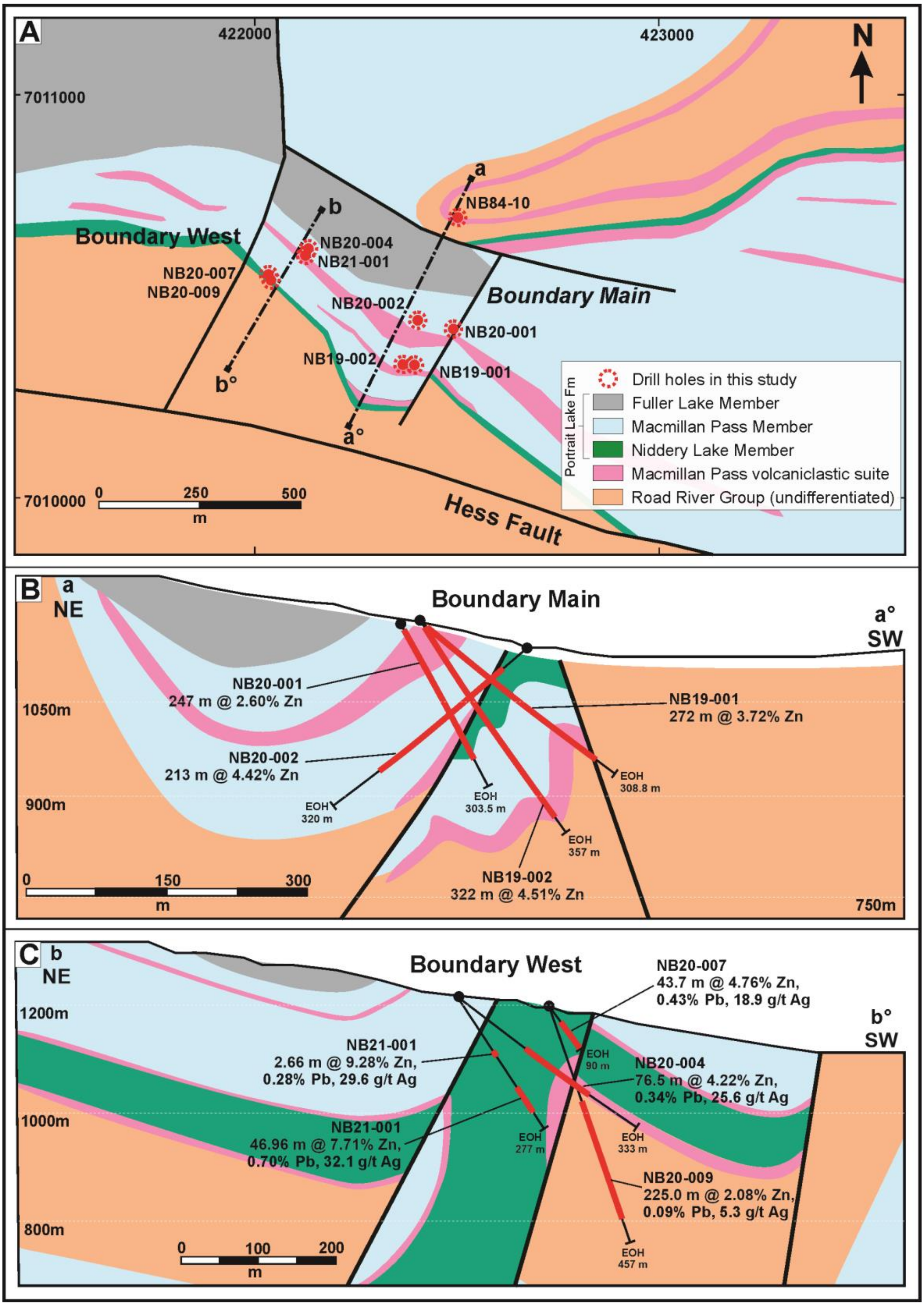

Fig. 3- 3: A) Geological map of the Boundary Zone deposit area, with details of the drill holes sampled in this study. The Macmillan Pass Member units comprise the mudstones, conglomerates, and diamictites of Turner and Rhodes (1990). B-C) Cross sections depicting mineralized sulfide intervals in the drill holes denoted by the red bar. The grades of Zn, Pb, and Ag are also shown. EOH indicates the end of the hole. Modified from Fireweed Metal Corp. (2018).

3.4.4. Secondary ion mass spectrometry (SIMS) U-Pb geochronology

U–Pb age determinations of fluorapatite were performed using the large geometry CAMECA 1280-HR SIMS instrument at the GFZ. Prior to analyses, two sample mounts containing polished rock pucks embedded in epoxy were ultrasonically cleaned in high-purity ethanol and then coated with a 35 nm thick, high-purity gold film to assure electrical conductivity during the analyses. The U–Pb analyses of the fluorapatite sample from the NB19-001 drill hole lasted over two consecutive days and employed a Köhler $^{16}O_2^-$ primary beam between 4.3 and 7.3 nA. A test using oxygen flooding, which is typically used for U-Pb analyses of zircon (Ireland & Williams, 2003), found no enhancement for Pb sensitivity, so it was not applied here. The $^{238}U^{16}O$ mass station was used for energy centering. Data were acquired in mono-collection mode using an ETP 133H electron multiplier (to which a 46.2 ns dead-time correction was applied based on a delay-line circuit in the pre-amplifier) and using a mass resolution of M/ΔM ≈ 4200 (at 10 % peak height). A single analysis took ca. 18 min., which included 80-second pre-sputtering of the target domain employing a 20 µm raster. Ellipse-shaped analytical spots (14–23 µm in diameter) were located in the center of rectangular (27 x 36 µm) pre-sputtered sample domains.

The U–Pb fractionation factor was established using the Pb/U vs. UO/U relationship, employing a power law fit as defined using reference material NW-1 with $^{206}Pb/^{238}U$ age of 1168.3 ± 4.5 Ma (Wu *et al.*, 2017). Data reduction was performed with the help of the Excel-based program developed by Martin Whitehouse (NORDSIM facility, Stockholm), while the Isoplot package (version 4.15; Ludwig, 2012) was used for age calculation and data visualization. A total of 16 locations were measured on 12 grains of NW-1 that were embedded in a separate mount: this required sample swapping between the unknowns and the reference material (NW-1). Based on post-analysis microscopic observations and detailed data evaluation, two analyses of NW-1 were rejected due to cracks. The ^{204}Pb-corrected concordia age calculated based on the remaining analyses was 1157 ± 24 Ma (2 σ; MSWD = 0.12; Grema *et al.*, 2024), which is in agreement with the TIMS-determined age of NW-1 (1168.3 Ma). 1 σ notation in the processed data corresponds to the overall uncertainty of the measurement, including a run component (1 standard error) and a reference material component (1 standard deviation).

3.4.5. Quantitative X-ray diffractometry (QXRD)

A total of 73 samples were selected for QXRD comprising 5-23 cm long quarter cores from mineralized drill hole intervals (except for the NB84-10 drill hole, where barren and weakly mineralized cores were sampled). The samples were initially crushed and powdered to <62 µm grain size using a jaw crusher and a mini ball mill, followed by micronizing to <10 µm in cyclohexane. The milled samples were air-dried, and randomly oriented powders were prepared in the sample holders for the diffractometer pattern collection. The XRD analyses were performed using a PANalytical Empyrean X-ray diffractometer, using 40 mA, 40 kV, and Cukα radiation. A step size of 0.02^{o} 2θ with 60 s/step was used from 4.6^{o} to 85^{o} 2θ. Preliminary mineral identification was conducted using the software EVA (Bruker, version 11.0.0.3) and reference patterns from the International Center for Diffraction Data (ICDD), crystallography database (COD), and inorganic crystal structure database (ICSD). The software Profex (version 5.0.2; Doebelin & Kleeberg, 2015), calibrated for the PANalytical Empyrean XRD, was used for quantitative Rietveld refinement. Results are reported in percentages with an uncertainty of <3 % for the quantitative analyses.

The clay size fraction (< 2 µm) analysis was conducted on selected barren and mineralized representative rock samples (n= 26). Selected samples were crushed and transferred into glass beakers filled with de-ionized water. The glass beakers were placed in an ultrasonic water bath for 10 - 15 minutes to bring the clays into suspension. The solution was then centrifuged at 1,100 rpm for 1 minute and oven-dried at 50^{o}C. 45 mg of the dried powder clay floccules were resuspended using 1.5 ml de-ionized water and placed on glass slides that were then air-dried and also treated with ethylene-glycol. Air-dried and ethylene-glycolated samples were analyzed by scanning from 2^{o} to 50^{o} 2θ and 2^{o} to 35^{o} 2θ, respectively, at step-width of 0.02^{o} 2θ intervals. Qualitative clay size fraction determinations were conducted using the software EVA (Bruker, version 11.0.0.3). The mineralogical identification of the whole rock and the clay size fraction is often affected by uncertainties due to peak overlap, shifting, broadening, correction, calibration, and structural disorder. Other complementary techniques, including polarizing microscopy, EPMA, and SEM analyses, were used to check for ambiguities and confirm the identifications and refinements.

3.5. Results

3.5.1. Geology of the Boundary Zone

The sulfide mineralization at the Boundary Zone was intersected over an area 2 km long, 200 to 800 m wide, and at between 20 m to 300 m depth (Figs. 3-3, 3-4). The nine drill holes described in this study intersect stratigraphic units of the Road River Group (including the Duo Lake Formation and possibly Steel Formation) and the Portrait Lake Formation (Fig. 3-5). Both the Late Ordovician to Early Silurian Duo Lake and Middle to Late Devonian Portrait Lake Formations host Zn mineralization at the Boundary Zone (Fig. 3-3b-c). The Portrait Lake Formation contains of the bulk of the mineralization (Fig. 3-3). The mineralized rocks in both strata preserve two main paragenetic stages (Fig. 3-6) with stratabound sulfides in mudstones that are crosscut by veins, stockworks, and breccias. Mineralized lenses intercepted in the drill holes in the eastern part of the Boundary Zone include 322 m of 4.51% Zn in NB19-002, 272 m of 3.72% Zn in NB19-001, and 225 m of 2.08% Zn in NB20-009 drill hole (Fig. 3-3b-c; Fireweed Metals Corporation, 2018).

3.5.2. Hand specimen and petrographic study of the host rocks

Duo Lake Formation: The Duo Lake Formation is the oldest unit sampled in this study and was intercepted in the NB20-009 drill hole (Fig. 3-4). The samples consist of grey to dark grey, finely laminated mudstones (Fig. 3-5a), which are variably cherty. Quartz forms a major part of the mineralogy and occurs as four main types (Fig. 3-6, classified based on Folk & Pittman, 1971). Detrital quartz (Qz$_{\text{-det,}}$ mostly <1 µm) is a relatively minor constituent and is dispersed in the matrix. Authigenic Qz-$_{\text{cryp}}$ (chalcedonic) and microquartz (Qz$_{\text{-mic}}$; grain sizes<20 µm) are the dominant phases. Megaquartz (Qz$_{\text{-mega}}$), with grain sizes >20 µm, forms mostly in veins or as pressure shadows around earlier mineral phases. The mudstones contain radiolarian-rich beds, often separated by mm to sub-mm thick layers of very fined-grained radiolarian-poor clay-rich layers. The radiolaria tests are partially preserved by Qz-$_{\text{cryp}}$ and Qz$_{\text{-mic}}$ (Fig. 3-7a-b) set in a Qz-$_{\text{cryp}}$ matrix containing microporosity (Fig. 3-7c) and pyrobitumen (Grema *et al.*, 2024a). Pyrite is disseminated in the mudstone with the matrix components draping around the crystals (Fig. 3-7c). Bedding parallel and high-angle stylolites are observed within the mudstones, often forming both parallel to mudstone laminae and at the interface between the matrix and the radiolarian silicified tests (Fig. 3-7a).

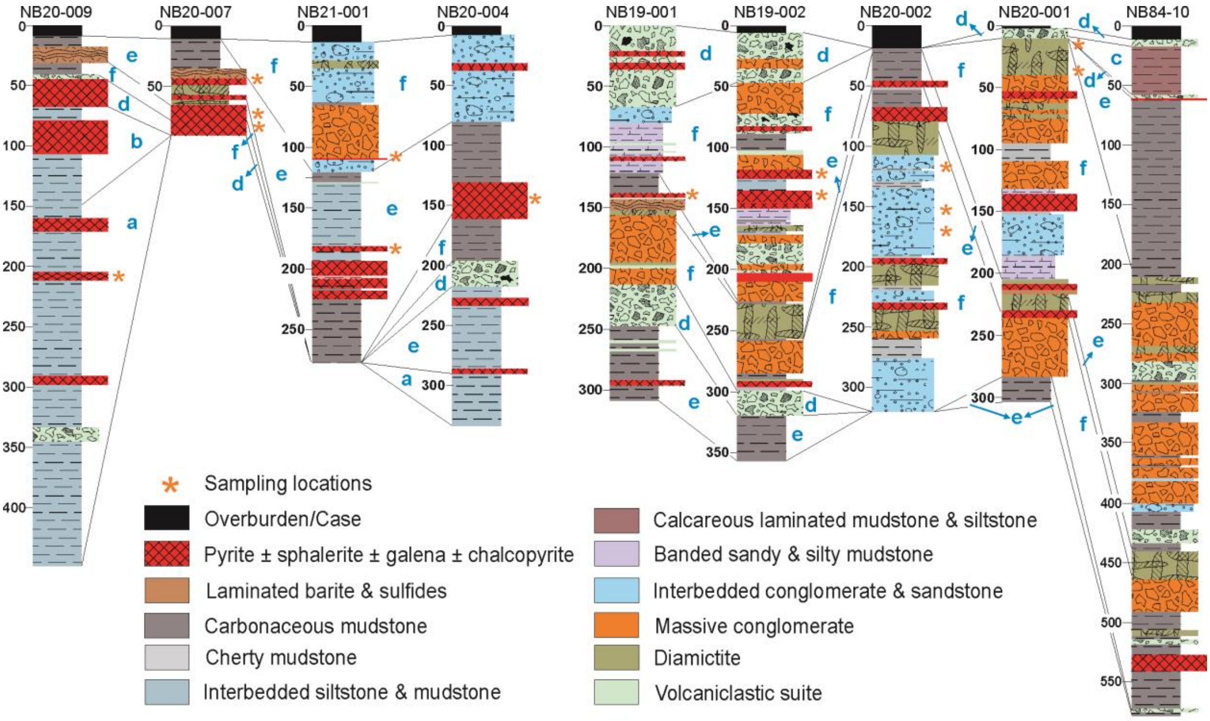

a= Duo Lake Formation; b= Steel Formation; c= Sapper Formation; d= Macmillan Pass Volcaniclastics, e= Niddery Lake Member; f= Macmillan Pass Member (mudstones, conglomerate, & diamictites)

Fig. 3- 4: Lithostratigraphic logs of the drill holes sampled in this study with sampling locations highlighted by the orange stars. Sulfide mineralized intervals are denoted by the red bars.

Portrait Lake Formation: The Niddery Lake Member comprises rhythmically intercalated cm-scale grey chert, pyrite, and dark grey to black, sometimes silty, mudstone layers (Fig. 3-5b). Mudstone layers vary in thickness from fine laminae (<10 mm) to beds up to 5 cm giving the rock a banded appearance. The cherty layers comprise Qz-$_{\text{cryp}}$ to Qz-$_{\text{mic}}$ (Fig. 3-7d) interbedded with layers that have radiolarian tests preserved by Qz-$_{\text{cryp}}$ (Fig. 3-7e), similar to the Duo Lake Formation (Fig. 3-7a). Notably, at certain stratigraphic intervals, the Niddery Lake Member mudstones comprise interbedded carbonaceous radiolarian-rich layers and bedded Qz-$_{\text{mic}}$ and nodular barite crystals. The barite forms an assemblage with phyllosilicate minerals, primarily illite, concentrated along laminae with differential compaction around the fluorapatite, barite, and pyrite mineral crystals (Fig. 3-7f).

The Macmillan Pass Member comprises intercalated mudstones, conglomerates, volcaniclastics, and diamictites. The mudstones have interbedded silty and black carbonaceous layers with fine-grained stratiform pyrite (Fig. 3-5c). The pyrite occasionally occurs as nodules and mm-sized grain aggregates. Subhedral to euhedral siderite crystals and minor dolomite are also disseminated in the mudstone matrix (Fig. 3-7g). Macmillan Pass Member interbedded conglomerates contain well-rounded to sub-angular, pebble-sized clasts of quartz, chert, and polylithic components (Fig. 3-5d). They can be clast-supported or matrix-supported with quartz, siderite, and sulfide minerals in the cement.

In the sampled intervals, lapilli tuffs dominate the volcaniclastic beds that are interbedded with the Macmillan Pass Member (Fig. 3-4). The clasts in the tuff are subrounded to angular, varying in size from mm to a few cm and exhibit hyaloclastic textures (Fig. 3-5e). Individual clasts and framework mineral grains in the lapilli tuffs are extensively altered and cemented by Fe-carbonates and phyllosilicates (Figs. 3-5e, 3-7h).

The diamictites comprise a diverse mixture of unsorted mudstone, conglomerate, and volcanic clasts within a sand- to clast-supported matrix (Fig. 3-5f). Barite, fluorapatite, siderite, pyrite, celsian, and phyllosilicate minerals are common (Fig. 3-7i-k). Deformation features such as fractures, quartz veins, and dissolution seams (stylolites) are common in the diamictites (Fig. 3-5f-g).

3.5.3. Paragenesis

Hand specimen identification, optical (transmitted and reflected light) microscopy, and EPMA techniques were combined to define a paragenesis comprising pre-ore, ore-stage I, and ore-stage II in the Duo Lake and Portrait Lake Formations. A summary of the paragenesis is given in Fig. 3-6 and described below.

Pre-ore stage: The pre-ore stage in the Duo Lake and Portrait Lake Formations is characterized by the formation of two pyrite generations, quartz, barite, and phyllosilicate minerals. Pre-ore pyrite (Py-0) comprises framboids (Py-0a) and anhedral to subhedral pyrite (Py-0b) that form in the interstitial pore spaces of the mudstones, concentrated along stratiform pyritic layers (e.g., Fig. 3-5b, c), or as disseminations in the matrices of mudstones, conglomerates, volcaniclastics, and diamictites (Fig. 3-7). The Py-0a crystals are mostly <10 µm in diameter and can form aggregates that are up to 150 µm in size; whereas Py-0b crystals are relatively coarser-grained (<120 µm) and often form an overgrowth on Py-0a.

In the Duo Lake Formation, Py-0a and b form as disseminated crystals in the mudstones but are relatively more abundant in the radiolarian-rich layers. Disseminated illite and organic matter are both abundant in the mudstones (Fig. 3-7c). In the Niddery Lake Member, Py-0a and b crystals are commonly concentrated along stratiform laminae in radiolarian-rich beds (Fig. 3-7d). Barite and fluorapatite are also commonly concentrated in the Niddery Lake Member mudstone (Fig. 3-7f).

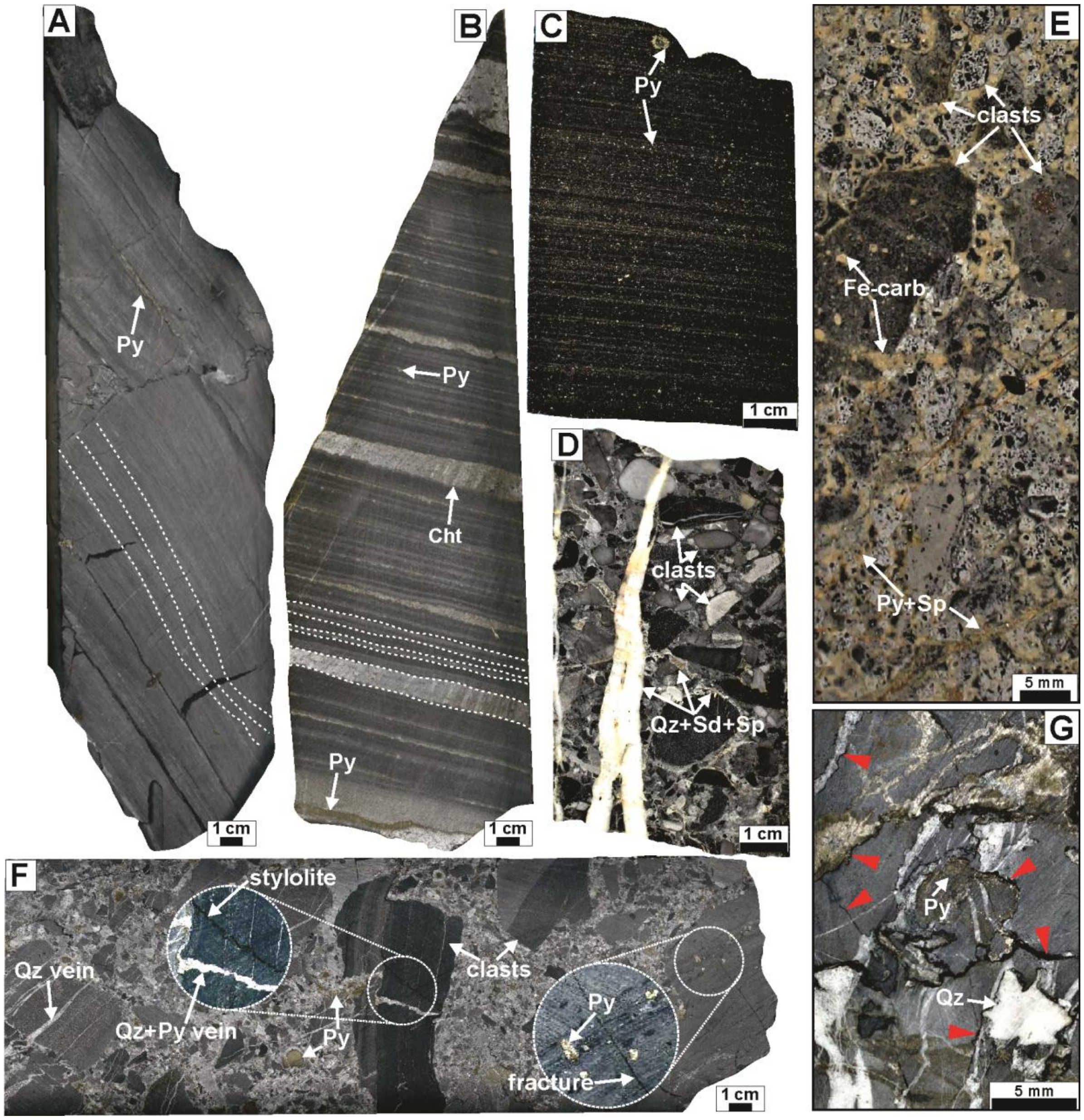

Fig. 3- 5: Hand specimen photographs of the Boundary Zone sulfide mineralization host rocks and structures. A) Hand specimen photograph of dark grey siliceous mudstone of the Duo Lake Formation. Pyrite grains are rare and occur mostly as sparse disseminations. B) Hand specimen photograph of the Niddery Lake Member comprising laminated mudstone and chert, with bedding parallel pyrite layers. C) Hand specimen photograph of finely laminated carbonaceous mudstone of the Macmillan Pass Member with rhythmic mm-scale pyrite-mudstone laminae. Coarse-grained pyrite and nodular grains are common. D) Hand specimen photograph of a pebble-sized conglomerate of the Macmillan Pass Member. Clasts are mostly siliceous fragments, cherts, and mudstones. The cement commonly consists of quartz, siderite, and sulfide minerals. E) Hand specimen photograph of Fe-carbonate cemented lapilli tuff with amygdular volcanic clasts. F) Hand specimen photograph of a diamictite with different mudstone fragments supported in a pebble-to-sandy matrix. G) Hand specimen photograph of black carbonaceous mudstone of the Niddery Lake Member, with stylolites (red arrows). Brt = barite, Cht = chert, Fe-carb. = iron carbonates, Py = pyrite, Qz = quartz, Sd = siderite, Sp = sphalerite.

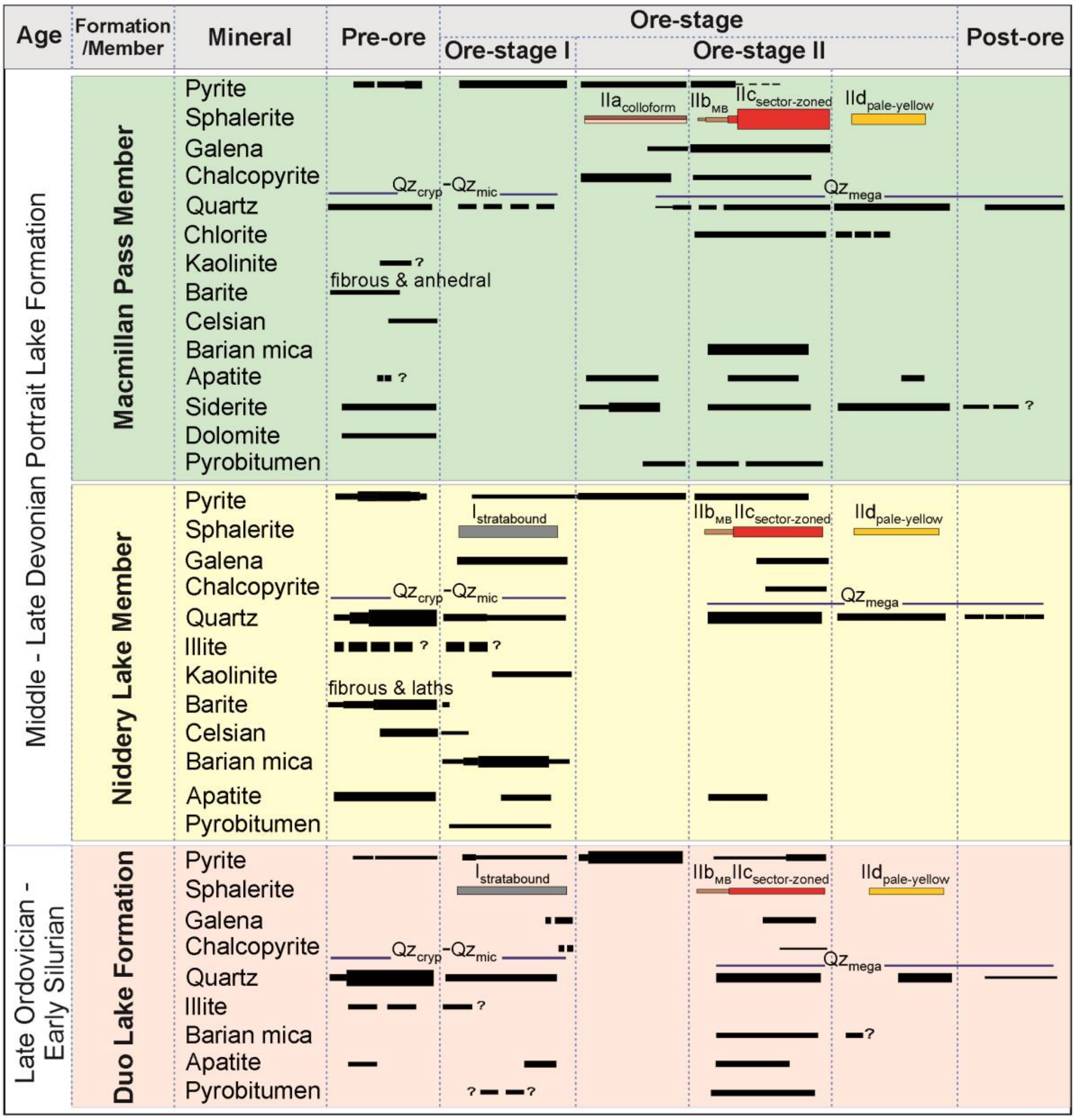

Fig. 3- 6: Simplified paragenetic sequence for the Boundary Zone sulfides and other major mineral phases. Segmented bars indicate uncertain temporal formation of mineral occurrence. Bar thickness indicates the relative abundance of the mineral phases.

The Macmillan Pass Member mudstone contains abundant Py-0a and b (Fig. 3-5c). Similar generations of pre-ore pyrite formed in the Macmillan Pass Member conglomerate and diamictite, mostly occurring in the groundmass around the clasts (e.g., Fig. 3-5f). However, euhedral Py-0b crystals often rim the margins of the clasts in a replacive texture. In volcaniclastics, subhedral to euhedral Py-0b is the volumetrically significant pre-ore pyrite generation and forms crude laminae in the lapilli tuff. Porous celsian, subhedral fluorapatite, and phyllosilicate minerals (predominantly illite, kaolinite, pyrophyllite, and muscovite) form as part of the pre-ore mineral assemblage in the volcaniclastics (Fig. 3-7h, j-k).

Ore-stage I: The first ore stage comprises stratabound sphalerite, galena, and pyrite with minor chalcopyrite and sulfosalts. The sulfide minerals are hosted by the cherty and carbonaceous (silty-) mudstones of the Duo Lake Formation (Fig. 3-8a) and Niddery Lake Member of the Portrait Lake Formation (Fig. 3-8b-c). Ore-stage I sulfide mineralization is absent in the Macmillan Pass Member mudstone, conglomerate, volcaniclastic, diamictite beds, and the Fuller Lake Member.

In the Duo Lake Formation, stratabound steel-grey Sp-I$_{\text{stratabound}}$ is disseminated or occurs in bedding parallel radiolarian-rich layers ranging from <1 mm to 50 cm thick (Figs. 3-8a, 3-9a-c). These mineralized beds are often interbedded with barren, very fine-grained mudstone (Fig. 3-9c). Sp-I$_{\text{stratabound}}$ is spherical (round to ellipsoidal) and frequently forms pseudomorphic replacement of radiolarian tests, with grain sizes that range from <10 µm to 1.5 mm (Fig. 3-9b-e). Qz-$_{\text{mic}}$ (Fig. 3-9e-f) and subhedral to euhedral crystals (Py-I) of pyrite (Fig. 3-9g) are associated with the Sp-I$_{\text{stratabound}}$. Minor anhedral galena, chalcopyrite (Fig. 3-9h), together with subhedral to euhedral inclusion-rich fluorapatite (Fig. 3-9i) are part of the assemblage together with pyrobitumen (Fig. 3-9f-g). The Sp-I$_{\text{stratabound}}$ crystals are often crosscut by pyrobitumen- and phyllosilicate-rich stylolites (Fig. 3-9j) that develop at the interface between mineralized and barren mudstone layers (Fig. 3-9c).

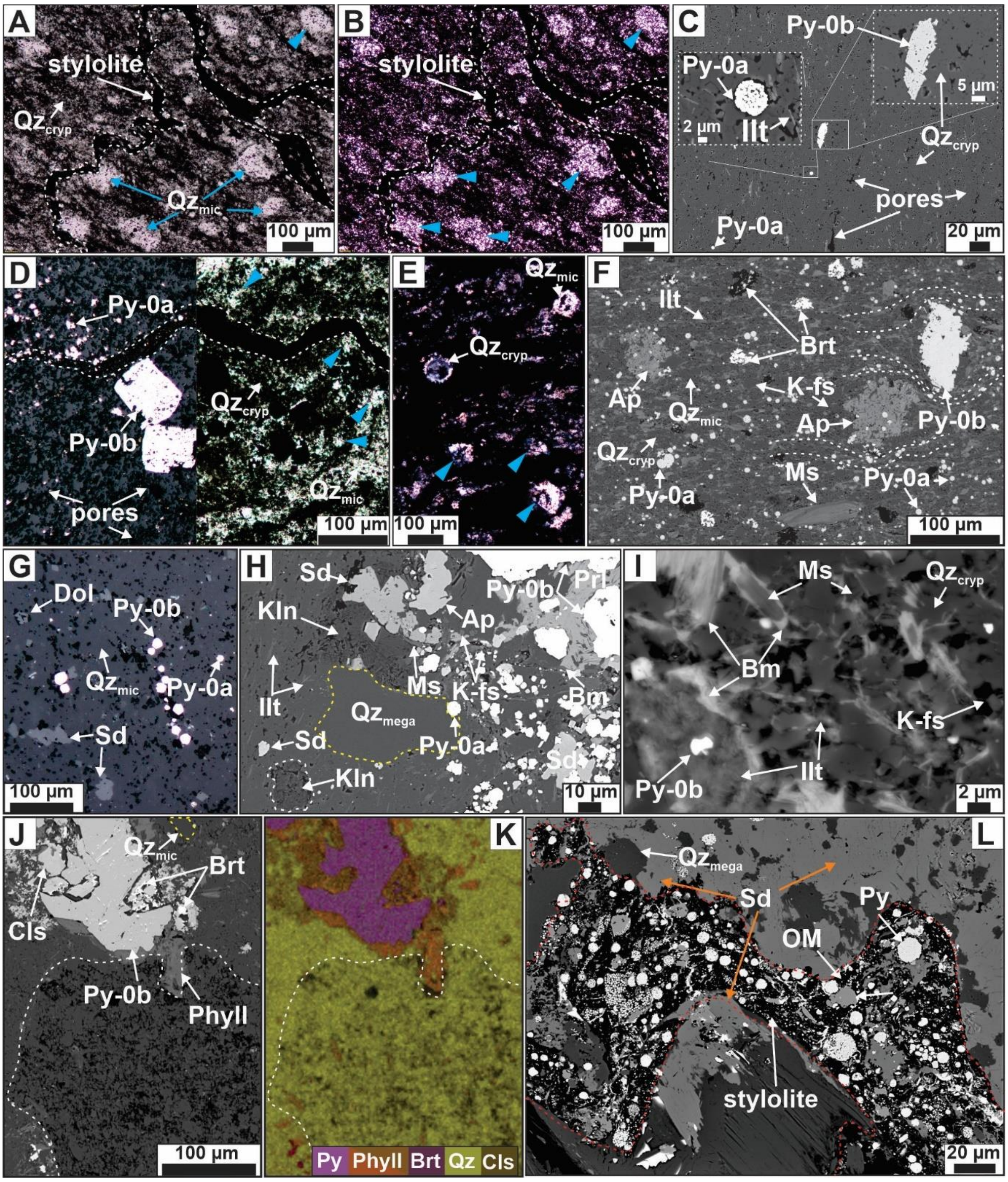

Fig. 3- 7: Representations of samples of the Boundary Zone host rocks highlighting the background mineralogical compositions: A) Transmitted and reflected light (B) photomicrographs of Duo Lake Formation mudstone showing silicified radiolarian tests that have been preserved. C) BSE image Duo Lake Formation with framboidal and subhedral pyrite set in a chert matrix. D) Reflected and transmitted light composite photomicrograph of the Niddery Lake Member with disseminated framboids and coarser subhedral to euhedral pyrite. Bedding parallel clay-rich layers are common in mudstone. E) Transmitted light photomicrograph of preserved radiolarian tests in the Niddery Lake Member. F) BSE image of siliceous mudstone of the Niddery Lake Member, showing patchy porous fluorapatite, barite, and pyrite. Dotted lines indicate differential compaction of the mudstone around the pyrite and fluorapatite crystals. G) Reflected light photomicrograph of mudstone of the Macmillan Pass

Member. Subhedral to euhedral dolomite and siderite are common. H) BSE image of diamictite with altered mudstone clast (left) and volcanic clast (right). Fluorapatite, phyllosilicates, and pyrite are common. I) BSE image of a mudstone clast showing the phyllosilicate minerals, microcrystalline quartz, and K-feldspar. J) BSE image of a mudstone clast of a diamictite, highlighting the replacement of barite by pyrite and celsian next to a trachytic volcanic clast (highlighted). K) False color image of J. L) Backscattered electron (BSE) image of a stylolite with fine-grained pyrite and phyllosilicate minerals. Ap = fluorapatite, Bm = barian-mica, Brt = barite, Cls = celsian, Dol = dolomite, Ilt = illite, K-fls = potassium feldspar, Kln = kaolinite, Ms = muscovite, OM = organic matter, Phyll = phyllosilicate minerals, Py = pyrite, Qz = quartz, Sd = siderite, Ser = sericite.

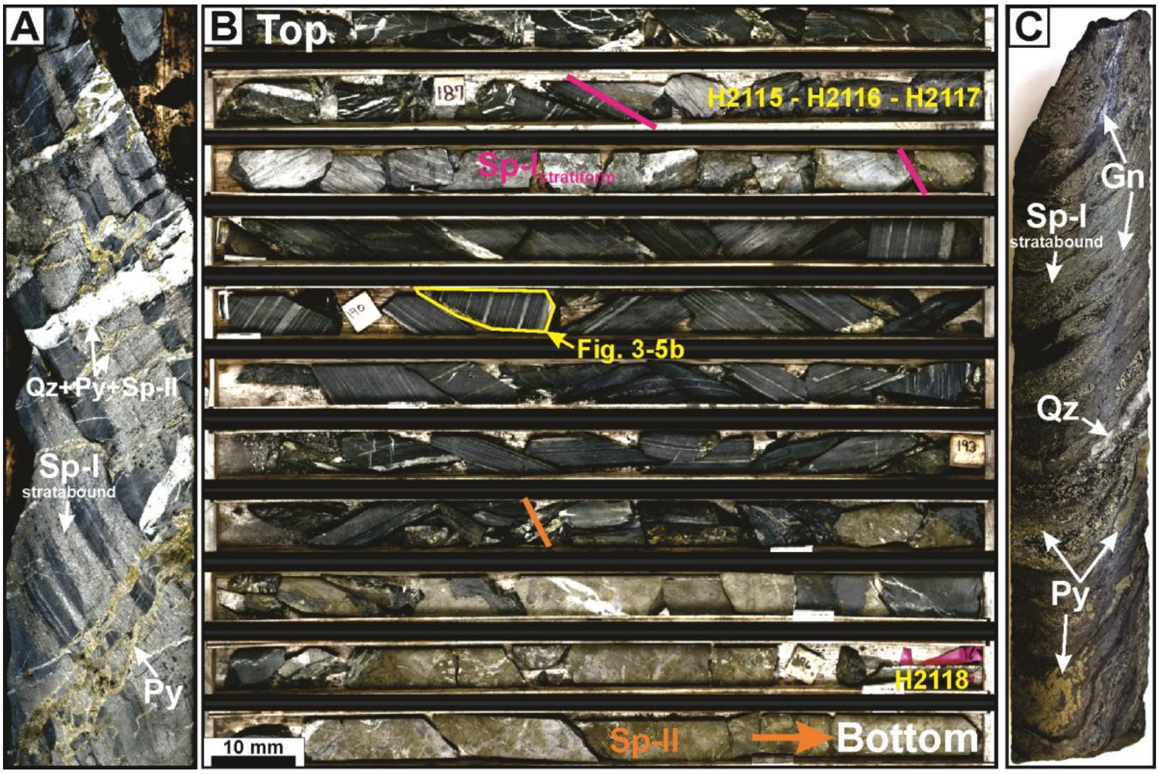

Fig. 3- 8: Representation of stratabound sulfide mineralization in the Duo Lake Formation and Niddery Lake Member: A) Photograph of a drill core sample of the siliceous mudstone showing sphalerite bedding parallel layers crosscut by quartz and sulfide veins. B) Photograph of drill core intersecting the Niddery Lake Member stratabound grey sphalerite at the top and massive pyrite-sphalerite layer at the bottom. NB21-001 hole, 185.7 – 197.3 m. C) Photograph of drill core sample of the Niddery Lake Member. Gn= galena, Py = pyrite, Qz = quartz, Sp= sphalerite.

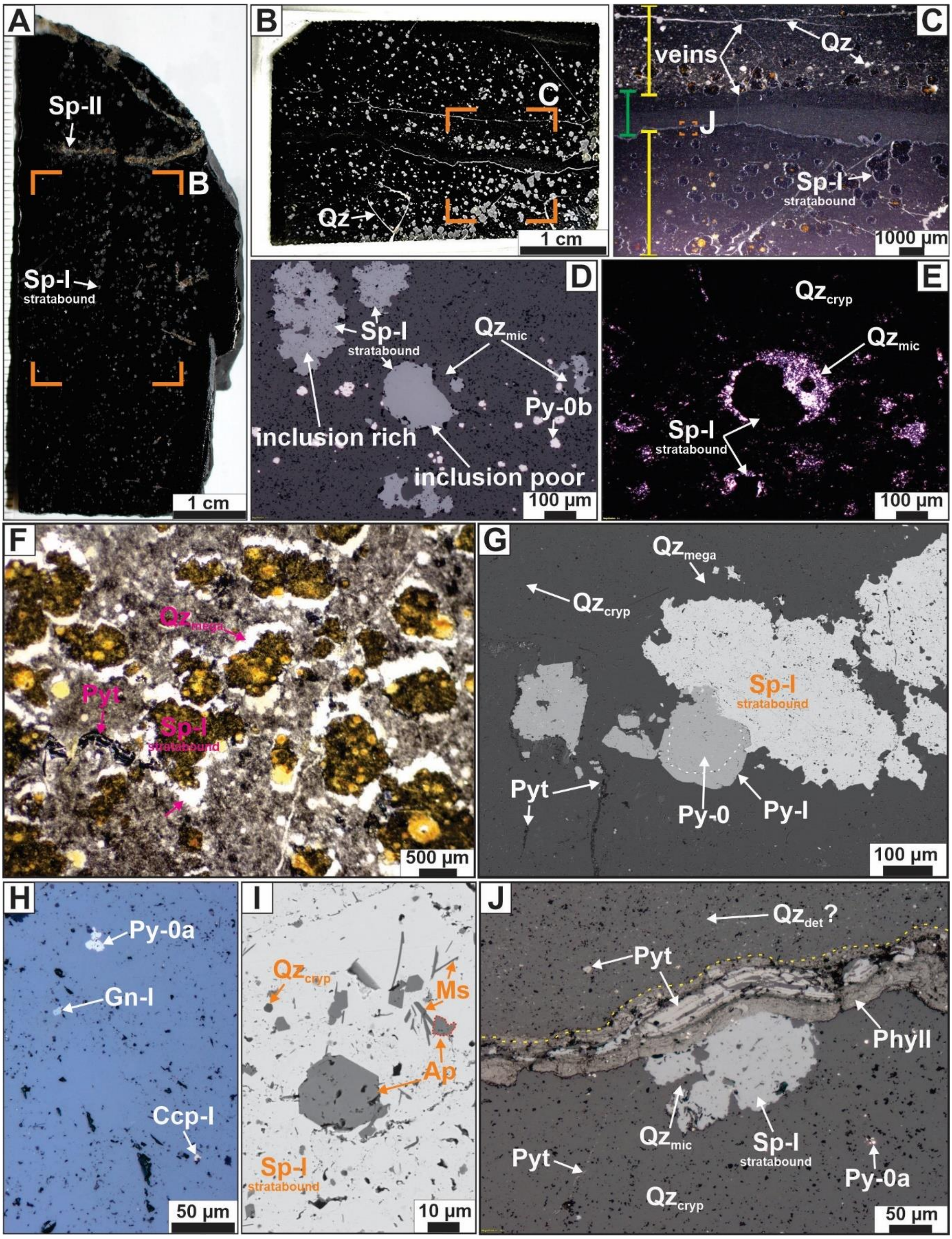

Fig. 3- 9: Representation of stratiform (ore-stage I) sulfide mineralization in the Duo Lake Formation: A) Hand specimen photograph of a mineralized sulfide layer with spherical coarse-grained sphalerite grains. Note the crosscutting vein of orange sphalerite. B) Thin section photograph of the area highlighted in A. Note the distinct spherical sphalerite grains set in the mudstone. C) Binocular photomicrograph of the area highlighted in B showing a dark grey mudstone layer separating two mineralized beds. D) Reflected light photomicrograph consisting of inclusion-rich and inclusion-poor sphalerite crystals. E) Cross-polarized

transmitted light photomicrograph of the image in D. Note how the sphalerite replaces the microquartz in the radiolarian tests. F) Binocular photomicrograph of spherical sphalerite set in a cherty matrix. G) BSE image of intergrown sphalerite and pyrite. Minor veinlets of pyrobitumen are present in the mudstone. H) Reflected light photomicrograph showing common inclusions within the sphalerite comprising galena, pyrite, chalcopyrite, and host rock matrix components. I) BSE image of subhedral to euhedral fluorapatite crystal intergrown with sphalerite. J) Reflected light photomicrograph of ore-stage I sphalerite cut across by stylolite. Ap = fluorapatite, K-fls = potassium feldspar, Ms = muscovite, Phyll = phyllosilicate minerals, Py = pyrite, Pyt = pyrobitumen, Qz = quartz, Sd = siderite, Ser = sericite, Sp = sphalerite.

Stratabound sulfides in siliceous mudstone beds of the Niddery Lake Member (Fig. 3-8b-c) are disseminated along bedding or occur in irregular layers (Fig. 3-10a) of grey sphalerite (Sp-$I_{stratabound}$), galena (Gn-I), and pyrite (Py-I; Fig. 3-10b). Here, Sp-$I_{stratabound}$ selectively and variably replace radiolaria (Fig. 3-10a-d), barite (Fig. 3-10e-i), and the mudstone matrix (Fig. 3-10j-o) with crystal sizes ranging from <5 µm to 300 µm (e.g., Fig. 3-10c, h). In the radiolarian-rich beds, Sp-$I_{stratabound}$ (Fig. 3-10b-c) form together with up to 130 µm size aggregates of Qz_{-mic} and Qz_{-mega} crystals that are surrounded by Qz_{-mic} in the matrix (Fig. 3-10d). In contrast, in the barite-rich mudstone beds, anhedral Sp-$I_{stratabound}$ and Py-I form pseudomorphs of lath-like barite and the matrix (Fig. 3-10f). They commonly contain inclusions of barite (Fig. 3-10g) and pre-ore Py-0a (Fig. 3-10h). Coarse-grained quartz and nodular Py-I are common in the matrix replacement intervals (Fig. 3-10j), where Sp-$I_{stratabound}$ often overgrows arsenic-rich Py-0a (Fig. 3-10k-o). The Gn-I crystals are <5 µm to 100 µm in size with the other sulfides or as minor crosscutting veinlets (e.g., Fig. 3-10l). Silver-Sb-Pb-bearing sulfosalts, including tetrahedrite and geocronite (Geo; Grema *et al*., 2024a), are intergrown with Sp-$I_{stratabound}$ and Gn-I in the stratabound mineralized strata. Barian mica and kaolinite (Fig. 3-10i) are both associated with the ore-stage I sulfides in the Niddery Lake Member.

Stylolites are present in mineralized and unmineralized Duo Lake and Portrait Lake Formations in bedding-parallel (e.g., Fig. 3-7d) and high-angle (e.g., Fig. 3-5g) forms. The stylolites in both barren and mineralized host rocks are characterized by dark seams that contain phyllosilicates, pyrobitumen, and pyrite (e.g., Fig. 3-7l). Notably, stylolites in mineralized samples from the Niddery Lake Member and Duo Lake Formation are observed to crosscut ore-stage I (e.g., Fig. 3-9j). In the conglomerate of the Macmillan Pass Member, stylolitic margins are common features of the ore-stage II mineralized veins, while such veins also truncate some stylolites (Fig. 3-11a inset).

Ore-stage II: Brecciation and veining are prominent in the Duo Lake and Portrait Lake Formation strata. The breccias and veins that develop are infilled, and the fragments are cemented by sulfide minerals, phyllosilicates, megaquartz (Qz$_{\text{-mega}}$), and siderite (Figs. 3-8a, 3-11). The fragment sizes are variable and comprise mainly angular morphology with sharp contacts with the sulfides that occasionally jigsaw fit together.

The ore-stage II is the most volumetrically significant stage of sulfide formation in the Boundary Zone (Fig. 3-11), best developed in the Macmillan Pass Member mudstones, conglomerates, volcaniclastics, and diamictites. Ore-stage II style mineralization comprises layers (Fig. 3-8b), veins, and breccias (Fig. 3-11a-c) of sphalerite (four generations), pyrite, galena, and chalcopyrite, some of which crosscut the ore-stage I stratabound sulfide mineralization (e.g., Figs. 3-9a, 3-12a). The major ore-stage II gangue mineral phases are an assemblage of Qz$_{\text{-mega}}$, siderite, fluorapatite, and pyrobitumen.

Banded colloform sphalerite (Sp-IIa$_{\text{-colloform}}$) mostly occurs in veins and breccias that are hosted by the Macmillan Pass Member (Fig. 3-11f). Bands of Sp-IIa$_{\text{-colloform}}$ (< 2.6 cm thick) formed at the margins of the wall rocks (Fig. 3-11c). Microscopically, Sp-IIa$_{\text{-colloform}}$ comprises alternating bands (Fig. 3-12b) of dark brown to opaque and light brown to pale yellow crystals (Fig. 3-12d). Chalcopyrite occurs in the Sp-IIa$_{\text{-colloform}}$ crystals as blebs (Fig. 3-12e) or as chalcopyrite disease. In contrast, minor galena (Gn-II) crystals are present as fine-grained inclusions, together with siderite and dolomite. Coarse-grained anhedral pyrite (Py-IIa) zones are sometimes intercalated with Sp-IIa$_{\text{-colloform}}$ (e.g., Fig. 3-11e) or form as anhedral to subhedral crystals in interstitial pore spaces of the Sp-IIa$_{\text{-colloform}}$ (Fig. 3-12f). Py-IIa also forms massive layers in brecciated mudstones that commonly underlie the stratabound mineralization (Figs. 3-8b).

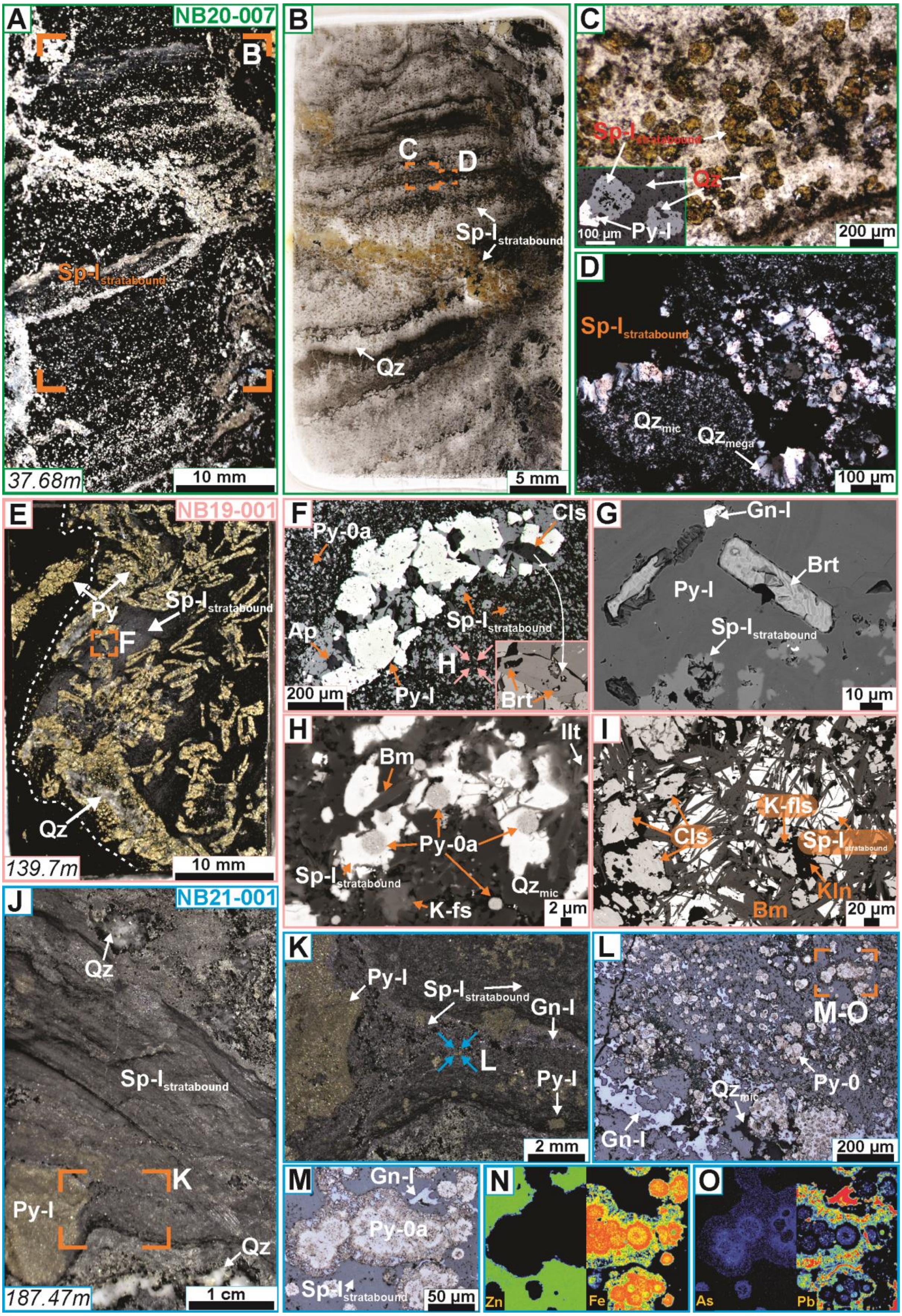

Fig. 3- 10: (Caption on the next page)

Fig. 3- 10 : Representation of stratiform (ore-stage I) sulfide mineralization in the Niddery Lake Member of the Portrait Lake Formation. A) Photograph of stratabound sphalerite. B) Thin section photograph of the area highlighted in A. C) Binocular photomicrograph of the area highlighted C in B. Spherical sphalerite grains are underlain by a dark, thin layer. Inset is a photomicrograph of intergrown sphalerite and quartz with spherical morphologies. D) Cross-polarized transmitted light photomicrograph of intergrown coarser quartz with sphalerite. E) Hand specimen photograph of Niddery Lake Member mudstone highlighting the mineralization-host rock interface that shows the nature of replacement style sulfide formation. Pyritized laths are common in the mineralized region. F) Reflected light photomicrograph of the area highlighted in E. Sphalerite forms in the mudstone matrix and the laths, comprising pyrite, celsian, and fluorapatite. G) BSE image of barite laths intergrown with pyrite and sphalerite. H) BSE image showing the nature of host rock replacement. Sphalerite primarily replaces pyrite framboids. I) BSE image of almost completely replaced mudstone with sphalerite, celsian, and barian-mica. J) Hand specimen photograph of fine-grained sulfide mineralization in the Niddery Lake Member with coarse pyrite and quartz grains. K) Binocular photomicrograph of the highlighted area in J. Fine-grained sphalerite and pyrite grains are set in mudstone that wraps around a pyrite nodule. L) Reflected light photomicrograph of a section similar to the highlighted area in K. Sphalerite and galena overgrow framboidal pyrite, almost entirely replacing the mudstone. M) Reflected light photomicrograph of the area highlighted in L. Pyrite framboids form the substrate for sphalerite and galena, set in the mudstone matrix. N-O) Electron probe microanalysis (EPMA) element distribution map of the area in M, showing Zn and Fe (N) and As and Pb (O) composite maps. Ap = fluorapatite, Bm = barian-mica, Brt = barite, Cls = celsian, Gn = galena, Ilt = illite, K-fls = potassium feldspar, Kln = kaolinite, Py = pyrite, Qz = quartz, Sp = sphalerite.

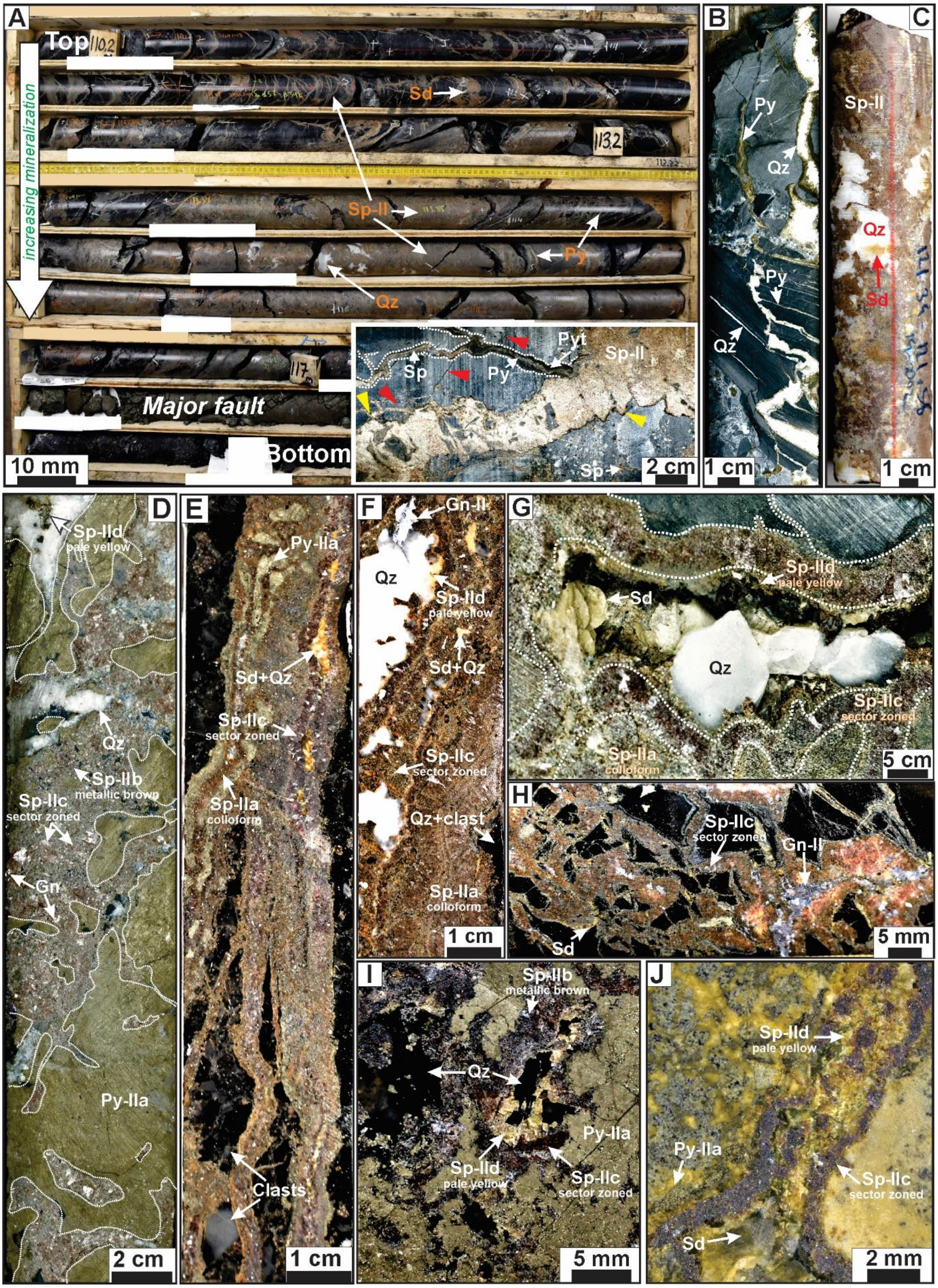

Fig. 3- 11 : (Caption on the next page)

Fig. 3- 11: Representation of the second stage (ore-stage II) sulfide mineralization. Mineralization forms in massive sulfide layers, veins, stockwork, and breccias. A) Drill core photograph of ore-stage II mineralized interval in NB19-001 drill hole. 110.1 – 119.95 m. The mineralization in the hanging wall increases significantly towards the major fault. Inset is a hand specimen photograph of a mineralized conglomerate. Sulfide veins appear intimately related to stylolites that also host sulfide minerals. Both barren (red arrows) and mineralized (yellow arrows) stylolites are shown. B) Ore stage II pyrite-quartz discordant veins cutting across diamictite and mudstone beds. Note the minor veins exploiting weak planes, for example, in the middle mudstone bed. C) Photograph of a high-grade interval massive vein sample comprising sphalerite and quartz. D) Hand specimen photograph of massive sulfide mineralization with multiple sphalerite generations and late-stage quartz. Note the fragments of the host mudstone (black) preserved in the sulfides. E) Hand specimen photograph of sulfide mineralized conglomerate. Sphalerite and pyrite bands alternate in the veins. F) Hand specimen photograph of a vein with three sphalerite generations. Colloform sphalerite forms at the margins of the vein. Galena, quartz, and siderite are common in the later sphalerite generations. G) Photograph of vein-hosted coarse-grained sulfide mineralization in the Macmillan Pass Member conglomerate. Early vein sphalerite consists of a colloform texture overgrown by coarse-grained red-brown sphalerite. Centimeter-scale euhedral quartz and siderite fill in the cavities in the veins. H) Hand specimen photograph of brecciated Macmillan Pass Member mudstone. Mudstone fragments are preserved within the sulfides in the breccia. Note the siderite grains that are distributed in the breccia. I) Hand specimen photograph of massive sulfide sample with pyrite and three generations of sphalerite. Colorless quartz appears intergrown with pale-yellow late sphalerite. J) Hand specimen photograph of sulfide mineralized lapilli tuff with sphalerite, siderite vein. The host rock is cemented by siderite, pyrite, and minor quartz. Gn = galena, Py = pyrite, Qz = quartz, Sd = siderite, Sp = sphalerite.

Two generations of coarse-grained sphalerite form overgrowths on Sp-IIa$_{\text{-colloform}}$. These two sphalerite textures are not limited to the veins and breccias of the Macmillan Pass Member but are also common in the massive pyrite replacement layers that underlie the stratabound mineralization. Coarse-grained black to metallic brown sphalerite (Sp-IIb$_{\text{-metallic-brown}}$) overgrows Py-IIa (Fig. 3-11i) and, rarely, the Sp-IIa$_{\text{-colloform}}$ in the veins. Sp-IIb$_{\text{-metallic-brown}}$ represents a minor component of the ore-stage II sulfide assemblage. Under transmitted light microscopy, Sp-IIb$_{\text{-metallic-brown}}$ has a highly porous texture (Fig. 3-12g) and is intergrown with fine-grained euhedral pyrite crystals (<25 µm; Py-IIb) and aggregates.

The volumetrically dominant sphalerite generation at Boundary Zone consists of very coarse-grained, up to 3 mm, red-brown sector-zoned sphalerite (Sp-IIc$_{\text{-sector-zoned}}$, Figs. 3-11, 3-12a, i). Sp-IIc$_{\text{-sector-zoned}}$ formed in veins that crosscut the Sp-I$_{\text{stratabound}}$ layers (e.g., Fig. 3-12a). In the veins, Sp-IIa$_{\text{-colloform}}$ sphalerite is almost always overgrown by Sp-IIc$_{\text{-sector-zoned}}$ (Fig. 3-12b). In contrast, in the breccia, Sp-IIc$_{\text{-sector-zoned}}$ is abundant and sometimes the only sphalerite formed (e.g., Fig. 3-11h). Under transmitted light, Sp-IIc$_{\text{-sector-zoned}}$ is occasionally rhythmically banded with red to colorless crystals (Fig. 3-12h).

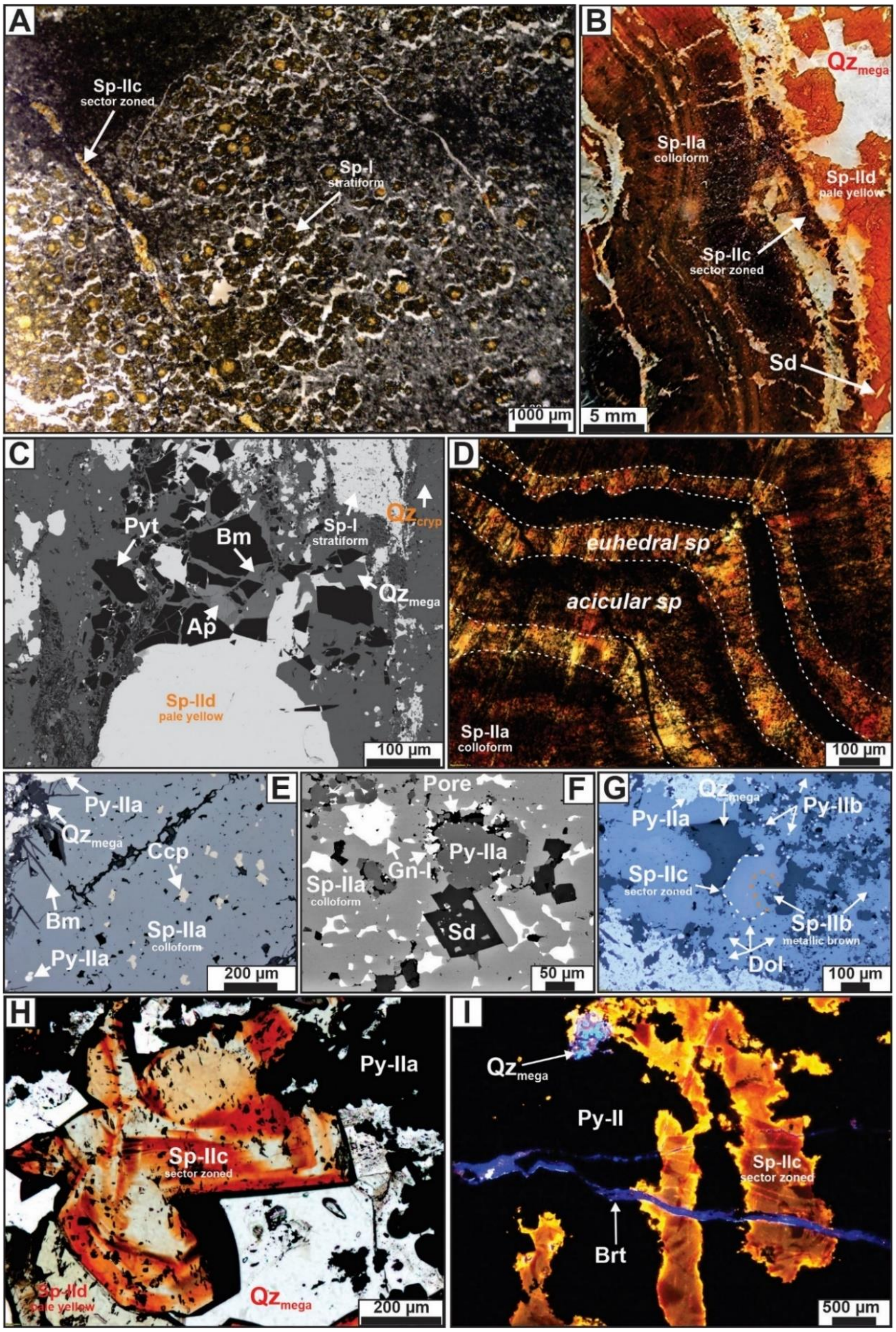

Fig. 3- 12: Binocular and BSE and photomicrographs showing the sulfide mineral textures of the ore stage II. A) Binocular photomicrograph of the Duo Lake Formation mudstone with an ore-stage II vein cutting across the stratabound ore-stage I mineralization. B) Thin section photograph of banded colloform sphalerite overgrown by later sphalerite generations. C) BSE image of a vein mineral assemblage in the Duo Lake Formation, consisting of sphalerite, pyrite,

fluorapatite, pyrobitumen, quartz, and barian-mica. D) Transmitted light photomicrographs of colloform sphalerite with a banded texture. E) Reflected light photomicrograph of colloform sphalerite with chalcopyrite blebs. F) BSE image of sphalerite, galena, and siderite dolomite intergrowth. Note the porosity around the anhedral pyrite aggregates and euhedral siderite crystals. G) Reflected light photomicrograph showing two generations of sphalerite: highly porous sphalerite and crystalline euhedral sphalerite intergrown with quartz. H) Transmitted plane polarized light photomicrograph highlighting the relationship between sector-zoned sphalerite and the pale-yellow sphalerite that forms an assemblage with quartz. I) Cathodoluminescence photomicrograph of a massive sulfide sample. A late-stage barite vein crosscuts pyrite and sphalerite. Ap = fluorapatite, Bm = barian-mica, Brt = barite, Ccp = chalcopyrite, Py = pyrite, Pyt = pyrobitumen, Qz = quartz, Sd = siderite, Sp = sphalerite.

A coarse-grained (<1 cm) galena generation (Gn-II), which can grow up to 1 cm, is commonly intergrown with Sp-IIc$_{\text{-sector-zoned}}$ in both veins (e.g., Fig. 3-11f) and breccias (e.g., Fig. 3-11h). Other coeval mineral phases include fluorapatite, and pyrobitumen (Fig. 3-12c), and minor subhedral to euhedral Qz$_{\text{-mega}}$ (Fig. 3-12i).

Finally, coarse-grained pale-yellow to transparent sphalerite (Sp-IId$_{\text{-pale-yellow}}$) is observed in the Duo Lake and Portrait Lake Formations. Sp-IId$_{\text{-pale-yellow}}$ primarily postdates earlier sphalerite and pyrite generations (e.g., Figs. 3-11i) and infill cavities within the rocks (e.g., Fig. 3-11i). The individual crystals of Sp-IId$_{\text{-pale-yellow}}$ range in size from 60 µm to mm-scale (Fig. 3-12b), and they are often associated with coarse cm-scale Qz$_{\text{-mega}}$ and siderite crystals in veins and breccias (Fig. 3-11).

3.5.4. Fluorapatite chemistry

The pre-ore, ore-stage I, and ore-stage II fluorapatite crystals from the Boundary Zone all plot in the fluorapatite region of the F-Cl-OH diagram (Fig. 3-13a), with median atoms per formula unit (a.p.f.u) F content of 2.54 (4.8 wt.%; Grema *et al.*, 2024a) and low Cl (Fig. 3-13b). Due to the beam-induced migration, poor precision, and high detection limit for F in EPMA analysis, the F content in these crystals is considered semi-quantitative and exceeds the maximum content (~3.8 wt.%) for stoichiometric fluorapatite (Piccoli & Candela, 2002).

Broadly, there is a lack of systematic variation in Sr, Mn, and REE+Y (La + Ce + Pr + Nd+Y) contents (Fig. 3-13c-d), except for higher Si content in the pre-ore fluorapatite and lower Sr (<1 wt.%) in the fluorapatite coeval with Sp-IIa$_{\text{-colloform}}$. In contrast, the Duo Lake Formation (median= 1.9 wt.% Sr and up to 9.4 wt.%) and Niddery Lake Member hosted fluorapatite with elevated Sr contents. A minor negative correlation exists between Ca and Sr, Mn, and REE+Y (Fig. 3-13d).

3.5.5. Fluorapatite U-Pb geochronology

Pre-ore, ore-stage I, and ore-stage II fluorapatite crystals were analyzed for U-Pb dating; however, most crystals had high non-radiogenic Pb contents and low U mass fractions. The common Pb and low U made the data reduction and reliable age determination impossible. Furthermore, fluorapatite crystals in the pre-ore stage and coeval with ore-stages I and II sphalerite generations (e.g., Fig. 3-12c) contained abundant inclusions and micro-porosity in the fine-grained samples. These features made it particularly challenging to avoid surface imperfections and generate acceptable analyses despite the good spatial resolution of the analytical method. The only successful dating was produced on fluorapatite crystals in a vein crosscutting ore-stage I (NB19-001 drill hole). All fluorapatite U-Pb results, together with pre-analysis and post-analysis images of the crystals, are provided as part of the data publication of Grema *et al.* (2024).

A total of fourteen measurements were produced on crystals in the NB19-001 sample, although eight of these results were rejected due to cracks, abundant inclusions, and/or porosity. Three of the remaining analyses did not show crater-related issues, while in the other three, there were some inclusions and porosity that could have potentially influenced U-Pb determinations. In the end, all six analyses were taken into account due to the fact that the data reduction yielded similar ^{207}Pb-corrected ages, with the weighted mean of 169 ± 10 Ma (2 σ, MSWD = 0.54, Fig. 3-13e-f). Given the complexity of the studied samples and general challenges related to U-Pb dating of minerals of the apatite supergroup, which commonly incorporate non-radiogenic Pb into the structure (e.g., Pan & Fleet, 2002), we were unable to rigorously assess uncertainties of our measurements. Therefore, based on the SIMS data obtained for six fluorapatite grains in veins hosted in the Niddery Lake Member (Table 3-1), we can assign a Middle Jurassic formation age.

3.5.6. Quantitative XRD mineralogy

The QXRD data are part of data publication in Grema *et al.* (2024) and are featured in Fig. 3-14. Apart from two samples with 1 - 4% sphalerite contents, the NB84-10 drill hole, comprised mainly of Macmillan Pass Member units, is unmineralized and is referred to as barren in the following section. The whole rock mineralogical compositions of mudstones plot dominantly in the siliceous mudstone and siltstone field of the quartz+feldspar-phyllosilicate-carbonate ternary diagram (Fig. 3-15a). The major groups of mineral phases from the QXRD data are summarized by host formation.

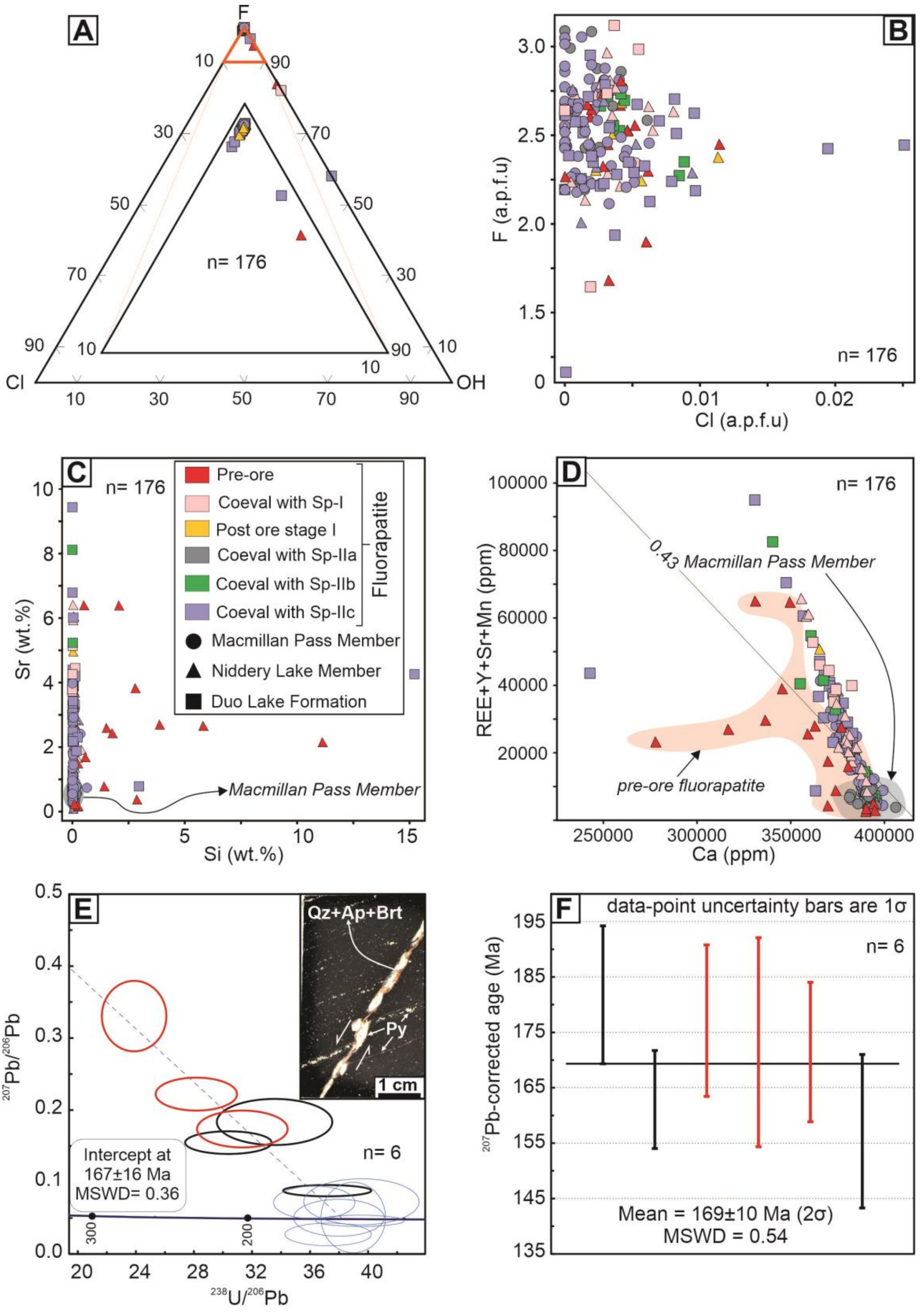

Fig. 3- 13: A) Fluorapatite F-Cl-OH ternary diagram of the major halogen composition. Inset is an enlarge part of the diagram indicated in orange color. B) Binary plot of Cl vs F calculated to a.p.f.u on basis of 26 oxygen atoms in fluorapatite obtained via EPMA. C) Binary plot of Si vs Sr (wt.%). D) Binary plot of Ca vs ΣREE+Y+Sr+Mn (in ppm). ΣREE= La+Ce+Pr+Nd. E) Tera-Wasserburg U-Pb concordia plot showing the SIMS fluorapatite geochronology results from post-ore stage veins in the Niddery Lake Member mudstone in the Boundary Zone (n =

6). Inset is the Niddery Lake Member sample with the dated fluorapatite (Ap) in a discordant vein. F) Weighted mean $^{206}Pb/^{238}U$ ages for the 6 post-ore fluorapatite crystals, with data point uncertainties indicated as 1σ. a.p.f.u= atoms per formula unit, ppm= parts per million, Sp= sphalerite.

Duo Lake Formation: Samples from the Duo Lake Formation mudstones are significantly enriched in quartz (mean= 64%), although massive sulfide samples contain minor quartz (minimum = 8%; Fig. 3-14a). No carbonate minerals were identified in the samples, except 3% calcite and 1% ankerite in samples H2094 and H2093, respectively. Microcline (up to 4%) is the dominant feldspar phase with <3% albite. Phyllosilicates are <2% in all the mudstones, except illite, which reaches 6% in one massive sulfide sample (Fig. 3-14b). Minor fluorapatite (~1%) has been detected in the samples; however, a brecciated sulfide-enriched sample comprised up to 5% fluorapatite. Pyrite and sphalerite are the dominant sulfide minerals. The volumetrically significant pyrite occurrences are in breccias and veins (16-77%) compared to 1-21% observed in stratabound mineralization with sphalerite. Comparatively significant sphalerite contents are hosted in stratabound layers (3-18%) and ≤2% in the breccias and veins.

Portrait Lake Formation: Lapilli tuff comprises ≤ 24% quartz (one quartz vein sample with 52%) but relatively high siderite (11-42%), illite (1-14%), and pyrophyllite (<1-15%) in the barren samples. One lapilli tuff sample (H1926) has a particularly high sulfide content with 51% sphalerite, 2% chalcopyrite, and <1% pyrite.

In the Niddery Lake Member, quartz content varies from <25% in the massive sulfide mineralized samples to 83% in the weakly stratabound sulfide mineralized samples. Carbonate minerals are almost absent from the bulk mineralogy of the Niddery Lake Member, with all phases <2%, except for ankerite, which reached 12% in two samples (H2115 and H2116) from the NB21-001 drill hole. Feldspar minerals are dominated by microcline (<1-6%), albite (<1-4%), and one stratabound mineralized sample with 5% celsian (H64). All other phyllosilicate minerals are <3% (Fig. 3-14b), except for samples in the NB19-001 drill hole with a significant amount of illite (1-10%) and the highest muscovite contents in the Boundary Zone (14-26%). Compared to all other lithologies, the Niddery Lake Member samples have less than 2% barite. Pyrite (1-85%) and sphalerite (<1-61%) are the dominant sulfide minerals. The Niddery Lake Member mudstones have the highest galena contents, reaching 14%, with minor chalcopyrite (0-3%) occurring in multiple samples.

Table 3- 1: SIMS U-Pb fluorapatite data for sample a5 from vein crosscutting ore-stage I. Ap= fluorapatite.

Sample name	**Analysis ID**	**^{207}Pb/^{206}Pb**	**1 SE (%)**	**^{208}Pb/^{206}Pb**	**1 SE (%)**	**^{204}Pb/^{206}Pb**	**1 SE (%)**	**^{206}Pb/^{238}U**	**1 SE (%)**	**^{238}U^{16}O/^{238}U**	**1 SE (%)**
H42	a5_Ap_Vein_2	0.1547	6.7	0.2841	11.0	0.0078	26.0	0.12	3.9	6.36	1.1
H42	a5_Ap_Vein_4	0.0880	5.9	0.1012	10.3	0.0026	32.2	0.10	2.5	6.37	0.7
H42	a5_Ap_Vein_8	0.2221	6.8	0.4679	8.6	0.0092	28.0	0.12	3.9	6.21	1.6
H42	a5_Ap_Vein_9	0.3305	9.8	0.8037	12.6	0.0172	26.8	0.16	4.9	6.37	1.6
H42	a5_Ap_Vein_11	0.1737	9.7	0.2718	13.9	0.0076	31.9	0.13	4.1	6.57	1.4
H42	a5_Ap_Icl_1	0.1834	11.5	0.3067	13.5	0.0068	49.9	0.12	4.8	6.52	1.4

^{232}Th^{16}O/^{238}U^{16}O	**1 SE (%)**	**^{40}Ca$_2$^{31}P^{16}O$_4$/^{238}U**	**1 SE (%)**	**^{206}Pb / Coeff**	**1 SE (%)**	**^{206}Pb/^{238}U^{16}O**	**1 SE (%)**	**^{204}Pb / Coeff**	**1 SE (%)**	**^{207}Pb corrected age (Ma)**	**1 σ (Ma)**
0.00	34.7	2712	4.9	14	3.4	0.02	3.8	0.11	25.8	182	12
0.00	22.3	967	2.9	29	4.1	0.02	2.5	0.08	33.8	163	9
0.02	6.9	2152	5.5	11	3.8	0.02	3.8	0.10	27.7	177	14
0.01	16.7	4382	3.3	8	4.5	0.02	5.2	0.13	25.6	173	19
0.00	17.2	2743	1.6	10	4.0	0.02	4.1	0.08	31.6	171	13
0.00	28.5	3750	5.7	7	4.7	0.02	4.8	0.05	50.7	157	14

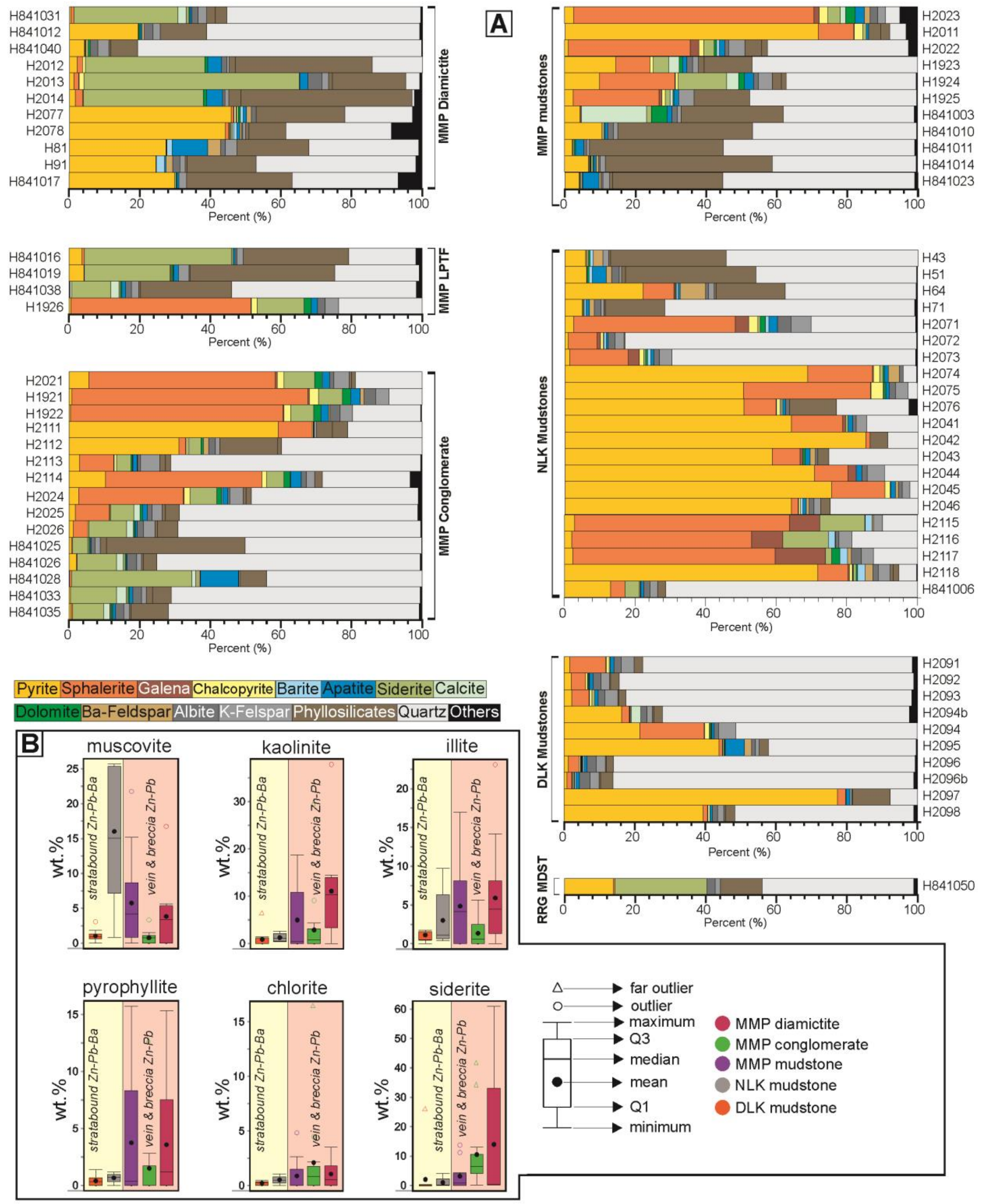

Fig. 3- 14: Results of QXRD and clay-size XRD analyses of samples from the Boundary Zone: A) Stacked back plots of QXRD results showing the mineralogical composition of selected samples. The samples are categorized based on the drill holes from which they were obtained. B) Box and whisker plots of dominant phyllosilicate mineral phases in the host rocks, sorted by the sulfide mineralization style. Siderite is common and comprises a significant component of the Macmillan Pass Member. CONG = Conglomerate, DLK = Duo Lake Formation, LPTF = Lapilli tuff, MDST = Mudstone, MMP = Macmillan Pass Member, MXSX = Massive sulfides, NLK = Niddery Lake Member, VCDM = Volcaniclastic diamictite.

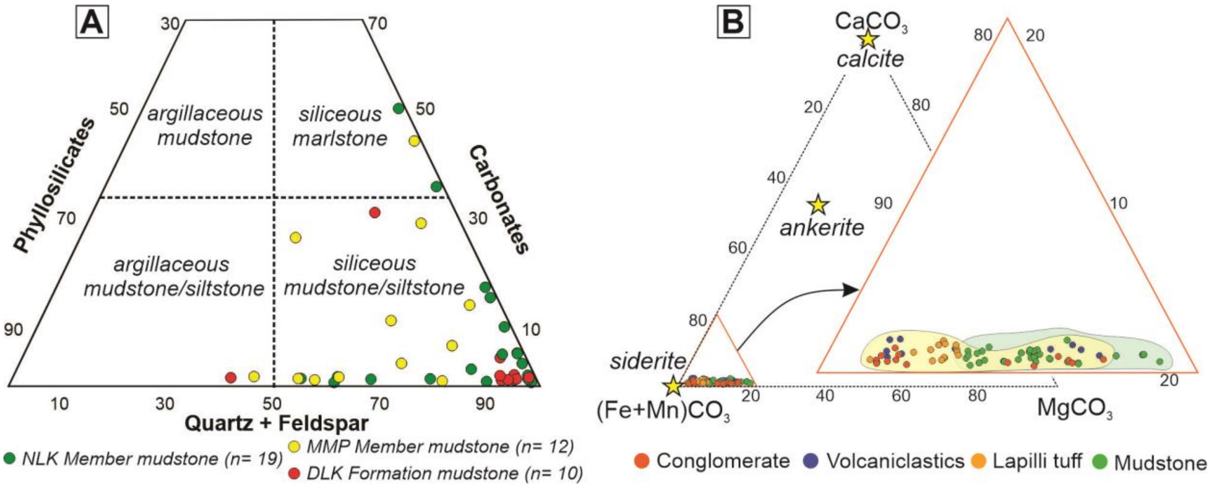

Fig. 3- 15: A) Mudstone QXRD compositional data of the Duo Lake and Portrait Lake Formations plotted in a quartz+feldspar-phyllosilicates-carbonate ternary plot. B) Ternary plots of siderite mineral chemistry from EPMA. Magnesium-rich siderite grains are relatively enriched in the mudstones (Grema *et al*., 2024a). DLK = Duo Lake Formation, MMP = Macmillan Pass Member, NLK = Niddery Lake Member.

In the barren Macmillan Pass Member mudstones, quartz varies between 37-75% compared to 4-47% (mean= 35%) in the mineralized samples. Except in two samples where dolomite (5%), calcite (19%), and siderite (11%) occur in the barren mudstones, the mineralized samples are typically more enriched in carbonates with siderite (1-14%) and minor dolomite and calcite (<3%). Microcline abundance is also higher in the mineralized samples, up to 5%, compared to the barren mudstones (<2%). Illite (2-17%), pyrophyllite (<1-16%), and muscovite (1-22%) are significant in the barren mudstones relative to <1% contents of the minerals in the mineralized samples except for muscovite (<2%, with one sample up to 15%). 10 to 68% sphalerite and 1 to 15% pyrite contents occur in the mudstone with minor galena, <3%, and chalcopyrite <2%.

The Macmillan Pass Member conglomerate unit has similar quartz content in the barren and mineralized samples; however, the former contains 4-34% siderite compared to <1-11% in the latter. Illite (1-6%), muscovite (1-3%), and pyrophyllite (2-13%) are higher in the barren conglomerates compared to <3% in the mineralized samples. Chlorite contents in the Boundary Zone are observed to be ≤ 5%, except in sample H2112, where chlorite content is 16%). Generally, samples with significant sphalerite (up to 67%) have chalcopyrite content between 1-3%.

The Macmillan Pass diamictite, mainly comprised of volcaniclastics, conglomerate, and mudstone fragments, has the lowest bulk quartz contents (mean= 20%) but the highest siderite (up to 61%), illite (<1-23%), kaolinite (<1-38%), and fluorapatite (<1-10%) than other lithologies in the Boundary Zone. Compared to other rocks, diamictite has the lowest sphalerite content, between <1-10% (mean= 2%) but mostly pyritized with 1-72% (mean= 28%) pyrite.

3.6. Discussion

The formation of sulfide mineralization at different stratigraphic levels at the Boundary Zone provides a unique cross-section of mineralizing processes in a classic CD-type district. In the following discussion, petrographic observations are combined with bulk mineralogy (QXRD) to develop a paragenetic model for the Boundary Zone system that can be compared with related systems in the Selwyn Basin (e.g., Howards Pass district and the neighboring Tom and Jason deposits).

3.6.1. Host rock composition and diagenesis

Sources and diagenesis of silica: The stratigraphic units that host the sulfide mineralization at Boundary Zone are highly siliceous (Figs. 3-7a-f and 3-14), similar to host units in the Howard's Pass (Morganti, 1979) and Macmillan Pass district (e.g., McClay, 1991; Magnall *et al.*, 2015) and, more broadly, the Red Dog district in Alaska (Dumoulin *et al.*, 2004).

At Boundary Zone, the Qz_{-cryp} and Qz_{-mic} in the mudstones are concentrated in beds that also preserve spherical to elliptical 'ghosts' of former radiolarian tests (Fig. 3-7a-b, e). The abundance of radiolarian ghosts in the sequence suggests there was a potentially significant flux of biogenic silica (as opal-A) during host rock deposition, consistent with previous work in the Macmillan Pass district (Magnall *et al.*, 2015). Importantly, the physical properties of biosiliceous mudstones are influenced by diagenetic transformations of opaline silica. Specifically, the transformation of opal-A to opal-CT (cristobalite and tridymite) results in a volume change and typically occurs at 40-50 °C, corresponding to depths of ~100 to 1,000 m (Potter *et al.*, 2005). The conversion of opal-CT to authigenic quartz then occurs at relatively higher burial temperatures (60-90 °C; Weller & Behl, 2017). Notably, the volume change associated with opaline silica diagenesis can result in inherited microporosity within authigenic quartz (Milliken & Olson, 2017), as preserved in the Qz_{-cryp} and Qz_{-mic} (e.g., Fig. 3-7a), which may have provided more permeable pathways in the sediments for subsequent fluid flow.

3.6.2. Barite, pyrite, and fluorapatite formation

The formation of disseminated barite and fluorapatite, with evidence of differential compaction of the surrounding host rock (e.g., Fig. 3-7f), is consistent with the formation during early diagenesis (Paytan *et al.*, 2002; Canet *et al.*, 2014; Salama *et al.*, 2018). Diagenetic barite has been described in the host rocks to the nearby Tom and Jason deposits (Carne, 1979; McClay, 1984; Magnall *et al.*, 2016a) and also in regionally correlative un-mineralized mudstones of the Canol Formation (Fernandes *et al.*, 2017; Grema *et al.*, 2022).

Diagenetic barite formation results from fluid mixing at a major redox boundary, where highly reducing methane and barium-rich fluids mix with sulfate in shallower pore fluids (Torres *et al.*, 2003). This redox boundary is known as the sulfate methane transition zone (SMTZ) and is also an important location of diagenetic pyrite formation due to sulfate reduction coupled with the anaerobic oxidation of methane (SR-AOM; Gonzalez-Muñoz *et al.*, 2012; Carter *et al.*, 2020). Importantly, pyrite formation at a pre-ore SMTZ has been suggested in both the host rocks in the Howard's Pass and Macmillan Pass districts (Magnall *et al.*, 2016a; Johnson *et al.*, 2018). The observed textures of Py-0a and b in both the Duo Lake and Portrait Lake Formations' mudstones, particularly their occurrence within pore spaces characterized by differential compaction around the crystals (Fig. 3-7f), are consistent with an early diagenetic precipitation model. These pre-ore pyrite crystals, together with barite, form an important component of the two-stage replacement model (Fig. 3-2c), where the assemblage is replaced by ore stage sulfide in the mudstones (Fig. 3-2d; Magnall *et al.*, 2020c).

At the Boundary Zone, the Niddery Lake Member hosts the volumetrically major, bedded barite, which differs stratigraphically from nearby occurrences. For example, stratiform barite formed during the Frasnian at the Tom and Jason deposits (Fuller Lake and Macmillan Pass Members; Carne, 1979; Turner, 1986; Goodfellow *et al.*, 1993) and in the uppermost mudstones of the Canol Formation (Fernandes *et al.*, 2017). The differences in stratigraphic level, volume, and textures of barite between the Boundary Zone and these locations may suggest the occurrence of another barite-bearing interval in the Macmillan Pass district. This horizon within the Givetian Niddery Lake Member (Abbott, 2013) in the Boundary Zone may be correlative with the reported Road River-Canol Formation boundary unit of Fraser and Hutchison (2017) and the hyper-enriched black shales (HEBS) reported across the Selwyn Basin and part of the Richardson Trough (Gadd *et al.*, 2020). Notably, significant barite formation (up to 62% from XRD analysis) is reported within this horizon in the Yukon (Fraser

& Hutchison, 2017; Kabanov, 2019) and has been linked to a period of anoxic sedimentation of carbonaceous sediments in the Selwyn Basin (Kabanov, 2019).

Fluorapatite: Fluorapatite formed in the pre-ore stage and ore-stage I and II in the Duo Lake and Portrait Lake Formations has also been observed to commonly occur in CD-type deposits and is variably interpreted to form during premineralization and ore-forming stages, as well as during recrystallization of existing apatite minerals (e.g., Red Dog District; Slack *et al.*, 2004b; Howard's Pass district; Gadd *et al.*, 2016a). The highest Si content is observed in the porous pre-ore fluorapatite hosted in the siliceous Niddery Lake Member. This pre-ore fluorapatite has been suggested to have formed during early diagenesis together with barite. The elevated Si content may reflect the abundance of silica during fluorapatite precipitation, where Si substitutes for P in the crystal lattice (Piccoli & Candela, 2002). The common occurrence of fluorapatite in the mudstones (e.g., Fig. 3-7f) suggests high primary productivity as authigenic apatite formation during diagenesis likely resulted from significant burial of P associated with organic matter decomposition (Berner *et al.*, 1993).

3.6.3. Timing and style of ore-stage I mineralization

Ore-stage I mineralization in the Duo Lake Formation and Niddery Lake Member formed by stratabound replacement of the biosiliceous mudstone (e.g., Figs. 3-9e, 3-10c), resulting in overgrowth of any pre-existing diagenetic Py-0a and b (e.g., Fig. 3-10e-h). The selective mineralization of radiolarite beds (e.g., Figs. 3-9c, 3-10c) suggests fluid flow was focused along these particular intervals. The $\text{Sp-I}_{\text{stratabound}}$ has replaced quartz within the radiolarian tests, indicating that the ore-stage I mineralization may have formed during the transformation of opaline silica to $\text{Qz}_{\text{-mic}}$ (Fig. 3-9). For example, the coexistence of $\text{Sp-I}_{\text{stratabound}}$, $\text{Qz-}_{\text{cryp,}}$ and $\text{Qz}_{\text{-mic}}$ all appear to have formed within pore space in the radiolarian tests (Fig. 3-9e). Certain $\text{Sp-I}_{\text{stratabound}}$ crystals exhibit distinct textures in correlation with the crystallinity of quartz. The replacement by radiolaria is marked by sphalerite featuring a smooth core domain with few inclusions, potentially representing a pseudomorph of opaline silica. In contrast, sphalerite with more inclusions is formed in association with inherited mudstone matrix pores and inclusions from the host rock (see Fig. 3-9d).

The biosiliceous nature of the host rock has resulted in some similarities in the style of ore-stage I mineralization of the Duo Lake Formation and the Niddery Lake Member, although there are also some key differences. The different gangue mineral assemblages within the two stratigraphic units appear to correspond with key differences in protolith composition, particularly the presence of barite within the Niddery Lake Member. For example, barite replacement by Sp-$I_{\text{stratabound}}$ is associated with kaolinite and Ba-bearing mica formation (Fig. 3-10f, i). This assemblage may be linked to the release of Al that was incorporated into radiolaria tests or diagenetic transformation of pre-existing illite and detrital muscovite (Friedman & Sanders, 1978; Steele *et al.*, 2009). The formation of significant barian-mica during ore-stage I could have been controlled by the release of Ba during barite replacement.

In contrast, the Duo Lake Formation contains a lower abundance of phyllosilicate minerals (Fig. 3-14a). In samples where the phyllosilicates form >3% of the bulk mineralogy, most are concentrated within mm to sub-mm scale laminae that separate mineralized beds (Fig. 3-9c) and commonly comprise illite (Fig. 3-14b). However, these phases are also concentrated along stylolitic seams together with pyrobitumen (Fig. 3-9j), which are a typical outcome of pressure solution (e.g., Cox & Whitford-Stark, 1987) or thermal organic matter maturation (e.g., Schulz *et al.*, 2016). The observed muscovite and minor illite in the mudstone are likely composed of detrital and pre-ore phases. For example, detrital muscovite occurs as inclusions within Sp-$I_{\text{stratabound}}$ where the fluorapatite crystals coeval with the sphalerite cut across the mineral (Fig. 3-9i).

3.6.4. Timing of ore-stage II mineralization

The second ore stage is the most volumetrically significant and is characterized by breccias and complex veins infilled by sphalerite, galena, pyrite, and minor chalcopyrite, all formed in four stages. The grade and intensity of ore-stage II diminish outward from the breccia zones into the surrounding host rock mudstones of the Duo Lake and Portrait Lake Formations, where sulfides are confined to smaller, more locally developed veins and breccias (e.g., Fig. 3-11a).

The stockwork style veins and breccias in ore-stage II exhibit textures similar to the feeder zone mineralization described at the Tom and Jason deposits (Magnall *et al.*, 2016b); however, in contrast to the Tom and Jason feeder zones, these are much more extensive and clear crosscutting relationships between ore-stage I and ore-stage II mineralization exist (Figs. 3-8a, 3-9a, 3-12a), suggesting two genetically distinct stages of fluid flow. For example, stylolites are common in both the Duo Lake and Portrait Lake Formations at the Boundary Zone, with some postdating ore-stage I (Fig. 3-9j), whereas others appear to be cut across by veins hosting ore-stage II mineralization (Fig. 3-11a inset).

The morphology of the fractures and breccias in the strata of both Duo Lake and Portrait Lake Formation, including the angularity of remnant rock fragments and sharp contacts with the sulfides (Fig. 3-11h), is consistent with fluid-induced hydrothermal brecciation (Jébrak, 1997). This suggests that ore-stage II mineralization may have formed simultaneously in these strata together with brecciation and vein formation or after the fracturing. For example, fluid overpressure could have led to fracture propagation along zones of weakness, such as pre-existing fractures and stylolites (Martín-Martín *et al.*, 2018).

The occurrence of significant pyrobitumen in the overmatured mudstones of the Duo Lake and Portrait Lake Formation, both disseminated in matrix pores, stylolites, and minor veins (e-g-. Fig. 3-9j), suggests that thermal cracking of liquid hydrocarbon has also occurred, which would also have contributed to increased pore pressures (Tian *et al.*, 2008). Fracturing along stylolite seams would have provided a particularly effective mechanism for increasing permeability and enhancing the flow of metalliferous hydrothermal fluids. Indeed, some of the margins of the mineralized veins and breccias resemble stylolites (Fig. 3-11a inset), with insoluble residues comprising pyrobitumen, phyllosilicates, pyrite, and quartz (Fig. 3-7l). Importantly, the significant organic matter in the host rocks as highlighted by the abundant pyrobitumen, may have acted as a reductant impacting the redox conditions during ore formation and resulting in the precipitation of sulfides and carbonate minerals such as siderite in reducing conditions.

In the Niddery Lake Member sample (Fig. 3-13e), the ore-stage I assemblage is crosscut by millimeter to centimetre-sized pyrite crystals that are coeval with fluorapatite, barite, and barian-mica in a vein. The U-Pb age of 169±10 Ma recorded by the fluorapatite (Fig. 3-13e) predates both the Late Jurassic – Early Cretaceous deformation in the Macmillan Pass region (Abbott, 1982; McClay, 1991) as well as the Early – Middle Cretaceous metamorphism and granitoid emplacement (Gordey *et al.*, 1991; Mair *et al.*, 2006). The discordant vein clearly crosscuts and postdates ore-stage I, however, the precise relationship with ore-stage II is unclear as an overlying fault obscures the observed fluorapatite vein continuation.

The coarse-grained pyrite crystals in the vein are associated with coeval Qz$_{\text{-mega}}$ pressure shadows, which are comparable to the low-grade metamorphic pyrite-quartz assemblage in matrix, veins, and quartz veins reported in the Macmillan Pass district (Ansdell *et al.*, 1989). Leighton *et al.* (2021a) compared the subgreenschist facies metamorphic pyrite to similar occurrences in the Howard's Pass district, which are interpreted to have formed during the Cordilleran Mesozoic orogeny (Lianxing & McClay, 1992). During the Jurassic, exotic terranes were accreted onto the northern parts of the ancestral North America margin, representing the onset of the Cordilleran orogeny and associated metallogenesis (Mair *et al.*, 2006; Nelson &

Colpron, 2007). If these veins formed as part of ore-stage II, it would imply that ore-stage II mineralization was coeval with Cordilleran deformation. However, the observation that high-angle stylolites (Fig. 3-7a) predate ore-stage II would require either (1) an older pre-Cordilleran phase of deformation, which is currently not documented in the area; or (2) that the high-angle stylolites formed during Cordilleran deformation, and that ore-stage II formed syn- to post-Cordilleran deformation.

3.6.5. Genesis of the Boundary Zone Zn-Pb±Ag and implications for CD-type mineral systems

In the Macmillan Pass district, the CD-type Zn-Pb±Ag mineralization at the Tom and Jason deposits is restricted to the Middle to Late Devonian Portrait Lake Formation (McClay, 1984; Goodfellow & Lydon, 2007). In this study, we describe a new deposit in the Macmillan Pass district where sulfide mineralization is both in the Middle to Late Devonian Portrait Lake Formation and in Late Ordovician-Early Silurian Duo Lake Formation strata. Furthermore, we have documented that ore formation occurred in two distinct stages (Fig. 3-16): a syn-diagenetic stratabound host rock replacement stage and a later crosscutting breccia and vein mineralization stage.

Several studies have suggested sub-seafloor syn-diagenetic replacement of host rock components as the main mechanism of stratiform and stratabound sulfide mineralization in CD-type deposits (Williams, 1978a; Kelley *et al.*, 2004; Reynolds *et al.*, 2021; Magnall *et al.*, 2023). Magnall *et al.* (2015) suggested that the presence of highly biosiliceous Late Devonian mudstones at the Tom and Jason area facilitated porosity preservation and permeability pathways that were exploited by the mineralizing fluids during sediment burial. Our findings support this interpretation as we demonstrate that the diagenetic opaline silica transformation occurred at the same time as the precipitation of Sp-I$_{\text{stratabound}}$. During this transformation, a sphalerite-galena-pyrite-fluorapatite assemblage formed in the biosiliceous mudstones of the Duo Lake Formation, whereas sphalerite-galena-pyrite-barian mica ± chalcopyrite ± sulfosalts formed in the Niddery Lake Member of the Portrait Lake Formation. The lack of systematic variation in REE+Y+Sr+Mn contents of fluorapatite coeval with ore-stage I sulfide from both strata (Fig. 3-13d) suggests a common fluid type. This supports the interpretation that the mineralization in both strata is the result of a similar replacement event in different aged host rocks located below the seafloor (Fig. 3-16a).

Indeed, the presence and abundance of quartz is key in the preservation of porosity in mudstones at depth during burial compaction in siliceous Late Ordovician to Early Silurian strata , and up to 60% porosity can be preserved to 100s m (Velde, 1996; Aplin & Macquaker, 2011; Milliken & Olson, 2017). The suggested compacted Duo Lake Formation at the time of the deposition of the Portrait Lake Formation was ~50 m deep at the Boundary Zone and implies that the former is likely to be reactive to hydrothermal fluids that could selectively replace host rock components. Selective host rock replacement (Magnall *et al.*, 2023) and pore-filling (Milliken *et al.*, 2016) are known to occur at depth during burial, and this supports the possibility of sulfide mineralization coupled with *in-situ* opaline silica transformation in the mudstone strata (Gao *et al.*, 2022).

Pre-ore authigenic barite and byproducts of its dissolution (pyrite, celsian, barian mica) form a significant component of the mineralogy in the Niddery Lake Member. This is comparable to the Tom and Jason deposit host rocks which also have thick packages of stratiform barite (McClay, 1984; Goodfellow & Rhodes, 1990; Magnall *et al.*, 2016a). The stratiform barite at Tom and Jason deposits are interpreted to have provided a sulfur source during ore formation (Magnall *et al.*, 2016a). We document petrographic evidence of overprinting pre-ore barite, pyrite, and celsian, with barian mica forming part of the ore-stage I assemblage at the Boundary Zone (Fig. 3-16). As such, tracing the Ba mass transfer associated with barite replacement into the gangue mineralogy will be important for understanding the lithogeochemical footprint of the mineralization.

With increasing burial diagenesis, progressive authigenic quartz cementation, and organic matter maturation would have affected the mechanical properties of the host rocks, leading to fluid overpressure buildup and non-tectonic fracturing (Tian *et al.*, 2008; Milliken & Olson, 2017; Abu-Mahfouz *et al.*, 2020). At Boundary Zone, fracturing, together with stylolitization, could have allowed for a subsequent fluid-induced brecciation driven by pore fluid pressure increase, thermal cracking, and in part by metalliferous hydrothermal fluid inflow. The aqueous fluids for ore-stage II high-grade Zn-Pb-Ag may have exploited these weaknesses, precipitating sphalerite, galena, pyrite, and associated chalcopyrite, siderite, and $\text{Qz}_{\text{-mega}}$ that infill and cement fractures and breccias (Fig. 3-16b). The multiple sphalerite generations in the breccias and veins imply episodic and repeated inflow of mineralizing fluids during ore-stage II formation (Fig. 3-16). The timing of the ore-stage II mineralization is not well constrained. Comparable CD-type multistage systems have been described in the Red Dog district of the Kuna Basin (Kelley *et al.*, 2004; Slack *et al.*, 2004b; Reynolds *et al.*, 2015) and the world-class George Fisher deposit in the Carpentaria Province (Chapman, 2004; Rieger *et al.*, 2023).

Based on textural observations and the coeval precipitation with sphalerite, the fluorapatite crystals are suggested to have a common origin with the ore-stage sulfides, which are hydrothermal in origin and precipitated at different periods during the two ore-forming stages. There is a general lack of systematic variation in the P_2O_5, CaO, and FeO (Grema *et al.*, 2024a). Additionally, the lack of significant Ca- and Na-bearing mineral phases in the ore stages and Na_2O content below the detection limit (138 ppm) in all fluorapatite likely reflect fluorapatite formation from F-rich and Ca- and Na-deficient fluids (Li & Zhou, 2015).

Fluorapatite crystals coeval with ore-stages I and II sulfides have elevated Sr content and REE+Y+Sr+Mn contents. Sr^{2+} readily and commonly substitutes for Ca^{2+} in apatite group minerals (Chakhmouradian *et al.*, 2002), while REEs are incorporated via coupled substitution reactions. The trends in the content of Sr in apatite minerals have been observed to be similar to Sr trends in the rocks hosting them (Belousova *et al.*, 2001; Piccoli & Candela, 2002; Mao *et al.*, 2016). These trends have also been related to REEs, where apatite minerals serve as the primary host of REEs (Mao *et al.*, 2016). The trend and REE incorporation suggest possible elevated Sr contents in rocks of the Duo Lake and Portrait Lake Formations at the Boundary Zone, as well as potential for REEs enrichment in the fluorapatite.

In summary, petrographic, mineralogic, and geochronological data allow constraints to be placed on many aspects of the Boundary Zone ore system. Biogenic silica transformation coincided with hydrothermal fluid inflow, resulting in syn-diagenetic stratabound mineralization that was later overprinted by breccia and vein sulfides of the second ore stage. Understanding the relationship between mineralization and regional-scale biosiliceous mudstone deposition, barite formation, and nearby fault system dynamics is essential for exploration targeting in the Boundary Zone area.

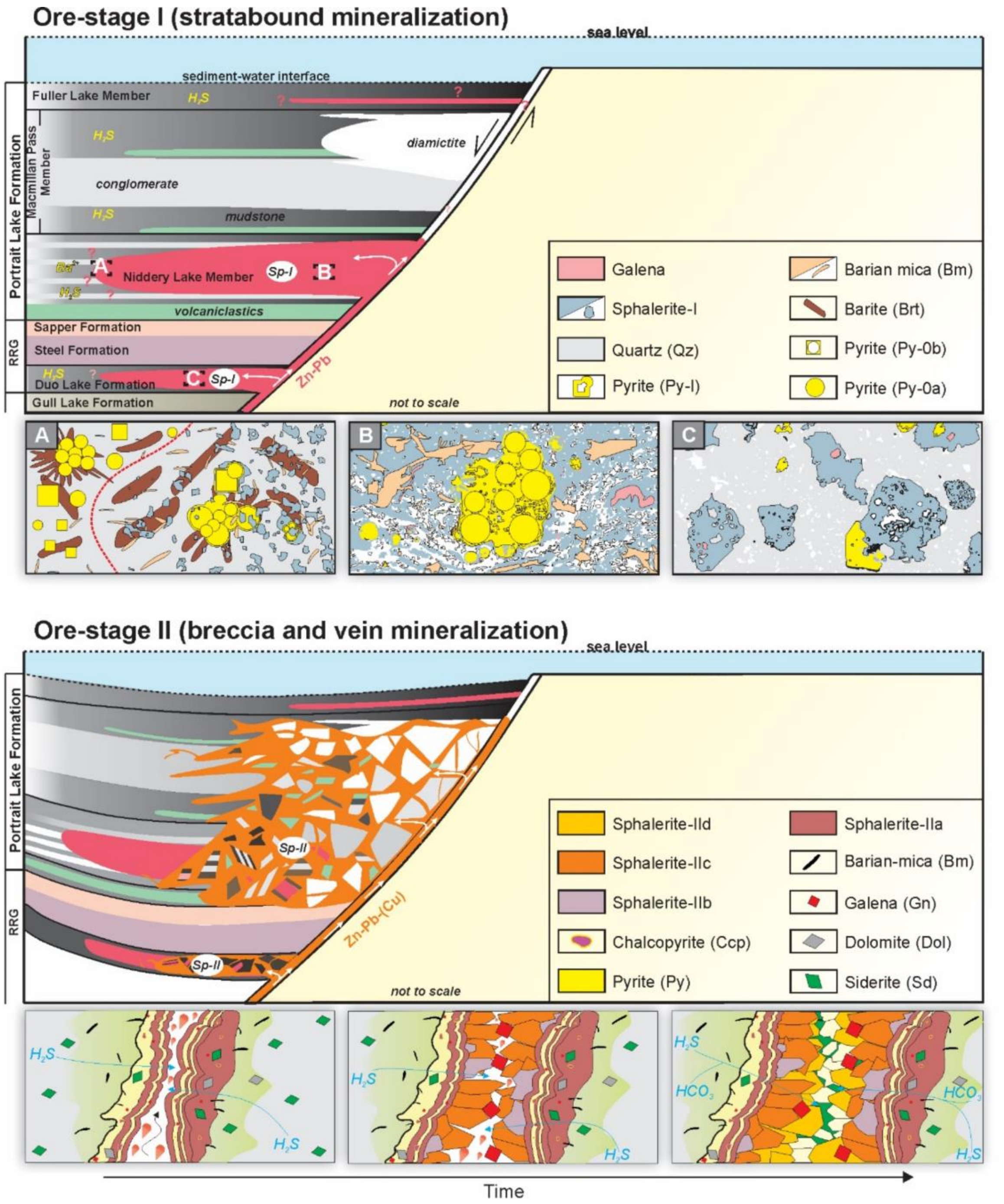

Fig. 3- 16: Schematic diagrams of the two stages in the development of Zn-Pb mineralization at the Boundary Zone that are accompanied by silicification and sericite alteration in the wall rocks. A) Three periods of stratiform sulfide mineralization developed in the Duo Lake Formation and the Portrait Lake Formation. In all cases, pre-ore Py-0 formed during early diagenesis through the interaction of H2S with reactive Fe in the mudstones. The flow of metalliferous hydrothermal fluid interacted with the host rocks where Sp-Istratiform, Gn-I, and Py-I form—barian-mica formed coeval with the sulfides in the Portrait Lake Formation, but not in the Duo Lake Formation. B) The second ore stage is initiated when relatively low-temperature hydrothermal fluid with increased Cu+ activity flows into veins and breccias, and Sp-IIa$_{\text{colloform}}$ precipitates together with Py-IIa and Ccp with minor siderite and dolomite. The formation of coarse-grained Sp-IIbmetallic brown and Sp-IIcsector zoned was accompanied by Gn-II that, together, formed the volumetrically major sulfide assemblage of the Boundary

Zone. The Sp-IIdpale yellow precipitated late, together with coarse-grained Qz and Sd. The thicknesses of the strata and inclinations are exaggerated and not to scale. Bm = barian-mica, Brt = barite, Ccp = chalcopyrite, Dol = dolomite, Gn = galena, Py = pyrite, Qz = quartz, Sd = siderite, Sp = sphalerite.

3.7. Conclusions

The host rocks, tectonic setting, formation mechanisms, and observed petrographic and mineralogical features suggest the Boundary Zone Zn-Pb-Ag deposit is another CD-type system in the Macmillan Pass district, Yukon, Canada. The mineralization is characterized by early syn-diagenetic stratabound replacement in biosiliceous mudstones of the Late Ordovician-Early Silurian Duo Lake Formation and Middle to Late Devonian Portrait Lake Formation, which is then overprinted by later breccia and vein mineralization. Syn-diagenetic ore-stage I stratabound sulfides formed mainly by replacing radiolarian tests during biogenic silica transformation in the mudstones. Barite replacement by sulfides adds to the significant ore-stage I mineralization that is coeval with barian-mica formation in the Niddery Lake Member. The dissolution-reprecipitation of quartz and barite dissolution generated permeability, which facilitated hydrothermal fluid flow. The ore-stage II mineralization is primarily hosted in crosscutting veins and breccias in the Duo Lake and Portrait Lake Formations and comprises multiple generations of sulfides, siderite, and quartz, preserving evidence of repeated hydrothermal fluid flow in the fractures. The timing of the mineralization in the two ore stages spans diagenetic periods of the host rocks that formed stratabound sulfides and vein and breccia-hosted sulfides that may be related to regional deformational events.

3.8. Acknowledgments

We are grateful for the financial support from the Helmholtz Recruitment Initiative grant to S. A. Gleeson, the Petroleum Technology Development Fund (PTDF), and the German Academic Exchange Service (DAAD) scholarship to H. M. Grema through co-financed funding (Nr. 57473408). We also appreciate funding from the Society of Economic Geologists (SEG) 2022 Student Research Grant Spora’s Explorers Fund (Nr. SRG 22-19) to H. M. Grema. Fireweed Metals Corp. is deeply appreciated for access to their database and for providing samples for this study. Profound appreciation for technical support during data generation to Uwe Dittmann and Christine Fischer (thin sections and mounts preparation), Franziska H. Wilke (EPMA), Dilara Topal (clay-size XRD), Frédéric Couffignal (SIMS), and Michael Wiedenbeck for help with U-Pb data reduction.

CHAPTER 4

Microthermometry and trace element chemistry of sphalerite in the Boundary Zone clastic-dominant Zn-Pb system, Yukon, Canada

Haruna M. Grema[a,b], Joseph M. Magnall[a], Sarah A. Gleeson[a,b], Marta Sośnicka[a,c], Jack E. Milton[d], Vitor R. Barrote[e], Hans-Martin Schulz[a]

[a]*GFZ German Research Centre for Geosciences, Telegrafenberg, 14473 Potsdam, Germany*
[b]*Institute of Geological Sciences, Freie Universität Berlin, Malteserstrasse 74-100, 12249 Berlin, Germany*
[c]*CSIRO Mineral Resources, 26 Dick Perry Avenue, Kensington, WA, 6151, Australia*
[d]*Fireweed Metals Corp., Suite 2800, Four Bentall Centre, 1055 Dunsmuir Street, Vancouver, V7X 1L2, British Columbia, Canada.*
[e]*Paul Scherrer Institute, Forschungsstrasse 111, 5232 Villigen, Switzerland*
[*]*Corresponding author: Haruna M. Grema. Email address: hgrema@gfz-potsdam.de*

Keywords: *Microthermometry • Sphalerite trace elements • LA-ICP-MS • Fluid inclusions • Clastic-dominated type deposits*

A supplementary data publication is available online in the GFZ Data Repository and is cited as Grema *et al.* (2024b) in this chapter. The data can be accessed through https://dataservices.gfz-potsdam.de/panmetaworks/review/66434e4a4731d6ada2a01378e4fbfa88375c14b81a0168c15b7140db3540ee3f/.

4.1. Abstract

The Boundary Zone Zn-Pb±Ag clastic-dominant (CD-type) deposit (Macmillan Pass district, Yukon, Canada) is the most recent discovery in the Selwyn Basin. The mineralized rocks at Boundary Zone comprise two distinct stratabound and vein-breccia ore stages hosted in Late Ordovician-Early Silurian Duo Lake and Middle-Late Devonian Portrait Lake Formations. This study aimed to constrain ore fluid properties and evaluate the distribution of critical metals using a combined investigation of sphalerite chemistry and fluid inclusions in quartz and sphalerite. Transmitted light microscopy was used to define fluid inclusion assemblages (FIAs), which were analyzed using Raman spectroscopy and microthermometry techniques. Sphalerite chemistry was investigated using electron probe microanalysis (EPMA) and in-situ laser ablation-inductively coupled plasma mass spectrometry (LA-ICP-MS), and the resulting dataset was evaluated using principal component analysis (PCA).

Two ore stages are identified: stratabound Sp-$I_{\text{stratabound}}$ defines ore-stage I, whereas four different sphalerite generations (Sp-IIa_{banded}, Sp-$IIb_{\text{metallic-brown}}$, Sp-$IIc_{\text{sector-zoned}}$, and Sp-$IId_{\text{pale-yellow}}$ coeval with Qz-III) characterize ore-stage II in both the Duo Lake and Portrait Lake Formations. Sphalerite chemistry varies between host strata and sphalerite generations; however, the PC1 cluster describes Cu, Ag, In, Ge, and Sn that are similar irrespective of host rock or sphalerite generation. Germanium and Ga are suggested to have been scavenged from the host rocks, whereas locally interbedded volcaniclastics are likely sources of Hg with concentrations >200 ppm in all generations of sphalerite.

The Sp-IIa_{banded} preserves $CO_2(\pm N_2)$-bearing FIAs with high-salinity (14-21 wt.% NaCl equiv.) and moderate homogenization temperatures (128-176 °C). The data suggests that the metalliferous hydrothermal fluid mixed with a fluid consisting of relatively lower homogenization temperatures and higher salinity brine that was buffered by the host rocks. The second low salinity (4–9 wt.% NaCl equiv.), moderate to high homogenization temperature (168–262 °C) $CO_2(\pm N_2 \pm CH_4 \pm H_2S)$-bearing fluid is characterized by Sp-$IIc_{\text{sector-zoned}}$ and Qz-III FIAs and signals a second pulse of hydrothermal fluid. Sulfide formation at the Boundary Zone could have resulted primarily from mixing of contrasting fluid types involving metalliferous hydrothermal fluids and reduced sulfur-rich porewaters. The two Zn-Pb±Ag mineralization stages at the Boundary Zone formed from separate mineralizing fluid pulses that repeatedly used the same source-pathway-sink.

4.2. Introduction

Sediment-hosted Zn-Pb deposits, which include Mississippi Valley-type (MVT-type), Irish-type, and clastic-dominated (CD-type) subtypes, account for more than half of the global Zn and Pb resources (Chapter 3, Leach *et al.*, 2010; Wilkinson, 2014; Mudd *et al.*, 2017). The increasing demand for critical and strategic metals for the green transition has driven a new wave of exploration activities and academic studies focused on deposit genesis and the spatial and temporal controls on mineralizing processes. Sphalerite (ZnS) is the primary Zn-bearing ore mineral and may also contain minor concentrations of critical elements such as germanium (Ge), gallium (Ga), and indium (In), which could be recovered as by-products (e.g., Frenzel *et al.*, 2019).

The solubilities of Zn, Ge, Ga, and In are largely controlled by temperature, pH, fS_2, salinity, and redox state in hydrothermal systems (Bernstein, 1985; Hemley & Hunt, 1992; Cooke *et al.*, 2000). However, constraining the physicochemical nature of the mineralizing fluids in CD-type deposits is challenging due to the fine-grained nature of stratiform and stratabound ore minerals which rarely contain measurable fluid inclusions. Additionally, coarser-grained mineralization in feeder zones beneath the fine-grained mineralization is rarely preserved or exposed in these deposits (Wilkinson, 2014). As a result, the knowledge of fluid properties is limited to a relatively small number of fluid inclusion studies in which data were derived from the analyses of gangue minerals (Gardner & Hutcheon, 1985; Ansdell *et al.*, 1989; Leitch & Lydon, 2000; Rajabi *et al.*, 2015b; Magnall *et al.*, 2016b), with few data from inclusions hosted in sphalerite (Leach *et al.*, 2004; Polito *et al.*, 2006; Yarmohammadi *et al.*, 2016; Mahmoodi *et al.*, 2018). This paucity of fluid inclusion temperature, salinity, and compositional data on the mineralizing fluids constitutes a barrier to understanding fundamental aspects of the CD-type mineral system.

Temperature exerts a first-order control on the incorporation of certain trace elements into the sphalerite crystal lattice (Möller, 1985; Cook *et al.*, 2009 and references therein). As a result, sphalerite chemistry has been used as a geothermometer to constrain the temperature of paleo-hydrothermal systems (e.g., Mladenova & Valchev, 1998), which is particularly useful when microthermometric data is limited. Notable sphalerite geothermometers include the Ga/Ge ratio (Möller, 1985), sphalerite FeS concentration (Kullerud, 1953; Scott & Barnes, 1971), Fe/Zn ratio (Keith *et al.*, 2014), and the widely accepted approach using Ge, Ga, In, Mn, and Fe concentrations (GGIMFis; Frenzel *et al.*, 2016). The GGIMFis approach has been shown to correlate well with fluid inclusion microthermometry (at temperatures <300 °C) and has been used to provide temperature estimates where microthermometric data are challenging to obtain (Bauer *et al.*, 2019; Cugerone *et al.*, 2021; Luo *et al.*, 2022; Torró *et al.*, 2022; Wang *et al.*, 2023; Yu *et al.*, 2024).

Trace element studies on sulfide minerals can also provide information on the chemistry of the ore formation and enrichment mechanisms (Roberts, 1982; Graham *et al.*, 2009; Bauer *et al.*, 2019). A large number of minor and trace elements, other than Ge, Ga, In, Mn, and Fe, are incorporated into sphalerite, either as inclusions or via substitution mechanisms for Zn or S in the crystal lattice (Cook *et al.*, 2009; Belissont *et al.*, 2014; Belissont *et al.*, 2016; Bonnet *et al.*, 2016; Bauer *et al.*, 2019; Zhuang *et al.*, 2019). The enrichment or depletion of these trace elements is influenced by factors such as the fluid source, fluid-rock interactions, and precipitation mechanisms (Viets *et al.*, 1992; Cook *et al.*, 2009), as well as by the temperature, pressure regimes, and sulfur activities during formation (Pfaff *et al.*, 2011). Furthermore, the quantification of trace elements can have implications for deposit resource evaluation and geometallurgical assessments (Frenzel *et al.*, 2019).

The Macmillan Pass district is one of three major CD-type Zn-Pb mineralized districts in the Selwyn Basin, Canada (Fig. 4-1a-b), with mineralization predominantly occurring as stratiform sulfides at the Tom, Jason, and End Zone deposits (Carne, 1979; Gardner & Hutcheon, 1985; Magnall *et al.*, 2016a). These mineralized systems are hosted in the Late Devonian strata of the Portrait Lake Formation, which comprises carbonaceous and siliceous mudstones and volcaniclastics (McClay, 1984; Gardner & Hutcheon, 1985). The newly discovered Boundary Zone deposit in the Macmillan Pass district hosts significant sulfide mineralization in Middle to Late Devonian Portrait Lake Formation and lesser amounts of mineralization within the Late Ordovician to Early Silurian Duo Lake Formation (Chapter 3). This deposit represents the first intersection of significant amounts of mineralization in two different stratigraphic intervals in a single location anywhere in the Selwyn Basin.

Previous fluid inclusion studies in the Macmillan Pass district are restricted to the Tom and Jason deposits (Gardner & Hutcheon, 1985; Ansdell *et al.*, 1989; Magnall *et al.*, 2016a). For example, fluid inclusions hosted in ankerite, siderite, and quartz from the Jason deposit preserved evidence of a mineralizing fluid with an average salinity of 9 wt.% (NaCl equiv.) and temperatures of ~250 °C (Gardner & Hutcheon, 1985). In contrast, Ansdell *et al.* (1989) analyzed fluid inclusions in ankerite and quartz and suggested the Tom deposit formed from a much lower temperature fluid (<150 °C) with low to intermediate salinities (3.5 - 12.5 wt.% NaCl equiv.).

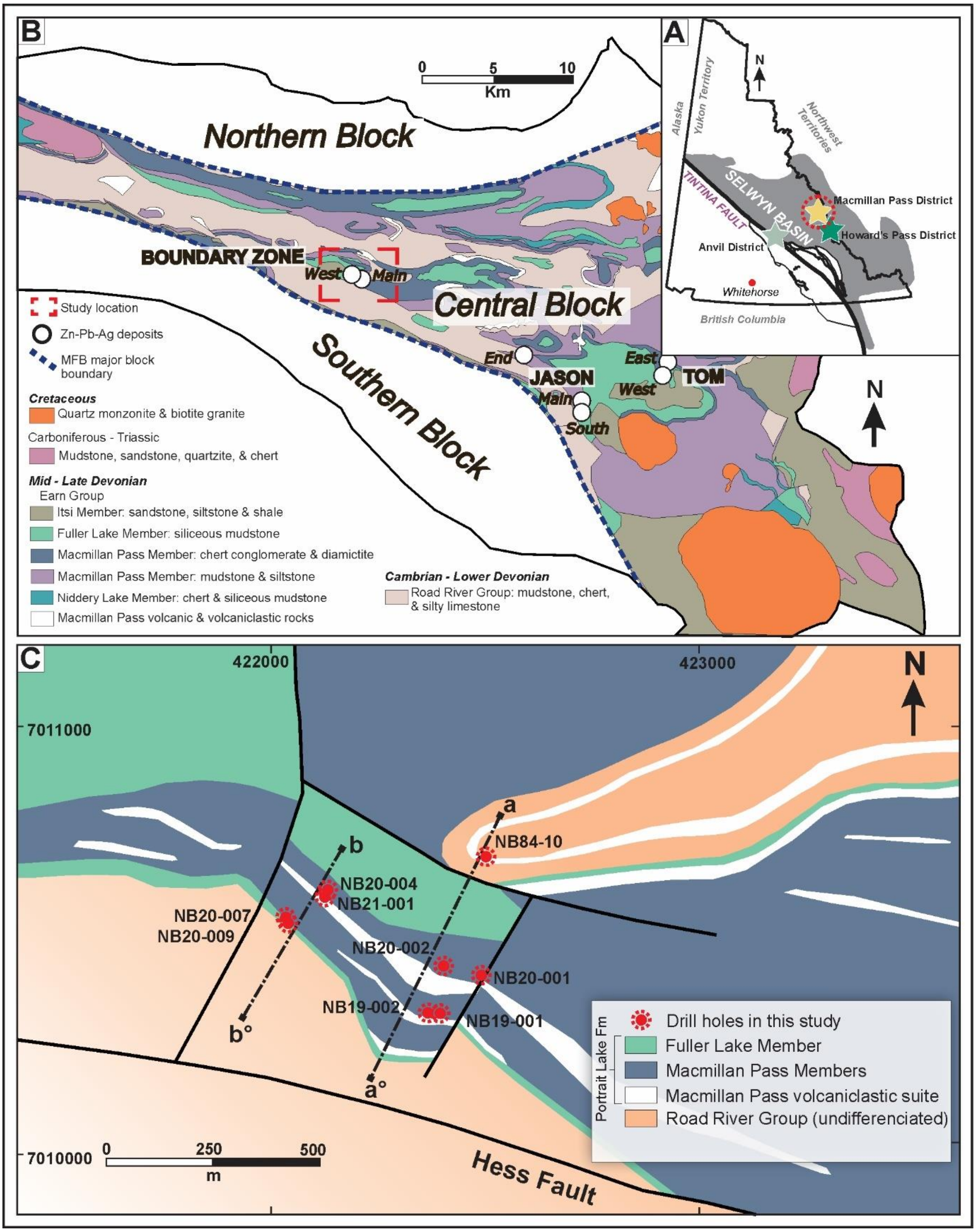

Fig. 4- 1: Geographic and geologic overview of the Boundary Zone deposit. A: Location map of the Selwyn Basin with the three major Zn mineralized districts highlighted by the three stars (Goodfellow, 2007). B) Geologic map of the Macmillan Fold Belt (MFB) in the Selwyn Basin. The locations of the Tom and Jason deposits and the Boundary Zone to the west are shown within the Central Block of the MFB (Abbott, 2013). C) Simplified geologic map of the Boundary Zone with the lithologies and sampled drill holes.

The most recent microthermometric and isotopic study in the district suggested that the fluid entering the feeder zones at the Tom and Jason was hot (>275 °C), had a relatively low pH, and cooled rapidly upon mixing with reducing diagenetic pore fluids, resulting in sulfide precipitation (Magnall *et al.*, 2016b). All the microthermometric studies in the Macmillan Pass district and the majority in other CD-type districts analyzed fluid inclusions in gangue minerals that are mainly part of coarse-grained feeder zone vein-hosted mineralization. Direct microthermometric studies on fluid inclusions hosted in sphalerite, for example, at the Red Dog district, could only be conducted on later stages of the paragenesis and do not constrain the ore-forming characteristics of the fine-grained, extensive stratabound ore that is typical of the mineralization (Leach *et al.*, 2004).

This study characterizes the physico-chemical character of the fluids responsible for Zn-Pb±Ag mineralization at the Boundary Zone deposit (Fig. 4-1c) utilizing sphalerite chemistry and sphalerite-quartz fluid inclusion composition and microthermometry. The study examines the nature of the fluids responsible for mineralization in the different stratigraphic intervals present at Boundary Zone in an effort to distinguish whether such mineralization formed together during a single mineralizing event or as separate discrete pulses with distinct fluid characteristics. To achieve this aim, i) sphalerite chemistry has been constrained using electron probe microanalysis (EPMA) and *in-situ* laser ablation-inductively coupled plasma mass spectrometry (LA-ICP-MS), and ii) sphalerite- and quartz-hosted fluid inclusions have been analyzed by laser Raman spectroscopy and microthermometry.

4.3. Background geology

The Selwyn Basin is located along the western continental margin of ancestral North America and comprises Late Proterozoic to Mississippian clastic and carbonate sedimentary rocks that have been deformed during the Mesozoic Cordilleran orogenesis (Mair *et al.*, 2006; Goodfellow, 2007a). The formation of the Selwyn Basin is attributed to widespread protracted extensional tectonics that resulted in the re-emergence of the Laurentian craton from the Rodinian supercontinent between 825 and 740 Ma (Martel *et al.*, 2011). The basal part of the stratigraphy comprises clastic sedimentary rocks of the Late Proterozoic to Cambrian Windermere Supergroup (Gordey & Anderson, 1993). The Cambrian strata are overlain by Early Ordovician deep-water carbonates of the Rabbitkettle Formation (Goodfellow, 2007a). These, in turn, are overlain by basinal mudstone and chert sequences of the Ordovician to Silurian Duo Lake, Steel, and Sapper Formations of the Road River Group. The Devonian to Mississippian Portrait Lake and Itsi Formations of the Earn Group were then deposited on top of these sequences (Abbott & Turner, 1991). At the base of the Earn Group, there are volcanic and volcaniclastic rocks that are also interbedded with the Portrait Lake Formation strata (Abbott, 2013). During the Jurassic to Cretaceous periods, the accretion of exotic terranes to ancestral North America resulted in the basinal strata of the Selwyn Basin being incorporated into the fold and thrust belt of the northern Cordillera (Mair *et al.*, 2006; Nelson & Colpron, 2007).

The Selwyn Basin (Fig. 4-1a) contains significant base metal resources in the form of volcanogenic massive sulfide (VMS) and CD-type deposits, as well as massive stratiform barite deposits. The CD-type Zn-Pb deposits are hosted by siliciclastic rocks deposited during three major periods: the Cambrian, Silurian, and Late Devonian (Goodfellow, 2007a), which respectively correspond with the Anvil (Pigage, 1991), Howard's Pass (Morganti, 1979), and Macmillan Pass districts (Carne, 1979; Gardner & Hutcheon, 1985).

4.3.1. Local Geology of the Boundary Zone area at Macmillan Pass district

The stratigraphy of the Macmillan Pass district (Fig. 4-1b) is dominated by the Duo Lake, Steel, and Sapper Formations of the Road River Group, as well as the Portrait Lake Formation of the Earn Group (Gardner & Hutcheon, 1985; Abbott, 2013). The Portrait Lake Formation is further subdivided into the Niddery Lake, Macmillan Pass, and Fuller Lake Members, all of which host sulfide mineralized rocks (Abbott, 1982; McClay, 1984; Bailes *et al.*, 1986; McClay & Bidwell, 1986; Turner, 1986; Magnall *et al.*, 2016b). The mineralogy and paragenesis at Boundary Zone are described in Chapter 3 and are briefly summarized here. There are two distinct stages of Zn-Pb sulfide mineralization (Figs. 4-2, 4-3) that are preceded by barite and quartz (Qz-0) formation: ore-stage I comprises stratiform and stratabound mineralization hosted by radiolarian and barite-rich mudstone beds of the Late Ordovician-Early Silurian Duo Lake Formation and the Middle Devonian Niddery Lake Member of the Portrait Lake Formation (Fig. 4-3a-b). Disseminated fine-grained grey sphalerite (Sp-I$_{\text{stratabound}}$), galena, and pyrite are the dominant sulfide minerals (Fig. 4-3f-h). Subhedral to euhedral quartz (Qz-I), barian-mica, and fluorapatite constitute the major gangue mineral phases associated with the ore-stage I mineralization. Minor pre-ore barite, Qz-0, and framboidal pyrite are common as inclusions in euhedral pyrite, quartz, and Sp-I$_{\text{stratabound}}$ (e.g., Fig. 4-3f-g).

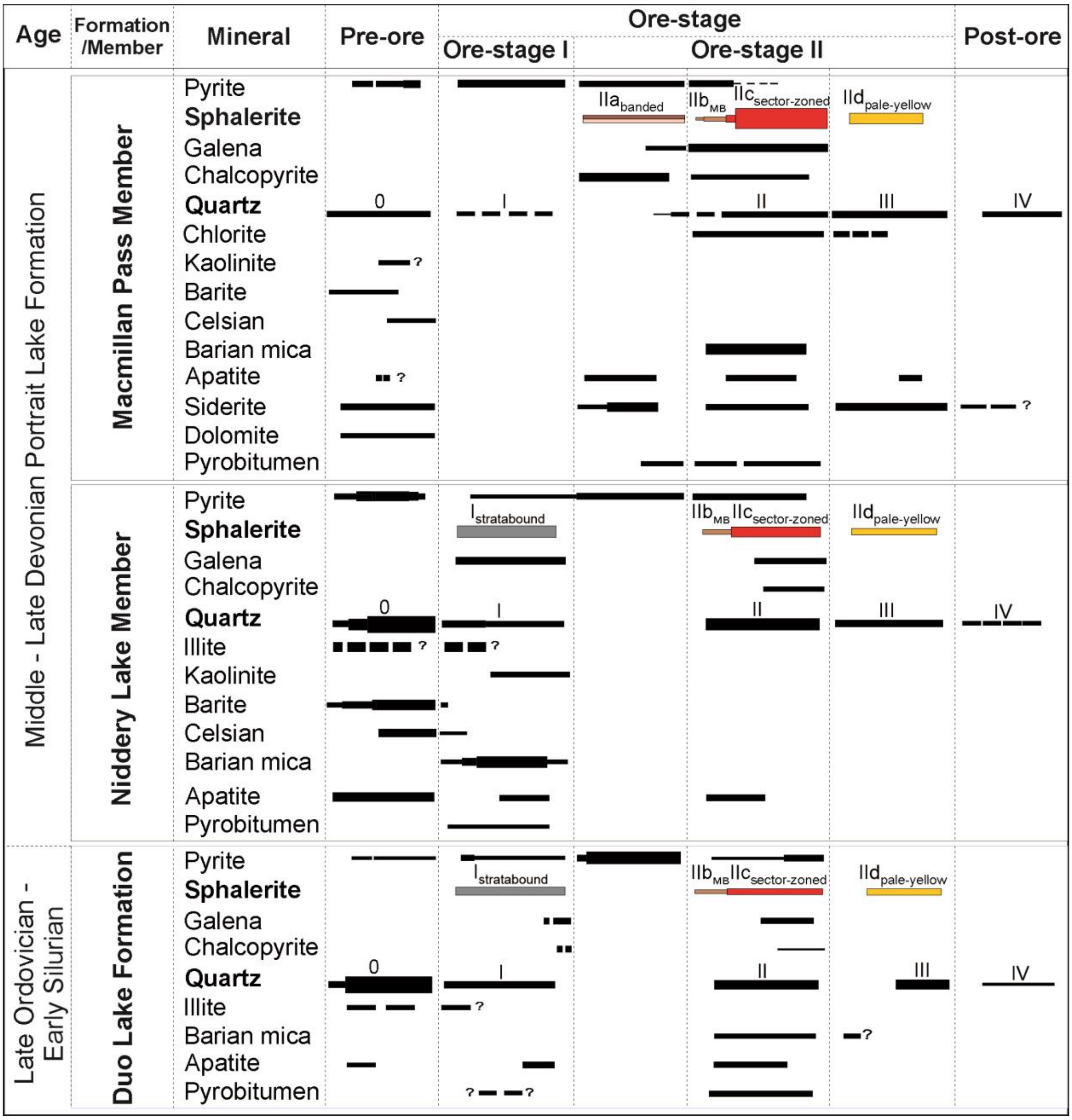

Fig. 4- 2: Comprehensive paragenetic chart of the Boundary Zone sulfide mineralization and associated gangue minerals. Fluid inclusion data were collected from (sphalerite) Sp-IIa$_{\text{banded}}$, Sp-$_{\text{IIcsector-zoned}}$, and (quartz) Qz-III.

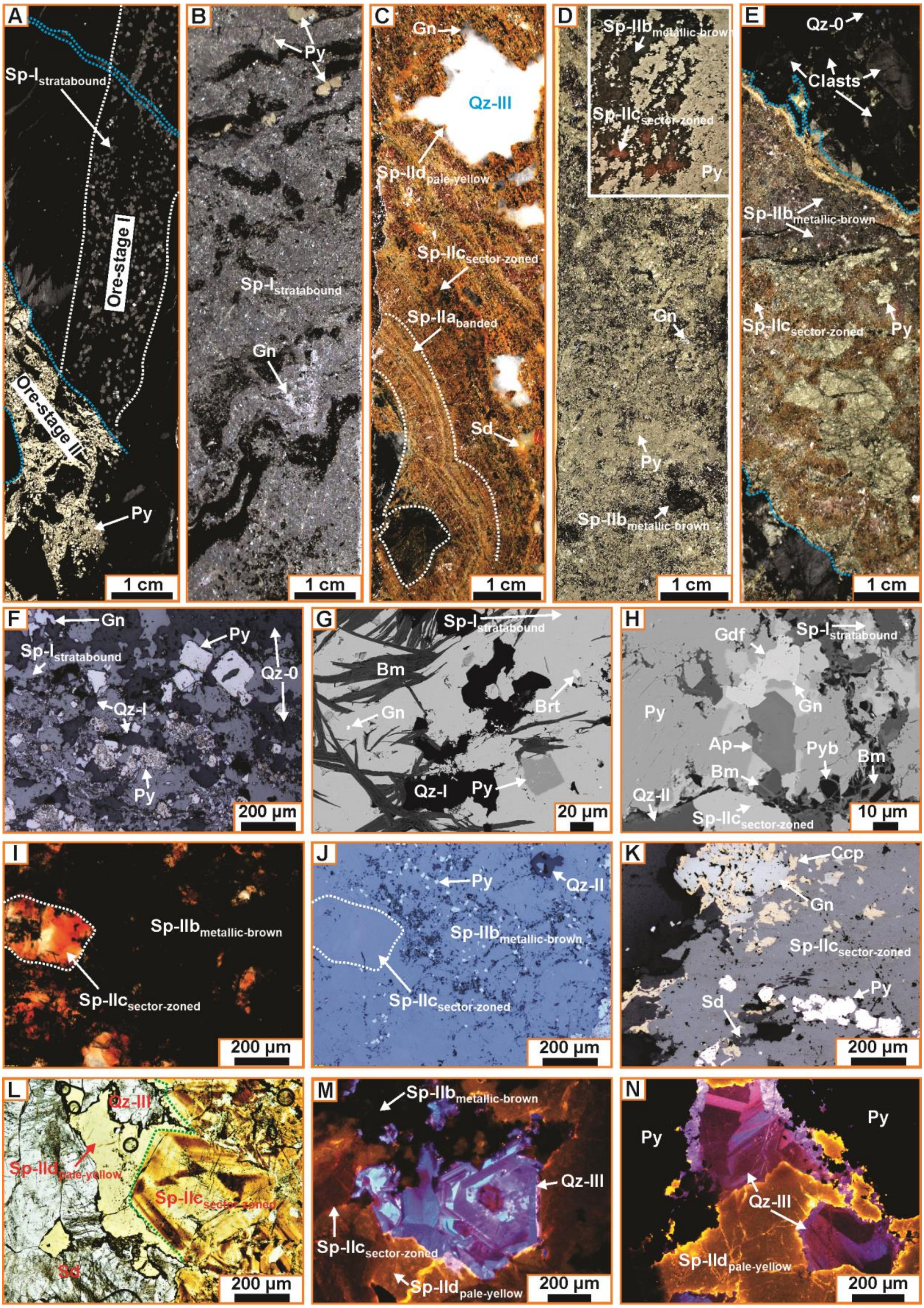

Fig. 4- 3: Representative samples depicting the mineralization styles and major mineralogical compositions. A) Hand specimen photograph of the Duo Lake Formation ore-stage I stratabound Sp-I$_{\text{stratabound}}$ mineralization cut across by pyrite (Py) and sphalerite veins of the ore

stage II (highlighted in blue dotted lines). Note the fragments of the host mudstone within the vein. B) Hand specimen photograph of ore-stage I stratabound mineralization with very fine-grained Sp-I$_{\text{stratabound}}$, coarse-grained galena (Gn), and nodular pyrite in the Niddery Lake Member of the Portrait Lake Formation. C) Hand specimen photograph of a massive vein with different types of ore-stage II sphalerite in the Macmillan Pass Member conglomerate. Sp-IIa$_{\text{banded}}$ is overgrown by Sp-IIc$_{\text{sector-zoned}}$. Very coarse-grained quartz (Qz-III) is intergrown with minor Sp-IId$_{\text{pale-yellow}}$ and siderite (Sd). D) Hand specimen photograph of massive pyrite-sphalerite with Sp-IIb$_{\text{metallic-brown}}$ and Sp-IIc$_{\text{sector-zoned}}$ (inset). E) Hand specimen of Macmillan Pass Member conglomerate hosting massive vein comprising of nodular pyrite, Sp-IIb$_{\text{metallic-brown,}}$ and Sp-IIc$_{\text{sector-zoned}}$. Pre-ore stage quartz (Qz-0) occurs mainly as cement. F) Reflected light photomicrograph of ore-stage I Sp-I$_{\text{stratabound}}$ intergrown with anhedral Gn and subhedral to euhedral Py. G) BSE image of ore stage I mineral association showing Sp-I$_{\text{stratabound}}$, Py, barian-mica (Bm), and Qz-I. Sp-I$_{\text{stratabound}}$ comprises of inclusions of pre-ore barite (Brt). H) BSE image of ore stages I and II in the Duo Lake Formation. Significant Py, fluorapatite (Ap), and pyrobitumen (Pyt) are associated with mineralization. I-J) Transmitted and reflected light photomicrograph of Sp-IIb$_{\text{metallic-brown}}$ with fine-grained euhedral Py and Sp-IIc$_{\text{sector-zoned}}$. K) Reflected light photomicrograph of ore-stage II mineralogical composition comprising Sp-IIc$_{\text{sector-zoned}}$, Py, Gn, chalcopyrite (Ccp), and Sd. L) Transmitted light photomicrograph of Sp-IIc$_{\text{sector-zoned}}$ overgrown by Sp-IId$_{\text{pale-yellow}}$ with Sd and Qz-III. M) Cathodoluminescence photomicrograph of Qz-III with three generations of sphalerite of ore-stage III. N) Cathodoluminescence photomicrograph of Sp-IId$_{\text{pale-yellow}}$ with Qz-III in massive Py.

Ore-stage II mineralization formed in veins and breccias that crosscut ore-stage I (e.g., Fig. 4-3a) within the Duo Lake and Portrait Lake Formations. There are four sub-generations of sphalerite in ore-stage II that represent a volumetrically significant sphalerite contribution to the mineral endowment at the Boundary Zone (Chapter 3; Fig. 3c-e). A banded Sp-IIa$_{\text{banded}}$ forms early in the veins and breccias and mainly in the Macmillan Pass Member (Fig. 4-3c). The bands comprise alternating fine-grained acicular and pale-yellow to orange-colored euhedral sphalerite. Formation of Sp-IIa$_{\text{banded}}$ is followed by precipitation of brown to black inclusion-rich sphalerite (Sp-IIb$_{\text{metallic-brown}}$). The Sp-IIb$_{\text{metallic-brown}}$ has a spongy texture and forms a relatively minor component in the massive pyrite alteration (Fig. 4-3d) and is coeval with fine-grained euhedral pyrite (Fig. 4-3i-j). A rhythmically banded and sector-zoned Sp-IIc$_{\text{sector-zoned}}$ occurs as the most significant sphalerite generation within ore-stage II. A subhedral, medium to coarse-grained quartz (Qz-II) is associated with this sphalerite (e.g., Fig. 4-3h). Minor chalcopyrite forms with porous pyrite and siderite. (Fig. 4-3k). The last sphalerite generation overgrows the earlier phases (Fig. 4-3l) and comprises a pale-yellow to transparent coarser-grained sphalerite (Sp-IId$_{\text{pale-yellow}}$). The Sp-IId$_{\text{pale-yellow}}$ forms an assemblage with siderite (Fig. 4-3c) and very coarse-grained milky and colorless crystalline quartz (Qz-III; Fig. 4-3m-n).

4.4. Methods

4.4.1. Sampling and petrography

A total of 73 drill core samples were obtained from nine drill holes at the Boundary Zone deposit. These samples include mineralized rocks from the Duo Lake and Portrait Lake Formations and contain stratabound, vein-, and breccia-hosted mineralization styles. Detailed petrographic, textural, and ore microscopy was conducted on 73 thin sections using a dual reflected and transmitted light Olympus BX51 polarizing microscope. For selected samples, a hot-cathode optical cathodoluminescence (CL) petrographic system was employed to observe luminescence and zonation in sphalerite and quartz. Doubly polished wafers (thicknesses ranging from 70 to 110 µm) were prepared from 26 samples containing coarse-grained sulfide minerals and associated gangue assemblages, and the optical microscope was used to determine and characterize fluid inclusion assemblages.

4.4.2. Electron probe microanalysis (EPMA)

Selected samples were carbon-coated (20 nm thick) and analyzed using a JEOL JXA-8530F Hyperprobe EPMA. Mineralogical, textural, and paragenetic relationships were investigated using backscattered electron (BSE) imaging and electron dispersive spectroscopy (EDS) analyses. Quantitative mineral chemistry data were acquired via wavelength dispersive spectroscopy (WDS). Operating conditions included a 1-3 µm beam diameter, 15 nA beam current, and 15 kV accelerating potential in both secondary electron and BSE modes. Calibration for element concentration used natural and synthetic materials, including reference material GaAs (As, Ga), copper (Cu), silver (Ag), rutile (Ti), sphalerite (Zn), pentlandite (Fe, Ni, S), stibnite (Sb), and galena (Pb). The sphalerite major and minor element results are available in the data publication of Grema *et al.* (2024b).

4.4.3. Laser ablation inductively coupled plasma mass spectrometry (LA-ICP-MS) and statistical treatment

Trace element concentrations in sphalerite were analyzed using the EleMap LA-ICP-MS facility at GFZ Potsdam. Laser ablation inductively coupled plasma mass spectrometry (LA-ICP-MS) analyses were conducted on 17 doubly polished wafers. The setup included a Thermo Scientific iCAP RQ quadrupole-ICP-MS, linked to a Teledyne Photon Machines Analyte Excite 193 nm ArF excimer-based LA system featuring a HelEx II 2-volume ablation cell. Aerosol generated from laser ablation was transported to the ICP-MS using helium (He) carrier gas mixed with argon (Ar) prior to plasma entry. The tuning of the LA system and ICP-MS was focused on minimizing laser-induced elemental fractionation, enhancing sensitivity, and reducing oxide and polyatomic interferences. Tuning parameters were based on the $^{238}U/^{232}Th$

ratio of SRM NIST610 for elemental fractionation and the ^{232}Th^{16}O/^{232}Th ratio for molecular interference.

Primary and secondary reference materials were measured in brackets between 10 to 15 unknowns. Ablation of sample targets was conducted for 30 seconds each, following a background measurement using a 50 µm spot diameter, a constant pulse rate of 10 Hz, and a laser energy density of 2-3 J/cm^2 in the sample surface. The following 48 masses over charge (m/z, no resolution of isobaric interference or doubly charged ions possible) were measured and referred to as: ^{23}Na, ^{24}Mg, ^{27}Al, ^{33}S, ^{34}S, ^{35}Cl, ^{39}K, ^{43}Ca, ^{44}Ca, ^{46}Ti, ^{47}Ti, ^{51}V, ^{52}Cr, ^{53}Cr, ^{55}Mn, ^{57}Fe, ^{58}Fe, ^{59}Co, ^{60}Ni, ^{63}Cu, ^{65}Cu, ^{66}Zn, ^{68}Zn, ^{71}Ga, ^{72}Ge, ^{73}Ge, ^{75}As, ^{76}Se, ^{77}Se, ^{79}Br, ^{95}Mo, ^{96}Mo, ^{107}Ag, ^{109}Ag, ^{111}Cd, ^{113}In, ^{115}In, ^{118}Sn, ^{121}Sb, ^{125}Te, ^{137}Ba, ^{200}Hg, ^{201}Hg, ^{202}Hg, ^{205}Tl, ^{206}Pb, ^{208}Pb, ^{209}Bi.

The Iolite4™ software package (version 4.7.1; Paton *et al.*, 2011) was utilized to process time-resolved mass spectra (Fig. 4-4) and examine each ablation signal. Trace element concentrations were determined using the iolite trace element Data Reduction Scheme. Heterogeneous ablation signals resulting from mineral inclusions were monitored from high Al, Ca, K, and Ba, and exceptionally low Zn and S counts per second were excluded. Cross-referencing laser ablation ICP-MS and EPMA measurements for Fe and Cu in sphalerite aided in evaluating data quality. After baseline subtraction modeled after the background measurements preceding each ablation, MUL-ZnS was the primary calibration reference material and was used to correct for analytical drift. Zinc concentrations obtained from sphalerite by EPMA were used as internal standard to correct for instrumental bias. UQAC-FeS-1 was the secondary calibrant used for all elements except for Ga, Ge, As, Cd, Sn, and Tl where NIST610 was used. The LA-ICP-MS sphalerite spot analysis results that are below detection limit (BDL) are indicated as such and available in the data publication of Grema *et al.* (2024b), along with the calculated lower detection limits (after Howell *et al.*, 2013), standard error (SE), and standard deviation (SD). Quality of the data was controlled by MASS-1, Cu-Bergen, UQAC-FeS-1, and MUL-ZnS and is reported in the data publication.

The trace element data was evaluated following the workflow described by Frenzel (2023). A log ratio transformation was applied to each analyte, followed by the multiple imputation technique of the Scikit-learn model-based imputation package, executed in Python, which operates in a round-robin fashion for imputing missing values (BDL). A principal component analysis (PCA) was then applied to reduce the dimensionality of the dataset using ioGas-64 (version 7.4). The PCA identified compositional vectors in the multivariate dataset and transformed them into Principal Components (PCs). These PCs are defined by eigenvectors, representing the correlations between the PCs and the individual analytes, and eigenvalues, indicating each PC's contribution to the variance in the original dataset. The robust M-estimation was used to assign low weightings to outlier samples.

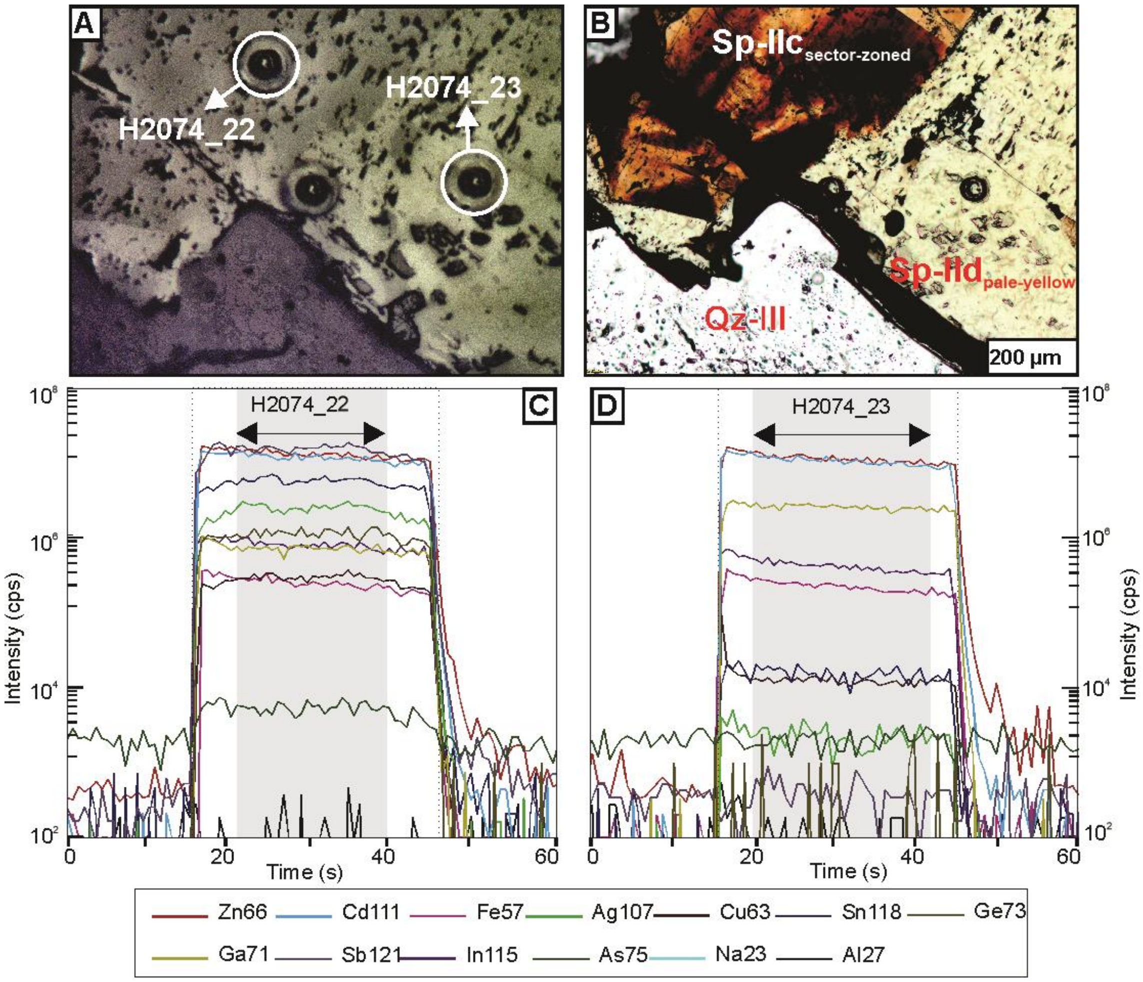

Fig. 4- 4: Representative time-resolved LA-ICP-MS depth profiles with locations in two sphalerite types. A) Reflected light photomicrograph of spots hit by laser during analysis. B) Transmitted light photomicrograph of the area in A, showing the sphalerite types and distribution of analyzed spots. C-D) Time-resolved LA-ICP-MS depth profiles for spots in A. The shaded areas show the profile span considered during quantification.

4.4.4. Laser Raman spectroscopy

Sphalerite- and quartz-hosted fluid inclusions were analyzed using a Horiba JobinYvon LabRAM HR Evolution confocal Raman spectrometer equipped with an Olympus optical microscope. Analyses were performed using a frequency-doubled Nd-YAG solid-state green laser with an excitation wavelength of 532 nm. Raman spectra were acquired in two spectral ranges: 200 to 1200 cm^{-1} for solid inclusions and host minerals and 1200 to 3200 cm^{-1} for vapor phases. Each spectrum was recorded with 2 × 20-second acquisition times, utilizing a x100 objective lens. A silicon reference material was used for internal calibration.

4.4.5. Fluid inclusion petrography and microthermometry

Microthermometry was performed using a Linkam THMS 600 heating-freezing stage attached to an Olympus BX53M microscope equipped with a QICAM FAST1394 camera. Calibration was conducted using synthetic Synflinc pure H_2O and H_2O-CO_2 fluid inclusion reference material, and the measurements had a reproducibility of ±0.1 °C. Fluid inclusion assemblages were identified and documented (see text below). Fluid inclusions that decrepitated during the analyses were discarded from the microthermometry dataset. The measured melting temperatures included $T_{m(CO2)}$, $T_{m(ice)}$, and T_m (clathrate), as well as homogenization temperatures: $T_{h(CO2)}$ and $T_{h(tot)}$ in some inclusions. However, many inclusions were too small and dark to observe $T_{m(clath)}$ and $T_{m(CO2)}$, so the full data set is only available for 18 out of 202 reported inclusion analyses (Grema *et al.*, 2024b).

The salinity values of the CO_2-bearing fluid inclusions in this study were calculated from the $T_{m(ice)}$ values using the HokieFlinc's H_2O-NaCl system (Steele-MacInnis *et al.*, 2012) instead of the H_2O-NaCl-CO_2 system (Steele-MacInnis, 2018) due to the lack of measurement of some of the key parameters required for the latter system, i.e., $T_{h(CO2)}$ and $T_{m(clath)}$ (Grema *et al.*, 2024b). A small number of samples of complete phase change measurements (i.e., with $T_{m(clath)}$) were used to verify the results using both approaches. This suggests that there is an approximate uncertainty in the salinity calculations for H_2O-CO_2-NaCl inclusions with ~3 wt.% NaCl equiv.

4.5. Results

4.5.1. Sphalerite minor and trace element chemistry

The sphalerite chemistry dataset includes 671 analyses. The integration window for each analysis was carefully selected to exclude analyses that clearly hit solid inclusions, resulting in 70 ablations being discarded. A summary of results for the different sphalerite generations across the Boundary Zone deposit (n=601) is provided in Table 4-1.

Duo Lake Formation: In the Duo Lake Formation, there is a positive correlation ($r^2 = 0.74$) between Fe and Mn concentrations in all the sphalerite generations. The lowest Mn concentrations are found in the Duo Lake Formation (Table 4-1). There is a consistent trend of decreasing Cu, Ag, Hg, Ge, Sn, and Pb concentrations from Sp-$I_{stratabound}$ to Sp-$IId_{pale-yellow}$, with an increase in the concentrations of Se and In. Sp-$I_{stratabound}$ of the Duo Lake Formation has high concentrations of Cu (GM = 883.2 ppm), Sb (285.3 ppm), Ag (33.7 ppm), Hg (1,218.6 ppm), Ge (211.8 ppm), Sn (24.6 ppm), and Pb (84.0 ppm) compared to Sp-IId$_{\text{pale-yellow}}$ (76.2 ppm Cu; 8.3 ppm Sb; 2.8 ppm Ag; 958.9 ppm Hg; 0.9 ppm Ge; and 4.1 ppm Pb). A Cu and Ge distribution map in the Sp-IIc$_{\text{sector-zoned}}$ shows enrichment in the red-colored sectors compared to the pale-yellow zones (Fig. 4-5g-h).

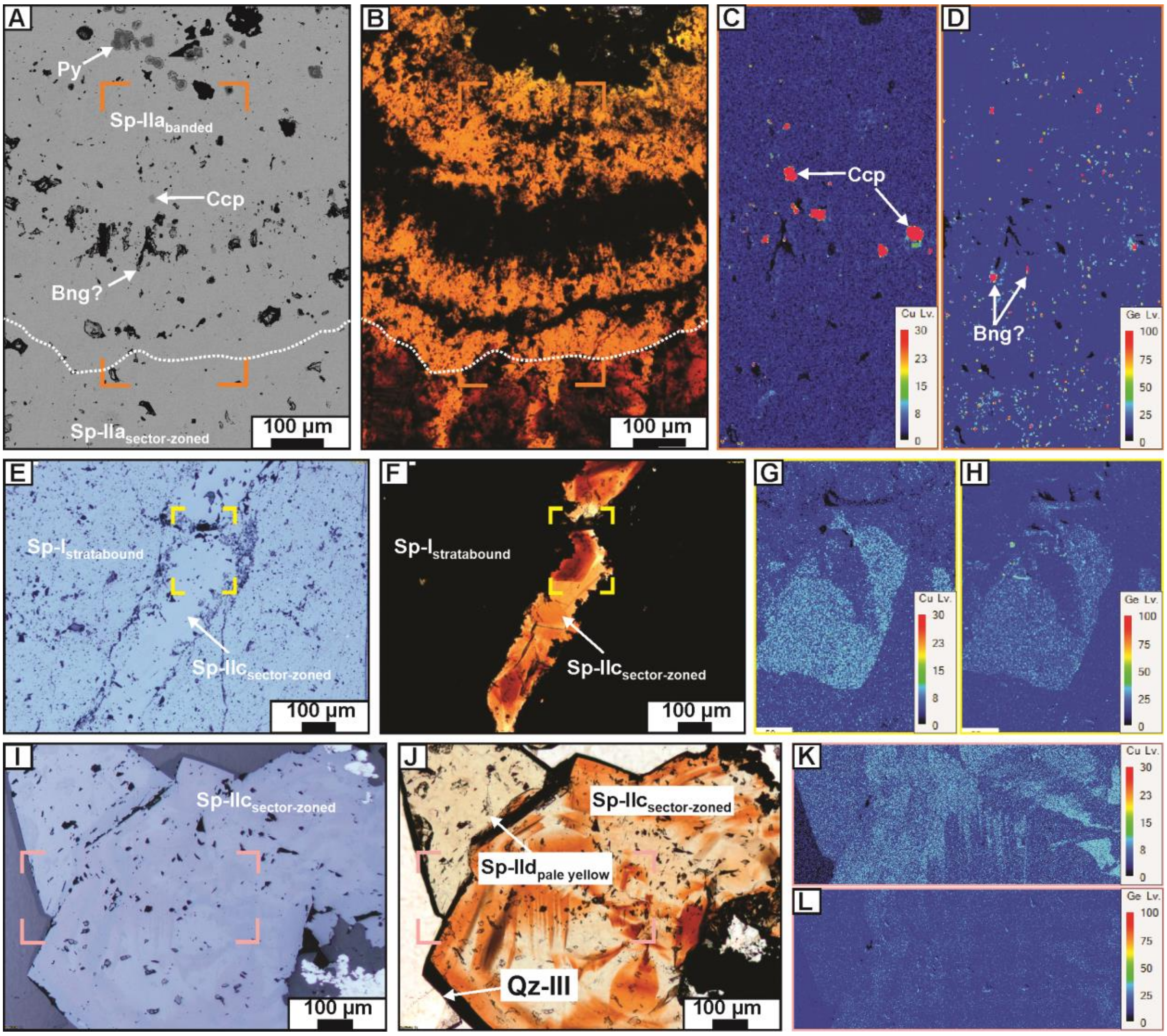

Fig. 4- 5: Photomicrographs and element maps of the three major sphalerite types in the ore stage II mineralization. A) BSE image of Sp-IIa$_{\text{banded}}$ that is inclusion rich. B) Transmitted light photomicrograph of the same area in A. C-D) element maps of Cu and Ge of the area highlighted in A. Note the chalcopyrite and likely brunogeierite inclusions. E) Reflected light photomicrograph of Sp-I$_{\text{stratabound}}$ of the Duo Lake Formation cut across by a vein containing Sp-IIc$_{\text{sector-zoned}}$. G-H) Element maps of the area highlighted in E, showing the distribution of Cu and Ge. I) Reflected light photomicrograph of Sp-IIc$_{\text{sector-zoned}}$ occurring in the massive pyrite sphalerite zone. J) Transmitted light photomicrograph of the same area in I, highlighting the rhythmic banding typical of the Sp-IIc$_{\text{sector-zoned}}$. K-L) Element map of the area highlighted in I showing the distribution of Cu and Ge.

Table 4- 1: Summary statistics for selected sphalerite LA-ICP-MS trace element results for the different generations. Min= minimum value, Max= maximum value, SD= standard deviation, GM= geometric mean, BDL= below detection limit. All elements are in ppm.

	Fe	**Mn**	**Cd**	**Cu**	**Ag**	**In**	**Ge**	**Ga**	**Co**	**Sn**	**As**	**Sb**	**V**	**Se**	**Hg**	**Pb**	**Ni**
Duo Lake Formation																	
Sp-I$_{\text{stratabound}}$ (n=29)																	
Min	6086.3	0.6	3032.1	176.8	4.7	<0.1	31.5	0.8	0.3	4.0	BDL	12.4	BDL	<0.1	752.8	6.1	3.3
Max	20312.3	87.4	4419.1	2858.6	70.2	17.7	650.5	140.5	2.6	53.0	38.8	554.6	76.4	15.8	1701.3	658.1	16.7
GM	15585.6	12.5	3880.1	883.2	33.7	3.7	211.8	20.9	1.4	24.6	3.6	285.3	44.7	2.9	1218.6	84.0	7.5
SD	3365.0	20.3	405.2	678.3	17.5	3.5	153.8	25.9	0.6	11.4	7.2	137.4	21.7	3.0	317.2	113.9	3.1
Sp-IIc$_{\text{sector-zoned}}$ (n=9)																	
Min	6610.8	0.5	4016.5	113.2	4.6	4.3	12.2	2.9	BDL	4.3	BDL	11.4	BDL	2.0	519.8	6.7	BDL
Max	20337.6	45.1	5524.7	2856.3	162.1	11.2	519.7	156.7	1.2	168.2	4.3	1331.9	58.2	12.2	848.1	235.1	5.7
GM	16348.0	21.1	4614.8	876.1	50.1	7.5	136.9	70.4	0.6	58.4	2.3	404.4	8.9	7.2	714.6	62.1	2.3
SD	4885.0	17.1	674.3	843.8	56.0	2.5	150.0	51.7	0.6	56.9	1.3	433.6	19.5	3.8	135.3	73.4	2.1
Sp-IId$_{\text{pale yellow}}$ (n=14)																	
Min	7522.5	0.6	3066.2	12.6	0.7	<0.1	0.7	3.5	BDL	<0.1	BDL	<0.1	BDL	BDL	477.4	<0.1	BDL
Max	24567.3	45.1	5637.6	263.1	10.3	19.5	1.6	22.9	2.1	2.1	BDL	44.9	34.4	17.6	1388.9	18.8	21.1
GM	17179.0	18.7	3891.9	76.2	2.8	6.1	0.9	12.2	1.4	0.8	-	8.3	2.7	9.8	958.9	4.1	9.2
SD	5706.8	16.5	932.6	78.2	2.6	6.8	0.2	6.8	0.7	0.7	-	12.1	9.1	5.5	351.1	5.0	7.2
Niddery Lake Member																	
Sp-I$_{\text{stratabound}}$ (n=67)																	
Min	1486.2	451.3	829.0	6.6	1.6	BDL	0.6	2.7	2.4	0.2	BDL	0.8	BDL	BDL	1227.0	3.3	<0.1
Max	7491.9	1146.8	1275.6	292.8	128.6	0.7	140.6	46.5	24.4	90.5	569.5	2221.9	57.7	40.6	1855.2	232623.9	288.3
GM	4901.6	737.1	1108.3	109.4	50.2	0.3	41.8	22.8	9.8	21.7	33.8	193.6	7.0	2.5	1502.3	11213.7	7.9
SD	1052.1	117.1	82.6	66.6	30.2	0.2	34.7	8.9	4.7	18.3	75.4	292.3	10.0	5.3	136.2	30486.2	35.7
Sp-IIb$_{\text{metallic brown}}$ (n=24)																	
Min	1875.3	134.9	2786.2	14.5	3.4	BDL	0.4	BDL	BDL	0.7	0.2	0.9	BDL	BDL	863.3	0.8	<0.1
Max	7586.3	3740.1	4879.6	1209.5	51.0	6.3	585.2	278.5	2.0	65.0	7.8	182.9	0.3	1.8	1859.4	680.6	1.4
GM	5325.0	919.9	3304.7	402.5	18.8	2.9	154.7	28.2	0.3	19.5	2.4	41.9	<0.1	0.6	1317.4	56.9	0.4
SD	1364.8	718.5	626.3	297.3	11.8	2.1	149.9	57.6	0.5	21.1	1.8	43.4	0.1	0.5	286.5	138.6	0.3
Sp-IIc$_{\text{sector-zoned}}$ (n=99)																	

Min	1480.4	6.2	2794.0	9.6	0.9	BDL	0.8	BDL	BDL	0.3	BDL	0.8	BDL	BDL	847.3	0.3	BDL
Max	29590.5	2789.8	8827.8	2963.7	1103.2	37.1	848.4	658.2	2.9	628.2	372.1	3233.5	213.6	12.1	2084.4	1190.1	10.9
GM	5714.3	772.8	4056.8	994.0	91.2	5.6	248.3	69.5	0.3	68.2	7.3	323.9	4.8	1.0	1372.2	77.9	0.7
SD	3367.0	505.4	1565.6	672.7	168.2	6.2	209.4	111.7	0.4	90.3	37.2	594.7	24.0	1.7	277.0	134.6	1.5
Sp-IId$_{\text{pale yellow}}$ (n=116)																	
Min	538.4	74.8	972.8	6.6	0.8	BDL	0.3	<0.1	BDL	BDL	BDL	0.2	BDL	<0.1	1002.4	<0.1	<0.1
Max	42316.1	1832.4	8118.4	805.6	94.8	14.3	301.5	727.2	26.7	67.0	37.3	204.7	25.2	4.6	2163.3	18719.6	26.7
GM	5061.6	889.5	2330.3	105.7	11.4	1.6	7.7	70.2	5.4	4.7	2.6	19.5	0.6	0.9	1479.0	1023.3	2.1
SD	3751.2	287.4	1737.5	164.6	13.8	2.9	32.9	139.9	6.5	7.9	4.7	29.6	2.5	0.7	293.9	3014.2	3.1
Macmillan Pass Member																	
Sp-IIa$_{\text{colloform}}$ (n=46)																	
Min	9894.3	10.3	1997.2	4.3	5.7	BDL	1.2	BDL	0.8	BDL	BDL	1.8	BDL	BDL	227.7	6.1	<0.1
Max	49911.0	2447.1	4323.1	4415.6	752.2	24.6	1309.5	310.5	34.8	358.4	8.0	1754.8	0.9	4.3	1031.1	3223.1	4.5
GM	35873.5	165.1	2987.9	798.2	89.6	2.6	514.6	32.4	9.5	19.9	2.0	273.1	<0.1	0.9	623.0	864.1	2.2
SD	10586.0	406.1	635.5	914.4	162.9	5.7	373.0	76.1	7.9	57.8	2.0	462.4	0.2	1.3	192.7	1092.3	1.2
Sp-IIb$_{\text{metallic brown}}$ (n=8)																	
Min	30707.0	11.5	1693.6	20.7	1.8	1.8	0.9	3.2	19.1	0.7	0.2	1.3	<0.1	0.6	274.8	1.1	0.6
Max	41635.3	46.4	3419.0	146.4	12.6	4.5	1.3	32.2	28.6	15.7	1.2	8.3	1.9	8.2	3695.1	8.3	1.8
GM	36997.0	23.3	1999.4	71.9	7.2	2.9	1.1	17.1	24.6	2.9	0.6	5.6	0.5	3.2	1009.4	4.4	1.0
SD	3385.9	10.7	580.6	45.6	3.5	0.9	0.1	10.4	2.9	5.2	0.4	2.6	0.7	2.4	1184.6	2.1	0.5
Sp-IIc$_{\text{sector-zoned}}$ (n=110)																	
Min	6969.9	4.2	1404.4	13.2	1.7	BDL	1.2	<0.1	0.5	BDL	<0.1	0.8	BDL	BDL	207.9	0.8	<0.1
Max	62108.0	432.0	4433.1	3538.4	554.4	58.8	1757.3	406.9	79.5	285.7	2380.0	2381.5	18.1	14.0	1124.3	2233.8	150.9
GM	30830.5	52.3	2597.6	556.9	54.1	4.7	401.6	42.0	9.7	20.2	110.1	165.1	0.9	3.2	580.0	140.4	8.7
SD	9595.1	68.7	890.5	682.8	76.9	7.4	342.6	65.0	10.5	36.8	339.9	340.6	2.7	3.4	225.3	331.0	23.3
Sp-IId$_{\text{pale yellow}}$ (n=66)																	
Min	15586.3	4.1	1587.3	3.4	0.7	0.7	0.6	<0.1	<0.1	<0.1	0.2	<0.1	BDL	0.3	211.5	<0.1	0.3
Max	54655.2	1470.2	4308.6	373.8	60.2	6.3	188.4	16.2	98.1	22.0	9890.4	242.3	16.3	14.8	852.7	2718.0	2776.8
GM	25541.4	53.0	2736.6	34.7	7.8	2.5	6.5	2.9	9.2	1.8	152.8	11.7	0.9	5.1	470.4	55.7	46.6
SD	7006.4	186.5	744.7	55.0	10.3	1.2	30.8	3.2	12.7	3.7	1217.1	30.9	3.0	4.5	210.1	336.3	341.3

Niddery Lake Member (Portrait Lake Formation): Compared to other units, Fe is uniformly low in all sphalerite generations in the Niddery Lake Member, whereas Mn is uniformly high (Table 4-1). The Cd concentrations vary with paragenesis: Sp-$I_{stratabound}$ has the lowest concentration (GM= 1,108.3 ppm), while there is an enrichment in Sp-$IIb_{metallic\text{-}brown}$ (3,304.7 ppm) and Sp-$IIc_{sector\text{-}zoned}$ (4,056.8 ppm), followed by a decrease in Sp-$IId_{pale\text{-}yellow}$ (2,330.3 ppm). The Hg concentrations are relatively consistent across all sphalerite generations, with slightly higher concentrations in Sp-$I_{stratabound}$ (GM= 1,502.3 ppm). The Cu, In, and Ge concentrations increase across the first three sphalerite generations; however, Sp-$IId_{pale\text{-}yellow}$ has the lowest concentrations of these elements. The element distribution map of the Sp-$IIc_{sector\text{-}zoned}$ highlights the enrichment of Ge and Cu in the red sectors of the sphalerite crystals (Fig. 4-5k-l).

Macmillan Pass Member (Portrait Lake Formation): The highest Fe concentrations are in the sphalerite hosted by the Macmillan Pass Member, with the earlier Sp-IIa_{banded} (GM= 35,873.5 ppm) and Sp-$IIb_{metallic\text{-}brown}$ (36,997.0 ppm) having relatively higher concentrations than the Sp-$IIc_{sector\text{-}zoned}$ (30,830.5 ppm) and Sp-$IId_{pale\text{-}yellow}$ (25,541.4 ppm). Manganese displays a similar but less pronounced trend compared to Fe. The concentrations of Cu, Ag, Sb, and Pb in the sphalerite generations follow oscillatory zoning pattern (Fig. 4-6). Notably, Ge concentrations are lower in Sp-$IIb_{metallic\text{-}brown}$ (GM= 1.1 ppm) and Sp-$IId_{pale\text{-}yellow}$ (6.5 ppm), compared to the enrichment observed in Sp-IIa_{banded} (514.6 ppm) and Sp-$IIc_{sector\text{-}zoned}$ (401.6 ppm). Microscopic inclusions of chalcopyrite and possibly brunogeierite ($Ge^{4+}Fe^{2+}{}_2O_4$) (Fig. 4-5c-d) were observed within the Sp-IIa_{banded} (Fig. 4-5c-d).

4.5.2. Principal component analysis (PCA)

For the PCA, elements typically incorporated into the sphalerite structure rather than those contained in mineral inclusion phases were selected: Fe, Mn, Cu, Ag, In, Ge, Ga, Co, Sn, As, Sb, Pb, Hg, Cd, and Ni. To ensure that all analyses (n = 601) could be included in the PCA, BDL were replaced by imputed values as described in *section 4.4.3*. The PCA, categorized by ore stages, is presented in Fig. 4-7. PC1 to PC4 describe >80% of the total variance in the dataset. In both ore-stages, elements cluster in three main groups. Notably, both ore stages preserve similar clustering of elements in PC1, independent of the host-rock type, whereas PC2 effectively separates sphalerite hosted by the Niddery Lake and Macmillan Pass Members (Fig. 4-7).

General trends were observed within the trace element concentrations. For example, high concentrations of Hg (>200 ppm) are recorded in all generations of sphalerite, with a slight inverse relationship observed between Hg and Fe (Fig. 4-6); some of the highest Hg concentrations are found in Fe-poor sphalerite. Germanium concentrations are consistently lower in Sp-IId$_{\text{pale-yellow}}$ compared to other sphalerite generations.

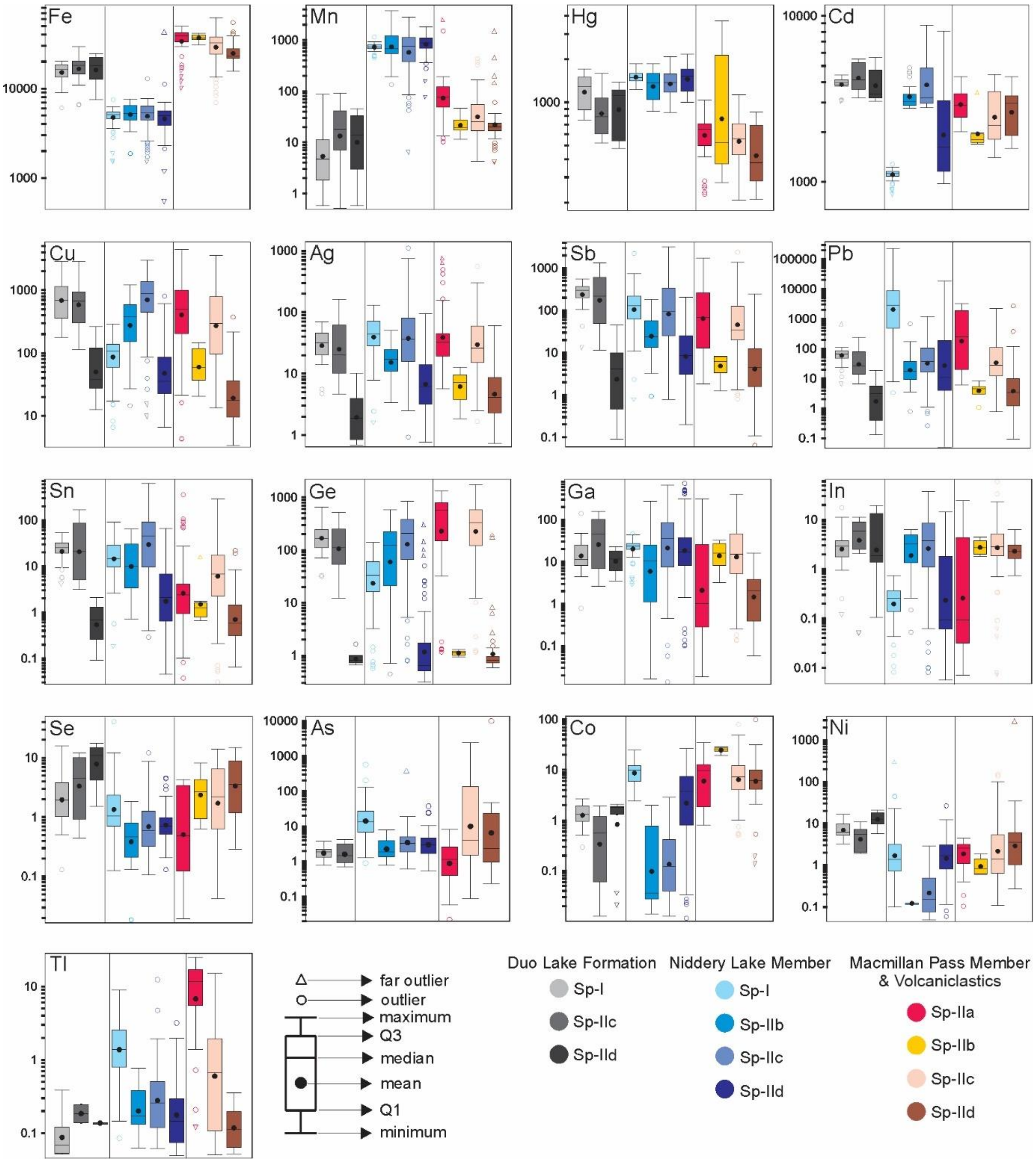

Fig. 4- 6: Box and whisker plots of minor and trace elements in sphalerite from the Duo Lake and Portrait Lake Formations. The panes with similar color shades are categorized according to the host rock, including the different sphalerite types. All the elements are plotted in ppm.

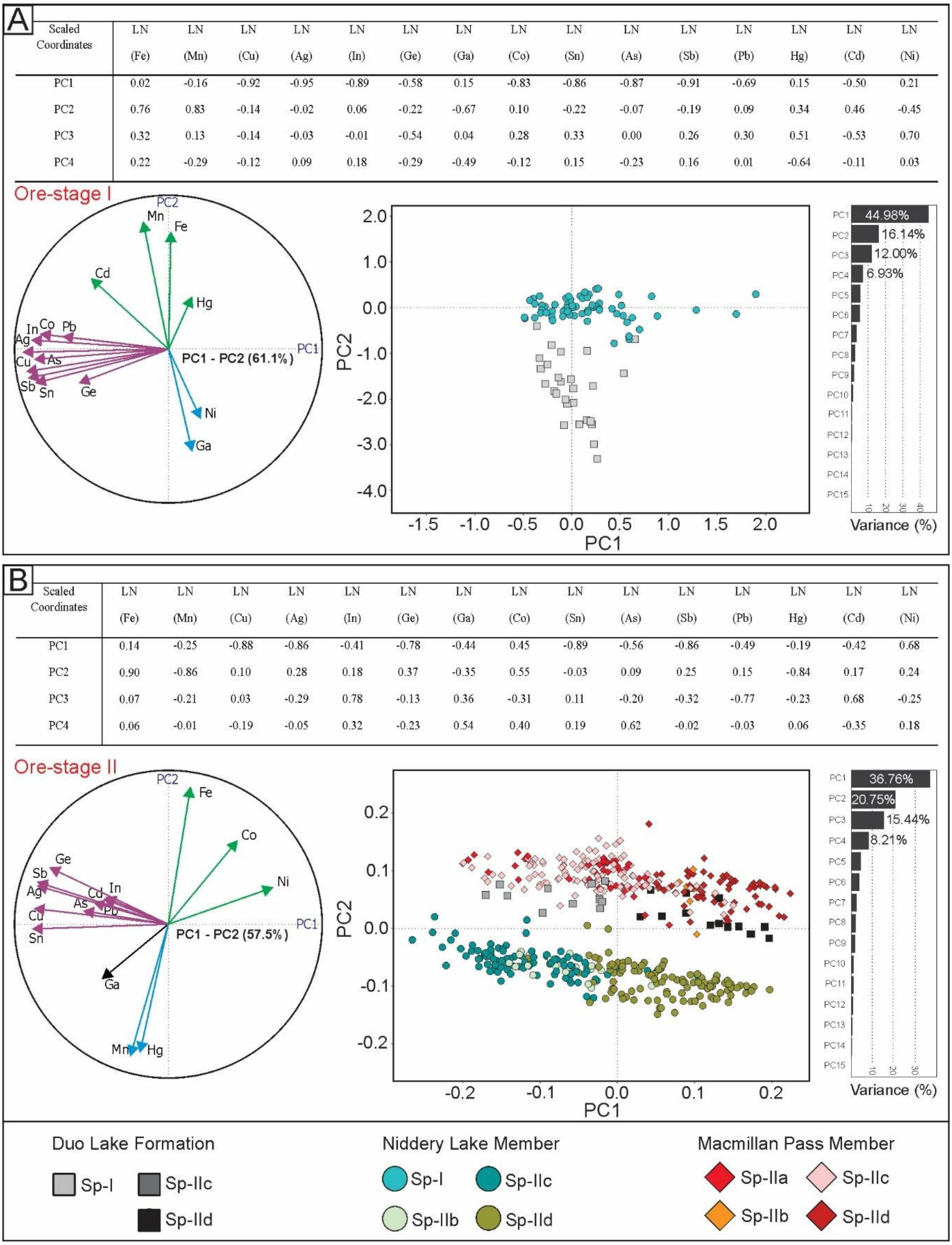

Scaled Coordinates	LN (Fe)	LN (Mn)	LN (Cu)	LN (Ag)	LN (In)	LN (Ge)	LN (Ga)	LN (Co)	LN (Sn)	LN (As)	LN (Sb)	LN (Pb)	LN Hg)	LN (Cd)	LN (Ni)
PC1	0.02	-0.16	-0.92	-0.95	-0.89	-0.58	0.15	-0.83	-0.86	-0.87	-0.91	-0.69	0.15	-0.50	0.21
PC2	0.76	0.83	-0.14	-0.02	0.06	-0.22	-0.67	0.10	-0.22	-0.07	-0.19	0.09	0.34	0.46	-0.45
PC3	0.32	0.13	-0.14	-0.03	-0.01	-0.54	0.04	0.28	0.33	0.00	0.26	0.30	0.51	-0.53	0.70
PC4	0.22	-0.29	-0.12	0.09	0.18	-0.29	-0.49	-0.12	0.15	-0.23	0.16	0.01	-0.64	-0.11	0.03

Scaled Coordinates	LN (Fe)	LN (Mn)	LN (Cu)	LN (Ag)	LN (In)	LN (Ge)	LN (Ga)	LN (Co)	LN (Sn)	LN (As)	LN (Sb)	LN (Pb)	LN Hg)	LN (Cd)	LN (Ni)
PC1	0.14	-0.25	-0.88	-0.86	-0.41	-0.78	-0.44	0.45	-0.89	-0.56	-0.86	-0.49	-0.19	-0.42	0.68
PC2	0.90	-0.86	0.10	0.28	0.18	0.37	-0.35	0.55	-0.03	0.09	0.25	0.15	-0.84	0.17	0.24
PC3	0.07	-0.21	0.03	-0.29	0.78	-0.13	0.36	-0.31	0.11	-0.20	-0.32	-0.77	-0.23	0.68	-0.25
PC4	0.06	-0.01	-0.19	-0.05	0.32	-0.23	0.54	0.40	0.19	0.62	-0.02	-0.03	0.06	-0.35	0.18

Fig. 4- 7: Principal component analysis (PCA) of 15 minor and trace elements from the LA-ICP-MS sphalerite geochemistry data. The PCA is categorized based on ore stages.

4.5.3. Fluid inclusion petrography

Fluid inclusion assemblages (FIAs) in sphalerite and quartz were targeted for microthermometry; however, only fluid inclusions that were ≥ 4 µm in size and formed ideal FIAs were suitable for measurements. Fluid inclusion assemblages were examined and measured in coarsely crystalline Sp-IIa$_{\text{banded}}$, Sp-IIc$_{\text{sector-zoned}}$, and Qz-III crystals hosted by both the Duo Lake and Portrait Lake Formations (Figs. 4-8, 4- 9). Fluid inclusions from the ore-stage I Sp-I$_{\text{stratabound}}$ and ore-stage II Sp-IIb$_{\text{metallic-brown}}$ and Sp-IId$_{\text{pale-yellow}}$ crystals could not be measured due to the fine-grained size, opaque nature of the sphalerite, or an absence of FIAs.

The FIAs were classified according to criteria from Goldstein (2003) and Roedder (1984) as primary, pseudosecondary, secondary, or indeterminate (i.e., assemblages with unclear origin relative to sphalerite or quartz growth zones). Primary and pseudosecondary FIAs in sphalerite and quartz were specifically targeted. Special attention was given to the relationship between the FIA and the crystal growth zones and that the FIA occurred in clusters in growth zones with similar phase proportions. Each FIA was examined to ascertain its origin, potential deformation features (e.g., necking down), re-equilibration due to host mineral recrystallization, and relationships with adjacent FIAs. Additionally, clusters and cloudy inclusions were carefully inspected to determine their paragenesis. The primary and pseudosecondary inclusions in sphalerite typically exhibited elongated, hexagonal, cylindrical, and negative crystal shapes. In contrast, secondary FIAs generally formed trails cutting across crystal boundaries that were often dark and <4 µm in size, though larger FIA trails were sometimes found in quartz crystals. In quartz, however, the fluid inclusions were dominated by more irregular shapes.

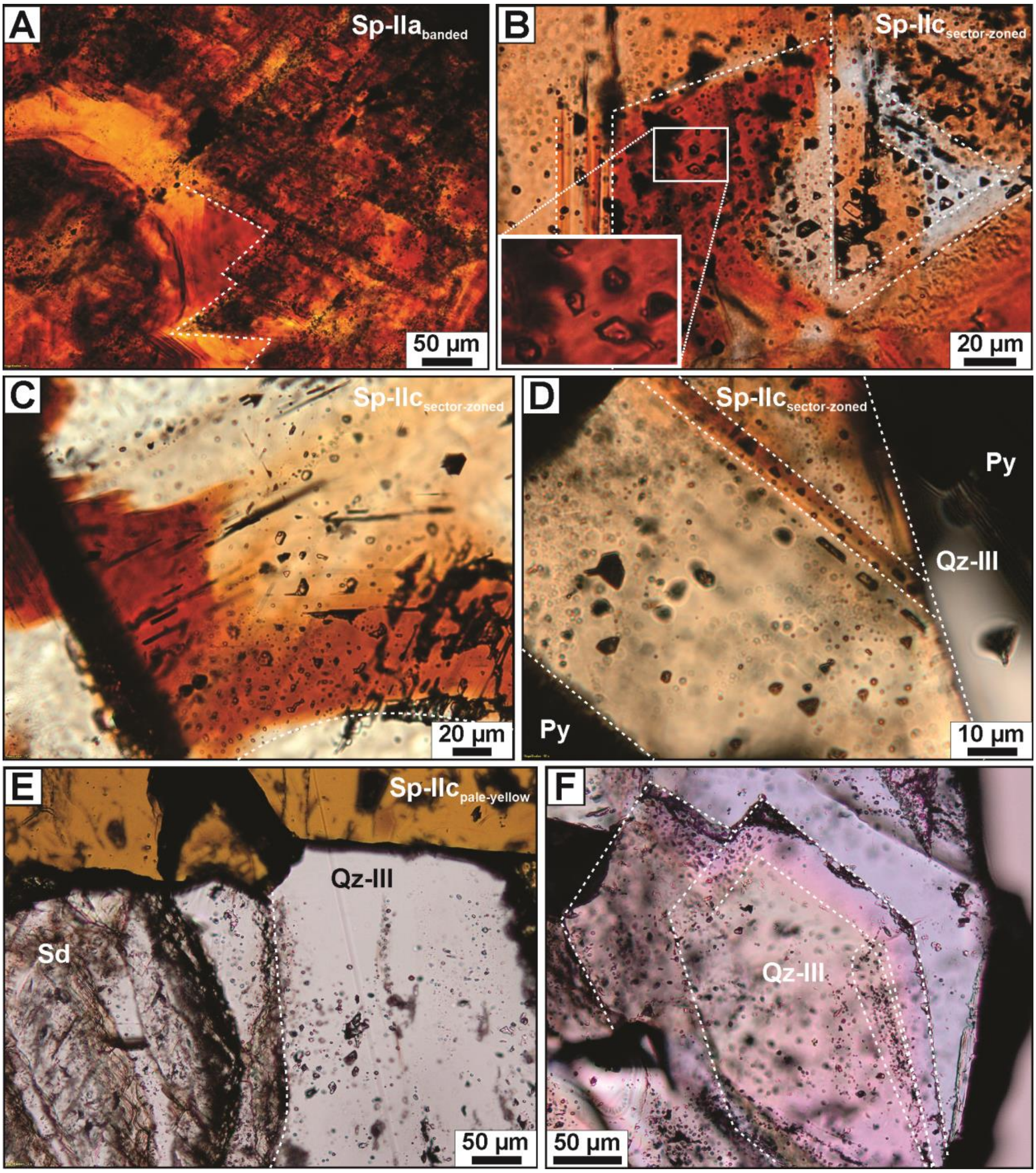

Fig. 4- 8: Fluid inclusion petrography of sphalerite and quartz in the Boundary Zone. A) Transmitted light photomicrograph of Sp-IIa$_{\text{banded}}$ with primary fluid inclusions decorating the growth zones. B) Transmitted light photomicrograph of two sub-types of Sp-IIc$_{\text{sector-zoned}}$, both hosting primary fluid inclusion assemblages at the growth zones (right side crystal) and clustered within the core (left side crystal). The inset shows a transmitted light photomicrograph of the highlighted area with two-phase fluid inclusions. C) Pseudosecondary fluid inclusions that terminated at the red band boundary with the pale-yellow band within the Sp-IIc$_{\text{sector-zoned}}$. D) Transmitted light photomicrograph of elongated primary fluid inclusions that decorate the Sp-IIc$_{\text{sector-zoned}}$ growth zones. E) Transmitted light photomicrograph of Qz-III intergrown with Sp-IId$_{\text{pale-yellow}}$ and siderite. F) Transmitted light photomicrograph of euhedral intergrown Qz-III crystals with fluid inclusion assemblages at the growth zones.

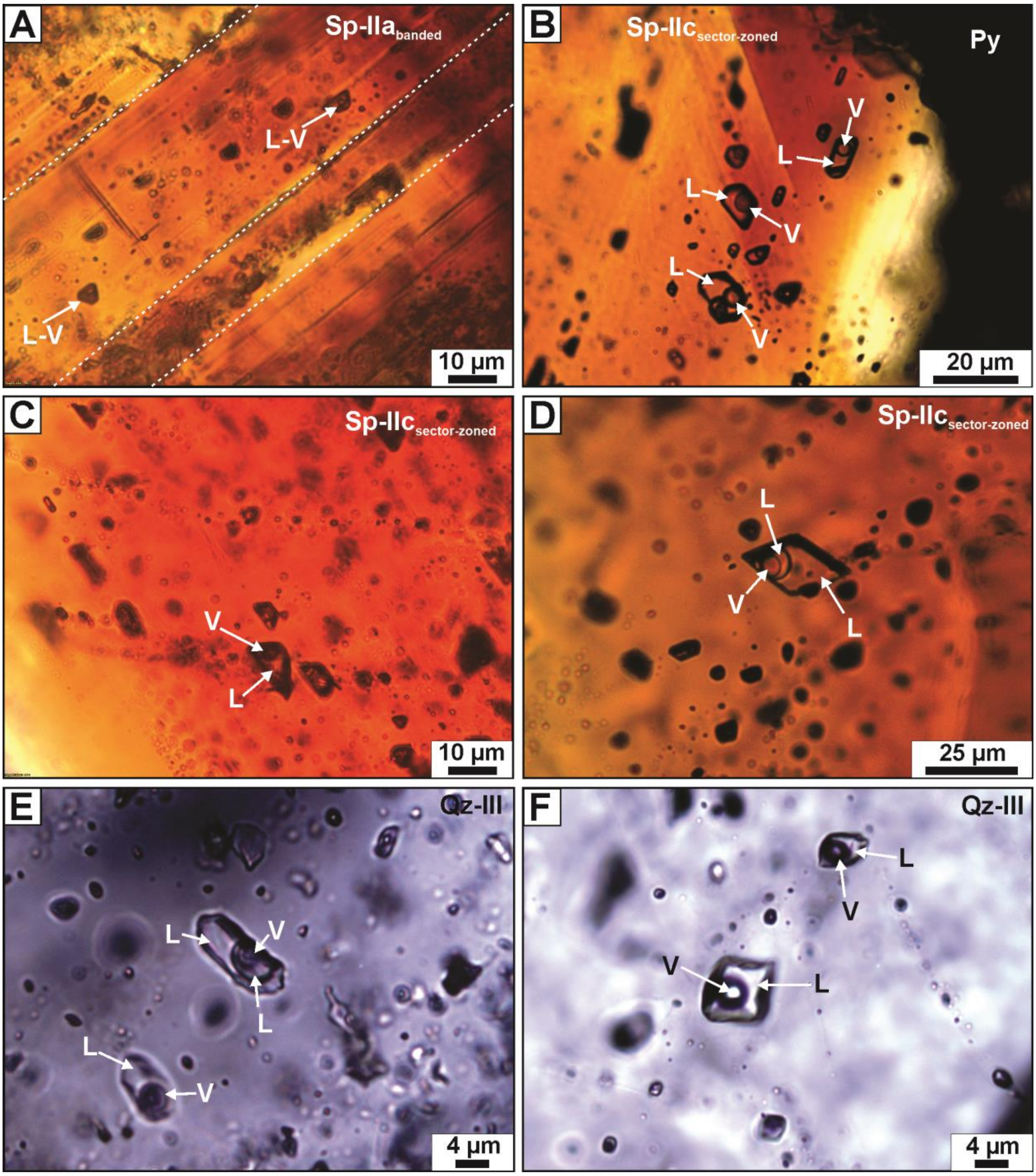

Fig. 4- 9: Fluid inclusion petrography of sphalerite and quartz. A) Transmitted light photomicrograph of primary fluid inclusions at the growth zones of Sp-IIa$_{banded}$. B) Transmitted light photomicrograph of Sp-IIc$_{sector-zoned}$ that shows two-phase L_{aq}-V_{carb} inclusions cluster. C) Transmitted light photomicrograph of aligned two-phase L_{aq}-V_{carb} inclusions in Sp-IIc$_{sector-zoned}$. D) Transmitted light photomicrograph of a three-phase L_{aq}-L_{carb}-V_{carb} fluid inclusion occurring together with two-phase inclusions in Sp-IIc$_{sector-zoned}$. E) Transmitted light photomicrograph of three-phase inclusions in Qz-III. F) Transmitted light Photomicrograph of two-phase inclusions in Qz-III.

4.5.4. Fluid inclusion microthermometry and Raman spectroscopy

The microthermometric data are provided as part of the data publication of Grema *et al.* (2024b) and summarized in Table 4-2. Two types of fluid inclusions in sphalerite and quartz were identified at room temperature. The first type comprises two-phase aqueous-carbonic (L_{aq}-V_{carb}) inclusions. Raman analyses show that, except for one FIA, all FIAs in sphalerite contain CO_2(±N_2) in the vapor bubbles (Fig. 4-10). The H_2O-CO_2 inclusions are ubiquitous in Sp-IIa_{banded} and Sp-$IIc_{sector\text{-}zoned}$, exhibiting consistent liquid-to-vapor ratios within individual FIAs. The second type comprised three-phase aqueous+liquid-carbonic+liquid-vapor (Laq-Lcarb-Vcarb) inclusions in sphalerite and quartz crystals.

Duo Lake Formation: Fluid inclusion assemblages were analyzed within Sp-$IIc_{sector\text{-}zoned}$ and Qz-III crystals in veins hosting ore-stage II mineralization, particularly in drillhole NB20-009. The Sp-$IIc_{sector\text{-}zoned}$ inclusions were exclusively secondary and generally displayed triangular-shaped inclusions in trails terminating at the boundaries of the sphalerite crystal bands. These secondary inclusions, consisting of L_{aq}-V_{carb} with CO_2(±N_2) vapor bubble, had high salinities ranging from 21 to 22 wt.% NaCl equiv. and low $T_{h(tot)}$ between 143 and 157 °C. No $T_{m(CO_2)}$ or $T_{m(clath)}$ measured.

Primary fluid inclusions were only measurable in Qz-III (Fig. 4-11), which is in textural equilibrium with Sp-$IId_{pale\text{-}yellow}$. These inclusions, formed in the growth zones of quartz crystals, often appeared cloudy with multiple layers of FIAs (not shown). All were three-phase (L_{aq}-L_{carb}-V_{carb}) inclusions, spherical or irregularly shaped, and up to 35 μm in size, with CO_2(N_2-CH_4)-rich vapor bubbles. The $T_{m(CO_2)}$ and $T_{h(CO_2)}$ values range from -56.9 to -56.8°C and 23.5 to 24.2°C, respectively, that homogenized to the liquid phase. The $T_{m(clath)}$ values are between 9.2 and 9.9 °C. The inclusions had low salinities between 4 and 6 wt.% NaCl equiv. ($T_{m(ice)}$= -3.9 to -2.1 °C) and moderate to high $T_{h(tot)}$ values ranging from 206 to 258 °C.

Niddery Lake Member (Portrait Lake Formation): Samples were obtained from drill holes NB20-007, NB20-004, and NB20-009. These samples were taken from massive pyrite intervals and comprised Sp-$IIc_{sector\text{-}zoned}$ and Qz-III. The Sp-$IIc_{sector\text{-}zoned}$ crystals have two sector-zoned dark red and red banding patterns that may suggest two subgenerations (Fig. 4-8b). These zones, potentially indicating distinct stages of sphalerite growth, have an unclear paragenetic relationship. In both subgenerations, primary FIAs occur in clusters or form in growth zones within the dark red bands and align parallel to the growth zones in the red bands. These type II inclusions (L_{aq}-V_{carb} with CO_2±N_2) occasionally preserve hydrocarbon-characteristic peaks as determined by Raman spectroscopy.

The melting temperature of solid CO_2 ($T_{m(CO_2)}$) and homogenization temperature of CO_2 ($T_{h(CO_2)}$) in the three-phase L_{aq}-L_{carb}-V_{carb} Sp-IIc$_{sector\text{-}zoned}$ fluid inclusions were measured only in this member, ranging from -58.2 to -56.9°C and from 26.0 to 27.1°C, respectively. $T_{m(clath)}$ temperatures are between 8.2 to 9.8 °C. The inclusions homogenize to the liquid phase and preserve low salinities of 4 – 9 wt.% (NaCl equiv.) and moderate-high $T_{h(tot)}$ of 168 – 249 °C. Two three-phase secondary FIAs occur with salinity of 14 – 16 wt.% NaCl equiv. and $T_{h(tot)}$ of 149 – 167 °C from the NB20-004 drill hole and another from the NB20-007 drill hole with salinity of 21 – 22 wt.% NaCl equiv. with $T_{h(tot)}$ of 159 – 171 °C.

In Qz-III, primary fluid inclusions of the L_{aq}-L_{carb}-V_{carb} type comprise vapor bubbles with CO_2 ±N_2-CH_4-H_2S and are notable for containing H_2S. Two inclusions comprise $T_{m(CO_2)}$ values of -57.0 and -57.2 °C, whereas $T_{h(CO_2)}$ values include 28 and 28.1 °C, respectively, with homogenization to the liquid phase. The $T_{m(clath)}$ temperatures are between 9.5 to 9.8 °C. These inclusions have calculated salinity values between 4 – 8 wt.% NaCl equiv. and $T_{h(tot)}$ values between 207 – 233 °C, consistent with pseudosecondary FIA measurements from Qz-III, which show salinities of 5 – 6 wt.% NaCl equiv. and $T_{h(tot)}$ values of 231 – 234 °C.

Macmillan Pass Member (Portrait Lake Formation): Samples were collected from veins and breccias across four drill holes (NB19-001, NB19-002, NB20-002, and NB21-001). In these samples, Sp-IIa$_{banded}$, Sp-IIc$_{sector\text{-}zoned}$, and Qz-III contained primary and pseudosecondary fluid inclusions. Sp-IIa$_{banded}$ samples from drill holes NB29-002 and NB21-001 comprised massive sulfide veins within the conglomerate unit. Primary FIAs in Sp-IIa$_{banded}$ typically formed assemblages of triangular and elongated inclusions along distinct growth zones within the sphalerite crystals, ranging in size from <1 to 12 μm. These inclusions appeared in dark red and yellow bands under transmitted light, with clusters hosted in the dark bands but primarily arranged along closely spaced growth zones. Pseudosecondary FIAs in Sp-IIa$_{banded}$, often terminating near crystal boundaries, showed more size variation (<1 – 10 μm) than primary inclusions.

Table 4- 2: Summary statistics of the CO_2-rich sphalerite (Sp) and quartz (Qz) hosted fluid inclusion data. There is an uncertainty in the salinity calculations of ~3 wt.% NaCl equiv. Refer to section 4.4.5 for details on the salinity calculations. Min= minimum value, Max= maximum value, SD= standard deviation.

Formation	Member	Mineral	Mineral paragenesis	Fluid inclusion origin	Fluid inclusion	T_h (total) (°C)				Salinity (wt.% NaCl equiv.)			
					n=	min	max	median	SD	min	max	median	SD
Duo Lake		Quartz	Qz-III	Primary	8	206	258	232	25	4	6	5.6	0.9
		Sphalerite	Sp-IIc	Secondary	9	132	158	148	8	21	22	21.5	0.4
Portrait Lake	Macmillan Pass	Quartz	Qz-III	Primary	31	206	262	230	17	4	7	6.1	0.9
				Pseudosecondary	9	208	230	225	7	6	8	6.7	0.7
		Sphalerite	Sp-IIa	Primary	25	128	176	155	14	14	21	17.7	1.8
			Sp-IIc	Primary	10	150	200	170	12	5	8	6.5	0.8
				Secondary	7	168	179	174	4	21	23	21.9	0.6
			Sp-IId	Unknown	6	150	176	167	10	10	12	10.1	0.7
	Niddery Lake	Quartz	Qz-III	Primary	9	207	233	231	8	4	8	5.6	1.1
				Pseudosecondary	5	199	234	231	15	5	6	5.2	0.4
		Sphalerite	Sp-IIc	Primary	40	168	249	214	24	4	9	6.1	1.3
				Secondary	36	149	234	169	25	14	22	20.1	2.3

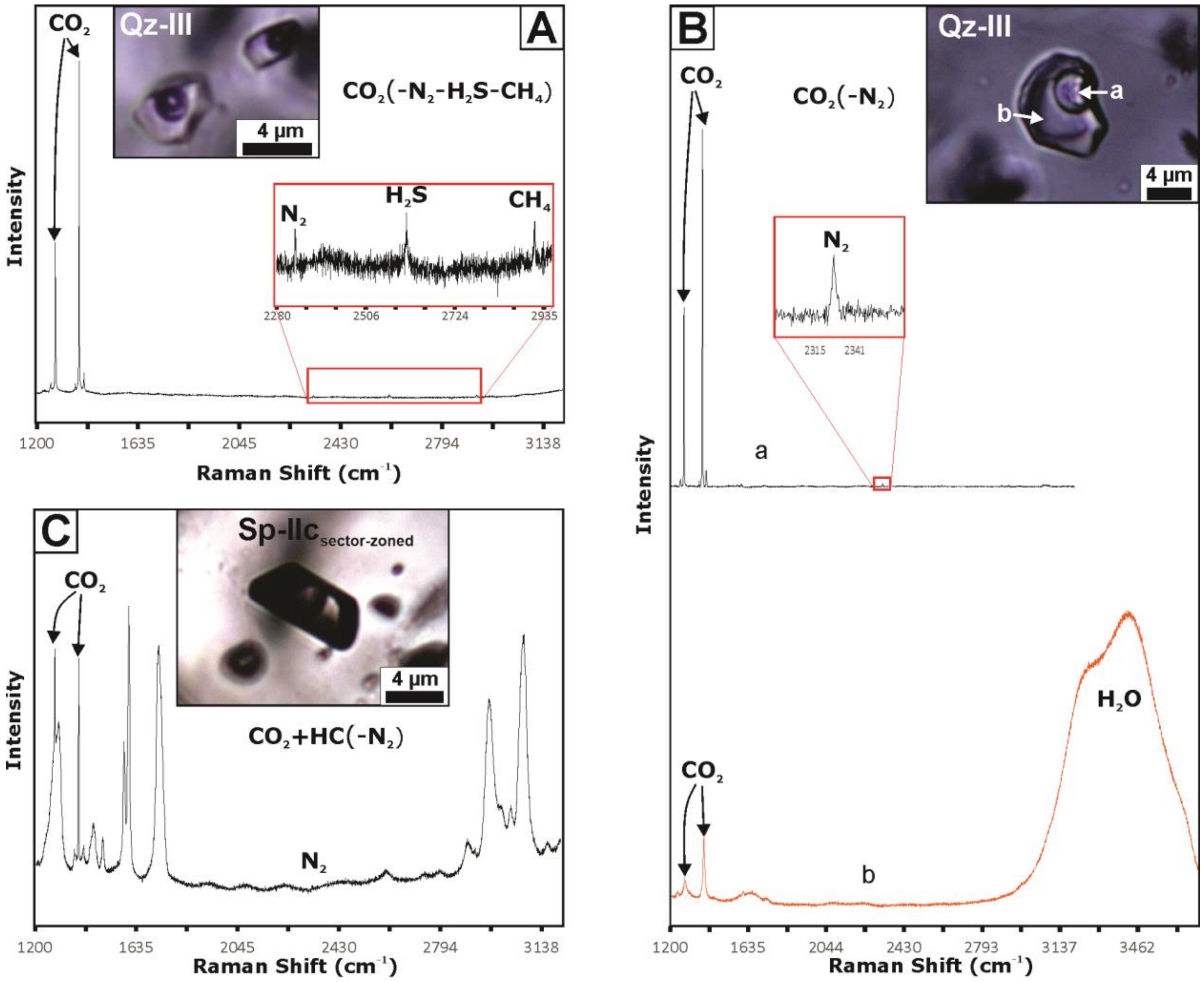

Fig. 4- 10: Raman spectra showing the different vapor and liquid inclusions composition. A) Raman spectrum of a vapor bubble in Qz-III showing $CO_2(N_2-H_2S-CH_4)$-bearing phase. B) Raman spectrum of vapor and liquid phases of an inclusion showing aqueous+liquidcarbonic+liquid-vapor (L_{aq}-L_{carb}-V_{carb}) inclusion with $CO_2(N_2)$ in Qz-III. C) Raman spectrum of hydrocarbon-bearing $CO_2(N_2)$ inclusion in Sp-IIc$_{sector-zoned}$.

Fluid inclusions in Sp-IIa$_{banded}$ have consistent vapor-to-liquid ratios, and all contain CO_2-bearing bubbles with very minor and variable amounts of N_2. Primary FIAs in Sp-IIa$_{banded}$, contain two-phase inclusions with $CO_2(\pm N_2)$-bearing bubbles, and salinity values ranging from 14 to 21 wt.% NaCl equiv. and $T_{h(tot)}$ between 128 and 176 °C. This contrasts with Sp-IIc$_{sector-zoned}$ overgrowths, where primary two-phase CO_2-N_2-bearing FIAs had lower salinities from 4 to 8 wt.% NaCl equiv. and $T_{h(tot)}$ between 137 and 200 °C. Secondary two-phase CO_2-N_2-bearing FIAs in Sp-IIc$_{sector-zoned}$ had salinities and $T_{h(tot)}$ of 21 to 23 wt.% NaCl equiv. and 168 to 179 °C, respectively. $T_{m(CO_2)}$ and $T_{m(clath)}$ temperatures were not measured.

Vein-hosted Qz-III crystals, coeval with siderite and Sp-IId$_{\text{pale-yellow}}$, preserved primary FIAs exclusively comprising $CO_2(\pm N_2 \pm CH_4)$-bearing two- and three-phase inclusions. The $T_{m(CO_2)}$ and $T_{h(CO_2)}$ values are in the ranges -57.9 to -56.8°C and 26.4 to 29.2°C (homogenizing to liquid phase), respectively, with $T_{m(clath)}$ temperatures between 8.3 to 9.7 °C. Estimated salinities in Qz-III ranged from 4 to 7 wt.% NaCl equiv. with $T_{h(tot)}$ of 207 to 262 °C. These values aligned with two-phase pseudosecondary FIAs of Qz-III, having salinities from 6 to 8 wt.% NaCl equiv. and $T_{h(tot)}$ values between 208 and 230 °C.

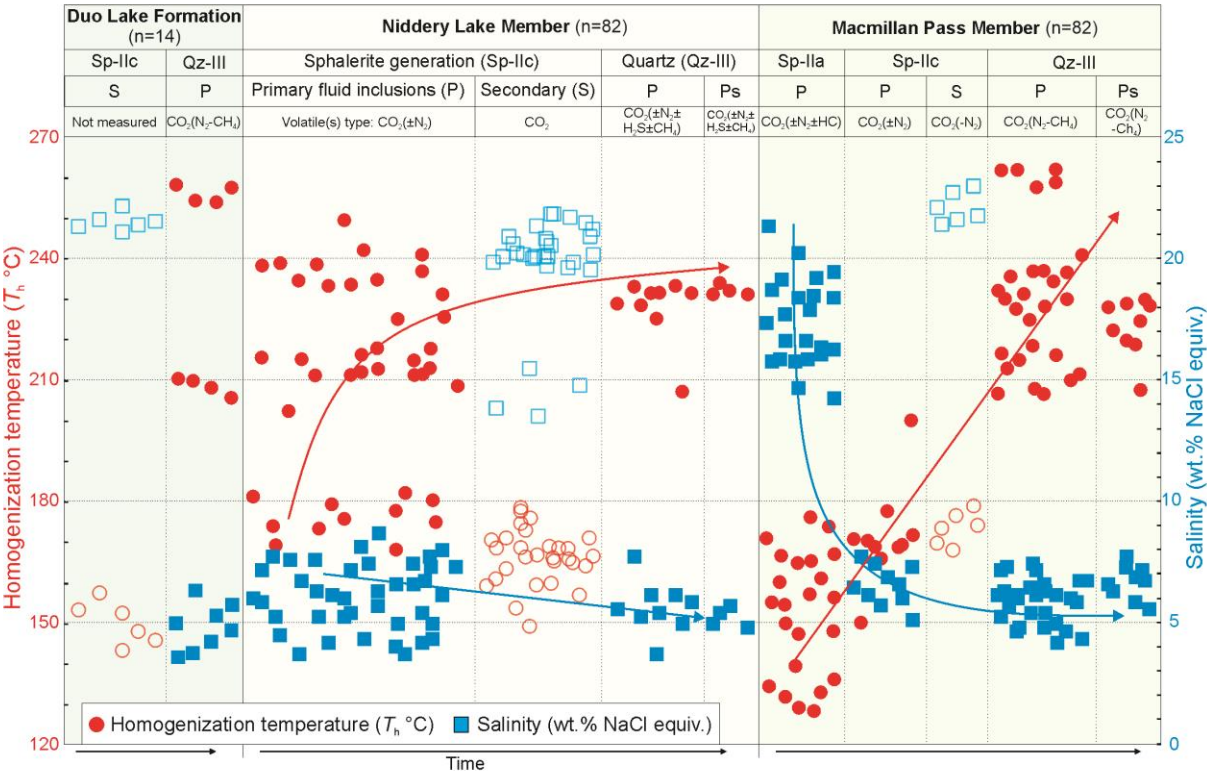

Fig. 4- 11: Plot of $T_{h(tot)}$ and salinity. All inclusions are CO_2-bearing. There is an uncertainty in the salinity calculations of +3 wt.% NaCl equiv. The data are separated by the fluid inclusion origin, host mineral phase, generations, and stratigraphic location in the Boundary Zone.

4.6. Discussion

4.6.1. The nature of fluid inclusion data in sphalerite and quartz at Boundary Zone

The fluid inclusions examined in this study are all obtained from sphalerite and quartz of ore-stage II (Figs. 4-2, 4-3). Microthermometric analysis and Raman spectroscopy of FIAs hosted in ore-stage II sphalerite and quartz show consistent $CO_2(\pm N_2 \pm CH_4 \pm H_2S)$ in the vapor bubbles of two-phase and three-phase fluid inclusions (Fig. 4-10) with variable T_h and salinity values (Fig. 4-11). The possibility that post-entrapment events may have impacted the integrity of the fluid inclusions, e.g., due to heating-induced partial leakage, must be assessed. It has been suggested that post-entrapment alteration of fluid inclusion properties is primarily a function of the host mineral strength and the sizes of the individual fluid inclusions (Wilkinson, 2010, and references therein). The lack of apparent covariation between $T_{h(tot)}$ and fluid inclusion sizes in sphalerite and quartz from the Boundary Zone indicates the absence of re-equilibration. Additionally, the $T_{h(tot)}$ values within the FIA are consistent, and variation exists between FIAs across the sphalerite generations (Fig 4-11), suggesting a general lack of post-entrapment modification. Furthermore, sphalerite and quartz-hosted fluid inclusions have been indicated to resist re-equilibration due to heating as a result of the relative strength of the minerals compared to others, e.g., calcite and barite (Wilkinson, 2010). In addition, at the Macmillan Pass district, the isotopic ($\delta^{13}C$ and $\delta^{18}O$) analyses of ankerite coeval with the Zn-Pb sulfide mineralization, the mineralogical assemblages, and preservation of host rock textures all indicate a lack of metamorphic or tectonic resetting (Magnall *et al.*, 2016a). Therefore, we consider that the fluids trapped within the primary and pseudosecondary inclusions in the sphalerite and quartz within the veins and breccias indeed preserved the original fluid properties during entrapment.

4.6.2. Homogenization temperatures and composition of fluids trapped in primary and pseudosecondary inclusions

Laser Raman spectroscopy analyses of vapor bubbles in the sphalerite generations and Qz-III reveal compositions dominated by CO_2 and accompanied by minor and variable N_2, H_2S, and CH_4. The pervasive presence of CO_2 in the two- and three-phase aqueous-carbonic fluid inclusions (Fig. 4-10) in both sphalerite and quartz indicates that the stage II ore-forming fluids were volatile-rich. The extensive siderite formation in the ore-stage II suggests the presence of CO_3-bearing fluids that could indicate high concentrations of CO_2. The minor concentrations of CH_4 and H_2S in fluid inclusions hosted by the Niddery Lake Member could be explained by organic matter degradation, CO_2 reduction, or thermogenic cracking processes (Hanor, 1980; Boetius *et al.*, 2000; Jørgensen & Kasten, 2006). An earlier study on the gas composition of fluid inclusions in quartz from feeder zone samples of the Tom and Jason deposits indicated minor H_2S, with the N_2 and CH_4 concentrations averaging 0.618 and 0.206 mol.%, respectively (Magnall *et al.*, 2016b); these components were suggested to have been released by organic matter thermal degradation (Magnall *et al.*, 2020c).

The salinity and $T_{h(tot)}$ data from FIAs hosted in ore-stage II sphalerite and Qz-III define two distinct fluids: (i) a high-salinity (14 to 21 wt.% NaCl equiv.), moderate $T_{h(tot)}$ (128 to 176 °C), $CO_2(\pm N_2)$ fluid preserved by the Sp-IIa$_{\text{banded}}$ FIAs, which is exclusively found in samples from the Macmillan Pass Member of the Portrait Lake Formation; and (ii) a low salinity (4 – 9 wt.% NaCl equiv.), moderate to high $T_{h(tot)}$ (168 – 262 °C), $CO_2(\pm N_2 \pm CH_4 \pm H_2S)$ bearing fluid characterized by FIAs in Sp-IIc$_{\text{sector-zoned}}$ and Qz-III, present in both the Duo Lake and Portrait Lake Formations. The high salinities observed in the Sp-IIa$_{\text{banded}}$ fluid inclusions far exceed that of seawater (3.5 wt.% NaCl equiv.). It has been suggested that saline hydrothermal fluids in sedimentary basins acquire salinity from evaporated seawater or through interactions with halite-bearing rock units (Cooke *et al.*, 2000). The absence of evaporite units in the Macmillan Pass district suggests that the high salinities in the Boundary Zone samples could ultimately be derived from evaporated seawater. Such highly saline fluids would remain unmodified as a result of buffering from interaction with volatiles (e.g., CO_2) that were released during fluid migration (e.g., Peng *et al.*, 2023). Salinity would have been important for ensuring that base metals were soluble as chloride complexes in reduced acidic brines (Tornos & Heinrich, 2008). The indication that the mineralizing fluid was reduced ($\Sigma SO_4 < \Sigma H_2S$) is supported by the presence of significant pyrobitumen in the mineralized veins and breccias despite the predominance of CO_2 as the carbon species in the fluid inclusions.

No measurable primary FIA was observed in sphalerite from the Duo Lake Formation. In the Niddery Lake Member of the Portrait Lake Formation, the median salinity and $T_{h(tot)}$ values in Sp-IIc$_{\text{sector-zoned}}$ primary FIAs are 6 wt.% NaCl equiv. and 214 °C, respectively. Similar low salinities (median= 7 wt.% NaCl equiv.) with median $T_{h(tot)}$ of 170 °C are preserved in Sp-IIc$_{\text{sector-zoned}}$ primary FIAs in the Macmillan Pass Member. The precipitation of Sp-IIc$_{\text{sector-zoned}}$ signals a second pulse of hydrothermal fluid with low salinity and moderate to high $T_{h(tot)}$ that is different from that associated with the earlier Sp-IIa$_{\text{banded}}$ in the veins and breccias during ore-stage II (Fig. 4-11). The textural banding and rhythmic oscillatory zoning in the Sp-IIc$_{\text{sector-zoned}}$ crystals are suggested to result from either self-organized non-equilibrium processes (Benedetto *et al.*, 2005) or changes in physicochemical conditions (Cook *et al.*, 2009). The similarities between fluid inclusions in Sp-IIc$_{\text{sector-zoned}}$ and those from Qz-III suggest similar fluids were responsible for the Sp-IIc$_{\text{sector-zoned}}$ and Sp-IId$_{\text{pale-yellow}}$ formation.

4.6.3. Minor and trace element distribution and substitution mechanisms in sphalerite

The chemistry of sphalerite in Zn-Pb deposits is influenced by a range of factors, including the temperature and composition (fS_2, pH, Eh) of the ore-forming fluids and contributions from host rock alteration (Cooke *et al.*, 2000; Cook *et al.*, 2009; Ye *et al.*, 2011; Wei *et al.*, 2018). Some of these factors are reflected in the results of the PCA for Boundary Zone sphalerite, which describes covariation between different groups of elements. The angle between the arrows in the PCA relates to the covariance of the elements in the overall dataset; where two elements are described by orthogonal arrows, they are uncorrelated, whereas if the angle between two elements is either close to 0° or 180°, they are positively or negatively correlated. Notably, there is a cluster of elements that are similar irrespective of ore stage or host rock, which are described by negative PC1 values (Cu, Ag, In, Ge, Sn, As, Sb, and Pb). The elements described by PC2 (Fe, Mn, and Hg) appear to show systematic variability between host units, suggesting they are related to fluid-rock interaction between units of differing composition.

The PC1 elements comprise mainly monovalent (Cu^{+}, Ag^{+}), trivalent (Sb^{3+}, Ga^{3+}, In^{3+}), and tetravalent (Sn^{4+}, Ge^{4+}) cations that have positive correlations with each other in ore stages I and II (Figs. 4-7, 4-12; an exception is noted in the correlation of Ge vs Cu in Sp-IId$_{\text{pale-yellow}}$) The positive correlation of Ge and Cu is a common feature in sphalerite (Cook *et al.*, 2009; Belissont *et al.*, 2014; Belissont *et al.*, 2016; Cugerone *et al.*, 2021). It has been suggested that coupled substitution involving monovalent cations, like Cu, facilitates Ge incorporation in the sphalerite lattice (Ye *et al.*, 2011; Belissont *et al.*, 2014; Cugerone *et al.*, 2020) via the reaction $Ge^{4+} + 2Cu^{+} \leftrightarrow 3Zn^{2+}$. However, a (Ga+Ge)/Cu ratio >1 in these samples (not shown) suggests significant enrichment of Ga and Ge relative to Cu, potentially involving vacancy-based incorporation Ge^{4+} + vacancy $\leftrightarrow 2Zn^{2+}$ or $2Ga^{3+}$ + vacancy $\leftrightarrow 3Zn^{2+}$ (Bonnet *et al.*, 2016). Sp-IId$_{\text{pale-yellow}}$ exhibits potential coupled substitution of monovalent cations with both tri- and tetravalent cations, e.g., $Ge^{4+} + 2Ag^{+} \leftrightarrow 3Zn^{2+}$ (Luo *et al.*, 2022). Indium concentrations in all sphalerite generations are low and, due to its proximity and correlation with Cu in the PCA, may have been incorporated via $In^{3+} + Cu^{+} \leftrightarrow 2Zn^{2+}$ (Cook *et al.*, 2009).

Iron, Mn, and Hg in PC2 could have been variably incorporated into sphalerite. The correlation between Fe and Mn (Fig. 4-7a) in the Duo Lake Formation could suggest coupled substitution for Zn^{2+} similar to Fe-Hg covariation in Macmillan Pass Member. Together with Cd, these elements are also known to directly substitute for Zn^{2+} (Benedetto *et al.*, 2005; Cook *et al.*, 2009; Ye *et al.*, 2011; Bonnet *et al.*, 2016). However, significant variations in the concentration of these minor and trace elements have been observed in Boundary Zone sphalerite, including within single sphalerite crystals (Fig. 4-5), across different sphalerite generations (Fig. 4-6), and in sphalerite from different strata (Table 4-1).

Systematic variability in Fe and Mn concentrations exists between different host units, whereas a general consistency in Fe and Mn concentrations is observed between the different sphalerite generations (Fig. 4-6). This would suggest that the host rock exerts a strong control on the Fe and Mn content of sphalerite. An exception to this pattern is observed as Fe and Mn concentrations decrease from Sp-IIa$_{\text{banded}}$ to Sp-IId$_{\text{pale-yellow}}$ within the Macmillan Pass Member vein and breccias. Iron displays a strong negative correlation with Mn and Hg in ore-stage II (Fig. 4-7b), whereas these elements positively correlate in ore-stage I (albeit weakly with regard to Hg). These varied correlations suggest potential competition between these elements (e.g., $Fe^{2+} \leftrightarrow Mn^{2+}$ or Hg^{2+}) during substitution due to size or charge balance considerations (Cook *et al.*, 2009). For instance, the negative correlation could be linked to redox conditions during mineralization, when Mn would be more stable and can substitute for Zn^{2+} in oxidizing environments, and Fe^{2+} might oxidize to Fe^{3+} (Robb, 2005), inhibiting its incorporation into sphalerite. Despite these correlations, direct substitutions, including $Mn^{2+} \leftrightarrow Zn^{2+}$, $Fe^{2+} \leftrightarrow Zn^{2+}$, $Cd^{2+} \leftrightarrow Zn^{2+}$, and $Hg^{2+} \leftrightarrow Zn^{2+}$ (Cook *et al.*, 2009) are expected for these elements in the Boundary Zone sphalerite. The Fe/Cd ratio that is up to 12 (Grema *et al.*, 2024b) implies a dominance of Zn substitution by Fe (Bonnet *et al.*, 2016), potentially accounting for the generally low Cd concentrations in the sphalerite generations.

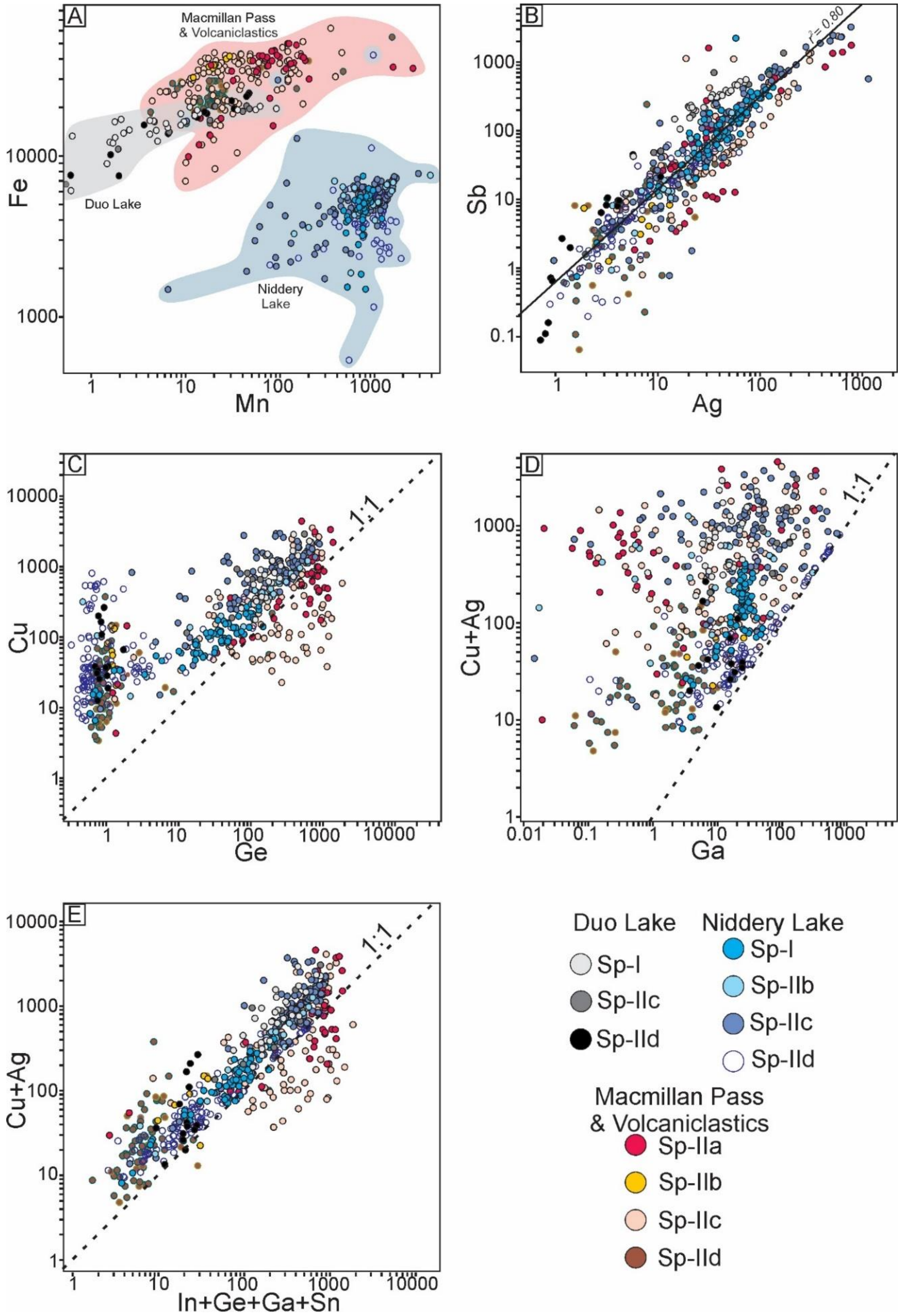

Fig. 4- 12: Element and element ratios biplots of Mn vs. Fe (A), Ag vs. Sb (B), Ge vs. Cu (C), Ga vs. Cu+Ag (D), and In+Ge+Ga+Sn vs. Cu+Ag (E). All the elements are plotted in ppm.

4.6.4. Potential sources of Ge, Ga, and Hg in sphalerite

Germanium and Ga may have been scavenged from siliciclastic and carbonaceous rocks of the Road River and Earn Groups or deeper within the Neoproterozoic stratigraphy. The comparable ionic radii of Ge^{4+} and Si^{4+} and those of Ga^{3+} and Al^{3+} allow for isomorphous substitution and possible enrichment in aluminosilicate-bearing rocks that could be leached by hydrothermal fluid infiltration (Höll *et al.*, 2007; Etschmann *et al.*, 2017). Alternatively, these elements could have been mobilized locally via the dissolution of aluminosilicate minerals during the formation of stylolites and foliations. Germanium is known to also adsorb onto organo-complexes (Höll *et al.*, 2007), form sulfate complexes, and bond to coal and lignite (Bernstein, 1985). This further supports local sourcing for the metals from the underlying siliceous and carbonaceous units. The incorporation of these elements in sphalerite (e.g., $\text{Sp-IIc}_{\text{sector-zoned}}$; Fig. 4-5g-h, k-l) could be reflected in the compositionally distinct sphalerite bands (Beaudoin, 2000; Pfaff *et al.*, 2011; Bonnet *et al.*, 2016).

Sphalerite can incorporate up to 41 wt.% Hg (Tauson & Abramovich, 1981); however, concentrations in CD-type deposits have been reported to occur <0.5 wt.% (Schwartz, 1997; Emsbo *et al.*, 2016 and references therein). Mercury in clastic rocks has been suggested to be derived from leaching of organic matter where microbial activities (e.g., sulfate reduction) fix HgS^0 or methylmercury in the sediments (Hein *et al.*, 2007; Steele *et al.*, 2009). The other important sources of Hg are submarine hydrothermal activity and volcanic eruptions (Pyle & Mather, 2003; Grasby *et al.*, 2019). The source of Hg in CD-type deposits is debated. It has been suggested that high Hg concentrations are related to local factors and that Hg is enriched in the host rocks prior to ore formation (e.g., Ryall, 1981). The Hg in sphalerite from CD-type deposits is commonly higher in Proterozoic strata than in Phanerozoic occurrences (Schwartz, 1997). Schwartz (1997) further suggested that the Hg from sphalerite in Phanerozoic strata results from fluid-rock interaction during mineralization.

Locally in the Selwyn Basin, elevated Hg concentrations have been reported in CD-type mineralized strata of the Middle to Late Devonian Portrait Lake Formation in the Macmillan Pass district (Goodfellow & Rhodes, 1990) and the Late Ordovician to Early Silurian Duo Lake Formation of the Howard's Pass district (Goodfellow *et al.*, 1983). Goodfellow *et al.* (1983) observed a decrease in the whole rock concentration of Hg in the host rocks with increasing distance from the mineralization at the Howard's Pass district and suggested that Hg enrichment is related to the mineralizing fluids. In the Boundary Zone, the Hg in sphalerite from different strata and generations overlap, with concentrations in the Duo Lake Formation and Niddery

Lake Member generally higher than those in the Macmillan Pass Member (except for Sp-IIb$_{\text{metallic-brown}}$ in Macmillan Pass Member). The occurrence of interbedded volcaniclastic units and the anomalously high Hg concentrations in sphalerite hosted in both the Duo Lake and Portrait Lake Formations suggest these rocks could be metal sources. Indeed, globally extensive volcanism is known to have produced anomalous Hg concentrations in Late Ordovician (Gong *et al.*, 2017; Jones *et al.*, 2017) and Late Devonian marine sedimentary rocks (Racki *et al.*, 2018; Rakociński *et al.*, 2021; Zhang *et al.*, 2021), coincident with major global mass extinction events (Raup & Sepkoski Jr, 1982; Stanley, 2016).

4.6.5. Trace element geothermometry

Fluid inclusion microthermometry provides evidence of $T_{\text{h(tot)}}$ variability across the sphalerite paragenesis. For example, the $T_{\text{h(tot)}}$ values from the Sp-IIa$_{\text{banded}}$ and Sp-IIc$_{\text{sector-zoned}}$ fluid inclusions indicate that $T_{\text{h(tot)}}$ increased from 128 to 262 °C extending to the higher $T_{\text{h(tot)}}$ Qz-III inclusions coeval with the Sp-IId$_{\text{pale-yellow}}$. However, the lack of microthermometry data for certain sphalerite generations (e.g., Sp-I$_{\text{stratabound}}$ and Sp-IIb$_{\text{metallic-brown}}$) underscores the importance of developing other temperature constraints. The GGIMFis geothermometer (Frenzel *et al.*, 2016) was used to calculate the temperatures (T_{cal}) of all of the sphalerite generations. Importantly, the T_{cal} yielded results broadly consistent with the measured $T_{\text{h(tot)}}$ from fluid inclusions in both sphalerite and quartz (Fig. 4-13).

The ore-stage I Sp-I$_{\text{stratabound}}$ predates the later ore-stage II vein and breccia-hosted mineralization at the Boundary Zone, where a clear crosscutting relationship between the two ore stages is observed (Figs. 4-3a, 4-5f). Chapter 3 showed that the ore stage I sulfides formed via subseafloor replacement of radiolarian- and barite-rich beds in siliceous and carbonaceous mudstones. The initial ore-forming fluids are responsible for the precipitation of Sp-I$_{\text{stratabound}}$, along with the associated sulfide and gangue mineral assemblages (Fig. 4-2). The estimated temperature for ore-stage I Sp-I$_{\text{stratabound}}$ in the Duo Lake Formation suggests formation T_{cal} ranging from 116 to 165 °C (mean = 144 °C). Similar, albeit slightly higher, T_{cal} ranging from 148 to 209 °C (mean = 178 °C) are recorded by Sp-I$_{\text{stratabound}}$ in the Niddery Lake Member. These comparable T_{cal} across the two stratigraphic intervals indicate that the sulfide mineralization occurred under similar physicochemical conditions.

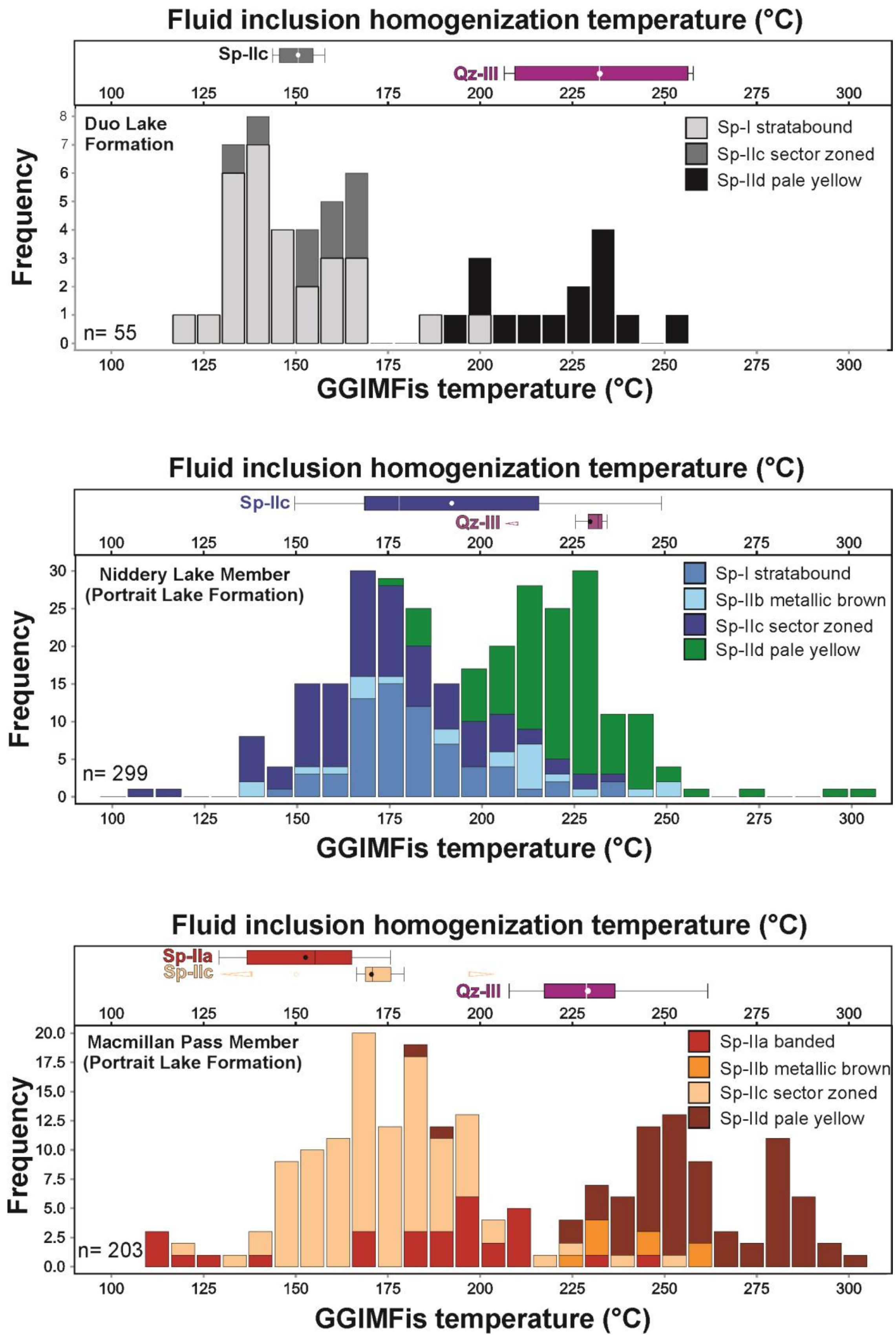

Fig. 4- 13: Summary box and whisker and histogram plots of both measured $T_{h(tot)}$ (horizontal) and GGIMFis estimated temperatures, T_{cal} (vertical).

The estimated formation temperature of Sp-IIa$_{\text{banded}}$ is different from Sp-IIb$_{\text{metallic-brown,}}$ where T$_{\text{(cal)}}$ is relatively high in both the Niddery Lake (190 °C) and Macmillan Pass (241 °C) Members. The Sp-IIb$_{\text{metallic-brown}}$ occurs exclusively in the massive pyrite zone coeval with fine-grained euhedral pyrite. Textural evidence suggests Sp-IIb$_{\text{metallic-brown}}$ formed via the replacement of massive pyrite and precipitated with fine-grained pyrite (Fig. 4-3j) resulting from a dissolution-reprecipitation reaction that may have been mediated by the mineralizing fluid (Altree-Williams *et al.*, 2015).

4.6.6. The Boundary Zone Zn-Pb±Ag deposit model

The Zn-Pb±Ag mineralization at the Boundary Zone formed in two genetically distinct ore-forming stages and is hosted by units of the Late Ordovician-Early Silurian Duo Lake and the Middle-Late Devonian Portrait Lake Formations (Chapter 3). The crosscutting relationships between the ore stages I and II (Chapter 3) indicate distinct fluid flow regimes and multiple mineralizing events at the Boundary Zone. The significant fine-grained stratabound sulfide mineralization that constitutes the ore-stage I is interpreted to have formed during diagenesis of the highly biosiliceous mudstones (up to 85 wt.% quartz; Chapter 3). The sulfides replaced the rock components, specifically opaline silica, during biogenic silica transformation in early diagenesis (Gao *et al.*, 2022). Sulfide formation is also significant in barite layers, with by-products such as barian mica forming locally. A vein that crosscut the ore-stage I contains fluorapatite with a Middle Jurassic age (169±10 Ma), constraining the stratabound mineralization to an earlier period of hydrothermal activity. The similarities in the ore-stage I stratabound mineralization textures and sulfide precipitation mechanism in the biosiliceous units of the Duo Lake and Portrait Lake Formations suggest a similar syn-diagenetic timing of mineralization at different times. The development of the metal trap for the ore stage I mineralization in the Late Devonian Niddery Lake Member occurred in the pre-ore environment. This process has been shown to be a regional feature involving reduced sulfur generation during early diagenetic processes related to the anaerobic oxidation of methane (Magnall *et al.*, 2016a; Fernandes *et al.*, 2017; Johnson *et al.*, 2018; Grema *et al.*, 2022).

The ore-stage I mineralization formed from a fluid with a broadly similar estimated temperature. The overlapping Sp-I$_{\text{stratabound}}$ GGIMFis geothermometry (T$_{\text{cal}}$) formation temperatures (~144 °C in Duo Lake and ~178 °C in Niddery Lake) further support this conclusion and confirm that the stratabound mineralization formed from a similar temperature. In essence, the ore-stage I likely formed from a moderate-temperature fluids that interacted with multiple stratigraphic levels in the Macmillan Pass in the late Paleozoic during the burial diagenesis of the host units. These fluid-rock interactions resulted in texturally and paragenetically similar Sp-$I_{stratabound}$ mineralization in the Duo Lake and Portrait Lake Formations. The style of ore stage I mineralization at the Boundary Zone is consistent with the CD-type subseafloor replacement model (Williams, 1978a, 1978b; Gadd *et al.*, 2017; Magnall *et al.*, 2020c; Reynolds *et al.*, 2021) and provides another example of stratabound mineralization which has formed along favorable stratigraphic horizons as host units undergo diagenesis at different times (this study; Chapter 3).

The volumetrically major ore-stage II vein and breccia sulfides have the highest grades, and sulfide mineralization was accompanied by pervasive siderite formation and silicification (Chapter 3). This mineralization stage formed after the ore-stage I and involved hydrothermal fluid-induced brecciation and veining of the Duo Lake and Portrait Lake Formations. The deformation and mineralization likely coincided with the regional Cordilleran orogenic events (~Jurassic to Cretaceous) in the Macmillan Pass region (Abbott, 1982; McClay, 1991; Mair *et al.*, 2006). The timing of the ore-stage II mineralization is supported by petrographic and mineralogical observations (Chapter 3) and by the brittle nature of the rocks, breccias, and stylolite formation.

The second pulse of mineralization that formed the vein and breccia ore-stage II occurred at higher $T_{h(tot)}$ (Figs. 4-11, 4-13) with more CO_2-rich fluids, leading to widespread siderite alteration. The multiple generations of sphalerite and total sulfide volume indicate these fluids brought in significant Zn into the system, with a mineralization style that is completely different from the stratabound ore stage I. The differences in sphalerite chemistry reflect fluid migration through the different host rocks, and local variations depending on the stratigraphic unit and the lithologies encountered could impact the trace element concentration. Specifically, it is likely that the host rock controlled elemental variation observed in ore stage II sphalerite; Figure 4-6 suggests that Fe and Mn, and to a lesser extent Hg, Cd, Ni, and Ga (defined by PC2; Fig. 4-7) were incorporated locally from the host rocks, rather than from the hydrothermal fluids. The physical and chemical composition of the fluids are also ideal for metal transport. Mineralizing fluids with $T_{h(tot)}$ of ~150 °C and >15 wt.% NaCl equiv. salinity, trapped in the Sp-IIa_{banded} fluid inclusions and those with relatively higher $T_{h(tot)}$ (~250°C) and low salinities (<10 wt.% NaCl equiv.) in Sp-$IIc_{sector\text{-}zoned}$ could potentially transport high concentrations of base metals in reduced fluids (Cooke *et al.*, 2000).

The occurrence of the two ore stages in the Duo Lake and Portrait Lake Formations, comparable fluid temperatures, and sphalerite trace element compositions suggest similar fluid flow pathways. The upward-migrating hydrothermal fluids likely utilized the same conduit during both mineralization stages. This implies that the sulfide mineralization at the Boundary Zone formed likely through the repeated reactivation of nearby deeply seated structure(s). These structures are likely in the form of (syn)sedimentary extensional normal faults in the Macmillan Pass (Abbott, 1982; Abbott & Turner, 1990) that were likely reactivated as thrusts during orogeny.

In summary, the Boundary Zone Zn-Pb±Ag system with the two distinct ore-forming stages and mineralization occurrence in two broad stratigraphic intervals represent the reactivation of deep-seated structures located adjacent to the Boundary Zone. The fluid salinity and $T_{\mathrm{h(tot)}}$ preserved in the fluid inclusions coupled with the sphalerite chemistry suggest that mixing contrasting fluid types, including a CO_2-rich hydrothermal fluid and a reduced sulfur-rich fluid, was likely the primary ore precipitation mechanism at the Boundary Zone. This is consistent with the CD-type formation model that suggests fluid cooling, boiling, mixing, or a combination of some of these processes as the primary mechanisms driving mineralization (Wilkinson, 2001). The metal sources could be located deeper in the stratigraphy, including units of the underlying Neoproterozoic strata. The mineralizing fluids likely utilized the extensional fault system as a fluid flow pathway.

4.6.7. Comparison to other similar CD-type Zn-Pb deposits globally

The geologic setting, host rock lithostratigraphy, ore body morphology, mineralization style, and mineralogical composition (Chapter 3) suggest the sulfide mineralization at Boundary Zone is another epigenetic CD-type Zn-Pb occurrence in the Macmillan Pass district. The Macmillan Pass district already contains the well-described Tom and Jason deposits. These deposits have similar replacement style stratabound mineralization in biosiliceous and barite-rich units of the Portrait Lake Formation (c.f. ore-stage II at Boundary Zone). Notably, mineralization in the underlying Duo Lake Formation has not been intercepted at either Tom or Jason. Vein and breccia style mineralization has also been described at the Tom and Jason deposits, although in contrast to Boundary Zone, it forms a feeder zone to the overlying stratabound mineralization. The fluid inclusion salinities and $T_{\mathrm{h(tot)}}$ from the Boundary Zone (Fig. 4-11) overlap with those from the Tom (<150 °C; 3.5 - 12.5 wt.% NaCl equiv.; Ansdell *et al.*, 1989) and Jason (~250 °C; 9 wt.% NaCl equiv.; Gardner & Hutcheon, 1985) deposits suggesting similar mineralizing fluid conditions. The temperature of the hydrothermal fluids entering the feeder zone of the Tom and Jason deposits ranges from ~275 to 300 °C (Magnall *et al.*, 2016b). Similarly, hot fluids at the Boundary Zone suggest that fluids may have been tapped from a similar source at different stages of basin evolution.

Beyond the Selwyn Basin, the Red Dog district deposits (Kuna Basin), and the Zn-Pb deposits of the Zarigan-Chahmir, Tiran, and Arak Basins (Iran) represent some of the other locations with well-preserved CD-type deposits in Phanerozoic rocks (Yaghubpur & Mehrabi, 1997; Ayuso *et al.*, 2004; Kelley *et al.*, 2004; Rajabi *et al.*, 2015a; Mahmoodi *et al.*, 2018). Microthermometric studies on these deposits provide important mineralizing fluid constraints for the mineral system, and the results are comparable to the data at the Boundary Zone. For example, the high salinity values observed in the Sp-IIa$_{\text{banded}}$ fluid inclusions are comparable to salinities from vein sphalerite at the Red Dog Zn-Pb-Ag district that are interpreted to have originated as reflux brines (Leach *et al.*, 2004). The trace element compositional variation observed in the Boundary Zone sphalerite generations is similar to the occurrence in the Red Dog district (Kelley *et al.*, 2004) and CD-type deposits elsewhere (Cook *et al.*, 2009 and references therein). For instance, the high Hg concentrations incorporated in the Boundary Zone sphalerite (Table 4-1) and the up to 3,650 ppm Hg (Kelley *et al.*, 2004) in sphalerite from the Red Dog district indicate that conditions during CD-type mineralization favor the accumulation of this element.

CD-type mineralization in the Arak Basin (northern Malayer-Esfahan metallogenic belt, Iran) comprises several Zn-Pb orebodies hosted in Jurassic units (Momenzadeh, 1976). Fluid inclusions from sphalerite, quartz, and siderite exhibit of mean salinities and $T_{h(tot)}$ of 5.8 wt.% NaCl equiv. (4 to 11.1 wt.% NaCl equiv.) and 208 °C (105 to 309 °C), respectively (Mahmoodi *et al.*, 2018). Quartz-hosted fluid inclusions from the Zarigan-Chahmir Basin (Central Iran) preserve fluid inclusions with 170 to 226 °C $T_{h(tot)}$, and salinity is 4.2 to 12.7 wt.% NaCl equiv. (Rajabi *et al.*, 2015b). Yarmohammadi *et al.* (2016) recorded salinities ranging between 4.4 to 6.3 wt.% NaCl equiv. and $T_{h(tot)}$ from 157 to 284 °C from fluid inclusions hosted in sphalerite, quartz, calcite, and dolomite in the Tiran Basin (southern Malayer-Esfahan metallogenic belt, Iran). All three CD-type occurrences in the Arak, Zarigan-Chahmir, and Tiran Basins are suggested to have formed via fluid mixing with salinity derived from seawater (Rajabi *et al.*, 2015b; Yarmohammadi *et al.*, 2016; Mahmoodi *et al.*, 2018). In all cases, (syn)sedimentary faults are regarded to have acted as pathways during hydrothermal fluid migration. The fluid inclusions' salinities and temperature values from the sphalerite and coeval gangue mineral assemblage are broadly consistent with microthermometric data from the Boundary Zone, where similar conclusions are also drawn.

4.6.8. Implications for Zn-Pb exploration in the Paleozoic strata of the Selwyn Basin

- The variable enrichment of Ge and Ga within different generations of sphalerite highlights the importance of constraining the deportment of these critical elements to specific paragenetic stages to better understand their origin and distribution. The Selwyn Basin could also be evaluated to determine whether economic levels of these elements occur.
- Ore stage 1 mineralization appears to have a common paragenesis and sphalerite composition in different stratigraphic units. Exploration programs targeting stratabound mineralization in Late Devonian units should also consider the prospectivity of older footwall units.
- The reactivation of key fault structures likely provided the permeability conduit for hot metal-bearing fluids and superimposed ore-forming events at different stages of basin evolution, ultimately resulting in greater metal endowment. This suggests that similar fault structures in the Selwyn Basin should be evaluated to determine their potential to serve as metalliferous fluid conduits.

4.7. Conclusions

The combined investigation of sphalerite chemistry and fluid inclusions contained in quartz and sphalerite has provided valuable constraints on the ore fluids that formed the Boundary Zone Zn-Pb±Ag CD-type deposit in the Macmillan Pass district. Five different sphalerite generations formed in two distinct ore-forming events in the Late Ordovician-Early Silurian Duo Lake and Middle to Late Devonian Portrait Lake Formations. Collectively, the measured fluid inclusion homogenization temperatures and sphalerite trace element geothermometry (GGIMFis) provide minimum trapping temperature constraints across the full paragenesis at the Boundary Zone deposit. Ore-stage I Sp-I$_{\text{stratabound}}$ formed when hydrothermal fluid with moderate homogenization temperature (~144 °C in Duo Lake and ~178 °C in Niddery Lake) mixed with reducing porefluids; the enrichment of Hg is tentatively linked with local volcanic activity. Fluid inclusions hosted in sphalerite and quartz indicate the involvement of at least two different fluids for the ore-stage II vein and breccia sulfides with contrasting salinity and homogenization temperatures and resultant sphalerite chemistry. The Sp-IIa$_{\text{banded}}$ of the ore-stage II formed from hydrothermal fluid with relatively low homogenization temperature and high salinity fluid and had the highest concentrations of Cu, Ge, and Tl. The lack of evaporite-bearing units in the Selwyn Basin indicates that the elevated salinities were likely the result of seawater evaporation rather than evaporite dissolution. The Sp-IIb$_{\text{metallic-brown}}$ and Sp-IIc$_{\text{sector-zoned}}$ precipitated from fluids with moderate to high homogenization temperature and low salinity. The precipitation of the volumetrically minor Sp-IId$_{\text{pale-yellow}}$, which is coeval with the late Qz-III, resulted from the dissolution-reprecipitation of earlier sphalerite. Importantly, the fluid inclusion data encompass the range of results generated in other Phanerozoic CD-type deposits, including the nearby Tom and Jason deposits within the Macmillan Pass district, Selwyn Basin, the Red Dog district in Kuna Basin, and the Arak, Zarigan-Chahmir, and Tiran Basins. Overall, this study highlights the multiple mineralization events at the Boundary Zone that resulted from the mixing of hydrothermal fluids and reduced porefluids that also scavenged metals from volcaniclastics and other siliciclastic units of the Road River and Earn Groups. Understanding the mechanisms of the two-stage Zn-Pb±Ag mineralization at the Boundary Zone deposit allows for rare insights into the $T_{\text{h(tot)}}$ and salinity constraints of CD-type mineral systems and critical element distributions with wide implications for the exploration of these deposits.

4.8. Acknowledgments

We are grateful to Fireweed Metals Corp. for providing drill core samples for this study. We sincerely appreciate Uwe Dittmann (thick and thin section preparations) and Franziska H. Wilke (EPMA) for their technical support during data generation. We also thank Volker Lüders for discussions during the conceptualization of the project.

4.9. Funding Information

Funding for this research was provided by the Helmholtz Recruitment Initiative grant to Sarah Gleeson, the Petroleum Technology Development Fund (PTDF), and the German Academic Exchange Service (DAAD) through co-financed funding (Nr. 57473408) to Haruna Grema.

CHAPTER 5

Conclusions and Future Research Outlook

5.1. Conclusions

The primary focus of this thesis was to produce a comprehensive, multifaceted investigation of samples from the Late Devonian Canol Formation of the Selwyn Basin and the newly discovered Boundary Zone deposit in the Macmillan Pass district, Yukon, Canada. This includes the pre-mineralization, ore stage, and post-mineralization processes associated with the clastic-dominated (CD-type) Zn-Pb metallogenesis at the Boundary Zone. The data generated on these samples provided valuable insights on some of the key questions surrounding the formation of these deposits, including i) what role did diagenesis play in the development of a metal trap? ii) What was the paragenesis and mechanism of ore formation and associated mineralogical alteration? iii) What were the physicochemical conditions of the mineralizing fluids and the controls on the geochemistry of sphalerite? This chapter summarizes the key findings from Chapters 2, 3, and 4 within the context of these research questions. While focusing on distinct aspects of the CD-type mineral system, each chapter contributed crucial insights that enhance our understanding of the paleoenvironment, ore genesis, and mineralizing fluid evolution, which collectively have implications for mineral exploration in the Selwyn Basin and increase our understanding of CD-type systems worldwide.

5.1.1. Reconstructing the diagenetic sulfur cycle in the Late Devonian Selwyn Basin

The local sulfur cycle is suggested to play a crucial role in the development of metal traps in CD-type deposit host rocks, where reduced sulfur is considered to have been derived from seawater sulfate (Leach *et al.*, 2005b; Leach *et al.*, 2010; Wilkinson, 2014; Williams, 2023). Barite-rich mudstone units can provide a potential source of sulfur for the metal trap and have been identified in multiple regions of CD-type mineralization (Turner, 1986; Edgerton, 1997; Johnson *et al.*, 2004; Kelley *et al.*, 2004). In the Selwyn Basin (Fig. 2-1a), temporal and sometimes spatial relationships exist between stratiform barite and CD-type sulfides in units that host the mineralization (e.g., Carne, 1979; McClay, 1984; Bailes *et al.*, 1986). There has been debate on the origin of the sulfide and barite formation; particularly whether they are formed in the water column on either side of an oxic-anoxic (sulfidic) redox boundary (Goodfellow & Jonasson, 1984; Goodfellow & Lydon, 2007) or during diagenetic processes (e.g., Magnall *et al.*, 2016a; Reynolds *et al.*, 2021).

The isotopic composition of coeval sulfide- and sulfate-bearing minerals (e.g., barite and pyrite) can provide an important record of the biogeochemical and thermochemical processes (Bottrell & Newton, 2006; Fike *et al.*, 2015; Pasquier *et al.*, 2021, and references therein) and were used to constrain the nature of the sulfur cycle in this study. High-resolution petrography and sulfur isotope microanalysis showed that stratiform barite and pyrite formed in two distinct paragenetic stages in the unmineralized Late Devonian Canol Formation during early diagenesis (Chapter 2). The first stage is characterized by the precipitation of microcrystalline barite and framboidal pyrite, with negative $\delta^{34}S_{Pyrite}$ values indicating microbial sulfate reduction (MSR) under open-system conditions. The textures and isotopic values of authigenic barite and sub- to euhedral pyrite from the second stage are consistent with formation under more restricted (anoxic), sulfate-limited conditions where sulfate resupply << sulfate reduction in the sediment column (Fig. 2-15). This sulfate-limited condition developed via progressive sulfate reduction coupled to anaerobic oxidation of methane (SR-AOM) at the sulfate-methane transition zone (SMTZ).

The stratiform barite-pyrite assemblage observed in the Canol Formation mudstones is comparable both in texture and isotopic values to a similar assemblage described in regionally correlative units at Tom and Jason deposits of the Macmillan Pass district, which was later overprinted by hydrothermal sulfides during CD-type mineralization in the Selwyn Basin (Magnall *et al.*, 2016a). Generally, the observation in the Late Devonian strata of the Selwyn Basin and other Lower Paleozoic basins (Maynard & Okita, 1991; Koski & Hein, 2003; Xu *et al.*, 2016) implies such diagenetic processes are a more general feature in Lower Paleozoic basins specifically on highly productive continental margins.

5.1.2. Paragenesis of sulfide mineralization in the Duo Lake and Portrait Lake Formations at the Boundary Zone

Detailed petrographic and mineralogical studies indicate that the Zn-Pb±Ag mineralization in the Late Ordovician-Early Silurian Duo Lake Formation and the Middle-Late Devonian Portrait Lake Formation at the Boundary Zone deposit formed in two stages (Chapter 3). The ore-stage I sulfides in the Duo Lake Formation and the Middle Devonian Niddery Lake Member of the Portrait Lake Formation occur primarily as stratabound mineralization comprising mainly sphalerite, pyrite, galena ± sulfosalts. The gangue assemblage is dominated by quartz in both units, with fluorapatite common in the Duo Lake Formation, while barian-mica occurs with the sulfides in the Niddery Lake Member. The mineralization in both units formed primarily via the replacement of opaline silica within the mudstones. Furthermore, pre-mineralization pyrite was overprinted by ore-stage sulfides in both units. Barite replacement by sulfides in the Niddery Lake Member was also observed. The similarities in host rock replacement style, ore textures, and comparable mineralogical assemblages suggest that the stratabound mineralization formed epigenetically in both units.

The stratabound mineralization are crosscut by the second ore stage that comprises four generations of sphalerite with galena, pyrite, and minor chalcopyrite, which suggests multiple pulses of hydrothermal fluids and metal precipitation (Chapter 3). This assemblage occurs in the Duo Lake and Portrait Lake Formations and represents the volumetrically significant ore stage. The ore-stage II is mostly hosted in veins and breccias that formed due to fluid-induced fracturing that exploited preexisting weaknesses within the host rock, as these structures often preserve stylolitic margins (Fig. 3-11a inset) that suggest the opening of stylolites during these fluid events.

In certain CD-type districts (Macmillan Pass), vein and breccia sulfide mineralization have been described in the footwall below the stratiform/stratabound sulfides and are considered feeder zones for the ore-forming fluids (Carne, 1979; Turner, 1986; Ansdell *et al.*, 1989; Goodfellow, 2004). In contrast, the vein and breccia hosted mineralization at Boundary Zone clearly crosscut and post-date the stratabound mineralization, suggesting a spatial but not temporal relationship (Chapter 3). In order to determine the absolute age(s) of these events, U-Pb geochronology using fluorapatite from the ore stages was conducted, albeit with limited success due to low U mass fractions and high non-radiogenic Pb concentrations. However, fluorapatite in a vein that crosscut ore-stage I gave a Middle Jurassic age that is earlier than the thrusting and folding event in the Late Jurassic–Early Cretaceous that affected strata in the Macmillan Pass region (Abbott, 1982; McClay, 1991). Although the relationship between the ore-stage II mineralization and the dated fluorapatite is unknown, the formation of the vein and breccia sulfides following the folding and faulting of the Duo Lake and Portrait Lake Formations suggest mineralization likely formed associated with a significant deformation event. The Cordilleran orogeny that occurred during the Jurassic may have likely coincided with the vein formation, suggesting that ore-stage II mineralization occurred contemporaneously and after the accretionary events (Mair *et al.*, 2006).

In summary, the textural relationship between the sulfides and the Duo Lake and Portrait Lake Formations, coupled with U-Pb dating, suggests that the Zn-Pb±Ag Boundary Zone mineralization formed epigenetically over a protracted duration. This interval spans from the diagenetic period when the replacive stratabound mineralization formed in biosiliceous (and barite-rich) mudstones to the time of the Cordilleran orogeny when the formation of vein and breccia-hosted mineralization occurred.

5.1.3. Mineralizing fluid characteristics at the Boundary Zone deposit

The occurrence of $CO_2(\pm N_2 \pm CH_4 \pm H_2S)$-bearing fluid inclusions in the banded ($\text{Sp-IIa}_{\text{banded}}$) and sector-zoned ($\text{Sp-IIc}_{\text{sector-zoned}}$) sphalerite generations, as well as in late quartz, suggested hydrothermal fluids interaction with volatile-rich fluids either locally or during migration. Both sulfate reduction and methanogenesis in organic matter-rich mudstones can generate these gaseous components (e.g., Chapter 1) that could have been available during hydrothermal fluid flows. Furthermore, the occurrence of trails of pyrobitumen both within intergranular pores in the mudstones and within veins and breccias (Chapter 3) indicates the occurrence of liquid hydrocarbons during different stages of the mineralization. The abiotic reaction between sulfate and these hydrocarbons would produce CO_2 and H_2S that could act as reductants and trap during sulfide precipitation at temperatures above 100 °C (Machel, 2001).

Collectively, the fluid inclusion measured homogenization temperatures ($T_{\text{h(tot)}}$) and GGIMFis sphalerite geothermometry temperature (T_{cal}) suggest the ore-stage I stratabound sphalerite and coeval assemblage formed at a relatively lower temperature in the Duo Lake (mean T_{cal}= 144 °C) and Portrait Lake (178 °C) Formations compared to the vein and breccia hosted sphalerite generations. The ore-stage II sphalerite formed from at least two fluid types with different salinities. Altogether, these T_{cal} and $T_{\text{h(tot)}}$ temperatures and salinity differences highlight that the different hydrothermal fluid pulses mixed with reduced sulfur-bearing fluids ultimately led to the precipitation of the sulfides.

The global volcanism during the Ordovician and Devonian periods released a significant amount of Hg into the Earth's environments (Gong *et al.*, 2017; Jones *et al.*, 2017; Racki *et al.*, 2018; Rakociński *et al.*, 2021; Zhang *et al.*, 2021). Mercury is an element that is known to accumulate in sphalerite (Tauson & Abramovich, 1981; Schwartz, 1997; Cook *et al.*, 2009). During sphalerite precipitation at the Boundary Zone, the incorporation of elements was primarily through direct (e.g., Hg) and coupled (e.g., Cu) substitution mechanisms for Zn in the crystal lattice as revealed by trace element analysis (Chapter 4). Certain metals, including Ge and Ga, occur in high concentrations in sphalerite and are suggested to have been scavenged from host rocks as these metals could have been incorporated into aluminosilicate mineral phases or adsorbed onto organo-complexes prior to leaching during fluid-rock interactions (Bernstein, 1985; Höll *et al.*, 2007; Etschmann *et al.*, 2017). For Hg, this is suspected of having been sourced from the volcaniclastics interbedded within the mineralized strata. Overall, mixing metalliferous fluids with reduced sulfur-bearing porewater in the presence of reductants such as CO_2 over a prolonged period led to Zn-Pb±Ag sulfide mineralization at the Boundary Zone deposit.

5.1.4. Broader implications for pre-mineralization paleoenvironment reconstruction and CD-type Zn-Pb exploration in the Selwyn Basin

High-resolution petrography coupled with isotopic microanalysis indicates diagenetic precipitation of multiple generations of barite and pyrite in the Canol Formation during the Late Devonian. The observations are consistent with the recent understanding that in other locations, similar pre-mineralization assemblages formed during early diagenesis at the SMTZ (Johnson *et al.*, 2004; Magnall *et al.*, 2016a; Cansu & Öztürk, 2020; Reynolds *et al.*, 2021; Zhou *et al.*, 2022; Liu *et al.*, 2023) in contrast to the earlier suggestion that barite formed together with ore sulfides due to exhalation of Zn-Pb-Ba-bearing hydrothermal fluids into stratified water column. Furthermore, petrographic observations in Chapter 2 and by Fernandes *et al.* (2017) clearly show that witherite, cymrite, and hyalophane replaced barite crystals during early diagenesis, and are not part of early hydrothermal assemblages, as suggested by Goodfellow and Rhodes (1990).

The $\delta^{34}S$ and $\delta^{18}O$ values from barite in this study and from other locations in the Selwyn Basin (Goodfellow & Jonasson, 1984; Magnall *et al.*, 2016a) indicate the existence of localized isotopic variations across the basin. This difference is likely controlled by localized changes in TOC fluxes, sulfate concentrations, sulfate reduction rates, and methane diffusion rates that facilitate SR-AOM processes (Deusner *et al.*, 2014; Hill *et al.*, 2014; Lin *et al.*, 2016a; Lin *et al.*, 2016b; Sultan *et al.*, 2016). Some of these factors have been highlighted as key in multiple CD-type mineralized barite-rich Paleozoic mudstone units in North American sedimentary basins (e.g., Turner, 1986; Edgerton, 1997; Johnson *et al.*, 2004; Kelley *et al.*, 2004; Slack *et al.*, 2004a; Johnson *et al.*, 2015; Gadd *et al.*, 2017; Magnall *et al.*, 2020a).

A similar pre-mineralization barite-pyrite assemblage that occurs in barite-rich mudstones of the Late Devonian Canol Formation (Chapter 2) has been observed in the CD-type stratabound mineralized Middle Devonian Niddery Lake Member at the Boundary Zone (Chapter 3); where the assemblage is overgrown and replaced by ore-stage sulfides (pyrite). This is similar to observations at other CD-type deposits in the Macmillan Pass district and in comparable districts elsewhere in Lower Paleozoic basins (Magnall *et al.*, 2016a; Cansu & Öztürk, 2020;

Reynolds *et al.*, 2021; Zhou *et al.*, 2022; Liu *et al.*, 2023). It is generally accepted that the ore stage sulfides in these districts formed either concomitant with host mudstone deposition or during burial diagenesis (Goodfellow, 1987; Magnall *et al.*, 2020c), and as such, the age of the host rock formation is often regarded as that of the mineralization. However, stratabound and vein and breccia mineralization in the Late Ordovician-Early Silurian Duo Lake Formation and in the Middle Devonian Niddery Lake Member at the Boundary Zone deposit indicate i) stratabound mineralization in CD-type system could form even during advanced (late) stages of burial diagenesis as long as fault conduits with metal-bearing hydrothermal fluids intersect favorable host strata and ii) post-depositional tectonic deformation could facilitate significant ore formation in these units.

Thirdly, the preservation of vein and breccia-hosted mineralization in the faulted Duo Lake and Portrait Lake Formations provided an opportunity to evaluate some critical aspects of the CD-type system, specifically, effects of constraints such as homogenization temperature, salinity, and redox states on the solubilities and precipitation of base and critical metals, including Zn, Pb, Cu, Ge, and Ga (Bernstein, 1985; Hemley *et al.*, 1992; Cooke *et al.*, 2000). Fluid inclusion microthermometry on sphalerite of different generations (and quartz) from the Boundary Zone deposit indicates multiple fluid types with different temperatures and salinities are responsible for the texturally diverse sphalerite with often varying chemistry that forms in some of these CD-type deposits.

Finally, the findings in this thesis add to our understanding of the pre-mineralization paleoredox conditions as well as the timing, formation, and distribution of Zn-Pb±Ag mineralization of the CD-type mineral system that accounts for the majority of the Zn and Pb resources globally. This is especially important when the need for base and critical metals essential for decarbonization, high-tech society applications, and the green transition are in greater demand. For future exploration programs, it is worth evaluating time-equivalent strata of the Late Ordovician-Early Silurian Duo Lake Formation and the Middle to Late Devonian Portrait Lake Formation at other known mineralized districts in the Selwyn Basin based on findings highlighted in Chapters 2, 3, and 4. The multiple mineralizing events identified during this research, spanning diagenetic stages to possible tectonic deformation periods that formed in multiple stratigraphic levels, broaden the search space in similar geologic settings and the potential for undiscovered ore bodies in the footwall of other known comparable deposits for instance, the Gataga district in the Kechika Trough.

5.2. Future research outlook

Based on findings from this thesis, the following directions for future research are suggested:

- *In-situ* microscale isotopic analyses have demonstrated the variability of $\delta^{34}S_{pyrite}$, $\delta^{34}S_{barite}$ and $\delta^{18}O_{barite}$ values, highlighting the importance of such analytical approaches in paleoenvironmental reconstruction in unmineralized mudstones (e.g., Chapter 2). These approaches, which were also used at Tom and Jason deposits (Magnall *et al.*, 2016a), have focused mainly on Late Devonian strata. Understanding the paleoredox conditions prevalent during the Late Ordovician – Early Silurian period and the nature of the sulfur cycling in these mudstones is pertinent. Combined sulfur ($\delta^{34}S$) and carbon ($\delta^{18}C$) isotopic investigation of Duo Lake Formation from the Howard's Pass district has already indicated that positive $\delta^{34}S_{pyrite}$ values were generated via anaerobic oxidation of methane (Johnson *et al.*, 2018). This approach could be used to determine whether similar methane-driven processes were prevalent at the Boundary Zone.
- Chapter 3 explores the paragenesis and alteration mineralogy of the Boundary Zone deposit using petrographic and mineralogical (QXRD) techniques. The paragenesis and mineralogical observations in this thesis need to be followed up by a study on the whole rock lithogeochemistry to examine the geochemical footprints. Looking at whole rock lithogeochemical data would also help to compare the overall base, critical, and deleterious element budget and distribution in different generations of sphalerite.
- Chapters 3 and 4 represent the first studies on the Boundary Zone deposit. The samples utilized for this research represent only a tiny fraction of the mineralization and of the whole system. The ongoing exploration drilling programs in the area and the potential availability of new intersections provide opportunities for further work on this CD-type deposit. Specifically, understanding the hydrothermal fluid regimes and flow path(s) in the Macmillan Pass district by applying other isotopic tools, for instance, Zn, Hg, and (multiple) S. This approach is likely to reveal the sources of metals and feeder structures that serve as conduits.
- U-Pb geochronology using fluorapatite was attempted to date the different mineralization stages at the Boundary Zone, with limited success. Other dating approaches targeting mineral phases coeval with ore sulfide generations or using different techniques could be employed to obtain absolute ages of the mineralization. For example, Re-Os dating of pyrite has been successfully used to determine the age of the CD-type mineralization, for example, at the Howard's Pass district (Kelley *et al.*,

2017) and Red Dog district (Reynolds *et al.*, 2021). Utilizing this approach in the Boundary Zone could allow for the determination of the multiple mineralization ages, as pyrite is common in pre-mineralization, in the ore, and in post-mineralization stages.

- Vein and breccia (or stockwork) mineralization have not been identified in the Howard's Pass and Anvil districts (Morganti, 1979; Abbott & Turner, 1990; Pigage, 1991), with Morganti (1979) suggesting that this style of mineralization is absent within 10 km of the Howard's Pass district. The occurrence of vein and breccia-hosted mineralization in Duo Lake Formation strata at the Boundary zone, together with similarities in stratigraphy and tectonic overprint at both the Howard's Pass and the Macmillan Pass districts, favor evaluating the possible occurrence of vein and breccia style mineralized zones at the Howard's Pass. Furthermore, the occurrence of alkaline basalt and synsedimentary extensional faults in the Anvil district that have been suggested to be Middle Cambrian to Early Ordovician (Jennings & Jilson, 1986; Abbott & Turner, 1990) suggest a favorable geologic setting for at least evaluating the potentials of vein and breccia ore sulfide occurrence.

6

REFERENCES

Abbott, J. G. (1982). Structure and stratigraphy of the Macmillan fold belt: Evidence for Devonian faulting. In *Yukon Geology and Exploration 1981* (pp. 22–33). Whitehorse, Yukon: Department of Indian Affairs and Northern Development (Canada), Northern Affairs Program, Exploration and Geological Services Division.

Abbott, J. G., Gordey, S. P., Tempelman-Kluit, D. J., & Morin, J. (1986). Setting of stratiform, sediment-hosted lead-zinc deposits in Yukon and northeastern British Columbia. *Geological Survey of Canada Open File, 2169*, 69-98.

Abbott, J. G., & Turner, R. J. W. (1990). *Mineral Deposits of the Northern Canadian Cordillera, Yukon-Northeastern British Columbia* (Vol. 14): Energy, Mines and Resources Canada.

Abbott, J. G., & Turner, R. J. W. (1991). Character and paleotectonic setting of Devonian stratiform sediment hosted Zn, Pb, Ba deposits, Macmillan Fold Belt, Yukon. In J. G. Abbott & R. J. W. Turner (Eds.), *Mineral Deposits of the Northern Canadian Cordillera, Yukon–Northeastern British Columbia [Field Trip 14]* (Vol. Open File 2169, pp. 99-136): Geological Survey of Canada.

Abbott, J. G. (2013). Bedrock geology of the Macmillan Pass area Yukon and adjacent Northwest Territories (NTS 105O/1,2 and parts of 105O/7,8 and 105P/4,5). *Yukon Geological Survey Geoscience Map 2013-1*. Retrieved from https://data.geology.gov.yk.ca/Reference/68069#InfoTab

Abu-Mahfouz, I. S., Cartwright, J., Idiz, E., Hooker, J. N., & Robinson, S. A. (2020). Silica diagenesis promotes early primary hydrocarbon migration. *Geology, 48*(5), 483-487. DOI: https://doi.org/10.1130/G47023.1

Aharon, P., & Fu, B. (2000). Microbial sulfate reduction rates and sulfur and oxygen isotope fractionations at oil and gas seeps in deepwater Gulf of Mexico. *Geochimica et Cosmochimica Acta, 64*(2), 233-246. DOI: https://doi.org/10.1016/S0016-7037(99)00292-6

Algeo, T. J., Luo, G. M., Song, H. Y., Lyons, T. W., & Canfield, D. E. (2015). Reconstruction of secular variation in seawater sulfate concentrations. *Biogeosciences, 12*(7), 2131-2151. DOI: https://doi.org/10.5194/bg-12-2131-2015

Ali, S. H., Giurco, D., Arndt, N., Nickless, E., Brown, G., Demetriades, A., Durrheim, R., Enriquez, M. A., Kinnaird, J., & Littleboy, A. (2017). Mineral supply for sustainable development requires resource governance. *Nature, 543*(7645), 367-372. DOI: https://doi.org/10.1038/nature21359

Aller, R. C., Madrid, V., Chistoserdov, A., Aller, J. Y., & Heilbrun, C. (2010). Unsteady diagenetic processes and sulfur biogeochemistry in tropical deltaic muds: Implications for oceanic isotope cycles and the sedimentary record. *Geochimica et Cosmochimica Acta, 74*(16), 4671-4692. DOI: https://doi.org/10.1016/j.gca.2010.05.008

Aloisi, G., Wallmann, K., Bollwerk, S. M., Derkachev, A., Bohrmann, G., & Suess, E. (2004). The effect of dissolved barium on biogeochemical processes at cold seeps. *Geochimica et Cosmochimica Acta, 68*(8), 1735-1748. DOI: https://doi.org/10.1016/j.gca.2003.10.010

Altree-Williams, A., Pring, A., Ngothai, Y., & Brugger, J. (2015). Textural and compositional complexities resulting from coupled dissolution–reprecipitation reactions in geomaterials. *Earth-Science Reviews, 150*, 628-651. DOI: https://doi.org/10.1016/j.earscirev.2015.08.013

Ansdell, K. M., Nesbitt, B. E., & Longstaffe, F. J. (1989). A fluid inclusion and stable-isotope study of the Tom Ba-Pb-Zn deposit, Yukon Territory, Canada. *Economic Geology, 84*(4), 841-856. DOI: https://doi.org/10.2113/gsecongeo.84.4.841

Antler, G., Turchyn, A. V., Rennie, V., Herut, B., & Sivan, O. (2013). Coupled sulfur and oxygen isotope insight into bacterial sulfate reduction in the natural environment. *Geochimica et Cosmochimica Acta, 118*, 98-117. DOI: https://doi.org/10.1016/j.gca.2013.05.005

Antler, G., & Pellerin, A. (2018). A critical look at the combined use of sulfur and oxygen isotopes to study microbial metabolisms in methane-rich environments. *Frontiers in microbiology, 9*. DOI: https://doi.org/10.3389/fmicb.2018.00519

Aplin, A. C., & Macquaker, J. H. S. (2011). Mudstone diversity: Origin and implications for source, seal, and reservoir properties in petroleum systems. *AAPG Bulletin, 95*(12), 2031-2059. DOI: https://doi.org/10.1306/03281110162

Arning, E. T., Gaucher, E. C., van Berk, W., & Schulz, H.-M. (2015). Hydrogeochemical models locating sulfate-methane transition zone in marine sediments overlying black shales: A new tool to locate biogenic methane? *Marine and Petroleum Geology, 59*, 563-574. DOI: https://doi.org/10.1016/j.marpetgeo.2014.10.004

Ayuso, R. A., Kelley, K. D., Leach, D. L., Young, L. E., Slack, J. F., Wandless, J. F., Lyon, A. M., & Dillingham, J. L. (2004). Origin of the red dog Zn-Pb-Ag deposits, Brooks Range, Alaska: evidence from regional Pb and Sr isotope sources. *Economic Geology, 99*(7), 1533-1553. DOI: https://doi.org/10.2113/gsecongeo.99.7.1533

Bailes, R. J., Smee, B. W., Blackader, D. W., & Gardner, H. D. (1986). Geology of the Jason lead-zinc-silver deposits, Macmillan Pass, eastern Yukon. In J. A. Morin (Ed.), *Mineral Deposits of Northern Cordillera* (Vol. 37, pp. 87-99): The Canadian Institute of Mining and Metallurgy.

Barnes, R. O., & Goldberg, E. D. (1976). Methane production and consumption in anoxic marine sediments. *Geology, 4*(5), 297-300. DOI: https://doi.org/10.1130/0091-7613(1976)4<297:MPACIA>2.0.CO;2

Bauer, M. E., Burisch, M., Ostendorf, J., Krause, J., Frenzel, M., Seifert, T., & Gutzmer, J. (2019). Trace element geochemistry of sphalerite in contrasting hydrothermal fluid systems of the Freiberg district, Germany: insights from LA-ICP-MS analysis, near-infrared light microthermometry of sphalerite-hosted fluid inclusions, and sulfur isotope geochemistry. *Mineralium Deposita, 54*(2), 237-262. DOI: https://doi.org/10.1007/s00126-018-0850-0

Beaudoin, G. (2000). Acicular sphalerite enriched in Ag, Sb, and Cu embedded within color-banded sphalerite from the Kokanee Range, British Columbia, Canada. *The Canadian Mineralogist, 38*(6), 1387-1398. DOI: https://doi.org/10.2113/gscanmin.38.6.1387

Belissont, R., Boiron, M.-C., Luais, B., & Cathelineau, M. (2014). LA-ICP-MS analyses of minor and trace elements and bulk Ge isotopes in zoned Ge-rich sphalerites from the Noailhac–Saint-Salvy deposit (France): Insights into incorporation mechanisms and ore deposition processes. *Geochimica et Cosmochimica Acta, 126*, 518-540. DOI: https://doi.org/10.1016/j.gca.2013.10.052

Belissont, R., Munoz, M., Boiron, M.-C., Luais, B., & Mathon, O. (2016). Distribution and oxidation state of Ge, Cu and Fe in sphalerite by μ-XRF and K-edge μ-XANES: insights into Ge incorporation, partitioning and isotopic fractionation. *Geochimica et Cosmochimica Acta, 177*, 298-314. DOI: https://doi.org/10.1016/j.gca.2016.01.001

Belousova, E. A., Walters, S., Griffin, W. L., & O'Reilly, S. Y. (2001). Trace-element signatures of apatites in granitoids from the Mt Isa Inlier, northwestern Queensland. *Australian Journal of Earth Sciences, 48*(4), 603-619. DOI: https://doi.org/10.1046/j.1440-0952.2001.00879.x

Benedetto, R. D., Bernardini, G. P., Costagliola, P., Plant, D., & Vaughan, D. J. (2005). Compositional zoning in sphalerite crystals. *American Mineralogist, 90*(8-9), 1384-1392. DOI: https://doi.org/10.2138/am.2005.1754

Berner, R. A. (1984). Sedimentary pyrite formation: an update. *Geochimica et cosmochimica Acta, 48*(4), 605-615. DOI: https://doi.org/10.1016/0016-7037(84)90089-9

Berner, R. A., Ruttenberg, K. C., Ingall, E. D., & Rao, J.-L. (1993). The nature of phosphorus burial in modern marine sediments. In R. Wollast, F. T. Mackenzie, & L. Chou (Eds.), *Interactions of C, N, P and S biogeochemical cycles and global change* (Vol. 4, pp. 365-378). Springer Berlin Heidelberg: Springer.

Bernstein, L. R. (1985). Germanium geochemistry and mineralogy. *Geochimica et Cosmochimica Acta, 49*(11), 2409-2422. DOI: https://doi.org/10.1016/0016-7037(85)90241-8

Betts, P. G., Giles, D., & Lister, G. S. (2003). Tectonic Environment of Shale-Hosted Massive Sulfide Pb-Zn-Ag Deposits of Proterozoic Northeastern Australia. *Economic Geology, 98*(3), 557-576. DOI: https://doi.org/10.2113/gsecongeo.98.3.557

Biddle, S. K., LaGrange, M. T., Harris, B. S., Fiess, K., Terlaky, V., & Gingras, M. K. (2021). A fine detail physico-chemical depositional model for Devonian organic-rich mudstones: A petrographic study of the Hare Indian and Canol Formations, Central Mackenzie Valley, Northwest Territories. *Sedimentary Geology, 414*, 105838. DOI: https://doi.org/10.1016/j.sedgeo.2020.105838

Blusson, S. L. (1978). Regional geological setting of lead-zinc deposits in Selwyn Basin. *Yukon, Current Research, Part A, Geological Survey of Canada, Paper*. 77-80.

Bodnar, R. J., & Bethke, P. M. (1984). Systematics of stretching of fluid inclusions; I, Fluorite and sphalerite at 1 atmosphere confining pressure. *Economic Geology, 79*(1), 141-161. DOI: https://doi.org/10.2113/gsecongeo.79.1.141

Bodnar, R. J. (2003). Reequilibration of fluid inclusions. In I. Samson, A. Anderson, & D. Marshall (Eds.), *Fluid inclusions: Analysis and interpretation* (Vol. 32, pp. 213): Mineralogical Association of Canada.

Boetius, A., Ravenschlag, K., Schubert, C. J., Rickert, D., Widdel, F., Gieseke, A., Amann, R., Jørgensen, B. B., Witte, U., & Pfannkuche, O. (2000). A marine microbial consortium apparently mediating anaerobic oxidation of methane. *Nature, 407*(6804), 623-626. DOI: https://doi.org/10.1038/35036572

Bonnet, J., Mosser-Ruck, R., Caumon, M.-C., Rouer, O., Andre-Mayer, A.-S., Cauzid, J., & Peiffert, C. (2016). Trace element distribution (Cu, Ga, Ge, Cd, and Fe) in sphalerite from the Tennessee MVT deposits, USA, by combined EMPA, LA-ICP-MS, Raman Spectroscopy, and crystallography. *The Canadian Mineralogist, 54*(5), 1261-1284. DOI: https://doi.org/10.3749/canmin.1500104

Borowski, W. S., Rodriguez, N. M., Paull, C. K., & Ussler, W. (2013). Are ^{34}S-enriched authigenic sulfide minerals a proxy for elevated methane flux and gas hydrates in the geologic record? *Marine and Petroleum Geology, 43*, 381-395. DOI: https://doi.org/10.1016/j.marpetgeo.2012.12.009

Böttcher, M. E., Oelschläger, B., Höpner, T., Brumsack, H.-J., & Rullkötter, J. (1998). Sulfate reduction related to the early diagenetic degradation of organic matter and "black spot" formation in tidal sandflats of the German Wadden Sea (southern North Sea): stable isotope (^{13}C, ^{34}S, ^{18}O) and other geochemical results. *Organic Geochemistry, 29*(5-7), 1517-1530. DOI: https://doi.org/10.1016/S0146-6380(98)00124-7

Böttcher, M. E., Sievert, S. M., & Kuever, J. (1999). Fractionation of sulfur isotopes during dissimilatory reduction of sulfate by a thermophilic gram-negative bacterium at 60 C. *Archives of microbiology, 172*(2), 125-128. DOI: https://doi.org/10.1007/s002030050749

Bottrell, S. H., & Newton, R. J. (2006). Reconstruction of changes in global sulfur cycling from marine sulfate isotopes. *Earth-Science Reviews, 75*(1-4), 59-83. DOI: https://doi.org/10.1016/j.earscirev.2005.10.004

Brennan, S. T., Lowenstein, T. K., & Horita, J. (2004). Seawater chemistry and the advent of biocalcification. *Geology, 32*(6), 473-476. DOI: https://doi.org/10.1130/g20251.1

Brunner, B., & Bernasconi, S. M. (2005). A revised isotope fractionation model for dissimilatory sulfate reduction in sulfate reducing bacteria. *Geochimica et Cosmochimica Acta, 69*(20), 4759-4771. DOI: https://doi.org/10.1016/j.gca.2005.04.015

Brunner, B., Bernasconi, S. M., Kleikemper, J., & Schroth, M. H. (2005). A model for oxygen and sulfur isotope fractionation in sulfate during bacterial sulfate reduction processes. *Geochimica et Cosmochimica Acta, 69*(20), 4773-4785. DOI: https://doi.org/10.1016/j.gca.2005.04.017

Bryant, R. N., Jones, C., Raven, M. R., Gomes, M. L., Berelson, W. M., Bradley, A. S., & Fike, D. A. (2019). Sulfur isotope analysis of microcrystalline iron sulfides using secondary ion mass spectrometry imaging: Extracting local paleo-environmental information from modern and ancient sediments. *Rapid Communications in Mass Spectrometry, 33*(5), 491-502. DOI: https://doi.org/10.1002/rcm.8375

Bryant, R. N., Jones, C., Raven, M. R., Owens, J. D., & Fike, D. A. (2020). Shifting modes of iron sulfidization at the onset of OAE-2 drive regional shifts in pyrite δ^{34}S records. *Chemical Geology, 553*. DOI: https://doi.org/10.1016/j.chemgeo.2020.119808

Buggisch, W. (1991). The global Frasnian-Famennian» Kellwasser Event «. *Geologische Rundschau, 80*, 49-72. DOI: https://doi.org/10.1007/BF01828767

Burnham, C. W. (1997). Magmas and hydrothermal fluids. In H. L. Barnes (Ed.), *Geochemistry of hydrothermal ore deposits* (3rd ed. pp. 63-123). New York: John Wiley & Sons.

Busenberg, E., & Plummer, L. N. (1986). The solubility of $BaCO_3$(cr) (witherite) in CO_2-H_2O solutions between 0 and 90° C, evaluation of the association constants of $BaHCO_3$+ (aq) and $BaCO_3^0$ (aq) between 5 and 80° C, and a preliminary evaluation of the thermodynamic properties of Ba2+ (aq). *Geochimica et Cosmochimica Acta, 50*(10), 2225-2233. DOI: https://doi.org/10.1016/0016-7037(86)90077-3

Canet, C., Anadon, P., Gonzalez-Partida, E., Alfonso, P., Rajabi, A., Perez-Segura, E., & Alba-Aldave, L. A. (2014). Paleozoic bedded barite deposits from Sonora (NW Mexico): Evidence for a hydrocarbon seep environment of formation. *Ore Geology Reviews, 56*, 292-300. DOI: https://doi.org/10.1016/j.oregeorev.2013.06.009

Canfield, D. E. (2001a). Biogeochemistry of sulfur isotopes. *Stable Isotope Geochemistry, 43*(1), 607-636. DOI: https://doi.org/10.2138/gsrmg.43.1.607

Canfield, D. E. (2001b). Isotope fractionation by natural populations of sulfate-reducing bacteria. *Geochimica et Cosmochimica Acta, 65*(7), 1117-1124. DOI: https://doi.org/10.1016/S0016-7037(00)00584-6

Canfield, D. E., Farquhar, J., & Zerkle, A. L. (2010). High isotope fractionations during sulfate reduction in a low-sulfate euxinic ocean analog. *Geology, 38*(5), 415-418. DOI: https://doi.org/10.1130/G30723.1

Cansu, Z., & Öztürk, H. (2020). Formation and genesis of Paleozoic sediment-hosted barite deposits in Turkey. *Ore Geology Reviews, 125*, 103700. DOI: https://doi.org/10.1016/j.oregeorev.2020.103700

Carne, R. C. (1979). Geological setting and stratiform lead-zinc-barite mineralization, Tom Claims, Macmillan Pass, Yukon Territory, Canada. In *Open-File Report* (Vol. 4, pp. 30): Department of Indian and Northern Affairs.

Carne, R. C., & Cathro, R. J. (1982). Sedimentary-exhalative (Sedex) Zn-Pb-Ag Deposits, Northern Canadian Cordillera. *Canadian Institute of Mining Bulletin, 75*, 66-78. Retrieved from https://cir.nii.ac.jp/crid/1571698599004001920

Carter, S. C., Paytan, A., & Griffith, E. M. (2020). Toward an Improved Understanding of the Marine Barium Cycle and the Application of Marine Barite as a Paleoproductivity Proxy. *Minerals, 10*(5). DOI: https://doi.org/10.3390/min10050421

Cecile, M. P. (1982). The Lower Paleozoic Misty Creek Embayment, Selwyn Basin, Yukon and Northwest Territories. *Geological Survey of Canada, Bulletin 335*, 78. DOI: https://doi.org/10.4095/111346

Cecile, M. P., Shakur, M. A., & Krouse, H. R. (1983). The isotopic composition of western Canadian barites and the possible derivation of oceanic sulphate $\delta^{34}S$ and $\delta^{18}O$ age curves. *Canadian Journal of Earth Sciences, 20*(10), 1528-1535. DOI: https://doi.org/10.1139/e83-142

Cecile, M. P. (2000). *Geology of the northeastern Niddery Lake map area, east-central Yukon and adjacent Northwest Territories* (0660179504). Retrieved from https://ostrnrcan-dostrncan.canada.ca/handle/1845/184938

Chakhmouradian, A. R., Reguir, E. P., & Mitchell, R. H. (2002). Strontium-apatite: New occurrences, and the extent of Sr-for-Ca substitution in apatite-group minerals. *Canadian Mineralogist, 40*(1), 121-136. DOI: https://doi.org/10.2113/gscanmin.40.1.121

Chapman, L. H. (2004). Geology and mineralization styles of the George Fisher Zn-Pb-Ag deposit, Mount Isa, Australia. *Economic Geology, 99*(2), 233-255. DOI: https://doi.org/10.2113/gsecongeo.99.2.233

Chen, D. Z., Wang, J. G., Racki, G., Li, H., Wang, C. Y., Ma, X. P., & Whalen, M. T. (2013). Large sulphur isotopic perturbations and oceanic changes during the Frasnian-Famennian transition of the Late Devonian. *Journal of the Geological Society, 170*(3), 465-476. DOI: https://doi.org/10.1144/jgs2012-037

Clark, I. D., Ilin, D., Jackson, R. E., Jensen, M., Kennell, L., Mohammadzadeh, H., Poulain, A., Xing, Y. P., & Raven, K. G. (2015). Paleozoic-aged microbial methane in an Ordovician shale and carbonate aquiclude of the Michigan Basin, southwestern Ontario. *Organic Geochemistry, 83-84*, 118-126. DOI: https://doi.org/10.1016/j.orggeochem.2015.03.006

Claypool, G. E., Holser, W. T., Kaplan, I. R., Sakai, H., & Zak, I. (1980). The age curves of sulfur and oxygen isotopes in marine sulfate and their mutual interpretation. *Chemical geology, 28*, 199-260. DOI: https://doi.org/10.1016/0009-2541(80)90047-9

Cobbett, R. N., Colpron, M., Crowley, J. L., Cordey, F., Blodgett, R. B., & Orchard, M. J. (2020). Late Devonian magmatism and clastic deposition in the upper Earn Group (central Yukon, Canada) mark the transition from passive to active margin along western Laurentia. *Canadian Journal of Earth Sciences, 58*(5), 471-494. DOI: https://doi.org/10.1139/cjes-2020-0161

Cook, N. J., Ciobanu, C. L., Pring, A., Skinner, W., Shimizu, M., Danyushevsky, L., Saini-Eidukat, B., & Melcher, F. (2009). Trace and minor elements in sphalerite: A LA-ICPMS study. *Geochimica et Cosmochimica Acta, 73*(16), 4761-4791. DOI: https://doi.org/10.1016/j.gca.2009.05.045

Cooke, D. R., Bull, S. W., Donovan, S., & Rogers, J. R. (1998). K-metasomatism and base metal depletion in volcanic rocks from the McArthur Basin, Northern Territory; implications for base metal mineralization. *Economic Geology, 93*(8), 1237-1263. DOI: https://doi.org/10.2113/gsecongeo.93.8.1237

Cooke, D. R., Bull, S. W., Large, R. R., & McGoldrick, P. J. (2000). The importance of oxidized brines for the formation of Australian proterozoic stratiform sediment-hosted

Pb-Zn (sedex) deposits. *Economic Geology and the Bulletin of the Society of Economic Geologists, 95*(1), 1-17. DOI: https://doi.org/10.2113/gsecongeo.95.1.1

Cox, M. A., & Whitford-Stark, J. L. (1987). Stylolites in the Caballos Novaculite, west Texas. *Geology, 15*(5), 439-442. DOI: https://doi.org/10.1130/0091-7613(1987)15<439:SITCNW>2.0.CO;2

Crawford, M. L., & Hollister, L. S. (1986). Metamorphic fluids: the evidence from fluid inclusions. In *Fluid—Rock Interactions during Metamorphism* (pp. 1-35): Springer.

Cugerone, A., Cenki-Tok, B., Oliot, E., Muñoz, M., Barou, F., Motto-Ros, V., & Le Goff, E. (2020). Redistribution of germanium during dynamic recrystallization of sphalerite. *Geology, 48*(3), 236-241. DOI: https://doi.org/10.1130/G46791.1

Cugerone, A., Cenki-Tok, B., Munoz, M., Kouzmanov, K., Oliot, E., Motto-Ros, V., & Le Goff, E. (2021). Behavior of critical metals in metamorphosed Pb-Zn ore deposits: example from the Pyrenean Axial Zone. *Mineralium Deposita, 56*(4), 685-705. DOI: https://doi.org/10.1007/s00126-020-01000-9

Cui, H., Kitajima, K., Spicuzza, M. J., Fournelle, J. H., Denny, A., Ishida, A., Zhang, F. F., & Valley, J. W. (2018). Questioning the biogenicity of Neoproterozoic superheavy pyrite by SIMS. *American Mineralogist, 103*(9), 1362-1400. DOI: https://doi.org/10.2138/am-2018-6489

Deusner, C., Holler, T., Arnold, G. L., Bernasconi, S. M., Formolo, M. J., & Brunner, B. (2014). Sulfur and oxygen isotope fractionation during sulfate reduction coupled to anaerobic oxidation of methane is dependent on methane concentration. *Earth and Planetary Science Letters, 399*, 61-73. DOI: https://doi.org/10.1016/j.epsl.2014.04.047

Dickens, G. R., O'Neil, J. R., Rea, D. K., & Owen, R. M. (1995). Dissociation of oceanic methane hydrate as a cause of the carbon isotope excursion at the end of the Paleocene. *Paleoceanography, 10*(6), 965-971. DOI: https://doi.org/10.1029/95PA02087

Dickens, G. R. (2001). Sulfate profiles and barium fronts in sediment on the Blake Ridge: Present and past methane fluxes through a large gas hydrate reservoir. *Geochimica Et Cosmochimica Acta, 65*(4), 529-543. DOI: https://doi.org/10.1016/S0016-7037(00)00556-1

Doebelin, N., & Kleeberg, R. (2015). Profex: a graphical user interface for the Rietveld refinement program BGMN. *Journal of applied crystallography, 48*(5), 1573-1580. DOI: https://doi.org/10.1107/S1600576715014685

Drake, H., Whitehouse, M. J., Heim, C., Reiners, P. W., Tillberg, M., Hogmalm, K. J., Dopson, M., Broman, C., & Åström, M. E. (2018). Unprecedented 34S-enrichment of pyrite formed following microbial sulfate reduction in fractured crystalline rocks. *Geobiology, 16*(5), 556-574. DOI: https://doi.org/10.1111/gbi.12297

Dumoulin, J. A., Harris, A. G., Blome, C. D., & Young, L. E. (2004). Depositional Settings, Correlation, and Age of Carboniferous Rocks in the Western Brooks Range, Alaska. *Economic Geology, 99*(7), 1355-1384. DOI: https://doi.org/10.2113/gsecongeo.99.7.1355

Edgerton, D. (1997). Reconstruction of the Red Dog Zn–Pb–Ba orebody, Alaska: implications for the vent environment during the mineralizing event. *Canadian Journal of Earth Sciences, 34*(12), 1581-1602. DOI: https://doi.org/10.1139/e17-128

Egger, M., Riedinger, N., Mogollón, J. M., & Jørgensen, B. B. (2018). Global diffusive fluxes of methane in marine sediments. *Nature Geoscience, 11*(6), 421-425. DOI: https://doi.org/10.1038/s41561-018-0122-8

Emsbo, P., Seal, R. R., Breit, G. N., Diehl, S. F., & Shah, A. K. (2016). *Sedimentary exhalative (sedex) zinc-lead-silver deposit model* (2328-0328). Retrieved from https://doi.org/10.3133/sir20105070N

Etschmann, B., Liu, W., Li, K., Dai, S., Reith, F., Falconer, D., Kerr, G., Paterson, D., Howard, D., & Kappen, P. (2017). Enrichment of germanium and associated arsenic and tungsten in coal and roll-front uranium deposits. *Chemical Geology, 463*, 29-49. DOI: https://doi.org/10.1016/j.chemgeo.2017.05.006

European Commission. (2023). *Study on the critical raw materials for the EU 2023 – Final report*. Retrieved from https://op.europa.eu/en/publication-detail/-/publication/57318397-fdd4-11ed-a05c-01aa75ed71a1

Falkner, K. K., Klinkhammer, G. P., Bowers, T. S., Todd, J. F., Lewis, B. L., Landing, W. M., & Edmond, J. M. (1993). The Behavior of Barium in Anoxic Marine Waters. *Geochimica Et Cosmochimica Acta, 57*(3), 537-554. DOI: https://doi.org/10.1016/0016-7037(93)90366-5

Farquhar, J., Wu, N. P., Canfield, D. E., & Oduro, H. (2010). Connections between Sulfur Cycle Evolution, Sulfur Isotopes, Sediments, and Base Metal Sulfide Deposits. *Economic Geology, 105*(3), 509-533. DOI: https://doi.org/10.2113/gsecongeo.105.3.509

Feng, D., Peng, Y., Bao, H., Peckmann, J., Roberts, H. H., & Chen, D. (2016). A carbonate-based proxy for sulfate-driven anaerobic oxidation of methane. *Geology, 44*(12), 999-1002. DOI: https://doi.org/10.1130/G38233.1

Fernandes, N. A. (2011). *Geology and Geochemistry of Late Devonian-Mississipian Sediment-Hosted Barite Sequences of the Selwyn Basin, NWT and Yukon, Canada.* (Master Of Science). University of Alberta, Edmonton, Alberta. Retrieved from https://doi.org/10.7939/R3F94H

Fernandes, N. A., Gleeson, S. A., Magnall, J. M., Creaser, R. A., Martel, E., Fischer, B. J., & Sharp, R. (2017). The origin of Late Devonian (Frasnian) stratiform and stratabound mudstone-hosted barite in the Selwyn Basin, Northwest Territories, Canada. *Marine and Petroleum Geology, 85*, 1-15. DOI: https://doi.org/10.1016/j.marpetgeo.2017.04.006

Fike, D. A., Bradley, A. S., & Rose, C. V. (2015). Rethinking the Ancient Sulfur Cycle. *Annual Review of Earth and Planetary Sciences, Vol 43, 43*(1), 593-622. DOI: https://doi.org/10.1146/annurev-earth-060313-054802

Fireweed Metals Corporation. (2018). *NI 43-101 Technical Report on the Macmillan Pass Zinc-Lead-Silver Project, Watson Lake & Mayo Mining Districts, Yukon Territory, Canada* (Retrieved from https://www.sedarplus.ca/csaparty/records/document.html?id=ae0cc3f232bf7f57382580749fff2ed8d50d46c04509eac9b8bfae5b24fd08dc).

Folk, R. L., & Pittman, J. S. (1971). Length-slow chalcedony; a new testament for vanished evaporites. *Journal of sedimentary research, 41*(4), 1045-1058. DOI: https://doi.org/10.1306/74D723F1-2B21-11D7-8648000102C1865D

Fraser, T. A., & Hutchison, M. P. (2017). Lithogeochemical characterization of the Middle-Upper Devonian Road River Group and Canol and Imperial formations on Trail River, east Richardson Mountains, Yukon: age constraints and a depositional model for fine-grained strata in the Lower Paleozoic Richardson trough. *Canadian Journal of Earth Sciences, 54*(7), 731-765. DOI: https://doi.org/10.1139/cjes-2016-0216

Fraser, T. A., Milton, J. E., & Gouwy, S. A. (2020). New geochemistry from old drill holes at the Tom property, Macmillan Pass, Yukon. In K. E. MacFarlane (Ed.), *Yukon Exploration and Geology 2020* (pp. 19–46): Yukon Geological Survey Energy, Mines and Resources Government of Yukon.

Frenzel, M., Ketris, M. P., & Gutzmer, J. (2014). On the geological availability of germanium. *Mineralium Deposita, 49*(4), 471-486. DOI: https://doi.org/10.1007/s00126-013-0506-z

Frenzel, M., Hirsch, T., & Gutzmer, J. (2016). Gallium, germanium, indium, and other trace and minor elements in sphalerite as a function of deposit type—A meta-analysis. *Ore Geology Reviews, 76*, 52-78. DOI: https://doi.org/10.1016/j.oregeorev.2015.12.017

Frenzel, M., Bachmann, K., Carvalho, J. R., Relvas, J. M., Pacheco, N., & Gutzmer, J. (2019). The geometallurgical assessment of by-products—geochemical proxies for the complex mineralogical deportment of indium at Neves-Corvo, Portugal. *Mineralium Deposita, 54*, 959-982. DOI: https://doi.org/10.1007/s00126-018-0849-6

Frenzel, M. (2023). Making sense of mineral trace-element data–How to avoid common pitfalls in statistical analysis and interpretation. *Ore Geology Reviews,* DOI: https://doi.org/10.1016/j.oregeorev.2023.105566

Friedman, G. M., & Sanders, J. E. (1978). *Principles of Sedimentology John Wiley and Sons*. New York: John Wiley & Sons.

Fritz, P., Basharmal, G., Drimmie, R., Ibsen, J., & Qureshi, R. (1989). Oxygen isotope exchange between sulphate and water during bacterial reduction of sulphate. *Chemical Geology: Isotope Geoscience Section, 79*(2), 99-105.

Gabrielse, H. (1967). Tectonic evolution of the northern Canadian Cordillera. *Canadian Journal of Earth Sciences, 4*(2), 271-298. DOI: https://doi.org/10.1139/e67-013

Gadd, M. G., Layton-Matthews, D., & Peter, J. M. (2016a). Non-hydrothermal origin of apatite in SEDEX mineralization and host rocks of the Howard's Pass district, Yukon, Canada. *American Mineralogist, 101*(5), 1061-1071. DOI: https://doi.org/10.2138/am-2016-5550

Gadd, M. G., Layton-Matthews, D., Peter, J. M., & Paradis, S. J. (2016b). The world-class Howard's Pass SEDEX Zn-Pb district, Selwyn Basin, Yukon. Part I: trace element compositions of pyrite record input of hydrothermal, diagenetic, and metamorphic fluids to mineralization. *Mineralium Deposita, 51*(3), 319-342. DOI: https://doi.org/10.1007/s00126-015-0611-2

Gadd, M. G., Layton-Matthews, D., Peter, J. M., Paradis, S., & Jonasson, I. R. (2017). The world-class Howard's Pass SEDEX Zn-Pb district, Selwyn Basin, Yukon. Part II: the roles of thermochemical and bacterial sulfate reduction in metal fixation. *Mineralium Deposita, 52*(3), 405-419. DOI: https://doi.org/10.1007/s00126-016-0672-x

Gadd, M. G., Peter, J. M., Hnatyshin, D., Creaser, R., Gouwy, S., & Fraser, T. (2020). A Middle Devonian basin-scale precious metal enrichment event across northern Yukon (Canada). *Geology, 48*(3), 242-246. DOI: https://doi.org/10.1130/G46874.1

Gao, P., Xiao, X. M., Hu, D. F., Lash, G. G., Liu, R. B., Cai, Y. D., Wang, Z. H., Zhang, B. Y., Yuan, T., & Liu, S. Y. (2022). Effect of silica diagenesis on porosity evolution of deep gas shale reservoir of the Lower Paleozoic Wufeng-Longmaxi formations, Sichuan Basin. *Marine and Petroleum Geology, 145*, 105873. DOI: https://doi.org/10.1016/j.marpetgeo.2022.105873

Gardner, H. D., & Hutcheon, I. (1985). Geochemistry, mineralogy, and geology of the Jason Pb-Zn deposits, Macmillan Pass, Yukon, Canada. *Economic Geology, 80*(5), 1257-1276. DOI: https://doi.org/10.2113/gsecongeo.80.5.1257

Gibson, G. M., Hutton, L. J., & Holzschuh, J. (2017). Basin inversion and supercontinent assembly as drivers of sediment-hosted Pb–Zn mineralization in the Mount Isa region, northern Australia. *Journal of the Geological Society, 174*(4), 773-786. DOI: https://doi.org/10.1144/jgs2016-10

Gill, B. C., Lyons, T. W., & Saltzman, M. R. (2007). Parallel, high-resolution carbon and sulfur isotope records of the evolving Paleozoic marine sulfur reservoir. *Palaeogeography Palaeoclimatology Palaeoecology, 256*(3-4), 156-173. DOI: https://doi.org/10.1016/j.palaeo.2007.02.030

Godwin, C. I., Sinclair, A. J., & Ryan, B. D. (1982). Lead isotope models for the genesis of carbonate-hosted Zn-Pb, shale-hosted Ba-Zn-Pb, and silver-rich deposits in the northern Canadian Cordillera. *Economic Geology, 77*(1), 82-94. DOI: https://doi.org/10.2113/gsecongeo.77.1.82

Goldberg, T., Mazumdar, A., Strauss, H., & Shields, G. (2006). Insights from stable S and O isotopes into biogeochemical processes and genesis of Lower Cambrian barite-pyrite concretions of South China. *Organic Geochemistry, 37*(10), 1278-1288. DOI: https://doi.org/10.1016/j.orggeochem.2006.04.013

Goldstein, R. H. (2003). Petrographic analysis of fluid inclusions. In: Samson, I., Anderson, A. and Marshall, D. (eds), *Fluid inclusions – analysis and interpretation*. Mineralogical Association of Canada, Short Course Series, Vol. 32, pp. 9-53.

Goldstein, R. H. (2012). Fluid inclusion geothermometry in sedimentary systems: From paleoclimate to hydrothermal. In N. B. Harris & K. E. Peters (Eds.), *Analyzing the Thermal History of Sedimentary Basins: Methods and Case Studies. Special Publication 103.* Society for Sedimentary Geology. Vol. 103.

Gomes, M. L., & Hurtgen, M. T. (2015). Sulfur isotope fractionation in modern euxinic systems: Implications for paleoenvironmental reconstructions of paired sulfate-sulfide isotope records. *Geochimica Et Cosmochimica Acta, 157*, 39-55. DOI: https://doi.org/10.1016/j.gca.2015.02.031

Gomes, M. L., & Johnston, D. T. (2017). Oxygen and sulfur isotopes in sulfate in modern euxinic systems with implications for evaluating the extent of euxinia in ancient oceans. *Geochimica et cosmochimica acta, 205*, 331-359. DOI: https://doi.org/10.1016/j.gca.2017.02.020

Gong, Q., Wang, X., Zhao, L., Grasby, S. E., Chen, Z.-Q., Zhang, L., Li, Y., Cao, L., & Li, Z. (2017). Mercury spikes suggest volcanic driver of the Ordovician-Silurian mass extinction. *Scientific Reports, 7*(1), 5304. DOI: https://doi.org/10.1038/s41598-017-05524-5

Gonzalez-Muñoz, M. T., Martinez-Ruiz, F., Morcillo, F., Martin-Ramos, J. D., & Paytan, A. (2012). Precipitation of barite by marine bacteria: A possible mechanism for marine barite formation. *Geology, 40*(8), 675-678. DOI: https://doi.org/10.1130/G33006.1

Goodfellow, W. D., Jonasson, I. R., & Morganti, J. M. (1983). Zonation of chalcophile elements about the Howard's pass (XY) Zn-Pb deposit, Selwyn Basin, Yukon. *Journal of Geochemical Exploration, 19*(1-3), 503-542. DOI: https://doi.org/10.1016/0375-6742(83)90044-4

Goodfellow, W. D., & Jonasson, I. R. (1984). Ocean stagnation and ventilation defined by δ34S secular trends in pyrite and barite, Selwyn Basin, Yukon. *Geology, 12*(10), 583-586. DOI: https://doi.org/10.1130/0091-7613(1984)12<583:OSAVDB>2.0.CO;2

Goodfellow, W. D. (1987). Anoxic stratified oceans as a source of sulphur in sediment-hosted stratiform ZnPb deposits (Selwyn Basin, Yukon, Canada). *Chemical Geology: Isotope Geoscience Section, 65*(3-4), 359-382. DOI: https://doi.org/10.1016/0168-9622(87)90014-5

Goodfellow, W. D., & Rhodes, D. (1990). Geological setting, geochemistry and origin of the Tom stratiform Zn-Pb-Ag-barite deposits. In J. G. Abbott & R. J. W. Turner (Eds.), *Mineral deposits of the northern Canadian Cordillera: Ottawa, International Association on the Genesis of Ore Deposits, Eighth Symposium, Field Trip* (Vol. 14, pp. 177-244).

Goodfellow, W. D., Lydon, J. W., & Turner, R. (1993). Geology and genesis of stratiform sediment-hosted (SEDEX) zinc-lead-silver sulphide deposits. In R. V. Kirkham, W. D. Sinclair, R. I. Thorpe, & J. M. Duke (Eds.), *Mineral Deposit Modeling*. Geological Association of Canada. pp. 201-251

Goodfellow, W. D., Cecile, M. P., & Leybourne, M. I. (1995). Geochemistry, petrogenesis, and tectonic setting of lower Paleozoic alkalic and potassic volcanic rocks, Northern Canadian Cordilleran Miogeocline. *Canadian Journal of Earth Sciences, 32*(8), 1236-1254. DOI: https://doi.org/10.1139/e95-101

Goodfellow, W. D. (2004). *Geology, genesis and exploration of SEDEX deposits, with emphasis on the Selwyn basin, Canada*. New Delhi: Narosa Publishing House.

Goodfellow, W. D. (2007). Mineral deposits of Canada: A synthesis of major deposit-types, district metallogeny, the evolution of geological provinces, and exploration methods.

In *Special Publication no. 5* (pp. 1068): Mineral Deposits Division, Geological Association of Canada.

Goodfellow, W. D., & Lydon, J. W. (2007). Sedimentary exhalative (SEDEX) deposits. In W. D. Goodfellow (Ed.), *Mineral deposits of Canada: A synthesis of major deposit types, district metallogeny, the evolution of geological provinces, and exploration methods* (Vol. 5, pp. 163-183): Mineral Deposits Division, Geological Association of Canada.

Gordey, S. P., Geldsetzer, H. H. J., Morrow, D. W., Bamber, E. W., Henderson, C. M., Richards, B. C., McGugan, A., Gibson, D. W., & Poulton, T. P. (1991). Upper Devonian to Middle Jurassic assemblages. In H. Gabrielse & C. J. Yorath (Eds.), *Geology of the Cordilleran orogen in Canada* (pp. 296): Geological Survey of Canada.

Gordey, S. P., & Anderson, R. G. (1993). Evolution of the northern Cordilleran miogeocline, Nahanni map area (105I), Yukon and Northwest Territories. In S. P. Gordey & R. G. Anderson (Eds.), *Memoir 428* (Vol. 428): Geological Survey of Canada.

Gordey, S. P., Macdonald, J. D., Turner, E. C., Long, D. G. F., Martel, E., & Fischer, B. J. (2010). Structural geology of the central Mackenzie Mountains. In E. Martel, E. C. Turner, & B. J. Fischer (Eds.), *Geology of the central Mackenzie Mountains of the northern Canadian Cordillera, Sekwi Mountain (105P), Mount Eduni (106A), and northwestern Wrigley Lake (95M) map areas, Northwest Territories* (pp. 215-250): Northwest Territories Geoscience Office.

Gordey, S. P. (2013). Evolution of the Selwyn basin region, Sheldon Lake (105J) and Tay River (105K) map areas, central Yukon Territory. *Geological Survey of Canada, Bulletin, 599*, 274.

Graham, G. E., Kelley, K. D., Slack, J. F., & Koenig, A. E. (2009). Trace elements in Zn–Pb–Ag deposits and related stream sediments, Brooks Range Alaska, with implications for Tl as a pathfinder element. *Geochemistry: Exploration, Environment, Analysis, 9*(1), 19-37. DOI: https://doi.org/10.1144/1467-7873/08-177

Grasby, S. E., Them II, T. R., Chen, Z., Yin, R., & Ardakani, O. H. (2019). Mercury as a proxy for volcanic emissions in the geologic record. *Earth-Science Reviews, 196*, 102880.

Greinert, J., Bollwerk, S. M., Derkachev, A., Bohrmann, G., & Suess, E. (2002). Massive barite deposits and carbonate mineralization in the Derugin Basin, Sea of Okhotsk: precipitation processes at cold seep sites. *Earth and Planetary Science Letters, 203*(1), 165-180. DOI: https://doi.org/10.1016/S0012-821x(02)00830-0

Grema, H. M., Magnall, J. M., Whitehouse, M. J., Gleeson, S. A., & Schulz, H.-M. (2021). Isotopic data of pyrite ($\delta^{34}S$) and barite ($\delta^{34}S$, $\delta^{18}O$) in the Canol Formation (Selwyn Basin, Canada). GFZ Data Services. DOI: https://doi.org/10.5880/GFZ.3.1.2021.006

Grema, H. M., Magnall, J. M., Whitehouse, M. J., Gleeson, S. A., & Schulz, H.-M. (2022). The Formation of Highly Positive $\delta^{34}S$ Values in Late Devonian Mudstones: Microscale Analysis of Pyrite ($\delta^{34}S$) and Barite ($\delta^{34}S$, $\delta^{18}O$) in the Canol Formation (Selwyn Basin, Canada). *Frontiers in Earth Science, 9:784824*. DOI: https://doi.org/10.3389/feart.2021.784824

Grema, H. M., Wudarska, A., Wilke, F. D. H., Schleicher, A. M., Milton, J. E., Magnall, J. M., Gleeson, S. A., & Schulz, H.-M. (2024a). Petrography, quantitative mineralogy, and U-

Pb geochronology of the Boundary Zone Zn-Pb-Ag prospect, Yukon, Canada. *GFZ Data Services.* https://doi.org/10.5880/GFZ.3.1.2024.007. *Please access via https://dataservices.gfz-potsdam.de/panmetaworks/review/4d977202cbc26dabe4526cfbbe177869faff51af98518d4411dadc5e14d71768/.*

Grema, H. M., Sośnicka, M., Barrote, V. R., Wilke, F. D. H., Milton, J. E., Magnall, J. M., Gleeson, S. A., Schulz, H.-M. (2024b): Sphalerite chemistry and fluid inclusion microthermometry data from the Zn-Pb±Ag Boundary Zone deposit, Yukon, Canada. *GFZ Data Services*. https://doi.org/10.5880/GFZ.3.1.2024.008. *Please access via https://dataservices.gfz-potsdam.de/panmetaworks/review/66434e4a4731d6ada2a01378e4fbfa88375c14b81a0168c15b7140db3540ee3f/*

Griffith, E. M., & Paytan, A. (2012). Barite in the ocean - occurrence, geochemistry and palaeoceanographic applications. *Sedimentology, 59*(6), 1817-1835. DOI: https://doi.org/10.1111/j.1365-3091.2012.01327.x

Grohol, M., & Veeh, C. (2023). Study on the critical raw materials for the EU 2023: final report. *Publications Office of the European Union European Commission, Directorate-General for Internal Market, Industry, Entrepreneurship and SMEs*. DOI: https://data.europa.eu/doi/10.2873/725585

Hanor, J. S. (1980). Dissolved methane in sedimentary brines; potential effect on the PVT properties of fluid inclusions. *Economic Geology, 75*(4), 603-609. DOI: https://doi.org/10.2113/gsecongeo.75.4.603

Hanor, J. S. (2000). Barite-celestine geochemistry and environments of formation. *Sulfate Minerals - Crystallography, Geochemistry and Environmental Significance, 40*(1), 193-275. DOI: https://doi.org/10.2138/rmg.2000.40.4

Hart, C. J. R., Goldfarb, R. J., Lewis, L. L., & Mair, J. L. (2004). The northern Cordilleran mid-Cretaceous plutonic province: Ilmenite/magnetite-series granitoids and intrusion-related mineralisation. *Resource Geology, 54*(3), 253-280. DOI: https://doi.org/10.1111/j.1751-3928.2004.tb00206.x

Hayward, N., Magnall, J. M., Taylor, M., King, R., McMillan, N., & Gleeson, S. A. (2021). The Teena Zn-Pb Deposit (McArthur Basin, Australia). Part I: Syndiagenetic Base Metal Sulfide Mineralization Related to Dynamic Subbasin Evolution. *Economic Geology, 116*(8), 1743-1768. DOI: https://doi.org/10.5382/econgeo.4846

Hein, J. R., Zierenberg, R. A., Maynard, J. B., & Hannington, M. D. (2007). Barite-forming environments along a rifted continental margin, Southern California Borderland. *Deep-Sea Research Part II-Topical Studies in Oceanography, 54*(11-13), 1327-1349. DOI: https://doi.org/10.1016/j.dsr2.2007.04.011

Hemley, J. J., Cygan, G. L., Fein, J. B., Robinson, G. R., & d'Angelo, W. M. (1992). Hydrothermal ore-forming processes in the light of studies in rock-buffered systems; I, Iron-copper-zinc-lead sulfide solubility relations. *Economic Geology, 87*(1), 1-22. DOI: https://doi.org/10.2113/gsecongeo.87.1.1

Hemley, J. J., & Hunt, J. P. (1992). Hydrothermal ore-forming processes in the light of studies in rock-buffered systems; II, Some general geologic applications. *Economic Geology,* *87*(1), 23-43. DOI: https://doi.org/10.2113/gsecongeo.87.1.2310.2113/gsecongeo.87.1.23

Hill, P. S., Tripati, A. K., & Schauble, E. A. (2014). Theoretical constraints on the effects of pH, salinity, and temperature on clumped isotope signatures of dissolved inorganic carbon species and precipitating carbonate minerals. *Geochimica Et Cosmochimica Acta, 125*, 610-652. DOI: https://doi.org/10.1016/j.gca.2013.06.018

Hitzman, M. W., & Large, D. E. (1986). A review and classification of the Irish carbonate hosted base metal deposits. In C. J. Andrew, R. W. A. Crowe, S. Finlay, W. M. Pennell, & J. Pyne (Eds.), *Geology and Genesis of Mineral Deposits in Ireland* (pp. 217 - 238).

Höll, R., Kling, M., & Schroll, E. (2007). Metallogenesis of germanium—A review. *Ore Geology Reviews, 30*(3), 145-180. DOI: https://doi.org/10.1016/j.oregeorev.2005.07.034

Horita, J., Zimmermann, H., & Holland, H. D. (2002). Chemical evolution of seawater during the Phanerozoic: Implications from the record of marine evaporites. *Geochimica Et Cosmochimica Acta, 66*(21), 3733-3756. DOI: https://doi.org/10.1016/S0016-7037(01)00884-5

Howell, D., Griffin, W. L., Pearson, N. J., Powell, W., Wieland, P., & O'Reilly, S. Y. (2013). Trace element partitioning in mixed-habit diamonds. *Chemical Geology, 355*, 134-143. DOI: https://doi.org/10.1016/j.chemgeo.2013.07.013

Huston, D. L., Stevens, B., Southgate, P. N., Muhling, P., & Wyborn, L. (2006). Australian Zn-Pb-Ag Ore-Forming Systems: A Review and Analysis. *Economic Geology, 101*(6), 1117-1157. DOI: https://doi.org/10.2113/gsecongeo.101.6.1117

Huston, D. L., Eglington, B. M., Pehrsson, S. J., & Piercey, S. J. (2022). *Global database of zinc-lead-bearing mineral deposits*. (1922446947). Canberra: Geoscience Australia Retrieved from http://dx.doi.org/10.11636/Record.2022.010

Huston, D. L., Champion, D. C., Czarnota, K., Duan, J., Hutchens, M., Paradis, S., Hoggard, M., Ware, B., Gibson, G. M., & Doublier, M. P. (2023). Zinc on the edge—isotopic and geophysical evidence that cratonic edges control world-class shale-hosted zinc-lead deposits. *Mineralium Deposita, 58*(4), 707-729. DOI: https://doi.org/10.1007/s00126-022-01153-9

Huston, D. L., & Gutzmer, J. (2023). Isotopes in Economic Geology, Metallogeny and Exploration—Future Challenges and Opportunities. In D. L. Huston & J. Gutzmer (Eds.), *Isotopes in Economic Geology, Metallogenesis and Exploration* (https://doi.org/10.1007/978-3-031-27897-6_16pp. 465-475): Springer, Cham.

International Zinc Association. (2022). *Energizing our Future*. Retrieved from https://www.zinc.org/wp-content/uploads/sites/30/2023/03/2022-Annual-Report.pdf

Ireland, T. R., Large, R. R., McGoldrick, P., & Blake, M. (2004). Spatial Distribution Patterns of Sulfur Isotopes, Nodular Carbonate, and Ore Textures in the McArthur River (HYC) Zn-Pb-Ag Deposit, Northern Territory, Australia. *Economic Geology, 99*(8), 1687-1709. DOI: https://doi.org/10.2113/gsecongeo.99.8.1687

Ireland, T. R., & Williams, I. S. (2003). Considerations in zircon geochronology by SIMS. *Zircon, 53*(1), 215-241. DOI: https://doi.org/10.2113/0530215

Jébrak, M. (1997). Hydrothermal breccias in vein-type ore deposits: A review of mechanisms, morphology and size distribution. *Ore Geology Reviews, 12*(3), 111-134. DOI: https://doi.org/10.1016/S0169-1368(97)00009-7

Jennings, D. S., & Jilson, G. A. (1986). Geology and sulfide deposits of Anvil Range, Yukon Territory. In J. A. Morin (Ed.), *Mineral Deposits of Northern Cordillera* (Special Volume 37 ed. pp. 319-361): Canadian Institute of Mining and Metallurgy.

Jewell, P. W. (2000). Bedded barite in the geologic record. *in Glenn, C.R., et al., eds., Marine authigenesis: From global to microbial: SEPM (Society for Sedimentary Geology), Special Publication 66*, 147 - 161.

Jiang, L., Fakhraee, M., Cai, C. F., & Worden, R. H. (2020). Sulfur Cycling During Progressive Burial in Sulfate-Rich Marine Carbonates. *Geochemistry Geophysics Geosystems, 21*(12). DOI: https://doi.org/10.1029/2020GC009383

Jiang, S.-Y., Wang, W., & Su, H.-M. (2023). Super-enrichment mechanisms of strategic critical metal deposits: current understanding and future perspectives. *Journal of Earth Science, 34*(4), 1295-1298. DOI: https://doi.org/10.1007/s12583-023-2001-5

John, E. H., Wignall, P. B., Newton, R. J., & Bottrell, S. H. (2010). δ34SCAS and δ18OCAS records during the Frasnian–Famennian (Late Devonian) transition and their bearing on mass extinction models. *Chemical Geology, 275*(3-4), 221-234. DOI: https://doi.org/10.1016/j.chemgeo.2010.05.012

Johnson, C. A., Kelley, K. D., & Leach, D. L. (2004). Sulfur and oxygen isotopes in barite deposits of the western Brooks Range, Alaska, and implications for the origin of the Red Dog massive sulfide deposits. *Economic Geology, 99*(7), 1435-1448. DOI: https://doi.org/10.2113/gsecongeo.99.7.1435

Johnson, C. A., Emsbo, P., Poole, F. G., & Rye, R. O. (2009). Sulfur- and oxygen-isotopes in sediment-hosted stratiform barite deposits. *Geochimica et cosmochimica acta, 73*(1), 133-147. DOI: https://doi.org/10.1016/j.gca.2008.10.011

Johnson, C. A., Slack, J., Falck, H., & Kelley, K. D. (2014). *Depositional environment of mudstone host rocks at the Howards Pass Zn-Pb deposits, Yukon Territory, Canada: Insights from iron speciation, sulfur isotopes, and bulk Fe/Al and Mo/TOC Ratios.* Paper presented at the Geological Society of America Abstracts with Programs 46: 250.

Johnson, C. A., Dumoulin, J. A., Burruss, R. A., & Slack, J. F. (2015). Depositional Conditions for the Kuna Formation, Red Dog Zn-Pb-Ag-Barite District, Alaska, Inferred from Isotopic and Chemical Proxies. *Economic Geology, 110*(5), 1143-1156. DOI: https://doi.org/10.2113/econgeo.110.5.1143

Johnson, C. A., Slack, J. F., Dumoulin, J. A., Kelley, K. D., & Falck, H. (2018). Sulfur isotopes of host strata for Howards Pass (Yukon–Northwest Territories) Zn-Pb deposits implicate anaerobic oxidation of methane, not basin stagnation. *Geology, 46*(7), 619-622.

Johnston, D. T. (2011). Multiple sulfur isotopes and the evolution of Earth's surface sulfur cycle. *Earth-Science Reviews, 106*(1-2), 161-183. DOI: https://doi.org/10.1016/j.earscirev.2011.02.003

Jonasson, I. R., Goodfellow, W. D., & Morin, J. A. (1986). Sedimentary and diagenetic textures, and deformation structures within the sulphide zone of the Howards Pass (XY) Zn-Pb deposit, Yukon and Northwest Territories. In M. J. A (Ed.), *Mineral deposits of northern Cordillera* (Vol. Special Volume 37, pp. 51-70): Canadian Institute of Mining and Metallurgy.

Jones, D. S., Martini, A. M., Fike, D. A., & Kaiho, K. (2017). A volcanic trigger for the Late Ordovician mass extinction? Mercury data from south China and Laurentia. *Geology, 45*(7), 631-634. DOI: https://doi.org/10.1130/G38940.1

Jørgensen, B. B., Böttcher, M. E., Lüschen, H., Neretin, L. N., & Volkov, I. I. (2004). Anaerobic methane oxidation and a deep H2S sink generate isotopically heavy sulfides in Black Sea sediments. *Geochimica et Cosmochimica Acta, 68*(9), 2095-2118. DOI: https://doi.org/10.1016/j.gca.2003.07.017

Jørgensen, B. B., & Kasten, S. (2006). Sulfur Cycling and Methane Oxidation. In H. D. Schulz & M. Zabel (Eds.), *Marine Geochemistry* (https://doi.org/10.1007/3-540-32144-6_8pp. 271-309). Berlin, Heidelberg: Springer.

Jørgensen, B. B., Findlay, A. J., & Pellerin, A. (2019). The Biogeochemical Sulfur Cycle of Marine Sediments. *Front Microbiol, 10*. DOI: https://doi.org/10.3389/fmicb.2019.00849

Jowitt, S. M., & McNulty, B. A. (2021). Battery and Energy Metals: Future Drivers of the Minerals Industry? *SEG Discovery, 127*, 11-18. DOI: https://doi.org/10.5382/2021-127.fea-01

Kabanov, P., & Gouwy, S. A. (2017). The Devonian Horn River Group and the basal Imperial Formation of the central Mackenzie Plain, NWT, Canada: multiproxy stratigraphic framework of a black shale basin. *Canadian Journal of Earth Sciences, 54*(4), 409-429. DOI: https://doi.org/10.1139/cjes-2016-0096

Kabanov, P. (2019). Devonian (c. 388–375 Ma) Horn River Group of Mackenzie Platform (NW Canada) is an open-shelf succession recording oceanic anoxic events. *Journal of the Geological Society, 176*(1), 29-45. DOI: https://doi.org/10.1144/jgs2018-075

Kah, L. C., Lyons, T. W., & Frank, T. D. (2004). Low marine sulphate and protracted oxygenation of the Proterozoic biosphere. *Nature, 431*(7010), 834-838. DOI: https://doi.org/10.1038/nature02974

Kah, L. C., Thompson, C. K., Henderson, M. A., & Zhan, R. B. (2016). Behavior of marine sulfur in the Ordovician. *Palaeogeography Palaeoclimatology Palaeoecology, 458*, 133-153. DOI: https://doi.org/10.1016/j.palaeo.2015.12.028

Kaplan, I. R., & Rittenberg, S. C. (1964). Microbiological Fractionation of Sulphur Isotopes. *J Gen Microbiol, 34*(2), 195-212. DOI: https://doi.org/10.1099/00221287-34-2-195

Keith, M., Haase, K. M., Schwarz-Schampera, U., Klemd, R., Petersen, S., & Bach, W. (2014). Effects of temperature, sulfur, and oxygen fugacity on the composition of sphalerite from submarine hydrothermal vents. *Geology, 42*(8), 699-702. DOI: https://doi.org/10.1130/G35655.1

Kelley, K. D., Leach, D. L., Johnson, C. A., Clark, J. L., Fayek, M., Slack, J. F., Anderson, V. M., Ayuso, R. A., & Ridley, W. I. (2004). Textural, Compositional, and Sulfur Isotope Variations of Sulfide Minerals in the Red Dog Zn-Pb-Ag Deposits, Brooks Range, Alaska: Implications for Ore Formation. *Economic Geology, 99*(7), 1509-1532. DOI: https://doi.org/10.2113/gsecongeo.99.7.1509

Kelley, K. D., Selby, D., Falck, H., & Slack, J. F. (2017). Re-Os systematics and age of pyrite associated with stratiform Zn-Pb mineralization in the Howards Pass district, Yukon and Northwest Territories, Canada. *Mineralium Deposita, 52*(3), 317-335. DOI: https://doi.org/10.1007/s00126-016-0663-y

Kirkham, G., Dunning, J., & Schleiss, W. (2012). *Update for Don deposit mineral resource estimate, Howard's Pass property, eastern Yukon: NI 43-101 Technical Report* Retrieved from www.sedar.com

Klemme, H. D., & Ulmishek, G. F. (1991). Effective petroleum source rocks of the world: stratigraphic distribution and controlling depositional factors. *AAPG bulletin, 75*(12), 1809-1851. DOI: https://doi.org/10.1306/0C9B2A47-1710-11D7-8645000102C1865D

Knittel, K., & Boetius, A. (2009). Anaerobic oxidation of methane: progress with an unknown process. *Annual review of microbiology, 63*, 311-334.

Koski, R. A., & Hein, J. R. (2003). *Stratiform barite deposits in the Roberts Mountains allochthon, Nevada: A review of potential analogs in modern sea-floor environments*. Retrieved from https://pubs.usgs.gov/bul/b2209-h/

Kullerud, G. (1953). The FeS-ZnS system, a geological thermometer. Griegs boktrykkeri, Norsk Geologisk Tidsskrift, *32(2-4), 61-147.*

Large, D. (1981). The geochemistry of the sedimentary rocks in the vicinity of the Tom Pb-Zn-Ba deposit, Yukon Territory, Canada. *Journal of Geochemical Exploration, 15*(1-3), 203-217. DOI: https://doi.org/10.1016/0375-6742(81)90063-7

Large, D. E. (1980). Geological parameters associated with sediment-hosted, submarine exhalative Pb-Zn deposits: An empirical model for mineral exploration. *Geologisches Jahrbuch, 40*, 59-130. Retrieved from https://cir.nii.ac.jp/crid/1571980076389034752

Large, R. R., Bull, S. W., McGoldrick, P. J., Walters, S., Derrick, G. M., & Carr, G. R. (2005). Stratiform and strata-bound Zn-Pb-Ag deposits in Proterozoic sedimentary basins, northern Australia. In J. W. Hedenquist, J. F. H. Thompson, R. J. Goldfarb, & J. P. Richards (Eds.), *One Hundredth Anniversary Volume* (https://doi.org/10.5382/AV100.28) .

Leach, D. L., Marsh, E., Bradley, D., Gardoll, S., & Huston, D. (2005a). *The distribution of SEDEX Pb-Zn deposits through Earth history.* Paper presented at the Mineral Deposit Research: Meeting the Global Challenge.

Leach, D. L., Sangster, D. F., Kelley, K. D., Large, R. R., Garven, G., Allen, C. R., Gutzmer, J., & Walters, S. (2005b). Sediment-Hosted Lead-Zinc Deposits: A Global Perspective.

In J. W. Hedenquist, J. F. H. Thompson, R. J. Goldfarb, & J. P. Richards (Eds.), *One Hundredth Anniversary Volume* (https://doi.org/10.5382/AV100.18).

Leach, D. L., Marsh, E., Emsbo, P., Rombach, C. S., Kelley, K. D., & Anthony, M. (2004). Nature of hydrothermal fluids at the shale-hosted red dog Zn-Pb-Ag deposits, Brooks Range, Alaska. *Economic Geology, 99*(7), 1449-1480. DOI: https://doi.org/10.2113/gsecongeo.99.7.1449

Leach, D. L., Bradley, D. C., Huston, D., Pisarevsky, S. A., Taylor, R. D., & Gardoll, S. J. (2010). Sediment-hosted lead-zinc deposits in Earth history. *Economic Geology, 105*(3), 593-625. DOI: https://doi.org/10.2113/gsecongeo.105.3.593

Leighton, C., Layton-Matthews, D., Peter, J. M., & Gadd, M. (2019). Application of pyrite chemistry to recognize a distal expression of hydrothermal activity in the MacMillan Pass SEDEX district, Yukon. In N. Rogers (Ed.), *Targeted Geoscience Initiative: 2018 report of activities* (Vol. Open File 8549, pp. 125–137): Geological Survey of Canada.

Leighton, C., Layton-Matthews, D., Peter, J. M., Gadd, M. G., Voinot, A., & Leybourne, M. I. (2021a). Paleoredox Conditions, Hydrothermal History, and Target Vectoring in the Macmillan Pass Base-Metal District, Yukon, Canada: 2-Pyrite Paragenesis and Mineral Chemistry. *Canadian Mineralogist, 59*(5), 1233-1259. DOI: https://doi.org/10.3749/canmin.2000077

Leighton, C., Leybourne, M. I., Layton-Matthews, D., Peter, J. M., Gadd, M. G., & Voinot, A. (2021b). Paleoredox Conditions, Hydrothermal History, and Target Vectoring in the Macmillan Pass Base-Metal District, Yukon, Canada: 1-Lithogeochemistry of Proximal and Distal Shales. *Canadian Mineralogist, 59*(5), 1207-1232. DOI: https://doi.org/10.3749/canmin.2000075

Leitch, C. H. B., & Lydon, J. W. (2000). Fluid inclusion petrography and microthermometry of the Sullivan deposit and surrounding area. *Geological Association of Canada, Mineral Deposits Division, 1*, 617-632.

Leloup, J., Loy, A., Knab, N. J., Borowski, C., Wagner, M., & Jørgensen, B. B. (2007). Diversity and abundance of sulfate-reducing microorganisms in the sulfate and methane zones of a marine sediment, Black Sea. *Environmental Microbiology, 9*(1), 131-142.

Li, X. C., & Zhou, M. F. (2015). Multiple stages of hydrothermal REE remobilization recorded in fluorapatite in the Paleoproterozoic Yinachang Fe-Cu-(REE) deposit, Southwest China. *Geochimica Et Cosmochimica Acta, 166*, 53-73. DOI: https://doi.org/10.1016/j.gca.2015.06.008

Lianxing, G., & McClay, K. R. (1992). Pyrite deformation in stratiform lead-zinc deposits of the Canadian Cordillera. *Mineralium Deposita, 27*, 169-181. DOI: https://doi.org/10.1007/BF00202540

Lin, Z. Y., Sun, X. M., Lu, Y., Xu, L., Gong, J. L., Lu, H. F., Teichert, B. M. A., & Peckmann, J. (2016a). Stable isotope patterns of coexisting pyrite and gypsum indicating variable methane flow at a seep site of the Shenhu area, South China Sea. *Journal of Asian Earth Sciences, 123*, 213-223. DOI: https://doi.org/10.1016/j.jseaes.2016.04.007

Lin, Z. Y., Sun, X. M., Peckmann, J., Lu, Y., Xu, L., Strauss, H., Zhou, H. Y., Gong, J. L., Lu, H. F., & Teichert, B. M. A. (2016b). How sulfate-driven anaerobic oxidation of methane affects the sulfur isotopic composition of pyrite: A SIMS study from the South China Sea. *Chemical Geology, 440*, 26-41. DOI: https://doi.org/10.1016/j.chemgeo.2016.07.007

Lin, Z. Y., Sun, X. M., Strauss, H., Lu, Y., Gong, J. L., Xu, L., Lu, H. F., Teichert, B. M. A., & Peckmann, J. (2017). Multiple sulfur isotope constraints on sulfate-driven anaerobic oxidation of methane: Evidence from authigenic pyrite in seepage areas of the South China Sea. *Geochimica et Cosmochimica Acta, 211*, 153-173. DOI: https://doi.org/10.1016/j.gca.2017.05.015

Liu, J. R., Pellerin, A., Izon, G., Wang, J. S., Antler, G., Liang, J. Q., Su, P. B., Jorgensen, B. B., & Ono, S. (2020). The multiple sulphur isotope fingerprint of a sub-seafloor oxidative sulphur cycle driven by iron. *Earth and Planetary Science Letters, 536*. DOI: https://doi.org/10.1016/j.epsl.2020.116165

Liu, X. T., Fike, D., Li, A. C., Dong, J., Xu, F. J., Zhuang, G. C., Rendle-Buhring, R., & Wan, S. M. (2019). Pyrite sulfur isotopes constrained by sedimentation rates: Evidence from sediments on the East China Sea inner shelf since the late Pleistocene. *Chemical Geology, 505*, 66-75. DOI: https://doi.org/10.1016/j.chemgeo.2018.12.014

Liu, Y., Song, Y., Fard, M., Hou, Z., Ma, W., & Yue, L. (2023). The Characteristics and Origin of Barite in the Giant Mehdiabad Zn-Pb-Ba Deposit, Iran. *Economic Geology, 118*(6), 1495-1519. DOI: https://doi.org/10.5382/econgeo.5014

Ludwig, K. R. (2012). *User's manual for Isoplot 3.75: A geochronological toolkit for Microsoft Excel*. Retrieved from http://www.bgc.org/isoplot_etc/isoplot/Isoplot3_75-4_15manual.pdf.

Luo, K., Cugerone, A., Zhou, M.-F., Zhou, J.-X., Sun, G.-T., Xu, J., He, K.-J., & Lu, M.-D. (2022). Germanium enrichment in sphalerite with acicular and euhedral textures: an example from the Zhulingou carbonate-hosted Zn (-Ge) deposit, South China. *Mineralium Deposita, 57*, 1343–1365. DOI: https://doi.org/10.1007/s00126-022-01112-4

Machel, H. G. (2001). Bacterial and thermochemical sulfate reduction in diagenetic settings - old and new insights. *Sedimentary Geology, 140*(1-2), 143-175. DOI: https://doi.org/10.1016/S0037-0738(00)00176-7

Magnall, J. M., Gleeson, S. A., & Paradis, S. (2015). The Importance of Siliceous Radiolarian-Bearing Mudstones in the Formation of Sediment-Hosted Zn-Pb ± Ba Mineralization in the Selwyn Basin, Yukon, Canada. *Economic Geology, 110*(8), 2139-2146. DOI: https://doi.org/10.2113/econgeo.110.8.2139

Magnall, J. M., Gleeson, S. A., Stern, R. A., Newton, R. J., Poulton, S. W., & Paradis, S. (2016a). Open system sulphate reduction in a diagenetic environment – Isotopic analysis of barite (δ^{34}S and δ^{18}O) and pyrite (δ^{34}S) from the Tom and Jason Late Devonian Zn–Pb–Ba deposits, Selwyn Basin, Canada. *Geochimica et Cosmochimica Acta, 180*, 146-163. DOI: https://doi.org/10.1016/j.gca.2016.02.015

Magnall, J. M., Gleeson, S. A., Blamey, N. J. F., Paradis, S., & Luo, Y. (2016b). The thermal and chemical evolution of hydrothermal vent fluids in shale hosted massive sulphide

(SHMS) systems from the MacMillan Pass district (Yukon, Canada). *Geochimica et Cosmochimica Acta, 193*, 251-273. DOI: https://doi.org/10.1016/j.gca.2016.07.020

Magnall, J. M., Gleeson, S. A., Poulton, S. W., Gordon, G. W., & Paradis, S. (2018). Links between seawater paleoredox and the formation of sediment-hosted massive sulphide (SHMS) deposits - Fe speciation and Mo isotope constraints from Late Devonian mudstones. *Chemical Geology, 490*, 45-60. DOI: https://doi.org/10.1016/j.chemgeo.2018.05.005

Magnall, J. M., Gleeson, S. A., Creaser, R. A., Paradis, S., Glodny, J., & Kyle, J. R. (2020a). The Mineralogical Evolution of the Clastic Dominant-Type Zn-Pb ± Ba Deposits at Macmillan Pass (Yukon, Canada)-Tracing Subseafloor Barite Replacement in the Layered Mineralization. *Economic Geology, 115*(5), 961-979. DOI: https://doi.org/10.5382/econgeo.4730

Magnall, J. M., Gleeson, S. A., Hayward, N., & Rocholl, A. (2020b). Massive sulfide Zn deposits in the Proterozoic did not require euxinia. *Geochemical Perspectives Letters, 13*, 19-24. DOI: https://doi.org/10.7185/geochemlet.2008

Magnall, J. M., Gleeson, S. A., & Paradis, S. (2020c). A new subseafloor replacement model for the Macmillan Pass clastic-dominant Zn-Pb±Ba deposits (Yukon, Canada). *Economic Geology, 115*(5), 953-959. DOI: https://doi.org/10.5382/econgeo.4719

Magnall, J. M., Hayward, N., Gleeson, S. A., Schleicher, A., Dalrymple, I., King, R., & Mahlstadt, N. (2021). The Teena Zn-Pb Deposit (McArthur Basin, Australia). Part II: Carbonate Replacement Sulfide Mineralization During Burial Diagenesis—Implications for Mineral Exploration. *Economic Geology, 116*(8), 1769–1801. DOI: https://doi.org/10.5382/econgeo.4845

Magnall, J. M., Wirth, R., Hayward, N., Gleeson, S. A., & Schreiber, A. (2023). Stratiform Host-Rock Replacement via Self-Sustaining Reactions in a Clastic-Dominated (CD-type) Zn Deposit. *Economic Geology, 118*(4), 823-836. DOI: https://doi.org/10.5382/econgeo.4988

Mahmoodi, P., Rastad, E., Rajabi, A., & Peter, J. M. (2018). Ore facies, mineral chemical and fluid inclusion characteristics of the Hossein-Abad and Western Haft-Savaran sediment-hosted Zn-Pb deposits, Arak Mining District, Iran. *Ore Geology Reviews, 95*, 342-365. DOI: https://doi.org/10.1016/j.oregeorev.2018.02.036

Mair, J. L., Hart, C. J. R., & Stephens, J. R. (2006). Deformation history of the northwestern Selwyn Basin, Yukon, Canada: Implications for orogen evolution and mid-Cretaceous magmatism. *Geological Society of America Bulletin, 118*(3-4), 304-323. DOI: https://doi.org/10.1130/B25763.1

Mao, M., Rukhlov, A. S., Rowins, S. M., Spence, J., & Coogan, L. A. (2016). Apatite Trace Element Compositions: A Robust New Tool for Mineral Exploration. *Economic Geology, 111*(5), 1187-1222. DOI: https://doi.org/10.2113/econgeo.111.5.1187

Marin-Carbonne, J., Remusat, L., Sforna, M. C., Thomazo, C., Cartigny, P., & Philippot, P. (2018). Sulfur isotope's signal of nanopyrites enclosed in 2.7 Ga stromatolitic organic remains reveal microbial sulfate reduction. *Geobiology, 16*(2), 121-138.

Martel, E., Turner, E. C., & Fischer, B. J. (2011). Geology of the central Mackenzie Mountains of the northern Canadian Cordillera. *Sekwi Mountain (105P), Mount Eduni (106A), and northwestern Wrigley Lake (95M) map-areas, Northwest Territories: Northwest Territories Geoscience Office, NWT Special, 1*, 423.

Martel, E. (2017). The Importance of Structural Mapping in Ore Deposits-A New Perspective on the Howard's Pass Zn-Pb District, Northwest Territories, Canada. *Economic Geology, 112*(6), 1285-1304. DOI: https://doi.org/10.5382/econgeo.2017.4510

Martín-Martín, J. D., Gomez-Rivas, E., Gómez-Gras, D., Travé, A., Ameneiro, R., Koehn, D., & Bons, P. D. (2018). Activation of stylolites as conduits for overpressured fluid flow in dolomitized platform carbonates. *Geological Society, London, Special Publications, 459*(1), 157-176. DOI: https://doi.org/10.1144/SP459.3

Martinez-Ruiz, F., Paytan, A., Gonzalez-Muñoz, M. T., Jroundi, F., Abad, M. M., Lam, P. J., Horner, T. J., & Kastner, M. (2020). Barite Precipitation on Suspended Organic Matter in the Mesopelagic Zone. *Frontiers in Earth Science, 8*. DOI: https://doi.org/10.3389/feart.2020.567714

Maynard, J. B., & Okita, P. M. (1991). Bedded Barite Deposits in the United-States, Canada, Germany, and China - 2 Major Types Based on Tectonic Setting. *Economic Geology and the Bulletin of the Society of Economic Geologists, 86*(2), 364-376. DOI: https://doi.org/10.2113/gsecongeo.86.2.364

McClay, K. R. (1984). The geology of the Tom deposit, MacMillan Pass, Yukon Territory, Canada: Geol. Assoc. Canada (Cordilleran Sec.). *Short Course Notes 2 (Pt. 2)*. 60-96.

McClay, K. R., & Bidwell, G. E. (1986). Geology of the Tom deposit, Macmillan Pass, Yukon. In J. A. Morin (Ed.), *Mineral Deposits of Northern Cordillera* (pp. 100-114): The Canadian Institute of Mining and Metallurgy.

McClay, K. R. (1991). Deformation of stratiform Zn-Pb (-barite) deposits in the northern Canadian Cordillera. *Ore Geology Reviews, 6*(5), 435-462. DOI: https://doi.org/10.1016/0169-1368(91)90040-E

Melero-García, E., Santisteban-Bailón, R., & García-Ruiz, J. M. (2009). Role of bulk pH during witherite biomorph growth in silica gels. *Crystal growth & design, 9*(11), 4730-4734. DOI: https://doi.org/10.1021/cg9005967

Milliken, K. L., Ergene, S. M., & Ozkan, A. (2016). Quartz types, authigenic and detrital, in the Upper Cretaceous Eagle Ford Formation, South Texas, USA. *Sedimentary Geology, 339*, 273-288. DOI: https://doi.org/10.1016/j.sedgeo.2016.03.012

Milliken, K. L., & Olson, T. (2017). Silica Diagenesis, Porosity Evolution, and Mechanical Behavior In Siliceous Mudstones, Mowry Shale (Cretaceous), Rocky Mountains, U.S.A. *Journal of Sedimentary Research, 87*(4), 366-387. DOI: https://doi.org/10.2110/jsr.2017.24

Milton, J. E., Hickey, K. A., Gleeson, S. A., & Friedman, R. M. (2017). New U-Pb constraints on the age of the Little Dal Basalts and Gunbarrel-related volcanism in Rodinia. *Precambrian Research, 296*, 168-180. DOI: https://doi.org/10.1016/j.precamres.2017.04.030

Mizutani, Y., & Rafter, T. A. (1973). Isotopic behaviour of sulphate oxygen in the bacterial reduction of sulphate. *Geochemical Journal, 6*(4), 183-191. DOI: https://doi.org/10.2343/geochemj.6.183

Mladenova, V., & Valchev, S. (1998). Ga/Ge ratio in sphalerite from the carbonate-hosted Sedmochislenitsi Deposit as a temperature indication of initial fluids. *Review of the Bulgarian Geological Society, 59*(2–3), 49-54.

Möller, P. (1985). Development and application of the Ga/Ge-geothermometer for sphalerite from sediment-hosted deposits. *Monograph Series on Mineral Deposits, 25*, 15-30.

Momenzadeh, M. (1976). Stratabound lead–zinc ores in the Lower Cretaceous and Jurassic sediments in the Malayer–Esfahan district (west central Iran), lithology, metal content, zonation and genesis. *Heidelberg, University of Heidelberg, 300*.

Monger, J. W. H., Price, R. A., & Tempelman-Kluit, D. J. (1982). Tectonic accretion and the origin of the two major metamorphic and plutonic welts in the Canadian Cordillera. *Geology, 10*(2), 70-75. DOI: https://doi.org/10.1130/0091-7613(1982)10<70:TAATOO>2.0.CO;2

Morganti, J. M. (1979). *The geology and ore deposits of the Howards Pass Area, Yukon and Northwest Territories: the origin of basinal sedimentary stratiform sulphides deposits.* (https://dx.doi.org/10.14288/1.0052838 PhD Thesis). University of British Columbia, BC.

Morrow, D. (2018). Devonian of the northern Canadian mainland sedimentary basin: a review. *Bulletin of Canadian Petroleum Geology, 66*(3), 623-694.

Mudd, G. M., Jowitt, S. M., & Werner, T. T. (2017). The world's lead-zinc mineral resources: Scarcity, data, issues and opportunities. *Ore Geology Reviews, 80*, 1160-1190. DOI: https://doi.org/10.1016/j.oregeorev.2016.08.010

Nabhan, S., Marin-Carbonne, J., Mason, P. R. D., & Heubeck, C. (2020). In situ S-isotope compositions of sulfate and sulfide from the 3.2 Ga Moodies Group, South Africa: A record of oxidative sulfur cycling. *Geobiology, 18*(4), 426-444. DOI: https://doi.org/10.1111/gbi.12393

Nelson, J., & Colpron, M. (2007). Tectonics and metallogeny of the British Columbia, Yukon and Alaskan Cordillera, 1.8 Ga to the present. In W. D. Goodfellow (Ed.), *Mineral deposits of Canada: A synthesis of major deposit-types, District Metallogeny, the evolution of geological provinces, and exploration methods* (Vol. Special Publication 5, pp. 755-791): Mineral Deposits Division, Geological Association of Canada.

Niu, D., Renock, D., Whitehouse, M., Leone, J., Rowe, H., Landis, J., Hamren, K., Symcox, C. W., & Sharma, M. (2016). A relict sulfate-methane transition zone in the mid-Devonian Marcellus Shale. *Geochimica Et Cosmochimica Acta, 182*, 73-87. DOI: https://doi.org/10.1016/j.gca.2016.03.004

Norford, B. S., & Orchard, M. J. (1985). Early Silurian age of rocks hosting lead-zinc mineralization at Howards Pass Yukon Territory and District of Mackenzie. *Geological Survey of Canada*. 83-18.

NRCan (Natural Resources Canada). (2021). Critical minerals: an opportunity for Canada. Retrieved from https://www.nrcan.gc.ca/our-natural-resources/minerals-mining/criticalminerals/23414

Ohmoto, H., & Goldhaber, M. B. (1997). Sulfur and carbon isotopes. In *Geochemistry of hydrothermal ore deposits* (3 ed. pp. 517–611): Wiley, New York.

Ootes, L., Gleeson, S. A., Turner, E., Rasmussen, K., Gordey, S., Falck, H., Martel, E., & Pierce, K. (2013). Metallogenic Evolution of the Mackenzie and Eastern Selwyn Mountains of Canada's Northern Cordillera, Northwest Territories: A Compilation and Review. *Geoscience Canada, 40*(1), 40-69. DOI: https://doi.org/10.12789/geocanj.2013.40.005

Pan, Y. M., & Fleet, M. E. (2002). Compositions of the apatite-group minerals: Substitution mechanisms and controlling factors. *Reviews in mineralogy and geochemistry, 48*(1), 13-49. DOI: https://doi.org/10.2138/rmg.2002.48.2

Parkes, R. J., Cragg, B. A., Bale, S. J., Getlifff, J. M., Goodman, K., Rochelle, P. A., Fry, J. C., Weightman, A. J., & Harvey, S. M. (1994). Deep bacterial biosphere in Pacific Ocean sediments. *Nature, 371*(6496), 410-413. DOI: https://doi.org/10.1038/371410a0

Pasquier, V., Sansjofre, P., Rabineau, M., Revillon, S., Houghton, J., & Fike, D. A. (2017). Pyrite sulfur isotopes reveal glacial-interglacial environmental changes. *Proceedings of the National Academy of Sciences, 114*(23), 5941-5945. DOI: https://doi.org/10.1073/pnas.1618245114

Pasquier, V., Bryant, R. N., Fike, D. A., & Halevy, I. (2021). Strong local, not global, controls on marine pyrite sulfur isotopes. *Science Advances, 7*(9), eabb7403. DOI: https://doi.org/10.1126/sciadv.abb7403

Paton, C., Hellstrom, J., Paul, B., Woodhead, J., & Hergt, J. (2011). Iolite: Freeware for the visualisation and processing of mass spectrometric data. *Journal of Analytical Atomic Spectrometry, 26*(12), 2508-2518. DOI: https://doi.org/10.1039/c1ja10172b

Paytan, A., Mearon, S., Cobb, K. M., & Kastner, M. (2002). Origin of marine barite deposits: Sr and S isotope characterization. *Geology, 30*(8), 747-750. DOI: https://doi.org/10.1130/0091-7613(2002)030<0747:Oombds>2.0.Co;2

Paytan, A., & Griffith, E. M. (2007). Marine barite: Recorder of variations in ocean export productivity. *Deep-Sea Research Part II-Topical Studies in Oceanography, 54*(5-7), 687-705. DOI: https://doi.org/10.1016/j.dsr2.2007.01.007

Pellerin, A., Antler, G., Holm, S. A., Findlay, A. J., Crockford, P. W., Turchyn, A. V., Jorgensen, B. B., & Finster, K. (2019). Large sulfur isotope fractionation by bacterial sulfide oxidation. *Sci Adv, 5*(7), eaaw1480. DOI: https://doi.org/10.1126/sciadv.aaw1480

Peng, H.-W., Fan, H.-R., Lecumberri-Sanchez, P., Lai, J.-Q., Hu, H.-L., Lan, T.-G., & Li, X.-H. (2023). Fluid evolution and ore genesis of the Tiantangshan granite-related vein-type Rb-Sn-W deposit, south China: constraints from LA-ICP-MS analyses of fluid inclusions. *Mineralium Deposita, 58*(4), 751-769. DOI: https://doi.org/10.1007/s00126-022-01155-7

Pfaff, K., Koenig, A., Wenzel, T., Ridley, I., Hildebrandt, L. H., Leach, D. L., & Markl, G. (2011). Trace and minor element variations and sulfur isotopes in crystalline and colloform ZnS: Incorporation mechanisms and implications for their genesis. *Chemical Geology, 286*(3-4), 118-134. DOI: https://doi.org/10.1016/j.chemgeo.2011.04.018

Piccoli, P. M., & Candela, P. A. (2002). Apatite in igneous systems. *Phosphates: Geochemical, Geobiological, and Materials Importance, 48*(1), 255-292. DOI: https://doi.org/10.2138/rmg.2002.48.6

Pigage, L. C. (1991). Field guide Anvil Pb-Zn-Ag district, Yukon Territory, Canada. In J. G. Abbott & R. J. W. Turner (Eds.), *Mineral Deposits of the Northern Canadian Cordillera, Yukon-northeastern British Columbia (Field Trip 14)* (Vol. Open File 2169, pp. 177-244): Geological Survey of Canada.

Polito, P. A., Kyser, T. K., Golding, S. D., & Southgate, P. N. (2006). Zinc deposits and related mineralization of the Burketown mineral field, including the world-class Century deposit, northern Australia: Fluid inclusion and stable isotope evidence for basin fluid sources. *Economic Geology, 101*(6), 1251-1273. DOI: https://doi.org/10.2113/gsecongeo.101.6.1251

Potter, P. E., Maynard, J. B., & Depetris, P. J. (2005). *Mud and mudstones: Introduction and overview* (1 ed.). Berlin Heidelberg: Springer.

Pyle, D. M., & Mather, T. A. (2003). The importance of volcanic emissions for the global atmospheric mercury cycle. *Atmospheric Environment, 37*(36), 5115-5124. DOI: https://doi.org/10.1016/j.atmosenv.2003.07.011

Racki, G., Rakociński, M., Marynowski, L., & Wignall, P. B. (2018). Mercury enrichments and the Frasnian-Famennian biotic crisis: A volcanic trigger proved? *Geology, 46*(6), 543-546. DOI: https://doi.org/10.1130/g40233.1

Rajabi, A., Canet, C., Rastad, E., & Alfonso, P. (2015a). Basin evolution and stratigraphic correlation of sedimentary-exhalative Zn–Pb deposits of the Early Cambrian Zarigan–Chahmir Basin, Central Iran. *Ore Geology Reviews, 64*, 328-353. DOI: https://doi.org/10.1016/j.oregeorev.2014.07.013

Rajabi, A., Rastad, E., Canet, C., & Alfonso, P. (2015b). The early Cambrian Chahmir shale-hosted Zn–Pb deposit, Central Iran: an example of vent-proximal SEDEX mineralization. *Mineralium Deposita, 50*(5), 571-590. DOI: https://doi.org/10.1007/s00126-014-0556-x

Rakociński, M., Pisarzowska, A., Corradini, C., Narkiewicz, K., Dubicka, Z., & Abdiyev, N. (2021). Mercury spikes as evidence of extended arc-volcanism around the Devonian–Carboniferous boundary in the South Tian Shan (southern Uzbekistan). *Scientific Reports, 11*(1), 1-15. DOI: https://doi.org/10.1038/s41598-021-85043-6

Raup, D. M., & Sepkoski Jr, J. J. (1982). Mass extinctions in the marine fossil record. *Science, 215*(4539), 1501-1503. DOI: https://doi.org/10.1126/science.215.4539.1501

Redmond, P. B. (2023). Irish-type Zn-Pb deposits in the context of global zinc supply. In C. J. Andrew, M. W. Hitzman, & G. Stanley (Eds.), *Irish-type Zn-Pb Deposits around the world* (https://doi.org/10.61153/WKKY6664pp. 19-34). Dublin: Irish Association for Economic Geology.

Reeburgh, W. S. (1976). Methane consumption in Cariaco Trench waters and sediments. *Earth and Planetary Science Letters, 28*(3), 337-344. DOI: https://doi.org/10.1016/0012-821X(76)90195-3

Reynolds, M. A., Gingras, M. K., Gleeson, S. A., & Stemler, J. U. (2015). More than a trace of oxygen: Ichnological constraints on the formation of the giant Zn-Pb-Ag ± Ba deposits, Red Dog district, Alaska. *Geology, 43*(10), 867-870. DOI: https://doi.org/10.1130/G36954.1

Reynolds, M. A., Gleeson, S. A., Creaser, R. A., Friedlander, B. A., Haywood, J. C., Hnatyshin, D., McCusker, J., & Waldron, J. W. F. (2021). Diagenetic Controls on the Formation of the Anarraaq Clastic-Dominated Zn-Pb-Ag Deposit, Red Dog District, Alaska. *Economic Geology, 116*(8), 1803-1824. DOI: https://doi.org/10.5382/econgeo.4849

Richardson, J. A., Keating, C., Lepland, A., Hints, O., Bradley, A. S., & Fike, D. A. (2019). Silurian records of carbon and sulfur cycling from Estonia: The importance of depositional environment on isotopic trends. *Earth and Planetary Science Letters, 512*, 71-82. DOI: https://doi.org/10.1016/j.epsl.2019.01.055

Rickard, D. (2012). The Evolution of the Sedimentary Sulfur Cycle. In A. J. van Loon (Ed.), *Sulfidic Sediments and Sedimentary Rocks* (https://doi.org/10.1016/b978-0-444-52989-3.00017-9 pp. 685-766). Amsterdam: Elsevier.

Rieger, P., Magnall, J. M., Gleeson, S. A., Lilly, R., Rocholl, A., & Kusebauch, C. (2020). Sulfur Isotope Constraints on the Conditions of Pyrite Formation in the Paleoproterozoic Urquhart Shale Formation and George Fisher Zn-Pb-Ag Deposit, Northern Australia. *Economic Geology, 115*(5), 1003-1020. DOI: https://doi.org/10.5382/econgeo.4726

Rieger, P., Magnall, J. M., Gleeson, S. A., & Oelze, M. (2023). Pyrite chemistry records a multistage ore forming system at the Proterozoic George Fisher massive sulfide Zn-Pb-Ag deposit, Mount Isa, Australia. *Frontiers in Earth Science, 11*, 164. DOI: https://doi.org/10.3389/feart.2023.892759

Ries, J. B., Fike, D. A., Pratt, L. M., Lyons, T. W., & Grotzinger, J. P. (2009). Superheavy pyrite (δ34Spyr> δ34SCAS) in the terminal Proterozoic Nama Group, southern Namibia: A consequence of low seawater sulfate at the dawn of animal life. *Geology, 37*(8), 743-746. DOI: https://doi.org/10.1130/G25775A.1

Robb, L. (2005). *Introduction to Ore Forming Processes,* . Oxford: Blackwell Publishing.

Roberts, F. I. (1982). Trace element chemistry of pyrite: A useful guide to the occurrence of sulfide base metal mineralization. *Journal of Geochemical Exploration, 17*(1), 49-62. DOI: https://doi.org/10.1016/0375-6742(82)90019-X

Rodríguez, A., Weis, P., Magnall, J. M., & Gleeson, S. A. (2021). Hydrodynamic constraints on ore formation by basin-scale fluid flow at continental margins: Modelling Zn metallogenesis in the Devonian Selwyn Basin. *Geochemistry, Geophysics, Geosystems*. DOI: https://doi.org/10.1029/2020GC009453

Roedder, E. (1984). Fluid inclusions: Washington. *DC, Mineralogical Society of America Reviews in Mineralogy, 12*, 644.

Ryall, W. (1981). The forms of mercury in some Australian stratiform Pb-Zn-Ag deposits of different regional metamorphic grades. *Mineralium Deposita, 16*, 425-435.

Rye, D. M., & Williams, N. (1981). Studies of the base metal sulfide deposits at McArthur River, Northern Territory, Australia; III, The stable isotope geochemistry of the HYC, Ridge, and Cooley deposits. *Economic Geology, 76*(1), 1-26. DOI: https://doi.org/10.2113/gsecongeo.76.1.1

Salama, W., Khirekesh, Z., Amini, A., & Bafti, B. S. (2018). Diagenetic evolution of the upper Devonian phosphorites, Alborz for Mountain Range, northern Iran. *Sedimentary Geology, 376*, 90-112. DOI: https://doi.org/10.1016/j.sedgeo.2018.08.001

Sangster, D. F. (2002). The role of dense brines in the formation of vent-distal sedimentary-exhalative (SEDEX) lead-zinc deposits: field and laboratory evidence. *Mineralium Deposita, 37*(2), 149-157. DOI: https://doi.org/10.1007/s00126-001-0216-9

Scanlan, E. (2022). *A geochemical study of Paleozoic alkaline magmatism in the Selwyn Basin and the potential relationship to Zn-Pb mineralization.* (PhD Thesis). Queen's University, Canada.

Schaarschmidt, A., Haase, K. M., Klemd, R., Keith, M., Voudouris, P. C., Alfieris, D., Strauss, H., & Wiedenbeck, M. (2021). Boiling effects on trace element and sulfur isotope compositions of sulfides in shallow-marine hydrothermal systems: Evidence from Milos Island, Greece. *Chemical Geology, 583*. DOI: https://doi.org/10.1016/j.chemgeo.2021.120457

Schodde, R. (2017). *Long term trends in global exploration–Are we finding enough metals?* Paper presented at the Fennoscandian Exploration and Mining Conference, Levi, Finland.

Schulz, H. M., Wirth, R., & Schreiber, A. (2016). Organic–inorganic rock–fluid interactions in stylolitic micro-environments of carbonate rocks: a FIB-TEM study combined with a hydrogeochemical modelling approach. *Geofluids, 16*(5), 909-924. DOI: https://doi.org/10.1111/gfl.12195

Schulz, K. J., DeYoung, J. H., Seal II, R. R., & Bradley, D. C. (2017). *Critical mineral resources of the United States: economic and environmental geology and prospects for future supply* (https://doi.org/10.3133/pp1802). Reston, Virginia: U.S. Department of the Interior, U.S. Geological Survey.

Schwartz, M. O. (1997). Mercury in zinc deposits: Economic geology of a polluting element. *International Geology Review, 39*(10), 905-923. DOI: https://doi.org/10.1080/00206819709465309

Scott, S. D., & Barnes, H. L. (1971). Sphalerite geothermometry and geobarometry. *Economic Geology, 66*(4), 653-669. DOI: https://doi.org/10.2113/gsecongeo.66.4.653

Seal, R. R., Alpers, C. N., & Rye, R. O. (2000). Stable isotope systematics of sulfate minerals. *Sulfate Minerals - Crystallography, Geochemistry and Environmental Significance, 40*(1), 541-602. DOI: https://doi.org/10.2138/rmg.2000.40.12

Sim, M. S., Ono, S. H., & Hurtgen, M. T. (2015). Sulfur isotope evidence for low and fluctuating sulfate levels in the Late Devonian ocean and the potential link with the mass extinction event. *Earth and Planetary Science Letters, 419*, 52-62. DOI: https://doi.org/10.1016/j.epsl.2015.03.009

Slack, J. F., Dumoulin, J. A., Schmidt, J. M., Young, L. E., & Rombach, C. S. (2004a). Paleozoic sedimentary rocks in the Red Dog Zn-Pb-Ag district and vicinity, western Brooks Range, Alaska: Provenance, deposition, and metallogenic significance. *Economic Geology, 99*(7), 1385-1414. DOI: https://doi.org/10.2113/gsecongeo.99.7.1385

Slack, J. F., Kelley, K. D., Anderson, V. M., Clark, J. L., & Ayuso, R. A. (2004b). Multistage hydrothermal silicification mad Fe-Tl-As-Sb-Ge-REE enrichment in the Red Dog Zn-Pb-Ag district, northern Alaska: Geochemistry, origin, and exploration applications. *Economic Geology, 99*(7), 1481-1508. DOI: https://doi.org/10.2113/gsecongeo.99.7.1481

Slack, J. F., Falck, H., Kelley, K. D., & Xue, G. G. (2017). Geochemistry of host rocks in the Howards Pass district, Yukon-Northwest Territories, Canada: implications for sedimentary environments of Zn-Pb and phosphate mineralization. *Mineralium Deposita, 52*(4), 565-593. DOI: https://doi.org/10.1007/s00126-016-0680-x

Smith, M. T., Dickinson, W. R., & Gehrels, G. E. (1993). Contractional Nature of Devonian-Mississippian Antler Tectonism Along the North-American Continental-Margin. *Geology, 21*(1), 21-24. DOI: https://doi.org/10.1130/0091-7613(1993)021<0021:Cnodma>2.3.Co;2

Solomon, M., & Heinrich, C. A. (1992). Are high-heat-producing granites essential to the origin of giant lead-zinc deposits at Mount Isa and McArthur River, Australia? *Exploration and Mining Geology, 1*(1), 85-91.

Stanley, S. M. (2016). Estimates of the magnitudes of major marine mass extinctions in earth history. *Proceedings of the National Academy of Sciences, 113*(42), E6325-E6334. DOI: https://doi.org/10.1073/pnas.1613094113

Steele-MacInnis, M., Lecumberri-Sanchez, P., & Bodnar, R. J. (2012). HokieFlincs_H2O-NaCl: A Microsoft Excel spreadsheet for interpreting microthermometric data from fluid inclusions based on the PVTX properties of H2O–NaCl. *Computers & Geosciences, 49*, 334-337. DOI: https://doi.org/10.1016/j.cageo.2012.01.022

Steele-MacInnis, M. (2018). Fluid inclusions in the system H2O-NaCl-CO2: An algorithm to determine composition, density and isochore. *Chemical Geology, 498*, 31-44. DOI: https://doi.org/10.1016/j.chemgeo.2018.08.022

Steele, J. H., Thorpe, S. A., & Turekian, K. K. (2009). *Marine chemistry and geochemistry*. USA: Academic Press.

Stetter, K. O., Fiala, G., Huber, R., Huber, G., & Segerer, A. (1990). Hyperthermophilic microorganisms. *FEMS Microbiology Reviews, 75*, 117-124.

Sultan, N., Garziglia, S., & Ruffine, L. (2016). New insights into the transport processes controlling the sulfate-methane-transition-zone near methane vents. *Scientific Reports, 6*. DOI: https://doi.org/10.1038/srep26701

Tauson, V. L., & Abramovich, M. G. (1981). Hydrothermal study of the ZnS-HgS system. *Geochemistry International, 17*(3), 117-128.

Taylor, R. D., Leach, D. L., Bradley, D. C., & Pisarevsky, S., A. . (2009). *Mineral resource data for Mississippi Valley-Type and clastic-dominated sediment-hosted lead-zinc deposits*. Retrieved from https://doi.org/10.3133/ofr20091297

Taylor, M. I., McMillan, N. E., Dalrymple, I. J., Hayward, N., & Phillips, N. (2017). Teena zinc-lead deposit. In N. Phillips (Ed.), *Monograph 32 - Australian Ore Deposits* (pp. 483): Australian Institute Mining and Metallurgy Bulletin.

Tian, H., Xiao, X. M., Wilkins, R. W. T., & Tang, Y. C. (2008). New insights into the volume and pressure changes during the thermal cracking of oil to gas in reservoirs: Implications for the in-situ accumulation of gas cracked from oils. *Aapg Bulletin, 92*(2), 181-200. DOI: https://doi.org/10.1306/09210706140

Tornos, F., & Heinrich, C. A. (2008). Shale basins, sulfur-deficient ore brines and the formation of exhalative base metal deposits. *Chemical Geology, 247*(1-2), 195-207. DOI: https://doi.org/10.1016/j.chemgeo.2007.10.011

Torres, M. E., Brumsack, H. J., Bohrmann, G., & Emeis, K. C. (1996). Barite fronts in continental margin sediments: a new look at barium remobilization in the zone of sulfate reduction and formation of heavy barites in diagenetic fronts. *Chemical Geology, 127*(1-3), 125-139. DOI: https://doi.org/10.1016/0009-2541(95)00090-9

Torres, M. E., Bohrmann, G., Dubé, T. E., & Poole, F. G. (2003). Formation of modern and Paleozoic stratiform barite at cold methane seeps on continental margins. *Geology, 31*(10), 897-900. DOI: https://doi.org/10.1130/G19652.1

Torró, L., Benites, D., Vallance, J., Laurent, O., Ortiz-Benavente, B. A., Chelle-Michou, C., Proenza, J. A., & Fontboté, L. (2022). Trace element geochemistry of sphalerite and chalcopyrite in arc-hosted VMS deposits. *Journal of geochemical exploration, 232*, 106882. DOI: https://doi.org/10.1016/j.gexplo.2021.106882

Torró, L., Millán-Nuñez, A. J., Benites, D., González-Jiménez, J. M., Laurent, O., Tavazzani, L., Vallance, J., Chelle-Michou, C., Proenza, J. A., Flores, C., Melgarejo, J. C., Rosas, S., & Fontboté, L. (2023). Germanium- and gallium-rich sphalerite in Mississippi Valley–type deposits: the San Vicente district and the Shalipayco deposit, Peru. *Mineralium Deposita, 58*(5), 853-880. DOI: https://doi.org/10.1007/s00126-023-01160-4

Trude, K. J., & Wilkinson, J. J. (2001). A mineralogical and fluid inclusion study of the Harberton Bridge Fe–Zn–Pb deposit, County Kildare, Ireland. *Journal of the Geological Society, 158*(1), 37-46. DOI: https://doi.org/10.1144/jgs.158.1.37

Turchyn, A. V., & Schrag, D. P. (2006). Cenozoic evolution of the sulfur cycle: Insight from oxygen isotopes in marine sulfate. *Earth and Planetary Science Letters, 241*(3-4), 763-779. DOI: https://doi.org/10.1016/j.epsl.2005.11.007

Turner, R. J. W. (1986). *The genesis of stratiform lead-zinc deposits, Jason property, Macmillan Pass, Yukon* (PhD thesis). Stanford University.

Turner, R. J. W., & Rhodes, D. (1990). *Boundary Creek zinc deposit (Nidd property), MacMillan Pass, Yukon: subseafloor sediment-hosted mineralization associated with volcanism along a late Devonian syndepositional fault* (Vol. Paper 90-1E): Geological Survey of Canada.

Turner, R. J. W. (1991). Jason stratiform Zn-Pb-barite deposit, Selwyn Basin, Canada (NTS 105-0-1): Geological setting, hydrothermal facies and genesis. In J. G. Abbott & R. J. W. Turner (Eds.), *Open File 2169 Mineral deposits of the northern Canadian Cordillera* (Vol. 14, pp. 137-175): Geological Survey of Canada.

United States Geological Survey. (2024). *Mineral commodity summaries 2024* (2024). Retrieved from Reston, VA: https://pubs.usgs.gov/periodicals/mcs2024/mcs2024.pdf

Valckx, N., Stuermer, M., Seneviratne, D., & Prasad, A. (2021). Metals Demand From Energy Transition May Top Current Global Supply. Retrieved from https://www.imf.org/en/Blogs/Articles/2021/12/08/metals-demand-from-energy-transition-may-top-current-global-supply

Velde, B. (1996). Compaction trends of clay-rich deep sea sediments. *Marine Geology, 133*(3-4), 193-201. DOI: https://doi.org/10.1016/0025-3227(96)00020-5

Viets, J. G., Hopkins, R. T., & Miller, B. M. (1992). Variations in minor and trace metals in sphalerite from mississippi valley-type deposits of the Ozark region; genetic implications. *Economic Geology, 87*(7), 1897-1905. DOI: https://doi.org/10.2113/gsecongeo.87.7.1897

Wang, L., Kusky, T., Zhang, Y., Lentz, D., Zhong, Y., Ding, W., Deng, H., Giddens, R., & Peng, S. (2021). Extreme Sulfur Isotope Fractionation of Hydrothermal Auriferous Pyrites from the SW Fringe of the Taupo Volcanic Zone, New Zealand: Implications for Epithermal Gold Exploration. *Results in Geochemistry,* https://doi.org/10.1016/j.ringeo.2021.100009

Wang, L., Zhang, Y., Han, R., & Xiaodong, L. (2023). LA-ICP-MS analyses of trace elements in zoned sphalerite: a study from the Maoping carbonate-hosted Pb-Zn (-Ge) deposit, Southwest China. *Ore Geology Reviews,* https://doi.org/10.1016/j.oregeorev.2023.105468

Wang, Z. C., & Li, G. Z. (1991). Barite and Witherite Deposits in Lower Cambrian Shales of South China - Stratigraphic Distribution and Geochemical Characterization. *Economic Geology and the Bulletin of the Society of Economic Geologists, 86*(2), 354-363. DOI: https://doi.org/10.2113/gsecongeo.86.2.354

Wei, C., Huang, Z., Yan, Z., Hu, Y., & Ye, L. (2018). Trace Element Contents in Sphalerite from the Nayongzhi Zn-Pb Deposit, Northwestern Guizhou, China: Insights into Incorporation Mechanisms, Metallogenic Temperature and Ore Genesis. *Minerals, 8*(11), 490. Retrieved from https://www.mdpi.com/2075-163X/8/11/490

Weller, R. M., & Behl, R. J. (2017). *Defining mechanical and compositional heterogeneity of highly siliceous mudstones: Upper Monterey Formation, Belridge Oil Field, San Joaquin Basin, California*. San Joaquin Basin, California: Search and Discovery.

Wilkinson, J. J. (2001). Fluid inclusions in hydrothermal ore deposits. *Lithos, 55*(1-4), 229-272. DOI: https://doi.org/10.1016/S0024-4937(00)00047-5

Wilkinson, J. J. (2010). A review of fluid inclusion constraints on mineralization in the Irish ore field and implications for the genesis of sediment-hosted Zn-Pb deposits. *Economic Geology, 105*(2), 417-442. DOI: https://doi.org/10.2113/gsecongeo.105.2.417

Wilkinson, J. J. (2014). 13.9 - Sediment-Hosted Zinc–Lead Mineralization: Processes and Perspectives. In H. D. Holland & K. K. Turekian (Eds.), *Treatise on Geochemistry* (Second ed., https://doi.org/10.1016/B978-0-08-095975-7.01109-8 pp. 219-249). Oxford: Elsevier.

Williams, N. (1978a). Studies of the base metal sulfide deposits at McArthur River, Northern Territory, Australia; I, The Cooley and Ridge deposits. *Economic Geology, 73*(6), 1005-1035. DOI: https://doi.org/10.2113/gsecongeo.73.6.1005

Williams, N. (1978b). Studies of the base metal sulfide deposits at McArthur River, Northern Territory, Australia; II, The sulfide-S and organic-C relationships of the concordant deposits and their significance. *Economic Geology, 73*(6), 1036-1056. DOI: https://doi.org/10.2113/gsecongeo.73.6.1036

Williams, N. (2023). Light-Element Stable Isotope Studies of the Clastic-Dominated Lead–Zinc Mineral Systems of Northern Australia and the North American Cordillera: Implications for Ore Genesis and Exploration. In D. Huston & J. Gutzmer (Eds.), *Isotopes in Economic Geology, Metallogenesis and Exploration* (https://doi.org/10.1007/978-3-031-27897-6_11pp. 329-372). Cham: Springer.

Wojcik, P. (2023). Zinc supply and influences from geology. In C. J. Andrew, M. W. Hitzman, & G. Stanley (Eds.), *Irish-type Zn-Pb Deposits around the world* (https://doi.org/10.61153/JHUL1893). Dublin: Irish Association for Economic Geology.

Wood, R. S., Lepland, A., Ogliore, R. C., Houghton, J., & Fike, D. A. (2021). Microscale δ34S heterogeneities in cold seep barite record variable methane flux off the Lofoten-Vesterålen Continental Margin, Norway. *Earth and Planetary Science Letters, 574*. DOI: https://doi.org/10.1016/j.epsl.2021.117164

Wu, F. Y., Mitchell, R. H., Li, Q. L., Zhang, C., & Yang, Y. H. (2017). Emplacement age and isotopic composition of the Prairie Lake carbonatite complex, Northwestern Ontario, Canada. *Geological Magazine, 154*(2), 217-236. DOI: https://doi.org/10.1017/S0016756815001120

Xu, L. G., Lehmann, B., Mao, J. W., Zheng, W., Ye, H. S., & Li, H. Y. (2016). Strontium, Sulfur, Carbon, and Oxygen Isotope Geochemistry of the Early Cambrian Strata-bound Barite and Witherite Deposits of the Qinling-Daba Region, Northern Margin of the Yangtze Craton, China. *Economic Geology, 111*(3), 695-718. DOI: https://doi.org/10.2113/econgeo.111.3.695

Yaghubpur, A., & Mehrabi, B. (1997). Kushk Zinc-Lead deposit, a typical black-shale-hosted deposit in Yazd state, Iran. *Journal of Sciences Islamic Republic of Iran, 8*, 117-125.

Yan, H., Pi, D., Jiang, S.-Y., Hao, W., Cui, H., Robbins, L. J., Mänd, K., Li, L., Planavsky, N. J., & Konhauser, K. O. (2020). Hydrothermally induced 34S enrichment in pyrite as an alternative explanation of the Late-Devonian sulfur isotope excursion in South China.

Geochimica et Cosmochimica Acta, 283, 1-21. DOI: https://doi.org/10.1016/j.gca.2020.05.017

Yardley, B. W. D., & Cleverley, J. S. (2015). The role of metamorphic fluids in the formation of ore deposits. In G. R. T. Jenkin, P. A. J. Lusty, I. McDonald, M. P. Smith, A. J. Boyce, & J. J. Wilkinson (Eds.), *Ore Deposits in an Evolving Earth* (Vol. Special Publications 393, pp. 117-134). London: Geological Society.

Yarmohammadi, A., Rastad, E., & Rajabi, A. (2016). Geochemistry, fluid inclusion study and genesis of the sediment-hosted Zn-Pb (±Ag±Cu) deposits of the Tiran basin, NW of Esfahan, Iran. *Neues Jahrbuch für Mineralogie-Abhandlungen (Journal of Mineralogy and Geochemistry), 193*(2), 183-203. DOI: https://doi.org/10.1127/njma/2016/0301

Ye, L., Cook, N. J., Ciobanu, C. L., Yuping, L., Qian, Z., Tiegeng, L., Wei, G., Yulong, Y., & Danyushevskiy, L. (2011). Trace and minor elements in sphalerite from base metal deposits in South China: A LA-ICPMS study. *Ore Geology Reviews, 39*(4), 188-217. DOI: https://doi.org/10.1016/j.oregeorev.2011.03.001

Yu, L., Zou, H., Li, M., Pirajno, F., Cao, H., Xiao, B., Yu, H., Wu, J., Shen, J., & Liu, X. (2024). Fingerprinting Pb-Zn mineralization events in the SW Yangtze Block, South China: A case from Yuanbaoshan deposit. *Ore Geology Reviews, 165*. DOI: https://doi.org/10.1016/j.oregeorev.2024.105878

Zan, B. W., Yan, J. X., Liu, S. G., Mou, C. L., & Ran, B. (2020). Llandovery (lower Silurian) nodular barite from the northern margin of Yangtze Block, South China, and its paleoceanographic implications. *Palaeogeography Palaeoclimatology Palaeoecology, 537*. DOI: https://doi.org/10.1016/j.palaeo.2019.109415

Zhang, F. F., Dahl, T. W., Lenton, T. M., Luo, G. M., Shen, S. Z., Algeo, T. J., Planavsky, N., Liu, J. S., Cui, Y., Qie, W. K., Romaniello, S. J., & Anbar, A. D. (2020). Extensive marine anoxia associated with the Late Devonian Hangenberg Crisis. *Earth and Planetary Science Letters, 533*. DOI: https://doi.org/10.1016/j.epsl.2019.115976

Zhang, J., Deng, C., Liu, W., Tang, Z., Wang, Y., Ye, T., Liang, W., & Liu, L. (2021). Mercury Anomalies Link to Extensive Volcanism Across the Late Devonian Frasnian–Famennian Boundary in South China. *Frontiers in Earth Science, 9*. DOI: https://doi.org/10.3389/feart.2021.691827

Zhou, X., Li, R., Tang, D., Huang, K.-J., Liu, K., & Ding, Y. (2022). Cold seep activity in the early Cambrian: Evidence from the world-class shale-hosted Tianzhu barite deposit, South China. *Sedimentary Geology, 439*, 106220. DOI: https://doi.org/10.1016/j.sedgeo.2022.106220

Zhou, X. Q., Chen, D. Z., Dong, S. F., Zhang, Y. Q., Guo, Z. H., Wei, H. Y., & Yu, H. (2015). Diagenetic barite deposits in the Yurtus Formation in Tarim Basin, NW China: Implications for barium and sulfur cycling in the earliest Cambrian. *Precambrian Research, 263*, 79-87. DOI: https://doi.org/10.1016/j.precamres.2015.03.006

Zhuang, L. L., Song, Y. C., Liu, Y. C., Fard, M., & Hou, Z. Q. (2019). Major and trace elements and sulfur isotopes in two stages of sphalerite from the world-class Angouran Zn-Pb deposit, Iran: Implications for mineralization conditions and type. *Ore Geology Reviews, 109*, 184-200. DOI: https://doi.org/10.1016/j.oregeorev.2019.04.009

7

APPENDICES

Appendix A

Supplementary data for Chapter 2 is published as open access data publication in the GFZ Data Repository with the title "Isotopic data of pyrite ($\delta^{34}S$) and barite ($\delta^{34}S$, $\delta^{18}O$) in the Canol Formation (Selwyn Basin, Canada)" by Grema, H. M., Magnall, J. M., Whitehouse, M. J., Gleeson, S. A., Schulz, H. -M. GFZ Data Services. https://doi.org/10.5880/GFZ.3.1.2021.006.

The data report consists of *in-situ* secondary ion mass spectrometry (SIMS) analyses of the isotopic compositions of pyrite ($\delta^{34}S_{pyrite}$; n= 200) and barite ($\delta^{34}S_{barite}$; n= 485, $\delta^{18}O_{barite}$; n= 338) from mudstones and siltstones of the Canol Formation, Northwest Territories, Canada.

Table A- 1: *In-situ* SIMS pyrite δ^{34}S values. Py= pyrite.

Sample ID	Sample location	Sample Depth (m)	Pyrite Type	δ^{34}S (‰)
S1_JM-mt2_py10	Harp	2	Py-1	-29.4
S52-c-2_py14	Harp	27	Py-1	-27.4
S52-c-2_py2	Harp	27	Py-1	-27.1
S52-c-2_py5	Harp	27	Py-1	-26.3
S52-c-2_py3	Harp	27	Py-1	-25.8
S52-c-2_py9	Harp	27	Py-1	-25.6
S52-c-2_py10	Harp	27	Py-1	-25.5
S52-c-2_py4	Harp	27	Py-1	-25.5
S52-c-2_py11	Harp	27	Py-1	-25.4
S52-c-2_py8	Harp	27	Py-1	-25.3
S52-c-2_py7	Harp	27	Py-1	-23.7
S52-c-2_py6	Harp	27	Py-1	-23.3
S52-c-3_py16	Harp	27	Py-1	-22.7
S52-c-3_py15	Harp	27	Py-1	-22.5
S52-c-3_py12	Harp	27	Py-1	-18.7
S52-c-3_py14	Harp	27	Py-1	-18.3
S52-c-3_py11	Harp	27	Py-1	-17.2
S1-A_py8	Harp	2	Py-1	-15.4
S52-c-2_py17	Harp	27	Py-1	-14.3
S52-c-2_py19	Harp	27	Py-1	-12.6
S52-c-2_py16	Harp	27	Py-1	-10.7
S1_JM-mt2_py7	Harp	2	Py-1	-9.6
S52-c-2_py18	Harp	27	Py-1	-9.4
S36_JM-mt1_py2	Harp	27	Py-2	9.4
S53a-c-1_py_112	Harp	27	Py-2	12.8
S53a_JM-mt2_py28	Harp	27	Py-2	13
S36_JM-mt1_py8	Harp	27	Py-2	13.3
S31_JM-mt2_py_areaA-	Harp	51	Py-2	13.6
S53a-c-1_py_119	Harp	27	Py-2	13.7
S1-A_py13	Harp	2	Py-2	15
S1_JM-mt2_py22	Harp	2	Py-2	15.8
S1_JM-mt2_py24	Harp	2	Py-2	15.8
S1_JM-mt2_py19	Harp	2	Py-2	15.9
S1_JM-mt2_py20	Harp	2	Py-2	16.1
S1_JM-mt2_py16	Harp	2	Py-2	16.2
S1_JM-mt2_py14	Harp	2	Py-2	16.5
S53a_JM-mt2_py12	Harp	27	Py-2	17
S36_JM-mt1_py6	Harp	27	Py-2	17.2
S31_JM-mt2_py7	Harp	51	Py-2	17.4
S53b_JM-mt2_py8	Harp	27	Py-2	17.7
S52_JM-mt1_py8	Harp	27	Py-2	18
S1_JM-mt2_py35	Harp	2	Py-2	18

S1_JM-mt2_py32	Harp	2	Py-2	18.1
S31_JM-mt2_py3	Harp	51	Py-2	18.2
S1_JM-mt2_py33	Harp	2	Py-2	18.4
S1-A_py6	Harp	2	Py-2	18.6
S53a-c-1_py_103	Harp	27	Py-2	19
S31_JM-mt2_py5	Harp	51	Py-2	19.8
S19_JM-mt2_py2	Harp	9.8	Py-2	19.9
S1_JM-mt2_py26	Harp	2	Py-2	20.4
S7_JM-mt1_py1	Bunk-1	43.8	Py-2	21.1
S1_JM-mt2_py34	Harp	2	Py-2	21.3
S1_JM-mt2_py30	Harp	2	Py-2	21.4
S53a-c-1_py_117	Harp	27	Py-2	21.7
S36_JM-mt1_py4	Harp	27	Py-2	22.3
S53a-c-1_py_102	Harp	27	Py-2	23.2
S19_JM-mt2_py3	Harp	9.8	Py-2	23.4
S20_JM-mt2_py1	Harp	9.8	Py-2	23.5
S1_JM-mt2_py9	Harp	2	Py-2	23.9
S1_JM-mt2_py25	Harp	2	Py-2	24.1
S53b_JM-mt2_py3	Harp	27	Py-2	24.2
S19_JM-mt2_py1	Harp	9.8	Py-2	24.7
S1-A_py5	Harp	2	Py-2	25.1
S53a-c-1_py_118	Harp	27	Py-2	25.2
S53a-c-1_py_107	Harp	27	Py-2	25.4
S53a_JM-mt2_py2	Harp	27	Py-2	25.6
S53a_JM-mt2_py20	Harp	27	Py-2	25.8
S53a_JM-mt2_py27	Harp	27	Py-2	26.1
S53a_JM-mt2_py25	Harp	27	Py-2	27.3
S53a-c_JM-mt2_py4	Harp	27	Py-2	27.7
S53a_JM-mt2_py22	Harp	27	Py-2	28.1
S53b_JM-mt2_py7	Harp	27	Py-2	28.7
S36_JM-mt1_py14	Harp	27	Py-2	29.3
S53b_JM-mt2_py4	Harp	27	Py-2	29.7
S53a-c-1_py_114	Harp	27	Py-2	29.8
S53a_JM-mt2_py1	Harp	27	Py-2	29.8
S53a-c_JM-mt2_py5	Harp	27	Py-2	30.1
S53a_JM-mt2_py24	Harp	27	Py-2	30.3
S53a_JM-mt2_py29	Harp	27	Py-2	30.4
S53a-c_JM-mt2_py9	Harp	27	Py-2	30.6
S53a-c-1_py_106	Harp	27	Py-2	31.2
S21_JM-mt1_py11	Cowan	5*	Py-2	31.3
S34_JM-mt1_py1	Axe	1	Py-2	31.4
S53a-c-1_py_105	Harp	27	Py-2	31.5
S34_JM-mt1_py8	Axe	1	Py-2	31.5
S53a_JM-mt2_py4	Harp	27	Py-2	31.6
S53a-c-1_py_108	Harp	27	Py-2	31.6
S1_JM-mt2_py29	Harp	2	Py-2	31.6

S34_JM-mt1_py21	Axe	1	Py-2	31.7
S53a-c-1_py_116	Harp	27	Py-2	31.8
S53a-c-1_py_109	Harp	27	Py-2	31.8
S52-c-3_py8	Harp	27	Py-2	31.9
S53a_JM-mt2_py18	Harp	27	Py-2	32.1
S34_JM-mt1_py24	Axe	1	Py-2	32.2
S53a-c-1_py_104	Harp	27	Py-2	32.3
S34_JM-mt1_py23	Axe	1	Py-2	32.3
S3_JM-mt2_py1	Harp	2	Py-2	32.3
S11_JM-mt1_py5	NAFCAC-1	38.5	Py-2	32.4
S53b_JM-mt2_py1	Harp	27	Py-2	32.5
S52-c-3_py1	Harp	27	Py-2	32.5
S21_JM-mt1_py20	Cowan	5*	Py-2	32.8
S52-c-3_py7	Harp	27	Py-2	32.8
S1_JM-mt2_py2	Harp	2	Py-2	32.8
S52-c-3_py2	Harp	27	Py-2	32.8
S53a-c_JM-mt2_py6	Harp	27	Py-2	32.8
S52-c-3_py10	Harp	27	Py-2	32.9
S53a-c-1_py_101	Harp	27	Py-2	32.9
S21_JM-mt1_py10	Cowan	5*	Py-2	32.9
S34_JM-mt1_py28	Axe	1	Py-2	33
S52-c-3_py3	Harp	27	Py-2	33.1
S52_JM-mt1_py6	Harp	27	Py-2	33.1
S1_JM-mt2_py4	Harp	2	Py-2	33.2
S22_JM-mt1_py16	Cowan	5*	Py-2	33.3
S21_JM-mt1_py19	Cowan	5*	Py-2	33.4
S52_JM-mt1_py7	Harp	27	Py-2	33.5
S22_JM-mt1_py20	Cowan	5*	Py-2	33.5
S52-c-3_py4	Harp	27	Py-2	33.6
S53b_JM-mt2_py2	Harp	27	Py-2	33.6
S52-c-3_py6	Harp	27	Py-2	33.7
S22_JM-mt1_py1	Cowan	5*	Py-2	33.8
S21_JM-mt1_py21	Cowan	5*	Py-2	34
S22_JM-mt1_py10	Cowan	5*	Py-2	34
S36_JM-mt1_py3	Harp	27	Py-2	34
S33_JM-mt1_py1	Axe	1	Py-2	34.1
S52-c-3_py5	Harp	27	Py-2	34.1
S53a-c-1_py10	Harp	27	Py-2	34.2
S52-c-3_py9	Harp	27	Py-2	34.2
S36_JM-mt1_py10	Harp	27	Py-2	34.2
S34_JM-mt1_py14	Axe	1	Py-2	34.2
S3_JM-mt2_py5	Harp	2	Py-2	34.4
S53a-c-1_py_111	Harp	27	Py-2	34.6
S22_JM-mt1_py19	Cowan	5*	Py-2	34.8
S53a-c-1_py_113	Harp	27	Py-2	34.8
S34_JM-mt1_py17	Axe	1	Py-2	34.9

S21_JM-mt1_py5	Cowan	5*	Py-2	35
S21_JM-mt1_py7	Cowan	5*	Py-2	35.3
S21_JM-mt1_py22	Cowan	5*	Py-2	35.3
S33_JM-mt1_py6	Axe	1	Py-2	35.4
S45_JM-mt2_py1	Wise	99	Py-2	35.4
S21_JM-mt1_py9	Cowan	5*	Py-2	35.4
S34_JM-mt1_py11	Axe	1	Py-2	35.6
S53a-c-1_py_110	Harp	27	Py-2	35.6
S33_JM-mt1_py7	Axe	1	Py-2	35.6
S53a_JM-mt2_py15	Harp	27	Py-2	35.7
S34_JM-mt1_py16	Axe	1	Py-2	35.7
S33_JM-mt1_py3	Axe	1	Py-2	35.8
S21_JM-mt1_py18	Cowan	5*	Py-2	35.9
S34_JM-mt1_py27	Axe	1	Py-2	36
S21_JM-mt1_py13	Cowan	5*	Py-2	36.1
S34_JM-mt1_py9	Axe	1	Py-2	36.2
S53a-c_JM-mt2_py7	Harp	27	Py-2	36.3
S52_JM-mt1_py9	Harp	27	Py-2	36.4
S34_JM-mt1_py5	Axe	1	Py-2	36.4
S22_JM-mt1_py9	Cowan	5*	Py-2	36.4
S33_JM-mt1_py8	Axe	1	Py-2	36.4
S34_JM-mt1_py7	Axe	1	Py-2	36.5
S1_JM-mt2_py27	Harp	2	Py-2	36.6
S33_JM-mt1_py4	Axe	1	Py-2	36.7
S52_JM-mt1_py4	Harp	27	Py-2	36.8
S34_JM-mt1_py4	Axe	1	Py-2	36.9
S21_JM-mt1_py2	Cowan	5*	Py-2	36.9
S34_JM-mt1_py19	Axe	1	Py-2	36.9
S22_JM-mt1_py4	Cowan	5*	Py-2	37
S22_JM-mt1_py8	Cowan	5*	Py-2	37.1
S21_JM-mt1_py3	Cowan	5*	Py-2	37.1
S34_JM-mt1_py22	Axe	1	Py-2	37.3
S21_JM-mt1_py23	Cowan	5*	Py-2	37.3
S34_JM-mt1_py6	Axe	1	Py-2	37.3
S21_JM-mt1_py4	Cowan	5*	Py-2	37.4
S21_JM-mt1_py12	Cowan	5*	Py-2	37.6
S34_JM-mt1_py2	Axe	1	Py-2	37.7
S21_JM-mt1_py8	Cowan	5*	Py-2	37.8
S34_JM-mt1_py12	Axe	1	Py-2	37.8
S22_JM-mt1_py5	Cowan	5*	Py-2	37.8
S52_JM-mt1_py1	Harp	27	Py-2	37.9
S22_JM-mt1_py3	Cowan	5*	Py-2	37.9
S34_JM-mt1_py25	Axe	1	Py-2	37.9
S52_JM-mt1_py10	Harp	27	Py-2	38.1
S34_JM-mt1_py29	Axe	1	Py-2	38.2
S22_JM-mt1_py7	Cowan	5*	Py-2	38.2

S21_JM-mt1_py24	Cowan	5*	Py-2	38.3
S21_JM-mt1_py16	Cowan	5*	Py-2	38.4
S21_JM-mt1_py6	Cowan	5*	Py-2	38.6
S34_JM-mt1_py15	Axe	1	Py-2	38.6
S11_JM-mt1_py1	NAFCAC-1	38.5	Py-2	38.7
S34_JM-mt1_py20	Axe	1	Py-2	38.7
S22_JM-mt1_py13	Cowan	5*	Py-2	38.8
S33_JM-mt1_py9	Axe	1	Py-2	38.9
S52_JM-mt1_py5	Harp	27	Py-2	39
S21_JM-mt1_py1	Cowan	5*	Py-2	39.4
S21_JM-mt1_py17	Cowan	5*	Py-2	39.8
S33_JM-mt1_py5	Axe	1	Py-2	40.3
S22_JM-mt1_py6	Cowan	5*	Py-2	40.4
S21_JM-mt1_py15	Cowan	5*	Py-2	40.5
S34_JM-mt1_py13	Axe	1	Py-2	40.6
S21_JM-mt1_py14	Cowan	5*	Py-2	41.4
S34_JM-mt1_py3	Axe	1	Py-2	41.5
S22_JM-mt1_py11	Cowan	5*	Py-2	42.1
S1_JM-mt2_py1	Harp	2	Py-2	42.9
S33_JM-mt1_py2	Axe	1	Py-2	44.5

Table A- 2: *In-situ* SIMS barite δ^{34}S and δ^{18}O values. Bt= barite.

Sample ID	Sample Location	Sample Depth (m)	Barite Texture	Barite Type	δ^{34}S (‰)	δ^{18}O (‰)
S34_JM-mt1_S-ba3	Axe	1	Nodular	Bt-2b	50.1	20.4
S34_JM-mt1_S-ba8	Axe	1	Nodular	Bt-2b	51.5	21.3
S34_JM-mt1_S-ba4	Axe	1	Nodular	Bt-2b	51.6	22
S33_JM-mt1_S-ba5	Axe	1	Nodular	Bt-2b	51.6	21.9
S33_JM-mt1_S-ba10	Axe	1	Nodular	Bt-2b	52.4	20.9
S33_JM-mt1_S-ba12	Axe	1	Nodular	Bt-2b	53.1	
S33_JM-mt1_S-ba11	Axe	1	Nodular	Bt-2b	53.5	
S33_JM-mt1_S-ba14	Axe	1	Nodular	Bt-2b	53.7	
S33_JM-mt1_S-ba13	Axe	1	Nodular	Bt-2b	53.8	
S34_JM-mt1_S-ba2	Axe	1	Nodular	Bt-2b	54	21
S34_JM-mt1_S-ba7	Axe	1	Nodular	Bt-2b	54.1	
S34_JM-mt1_S-ba16	Axe	1	Nodular	Bt-2b	54.2	
S34_JM-mt1_S-ba5	Axe	1	Nodular	Bt-2b	54.4	
S34_JM-mt1_S-ba17	Axe	1	Nodular	Bt-2b	54.4	
S34_JM-mt1_S-ba11	Axe	1	Nodular	Bt-2b	54.8	21.5
S34_JM-mt1_S-ba19	Axe	1	Nodular	Bt-2b	54.8	
S33_JM-mt1_S-ba7	Axe	1	Nodular	Bt-2b	55.1	
S33_JM-mt1_S-ba6	Axe	1	Nodular	Bt-2b	55.1	
S34_JM-mt1_S-ba13	Axe	1	Nodular	Bt-2b	55.4	
S33_JM-mt1_S-ba8	Axe	1	Nodular	Bt-2b	55.4	
S34_JM-mt1_S-ba6	Axe	1	Nodular	Bt-2b	55.8	21.9
S33_JM-mt1_S-ba9	Axe	1	Nodular	Bt-2b	56.6	
S34_JM-mt1_S-ba10	Axe	1	Nodular	Bt-2b	56.7	21.8
S34_JM-mt1_S-ba18	Axe	1	Nodular	Bt-2b	57	
S34_JM-mt1_S-ba15	Axe	1	Nodular	Bt-2b	57.1	
S34_JM-mt1_S-ba12	Axe	1	Nodular	Bt-2b	57.8	
S34_JM-mt1_S-ba1	Axe	1	Nodular	Bt-2b	59.2	20.4
S34_JM-mt1_S-ba9	Axe	1	Nodular	Bt-2b	59.5	21.7
S34_JM-mt1_S-ba14	Axe	1	Nodular	Bt-2b	59.8	
S33_JM-mt1_S-ba1	Axe	1	Vein	Bt-2c	44.4	16.6
S33_JM-mt1_S-ba2	Axe	1	Vein	Bt-2c	49.8	20.4
S33_JM-mt1_S-ba4	Axe	1	Vein	Bt-2c	51.1	21.5
S6_JM-mt2_S-ba1	NAFCAC -2	1	Disseminated	Bt-1.	15.3	
S21_JM-mt1_S-ba2	Cowan	3	Nodular	Bt-2b	57.9	23.3
S21_JM-mt1_S-ba3	Cowan	3	Nodular	Bt-2b	58.2	
S21_JM-mt1_S-ba9	Cowan	3	Nodular	Bt-2b	58.7	23
S21_JM-mt1_S-ba11	Cowan	3	Nodular	Bt-2b	58.7	23.1
S21_JM-mt1_S-ba10	Cowan	3	Nodular	Bt-2b	59.1	23.7
S21_JM-mt1_S-ba14	Cowan	3	Nodular	Bt-2b	60.8	
S21_JM-mt1_S-ba8	Cowan	3	Nodular	Bt-2b	61	22.7
S21_JM-mt1_S-ba4	Cowan	3	Nodular	Bt-2b	61.3	23.4
S21_JM-mt1_S-ba7	Cowan	3	Nodular	Bt-2b	61.6	

S21_JM-mt1_S-ba12	Cowan	3	Nodular	Bt-2b	61.8	23
S21_JM-mt1_S-ba18	Cowan	3	Nodular	Bt-2b	61.9	
S22_JM-mt1_S-ba2	Cowan	3	Nodular	Bt-2b	62.2	
S21_JM-mt1_S-ba13	Cowan	3	Nodular	Bt-2b	62.4	
S21_JM-mt1_S-ba27	Cowan	3	Nodular	Bt-2b	62.8	23.3
S21_JM-mt1_S-ba29	Cowan	3	Nodular	Bt-2b	62.9	
S21_JM-mt1_S-ba25	Cowan	3	Nodular	Bt-2b	63.1	22.6
S21_JM-mt1_S-ba6	Cowan	3	Nodular	Bt-2b	63.2	
S22_JM-mt1_S-ba4	Cowan	3	Nodular	Bt-2b	63.2	23.5
S21_JM-mt1_S-ba16	Cowan	3	Nodular	Bt-2b	63.3	22.1
S22_JM-mt1_S-ba13	Cowan	3	Nodular	Bt-2b	63.7	
S22_JM-mt1_S-ba11	Cowan	3	Nodular	Bt-2b	64.2	23.2
S21_JM-mt1_S-ba24	Cowan	3	Nodular	Bt-2b	64.2	22.7
S22_JM-mt1_S-ba8	Cowan	3	Nodular	Bt-2b	64.3	
S21_JM-mt1_S-ba23	Cowan	3	Nodular	Bt-2b	64.4	22.3
S22_JM-mt1_S-ba12	Cowan	3	Nodular	Bt-2b	64.6	23.2
S21_JM-mt1_S-ba31	Cowan	3	Nodular	Bt-2b	64.7	23
S22_JM-mt1_S-ba5	Cowan	3	Nodular	Bt-2b	64.9	
S22_JM-mt1_S-ba9	Cowan	3	Nodular	Bt-2b	65.2	23.3
S21_JM-mt1_S-ba17	Cowan	3	Nodular	Bt-2b	65.3	
S22_JM-mt1_S-ba17	Cowan	3	Nodular	Bt-2b	65.5	21.1
S22_JM-mt1_S-ba6	Cowan	3	Nodular	Bt-2b	65.6	22.7
S21_JM-mt1_S-ba26	Cowan	3	Nodular	Bt-2b	65.7	23.1
S21_JM-mt1_S-ba1	Cowan	3	Nodular	Bt-2b	65.8	23
S22_JM-mt1_S-ba7	Cowan	3	Nodular	Bt-2b	65.9	
S21_JM-mt1_S-ba20	Cowan	3	Nodular	Bt-2b	66	23.2
S22_JM-mt1_S-ba19	Cowan	3	Nodular	Bt-2b	66.1	22.7
S21_JM-mt1_S-ba30	Cowan	3	Nodular	Bt-2b	66.5	22.8
S21_JM-mt1_S-ba21	Cowan	3	Nodular	Bt-2b	66.7	23.2
S22_JM-mt1_S-ba22	Cowan	3	Nodular	Bt-2b	66.7	
S22_JM-mt1_S-ba10	Cowan	3	Nodular	Bt-2b	66.8	
S21_JM-mt1_S-ba5	Cowan	3	Nodular	Bt-2b	66.9	23.3
S22_JM-mt1_S-ba3	Cowan	3	Nodular	Bt-2b	66.9	
S21_JM-mt1_S-ba19	Cowan	3	Nodular	Bt-2b	67	22.4
S22_JM-mt1_S-ba16	Cowan	3	Nodular	Bt-2b	67.1	
S21_JM-mt1_S-ba28	Cowan	3	Nodular	Bt-2b	67.1	23.4
S22_JM-mt1_S-ba21	Cowan	3	Nodular	Bt-2b	67.1	
S21_JM-mt1_S-ba15	Cowan	3	Nodular	Bt-2b	67.5	22.7
S22_JM-mt1_S-ba1	Cowan	3	Nodular	Bt-2b	67.7	23.2
S22_JM-mt1_S-ba20	Cowan	3	Nodular	Bt-2b	67.8	
S21_JM-mt1_S-ba22	Cowan	3	Nodular	Bt-2b	67.9	23
S12_JM-mt1_S-ba14	NAFCAC-1	5	Laminated	Bt-2a	37.1	
S12_JM-mt1_S-ba13	NAFCAC-1	5	Laminated	Bt-2a	38.6	19.5
S12_JM-mt1_S-ba15	NAFCAC-1	5	Laminated	Bt-2a	39.7	

S12_JM-mt1_S-ba12	NAFCAC-1	5	Laminated	Bt-2a	39.9	20
S12_JM-mt1_S-ba9	NAFCAC-1	5	Laminated	Bt-2a	40.3	19.9
S12_JM-mt1_S-ba17	NAFCAC-1	5	Laminated	Bt-2a	41	20.4
S12_JM-mt1_S-ba18	NAFCAC-1	5	Laminated	Bt-2a	41.6	
S12_JM-mt1_S-ba19	NAFCAC-1	5	Laminated	Bt-2a	41.7	
S12_JM-mt1_S-ba16	NAFCAC-1	5	Laminated	Bt-2a	42.1	20.2
S12_JM-mt1_S-ba4	NAFCAC-1	5	Laminated	Bt-2a	42.5	
S12_JM-mt1_S-ba20	NAFCAC-1	5	Laminated	Bt-2a	43.9	20.5
S12_JM-mt1_S-ba2	NAFCAC-1	5	Laminated	Bt-2a	46	
S12_JM-mt1_S-ba10	NAFCAC-1	5	Laminated	Bt-2a	46.4	
S12_JM-mt1_S-ba1	NAFCAC-1	5	Laminated	Bt-2a	46.5	
S12_JM-mt1_S-ba8	NAFCAC-1	5	Laminated	Bt-2a	46.5	20.3
S12_JM-mt1_S-ba6	NAFCAC-1	5	Laminated	Bt-2a	46.6	
S12_JM-mt1_S-ba3	NAFCAC-1	5	Laminated	Bt-2a	46.6	
S12_JM-mt1_S-ba5	NAFCAC-1	5	Laminated	Bt-2a	46.8	
S12_JM-mt1_S-ba11	NAFCAC-1	5	Laminated	Bt-2a	46.9	
S12_JM-mt1_S-ba7	NAFCAC-1	5	Laminated	Bt-2a	47	
S12_JM-mt1_S-ba22	NAFCAC-1	5	Laminated	Bt-2a	47	20.4
S12_JM-mt1_S-ba21	NAFCAC-1	5	Laminated	Bt-2a	47.1	20.4
S13_JM-mt2_S-ba7	NAFCAC-1	14.1	Nodular	Bt-2b	38.8	20
S13_JM-mt2_S-ba13	NAFCAC-1	14.1	Nodular	Bt-2b	39.7	17.7
S13B_JM-mt2_S-ba15	NAFCAC-1	14.1	Nodular	Bt-2b	39.7	19.6
S13_JM-mt2_S-ba14	NAFCAC-1	14.1	Nodular	Bt-2b	40	19
S13_JM-mt2_S-ba17	NAFCAC-1	14.1	Nodular	Bt-2b	40.1	-5.5
S13B_JM-mt2_S-ba13	NAFCAC-1	14.1	Nodular	Bt-2b	40.5	19.7
S13_JM-mt2_S-ba16	NAFCAC-1	14.1	Nodular	Bt-2b	40.7	19.7
S13B_JM-mt2_S-ba18	NAFCAC-1	14.1	Nodular	Bt-2b	41.1	19.5
S13B_JM-mt2_S-ba27	NAFCAC-1	14.1	Nodular	Bt-2b	41.3	19.6
S13B_JM-mt2_S-ba30	NAFCAC-1	14.1	Nodular	Bt-2b	41.5	20.3
S13B_JM-mt2_S-ba8	NAFCAC-1	14.1	Nodular	Bt-2b	41.8	20

S13_JM-mt2_S-ba9	NAFCAC-1	14.1	Nodular	Bt-2b	41.9	19.6
S13_JM-mt2_S-ba6	NAFCAC-1	14.1	Nodular	Bt-2b	41.9	19.5
S13_JM-mt2_S-ba1	NAFCAC-1	14.1	Nodular	Bt-2b	41.9	19.9
S13B_JM-mt2_S-ba24	NAFCAC-1	14.1	Nodular	Bt-2b	41.9	20
S13_JM-mt2_S-ba2	NAFCAC-1	14.1	Nodular	Bt-2b	42	20
S13_JM-mt2_S-ba10	NAFCAC-1	14.1	Nodular	Bt-2b	42.1	
S13B_JM-mt2_S-ba6	NAFCAC-1	14.1	Nodular	Bt-2b	42.1	19.5
S13B_JM-mt2_S-ba10	NAFCAC-1	14.1	Nodular	Bt-2b	42.2	20
S13_JM-mt2_S-ba11	NAFCAC-1	14.1	Nodular	Bt-2b	42.3	19.7
S13_JM-mt2_S-ba12	NAFCAC-1	14.1	Nodular	Bt-2b	42.3	15.9
S13_JM-mt2_S-ba8	NAFCAC-1	14.1	Nodular	Bt-2b	42.3	20.1
S13B_JM-mt2_S-ba26	NAFCAC-1	14.1	Nodular	Bt-2b	42.4	19.8
S13_JM-mt2_S-ba18	NAFCAC-1	14.1	Nodular	Bt-2b	42.4	20.1
S13B_JM-mt2_S-ba12	NAFCAC-1	14.1	Nodular	Bt-2b	42.4	20
S13B_JM-mt2_S-ba23	NAFCAC-1	14.1	Nodular	Bt-2b	42.4	19.6
S13B_JM-mt2_S-ba20	NAFCAC-1	14.1	Nodular	Bt-2b	42.4	17.8
S13_JM-mt2_S-ba19	NAFCAC-1	14.1	Nodular	Bt-2b	42.4	19.8
S13_JM-mt2_S-ba20	NAFCAC-1	14.1	Nodular	Bt-2b	42.5	8.8
S13_JM-mt2_S-ba5	NAFCAC-1	14.1	Nodular	Bt-2b	42.5	19.5
S13B_JM-mt2_S-ba31	NAFCAC-1	14.1	Nodular	Bt-2b	42.5	20
S13B_JM-mt2_S-ba7	NAFCAC-1	14.1	Nodular	Bt-2b	42.5	19.8
S13_JM-mt2_S-ba3	NAFCAC-1	14.1	Nodular	Bt-2b	42.7	19.5
S13B_JM-mt2_S-ba25	NAFCAC-1	14.1	Nodular	Bt-2b	42.7	20
S13B_JM-mt2_S-ba14	NAFCAC-1	14.1	Nodular	Bt-2b	42.7	19.5
S13B_JM-mt2_S-ba21	NAFCAC-1	14.1	Nodular	Bt-2b	42.7	19.4
S13_JM-mt2_S-ba15	NAFCAC-1	14.1	Nodular	Bt-2b	42.7	
S13B_JM-mt2_S-ba32	NAFCAC-1	14.1	Nodular	Bt-2b	42.8	19.9
S13B_JM-mt2_S-ba2	NAFCAC-1	14.1	Nodular	Bt-2b	42.8	19.8
S13B_JM-mt2_S-ba9	NAFCAC-1	14.1	Nodular	Bt-2b	42.9	18.5
S13_JM-mt2_S-ba4	NAFCAC-1	14.1	Nodular	Bt-2b	42.9	20

S13B_JM-mt2_S-ba19	NAFCAC-1	14.1	Nodular	Bt-2b	43	20.1
S13B_JM-mt2_S-ba22	NAFCAC-1	14.1	Nodular	Bt-2b	43.2	19.4
S13B_JM-mt2_S-ba34	NAFCAC-1	14.1	Nodular	Bt-2b	43.3	20.3
S13B_JM-mt2_S-ba4	NAFCAC-1	14.1	Nodular	Bt-2b	43.4	19.6
S13B_JM-mt2_S-ba16	NAFCAC-1	14.1	Nodular	Bt-2b	43.5	19.3
S13B_JM-mt2_S-ba5	NAFCAC-1	14.1	Nodular	Bt-2b	43.5	19.8
S13B_JM-mt2_S-ba1	NAFCAC-1	14.1	Nodular	Bt-2b	44.3	19.8
S13B_JM-mt2_S-ba29	NAFCAC-1	14.1	Nodular	Bt-2b	44.5	20.2
S13B_JM-mt2_S-ba11	NAFCAC-1	14.1	Nodular	Bt-2b	45.9	19.4
S13B_JM-mt2_S-ba33	NAFCAC-1	14.1	Nodular	Bt-2b	46.1	19
S13B_JM-mt2_S-ba28	NAFCAC-1	14.1	Nodular	Bt-2b	46.1	19.1
S13B_JM-mt2_S-ba17	NAFCAC-1	14.1	Nodular	Bt-2b	46.4	19.6
S13B_JM-mt2_S-ba35	NAFCAC-1	14.1	Nodular	Bt-2b	48	17.7
S13B_JM-mt2_S-ba3	NAFCAC-1	14.1	Nodular	Bt-2b	48	19.8
S5_JM-mt2_S-ba3	Anita	18	Nodular	Bt-2b	44.6	19.6
S5_JM-mt2_S-ba8	Anita	18	Nodular	Bt-2b	45.7	20.1
S5_JM-mt2_S-ba19	Anita	18	Nodular	Bt-2b	45.8	20
S5_JM-mt2_S-ba18	Anita	18	Nodular	Bt-2b	45.9	19.9
S5_JM-mt2_S-ba4	Anita	18	Nodular	Bt-2b	46.2	19.5
S5_JM-mt2_S-ba2	Anita	18	Nodular	Bt-2b	46.3	20.3
S5_JM-mt2_S-ba6	Anita	18	Nodular	Bt-2b	46.4	20.4
S5_JM-mt2_S-ba17	Anita	18	Nodular	Bt-2b	46.5	19.2
S5_JM-mt2_S-ba11	Anita	18	Nodular	Bt-2b	46.5	20.3
S5_JM-mt2_S-ba7	Anita	18	Nodular	Bt-2b	46.6	19.8
S5_JM-mt2_S-ba23	Anita	18	Nodular	Bt-2b	46.7	21
S5_JM-mt2_S-ba25	Anita	18	Nodular	Bt-2b	46.7	20.4
S5_JM-mt2_S-ba20	Anita	18	Nodular	Bt-2b	46.8	19.9
S5_JM-mt2_S-ba22	Anita	18	Nodular	Bt-2b	46.9	20.1
S5_JM-mt2_S-ba13	Anita	18	Nodular	Bt-2b	47	19.6
S5_JM-mt2_S-ba21	Anita	18	Nodular	Bt-2b	47.8	19.7
S5_JM-mt2_S-ba14	Anita	18	Nodular	Bt-2b	49	19.8
S5_JM-mt2_S-ba16	Anita	18	Nodular	Bt-2b	49.6	20
S5_JM-mt2_S-ba24	Anita	18	Nodular	Bt-2b	50.4	20.5
S5_JM-mt2_S-ba5	Anita	18	Nodular	Bt-2b	50.5	21.8
S5_JM-mt2_S-ba10	Anita	18	Nodular	Bt-2b	51	18.7
S5_JM-mt2_S-ba9	Anita	18	Nodular	Bt-2b	51.2	18.6
S5_JM-mt2_S-ba1	Anita	18	Nodular	Bt-2b	52.3	20.4
S5_JM-mt2_S-ba12	Anita	18	Nodular	Bt-2b	52.8	20.6

S4_JM-mt2_S-ba8	Axe	20	Nodular	Bt-2b	44.3	20
S4_JM-mt2_S-ba21	Axe	20	Nodular	Bt-2b	45	20.1
S4_JM-mt2_S-ba25	Axe	20	Nodular	Bt-2b	45.1	19.2
S4_JM-mt2_S-ba31	Axe	20	Nodular	Bt-2b	45.1	20
S4_JM-mt2_S-ba3	Axe	20	Nodular	Bt-2b	45.3	20
S4_JM-mt2_S-ba7	Axe	20	Nodular	Bt-2b	45.5	21.1
S4_JM-mt2_S-ba29	Axe	20	Nodular	Bt-2b	45.7	19.9
S4_JM-mt2_S-ba5	Axe	20	Nodular	Bt-2b	45.7	19.7
S4_JM-mt2_S-ba12	Axe	20	Nodular	Bt-2b	45.7	21.7
S4_JM-mt2_S-ba11	Axe	20	Nodular	Bt-2b	45.8	20.2
S4_JM-mt2_S-ba18	Axe	20	Nodular	Bt-2b	46.1	20.9
S4_JM-mt2_S-ba47	Axe	20	Nodular	Bt-2b	46.1	20.7
S4_JM-mt2_S-ba30	Axe	20	Nodular	Bt-2b	46.2	20
S4_JM-mt2_S-ba16	Axe	20	Nodular	Bt-2b	46.3	20.1
S4_JM-mt2_S-ba45	Axe	20	Nodular	Bt-2b	46.3	20.7
S4_JM-mt2_S-ba9	Axe	20	Nodular	Bt-2b	46.5	19.3
S4_JM-mt2_S-ba10	Axe	20	Nodular	Bt-2b	46.5	20.7
S4_JM-mt2_S-ba37	Axe	20	Nodular	Bt-2b	46.5	
S4_JM-mt2_S-ba42	Axe	20	Nodular	Bt-2b	46.5	20.9
S4_JM-mt2_S-ba19	Axe	20	Nodular	Bt-2b	46.6	20.1
S4_JM-mt2_S-ba26	Axe	20	Nodular	Bt-2b	46.6	20.2
S4_JM-mt2_S-ba36	Axe	20	Nodular	Bt-2b	46.6	20.2
S4_JM-mt2_S-ba27	Axe	20	Nodular	Bt-2b	47	19.8
S4_JM-mt2_S-ba43	Axe	20	Nodular	Bt-2b	47	20.4
S4_JM-mt2_S-ba28	Axe	20	Nodular	Bt-2b	47.2	19.5
S4_JM-mt2_S-ba23	Axe	20	Nodular	Bt-2b	47.7	20.4
S4_JM-mt2_S-ba40	Axe	20	Nodular	Bt-2b	47.9	20.3
S4_JM-mt2_S-ba24	Axe	20	Nodular	Bt-2b	48	20.6
S4_JM-mt2_S-ba6	Axe	20	Nodular	Bt-2b	48.4	20.6
S4_JM-mt2_S-ba22	Axe	20	Nodular	Bt-2b	48.5	20.3
S4_JM-mt2_S-ba32	Axe	20	Nodular	Bt-2b	48.7	19.9
S4_JM-mt2_S-ba4	Axe	20	Nodular	Bt-2b	48.8	20.7
S4_JM-mt2_S-ba38	Axe	20	Nodular	Bt-2b	48.9	20.4
S4_JM-mt2_S-ba15	Axe	20	Nodular	Bt-2b	49	20.2
S4_JM-mt2_S-ba20	Axe	20	Nodular	Bt-2b	49.3	20.2
S4_JM-mt2_S-ba39	Axe	20	Nodular	Bt-2b	49.6	20.7
S4_JM-mt2_S-ba17	Axe	20	Nodular	Bt-2b	49.8	20.2
S4_JM-mt2_S-ba35	Axe	20	Nodular	Bt-2b	50.5	20.4
S4_JM-mt2_S-ba14	Axe	20	Nodular	Bt-2b	50.5	20
S4_JM-mt2_S-ba34	Axe	20	Nodular	Bt-2b	50.9	20.2
S4_JM-mt2_S-ba46	Axe	20	Nodular	Bt-2b	51.2	21.1
S4_JM-mt2_S-ba2	Axe	20	Nodular	Bt-2b	51.5	19.3
S4_JM-mt2_S-ba44	Axe	20	Nodular	Bt-2b	52	20.6
S4_JM-mt2_S-ba13	Axe	20	Nodular	Bt-2b	52.2	20.1
S4_JM-mt2_S-ba41	Axe	20	Nodular	Bt-2b	52.2	21
S4_JM-mt2_S-ba1	Axe	20	Nodular	Bt-2b	53.7	19.9

S4_JM-mt2_S-ba33	Axe	20	Nodular	Bt-2b	53.9	20.1
S36_JM-mt1_S-ba20	Harp	27	Disseminated	Bt-1.	51.9	22.7
S36_JM-mt1_S-ba18	Harp	27	Disseminated	Bt-1.	56.3	23.5
S36_JM-mt1_S-ba19	Harp	27	Disseminated	Bt-1.	58.3	22.9
S36_JM-mt1_S-ba6	Harp	27	Laminated	Bt-2a	51.1	23.2
S37_JM-mt1_S-ba5a	Harp	27	Laminated	Bt-2a	51.3	23.3
S52_JM-mt1_S-ba15	Harp	27	Laminated	Bt-2a	51.3	
S36_JM-mt1_S-ba1	Harp	27	Laminated	Bt-2a	51.4	
S37_JM-mt1_S-ba17	Harp	27	Laminated	Bt-2a	51.4	
S37_JM-mt1_S-ba11	Harp	27	Laminated	Bt-2a	51.4	
S37_JM-mt1_S-ba15	Harp	27	Laminated	Bt-2a	51.4	
S52_JM-mt1_S-ba11	Harp	27	Laminated	Bt-2a	51.5	
S36_JM-mt1_S-ba3	Harp	27	Laminated	Bt-2a	51.5	20.7
S37_JM-mt1_S-ba13	Harp	27	Laminated	Bt-2a	51.5	
S37_JM-mt1_S-ba7	Harp	27	Laminated	Bt-2a	51.6	
S37_JM-mt1_S-ba2	Harp	27	Laminated	Bt-2a	51.6	23.6
S37_JM-mt1_S-ba10	Harp	27	Laminated	Bt-2a	51.6	
S37_JM-mt1_S-ba1	Harp	27	Laminated	Bt-2a	51.7	22.6
S37_JM-mt1_S-ba8	Harp	27	Laminated	Bt-2a	51.7	
S37_JM-mt1_S-ba4	Harp	27	Laminated	Bt-2a	51.7	
S37_JM-mt1_S-ba16	Harp	27	Laminated	Bt-2a	51.8	
S37_JM-mt1_S-ba14	Harp	27	Laminated	Bt-2a	51.8	23.3
S37_JM-mt1_S-ba12	Harp	27	Laminated	Bt-2a	51.8	23.4
S52_JM-mt1_S-ba1	Harp	27	Laminated	Bt-2a	51.8	
S52_JM-mt1_S-ba5	Harp	27	Laminated	Bt-2a	51.8	23.7
S52_JM-mt1_S-ba2	Harp	27	Laminated	Bt-2a	51.9	
S36_JM-mt1_S-ba5	Harp	27	Laminated	Bt-2a	51.9	21.5
S52_JM-mt1_S-ba13	Harp	27	Laminated	Bt-2a	51.9	
S37_JM-mt1_S-ba6	Harp	27	Laminated	Bt-2a	51.9	
S52_JM-mt1_S-ba7	Harp	27	Laminated	Bt-2a	51.9	
S52_JM-mt1_S-ba6	Harp	27	Laminated	Bt-2a	52	
S52_JM-mt1_S-ba14	Harp	27	Laminated	Bt-2a	52	
S52_JM-mt1_S-ba9	Harp	27	Laminated	Bt-2a	52.1	
S36_JM-mt1_S-ba2	Harp	27	Laminated	Bt-2a	52.2	22.2
S36_JM-mt1_S-ba7	Harp	27	Laminated	Bt-2a	52.2	23.4
S37_JM-mt1_S-ba3	Harp	27	Laminated	Bt-2a	52.2	
S52_JM-mt1_S-ba10	Harp	27	Laminated	Bt-2a	52.2	
S52_JM-mt1_S-ba4	Harp	27	Laminated	Bt-2a	52.3	23.3
S52_JM-mt1_S-ba3	Harp	27	Laminated	Bt-2a	52.3	
S52_JM-mt1_S-ba8	Harp	27	Laminated	Bt-2a	52.7	
S36_JM-mt1_S-ba4	Harp	27	Laminated	Bt-2a	52.8	22.3
S37_JM-mt1_S-ba5b	Harp	27	Laminated	Bt-2a	54	
S36_JM-mt1_S-ba8	Harp	27	Laminated	Bt-2a	54.2	22
S52_JM-mt1_S-ba12	Harp	27	Laminated	Bt-2a	55	
S37_JM-mt1_S-ba9	Harp	27	Laminated	Bt-2a	60.1	23.3
S36_JM-mt1_S-ba11	Harp	27	Nodular	Bt-2b	50	23.1

S53b_JM-mt2_S-ba6	Harp	27	Nodular	Bt-2b	50.5	23.6
S52-c1_JM-mt1_S-ba9	Harp	27	Nodular	Bt-2b	50.6	
S52-c1_JM-mt1_S-ba26	Harp	27	Nodular	Bt-2b	50.8	23
S52-c1_JM-mt1_S-ba18	Harp	27	Nodular	Bt-2b	50.8	
S53b_JM-mt2_S-ba18	Harp	27	Nodular	Bt-2b	50.8	23.3
S52-c1_JM-mt1_S-ba10	Harp	27	Nodular	Bt-2b	50.9	
S52-c1_JM-mt1_S-ba21	Harp	27	Nodular	Bt-2b	51	
S53b_JM-mt2_S-ba23	Harp	27	Nodular	Bt-2b	51	23.4
S53b_JM-mt2_S-ba21	Harp	27	Nodular	Bt-2b	51	23
S53b_JM-mt2_S-ba24	Harp	27	Nodular	Bt-2b	51.1	23.4
S53b_JM-mt2_S-ba4	Harp	27	Nodular	Bt-2b	51.2	23.5
S52-c1_JM-mt1_S-ba22	Harp	27	Nodular	Bt-2b	51.2	
S52-c1_JM-mt1_S-ba14	Harp	27	Nodular	Bt-2b	51.2	
S53b_JM-mt2_S-ba20	Harp	27	Nodular	Bt-2b	51.3	23.6
S36_JM-mt1_S-ba15	Harp	27	Nodular	Bt-2b	51.3	
S53b_JM-mt2_S-ba22	Harp	27	Nodular	Bt-2b	51.3	23.6
S53b_JM-mt2_S-ba5	Harp	27	Nodular	Bt-2b	51.3	23.3
S36_JM-mt1_S-ba13	Harp	27	Nodular	Bt-2b	51.4	
S52-c1_JM-mt1_S-ba11	Harp	27	Nodular	Bt-2b	51.4	
S53b_JM-mt2_S-ba7	Harp	27	Nodular	Bt-2b	51.4	23.1
S53b_JM-mt2_S-ba17	Harp	27	Nodular	Bt-2b	51.4	23.2
S52-c1_JM-mt1_S-ba17	Harp	27	Nodular	Bt-2b	51.5	
S53b_JM-mt2_S-ba2	Harp	27	Nodular	Bt-2b	51.5	
S53b_JM-mt2_S-ba1	Harp	27	Nodular	Bt-2b	51.5	23.6
S53b_JM-mt2_S-ba25	Harp	27	Nodular	Bt-2b	51.5	23.8
S36_JM-mt1_S-ba12	Harp	27	Nodular	Bt-2b	51.6	
S53b_JM-mt2_S-ba19	Harp	27	Nodular	Bt-2b	51.7	23.2
S52-c1_JM-mt1_S-ba12	Harp	27	Nodular	Bt-2b	51.7	
S52-c1_JM-mt1_S-ba4	Harp	27	Nodular	Bt-2b	51.8	
S52-c1_JM-mt1_S-ba20	Harp	27	Nodular	Bt-2b	51.8	23.3
S53b_JM-mt2_S-ba16	Harp	27	Nodular	Bt-2b	51.8	23.3
S53b_JM-mt2_S-ba3	Harp	27	Nodular	Bt-2b	51.8	23.6
S52-c1_JM-mt1_S-ba7	Harp	27	Nodular	Bt-2b	51.9	
S53b_JM-mt2_S-ba12	Harp	27	Nodular	Bt-2b	51.9	23
S53b_JM-mt2_S-ba14	Harp	27	Nodular	Bt-2b	51.9	23.9
S52-c1_JM-mt1_S-ba3	Harp	27	Nodular	Bt-2b	52	
S52-c1_JM-mt1_S-ba24	Harp	27	Nodular	Bt-2b	52	
S53b_JM-mt2_S-ba15	Harp	27	Nodular	Bt-2b	52	23.7
S52-c1_JM-mt1_S-ba15	Harp	27	Nodular	Bt-2b	52.1	23.2
S52-c1_JM-mt1_S-ba1	Harp	27	Nodular	Bt-2b	52.2	22.9
S52-c1_JM-mt1_S-ba19	Harp	27	Nodular	Bt-2b	52.2	
S53b_JM-mt2_S-ba11	Harp	27	Nodular	Bt-2b	52.2	23.3
S36_JM-mt1_S-ba14	Harp	27	Nodular	Bt-2b	52.3	23.2
S36_JM-mt1_S-ba9	Harp	27	Nodular	Bt-2b	52.3	
S52-c1_JM-mt1_S-ba16	Harp	27	Nodular	Bt-2b	52.3	
S36_JM-mt1_S-ba17	Harp	27	Nodular	Bt-2b	52.7	

S52-c1_JM-mt1_S-ba6	Harp	27	Nodular	Bt-2b	52.7	23.4
S52-c1_JM-mt1_S-ba5	Harp	27	Nodular	Bt-2b	52.7	
S53b_JM-mt2_S-ba9	Harp	27	Nodular	Bt-2b	52.8	23
S52-c1_JM-mt1_S-ba8	Harp	27	Nodular	Bt-2b	53	
S36_JM-mt1_S-ba16	Harp	27	Nodular	Bt-2b	53	
S53b_JM-mt2_S-ba13	Harp	27	Nodular	Bt-2b	53.4	23.5
S36_JM-mt1_S-ba10	Harp	27	Nodular	Bt-2b	54	
S53b_JM-mt2_S-ba10	Harp	27	Nodular	Bt-2b	54.1	23.6
S52-c1_JM-mt1_S-ba25	Harp	27	Nodular	Bt-2b	54.5	
S52-c1_JM-mt1_S-ba13	Harp	27	Nodular	Bt-2b	54.8	
S52-c1_JM-mt1_S-ba23	Harp	27	Nodular	Bt-2b	55.5	23.1
S53b_JM-mt2_S-ba8	Harp	27	Nodular	Bt-2b	57.8	23.3
S52-c1_JM-mt1_S-ba2	Harp	27	Nodular	Bt-2b	60.5	23.2
S14_JM-mt2_S-ba21	Axe	36.37	Nodular	Bt-2b	40	19.7
S14-B_JM-mt2_S-ba20	Axe	36.37	Nodular	Bt-2b	41.4	17.5
S14-B_JM-mt2_S-ba21	Axe	36.37	Nodular	Bt-2b	41.6	20.5
S14_JM-mt2_S-ba11	Axe	36.37	Nodular	Bt-2b	41.9	20.6
S14_JM-mt2_S-ba14	Axe	36.37	Nodular	Bt-2b	42.1	19.7
S14_JM-mt2_S-ba19	Axe	36.37	Nodular	Bt-2b	42.1	20.1
S14-B_JM-mt2_S-ba19	Axe	36.37	Nodular	Bt-2b	42.3	
S14_JM-mt2_S-ba27	Axe	36.37	Nodular	Bt-2b	42.5	20.6
S14_JM-mt2_S-ba7	Axe	36.37	Nodular	Bt-2b	42.6	20.7
S14_JM-mt2_S-ba13	Axe	36.37	Nodular	Bt-2b	43.1	19.9
S14-B_JM-mt2_S-ba14	Axe	36.37	Nodular	Bt-2b	43.2	20
S14_JM-mt2_S-ba17	Axe	36.37	Nodular	Bt-2b	43.3	20.3
S14-B_JM-mt2_S-ba11	Axe	36.37	Nodular	Bt-2b	43.3	18.2
S14_JM-mt2_S-ba28	Axe	36.37	Nodular	Bt-2b	43.3	20
S14_JM-mt2_S-ba24	Axe	36.37	Nodular	Bt-2b	43.6	19.6
S14_JM-mt2_S-ba25	Axe	36.37	Nodular	Bt-2b	43.7	20.7
S14-B_JM-mt2_S-ba22	Axe	36.37	Nodular	Bt-2b	43.8	18.2
S14-B_JM-mt2_S-ba13	Axe	36.37	Nodular	Bt-2b	43.9	
S14_JM-mt2_S-ba29	Axe	36.37	Nodular	Bt-2b	43.9	20.2
S14-B_JM-mt2_S-ba4	Axe	36.37	Nodular	Bt-2b	43.9	20.4
S14_JM-mt2_S-ba30	Axe	36.37	Nodular	Bt-2b	44.1	20.4
S14-B_JM-mt2_S-ba12	Axe	36.37	Nodular	Bt-2b	44.1	20.6
S14_JM-mt2_S-ba15	Axe	36.37	Nodular	Bt-2b	44.2	20.7
S14_JM-mt2_S-ba31	Axe	36.37	Nodular	Bt-2b	44.3	19.8
S14-B_JM-mt2_S-ba23	Axe	36.37	Nodular	Bt-2b	44.3	
S14_JM-mt2_S-ba2	Axe	36.37	Nodular	Bt-2b	44.3	20.2
S14-B_JM-mt2_S-ba6	Axe	36.37	Nodular	Bt-2b	44.4	20.3
S14_JM-mt2_S-ba26	Axe	36.37	Nodular	Bt-2b	44.5	20.6
S14-B_JM-mt2_S-ba8	Axe	36.37	Nodular	Bt-2b	44.5	20.1
S14-B_JM-mt2_S-ba1	Axe	36.37	Nodular	Bt-2b	44.6	
S14-B_JM-mt2_S-ba3	Axe	36.37	Nodular	Bt-2b	44.7	19.7
S14_JM-mt2_S-ba12	Axe	36.37	Nodular	Bt-2b	44.7	19.8
S14-B_JM-mt2_S-ba9	Axe	36.37	Nodular	Bt-2b	44.7	20.4

S14_JM-mt2_S-ba16	Axe	36.37	Nodular	Bt-2b	44.8	20.2
S14_JM-mt2_S-ba20	Axe	36.37	Nodular	Bt-2b	44.8	20.1
S14_JM-mt2_S-ba22	Axe	36.37	Nodular	Bt-2b	45.1	20.4
S14_JM-mt2_S-ba18	Axe	36.37	Nodular	Bt-2b	45.1	20
S14_JM-mt2_S-ba6	Axe	36.37	Nodular	Bt-2b	45.4	20.3
S14_JM-mt2_S-ba1	Axe	36.37	Nodular	Bt-2b	45.4	20.5
S14_JM-mt2_S-ba8	Axe	36.37	Nodular	Bt-2b	45.4	20.9
S14-B_JM-mt2_S-ba17	Axe	36.37	Nodular	Bt-2b	45.5	20.2
S14-B_JM-mt2_S-ba7	Axe	36.37	Nodular	Bt-2b	45.6	20
S14_JM-mt2_S-ba3	Axe	36.37	Nodular	Bt-2b	45.6	20.6
S14_JM-mt2_S-ba23	Axe	36.37	Nodular	Bt-2b	45.6	19.2
S14-B_JM-mt2_S-ba10	Axe	36.37	Nodular	Bt-2b	45.7	20.6
S14-B_JM-mt2_S-ba2	Axe	36.37	Nodular	Bt-2b	45.7	20.5
S14_JM-mt2_S-ba4	Axe	36.37	Nodular	Bt-2b	45.7	20.3
S14-B_JM-mt2_S-ba15	Axe	36.37	Nodular	Bt-2b	46	20.9
S14_JM-mt2_S-ba5	Axe	36.37	Nodular	Bt-2b	46	20.1
S14-B_JM-mt2_S-ba5	Axe	36.37	Nodular	Bt-2b	46.2	19.5
S14-B_JM-mt2_S-ba16	Axe	36.37	Nodular	Bt-2b	46.6	20.4
S14_JM-mt2_S-ba10	Axe	36.37	Nodular	Bt-2b	46.9	20.5
S14_JM-mt2_S-ba9	Axe	36.37	Nodular	Bt-2b	47	19.3
S14-B_JM-mt2_S-ba18	Axe	36.37	Nodular	Bt-2b	47.1	19.2
S11_JM-mt1_S-ba12	NAFCAC-1	38.5	Disseminated	Bt-1.	51.5	20
S11_JM-mt1_S-ba2	NAFCAC-1	38.5	Disseminated	Bt-1.	57.1	21
S11_JM-mt1_S-ba5	NAFCAC-1	38.5	Disseminated	Bt-1.	58.2	20.2
S11_JM-mt1_S-ba1	NAFCAC-1	38.5	Disseminated	Bt-1.	58.4	21.7
S11_JM-mt1_S-ba6	NAFCAC-1	38.5	Disseminated	Bt-1.	58.5	20.9
S11_JM-mt1_S-ba4	NAFCAC-1	38.5	Disseminated	Bt-1.	58.9	19.4
S11_JM-mt1_S-ba7	NAFCAC-1	38.5	Disseminated	Bt-1.	59.2	21.6
S11_JM-mt1_S-ba11	NAFCAC-1	38.5	Disseminated	Bt-1.	59.6	21.6
S11_JM-mt1_S-ba13	NAFCAC-1	38.5	Disseminated	Bt-1.	59.9	21.2
S11_JM-mt1_S-ba10	NAFCAC-1	38.5	Disseminated	Bt-1.	60.7	21.1
S11_JM-mt1_S-ba3	NAFCAC-1	38.5	Disseminated	Bt-1.	61.2	18.4
S23_JM-mt1_S-ba4	Axe	40	Nodular	Bt-2b	43.5	18.7
S23_JM-mt1_S-ba1	Axe	40	Nodular	Bt-2b	43.9	
S23_JM-mt1_S-ba9	Axe	40	Nodular	Bt-2b	44.2	20.2
S23_JM-mt1_S-ba2	Axe	40	Nodular	Bt-2b	44.7	
S23_JM-mt1_S-ba7	Axe	40	Nodular	Bt-2b	45	
S23_JM-mt1_S-ba11	Axe	40	Nodular	Bt-2b	45.7	
S23_JM-mt1_S-ba6	Axe	40	Nodular	Bt-2b	45.9	
S23_JM-mt1_S-ba3	Axe	40	Nodular	Bt-2b	45.9	

S23_JM-mt1_S-ba5	Axe	40	Nodular	Bt-2b	46	20
S23_JM-mt1_S-ba10	Axe	40	Nodular	Bt-2b	46.1	
S23_JM-mt1_S-ba8	Axe	40	Nodular	Bt-2b	47	21
S7_JM-mt1_S-ba9	Bunk-1	43.8	Nodular	Bt-2b	44	20.1
S7_JM-mt1_S-ba19	Bunk-1	43.8	Nodular	Bt-2b	44.2	
S7_JM-mt1_S-ba21	Bunk-1	43.8	Nodular	Bt-2b	44.3	20.6
S7_JM-mt1_S-ba11	Bunk-1	43.8	Nodular	Bt-2b	44.3	
S7_JM-mt1_S-ba10	Bunk-1	43.8	Nodular	Bt-2b	44.4	
S7_JM-mt1_S-ba20	Bunk-1	43.8	Nodular	Bt-2b	44.5	20.3
S7_JM-mt1_S-ba8	Bunk-1	43.8	Nodular	Bt-2b	44.6	20.8
S7_JM-mt1_S-ba7	Bunk-1	43.8	Nodular	Bt-2b	44.6	
S7_JM-mt1_S-ba22	Bunk-1	43.8	Nodular	Bt-2b	44.6	21.2
S7_JM-mt1_S-ba16	Bunk-1	43.8	Nodular	Bt-2b	45.1	
S7_JM-mt1_S-ba17	Bunk-1	43.8	Nodular	Bt-2b	45.2	
S7_JM-mt1_S-ba15	Bunk-1	43.8	Nodular	Bt-2b	45.2	21.1
S7_JM-mt1_S-ba13	Bunk-1	43.8	Nodular	Bt-2b	45.4	
S7_JM-mt1_S-ba12	Bunk-1	43.8	Nodular	Bt-2b	45.5	
S7_JM-mt1_S-ba23	Bunk-1	43.8	Nodular	Bt-2b	45.5	
S7_JM-mt1_S-ba2	Bunk-1	43.8	Nodular	Bt-2b	45.8	
S7_JM-mt1_S-ba14	Bunk-1	43.8	Nodular	Bt-2b	45.8	21
S7_JM-mt1_S-ba3	Bunk-1	43.8	Nodular	Bt-2b	45.9	20.2
S7_JM-mt1_S-ba5	Bunk-1	43.8	Nodular	Bt-2b	46.1	21
S7_JM-mt1_S-ba18	Bunk-1	43.8	Nodular	Bt-2b	46.3	20.9
S7_JM-mt1_S-ba1	Bunk-1	43.8	Nodular	Bt-2b	46.6	
S7_JM-mt1_S-ba6	Bunk-1	43.8	Nodular	Bt-2b	47	
S7_JM-mt1_S-ba4	Bunk-1	43.8	Nodular	Bt-2b	47.4	
S32_JM-mt2_S-ba4	NAFCAC-2	62.7	Nodular	Bt-2b	62.2	23.3
S32_JM-mt2_S-ba11	NAFCAC-2	62.7	Nodular	Bt-2b	63	23
S32_JM-mt2_S-ba15	NAFCAC-2	62.7	Nodular	Bt-2b	63.1	22.8
S32_JM-mt2_S-ba18	NAFCAC-2	62.7	Nodular	Bt-2b	63.5	
S32_JM-mt2_S-ba18	NAFCAC-2	62.7	Nodular	Bt-2b	63.5	23.3
S32_JM-mt2_S-ba26	NAFCAC-2	62.7	Nodular	Bt-2b	63.5	
S32_JM-mt2_S-ba26	NAFCAC-2	62.7	Nodular	Bt-2b	63.6	22.9
S32_JM-mt2_S-ba7	NAFCAC-2	62.7	Nodular	Bt-2b	63.7	23.8
S32_JM-mt2_S-ba12	NAFCAC-2	62.7	Nodular	Bt-2b	63.7	22.9
S32_JM-mt2_S-ba17	NAFCAC-2	62.7	Nodular	Bt-2b	64	22.8
S32_JM-mt2_S-ba17	NAFCAC-2	62.7	Nodular	Bt-2b	64	
S32_JM-mt2_S-ba30	NAFCAC-2	62.7	Nodular	Bt-2b	64.1	
S32_JM-mt2_S-ba21	NAFCAC-2	62.7	Nodular	Bt-2b	64.2	23

S32_JM-mt2_S-ba21	NAFCAC -2	62.7	Nodular	Bt-2b	64.2	
S32_JM-mt2_S-ba20	NAFCAC -2	62.7	Nodular	Bt-2b	64.2	23
S32_JM-mt2_S-ba20	NAFCAC -2	62.7	Nodular	Bt-2b	64.2	
S32_JM-mt2_S-ba19	NAFCAC -2	62.7	Nodular	Bt-2b	64.5	
S32_JM-mt2_S-ba23	NAFCAC -2	62.7	Nodular	Bt-2b	64.5	
S32_JM-mt2_S-ba19	NAFCAC -2	62.7	Nodular	Bt-2b	64.5	23.3
S32_JM-mt2_S-ba23	NAFCAC -2	62.7	Nodular	Bt-2b	64.5	
S32_JM-mt2_S-ba14	NAFCAC -2	62.7	Nodular	Bt-2b	64.5	23.2
S32_JM-mt2_S-ba5	NAFCAC -2	62.7	Nodular	Bt-2b	64.7	21.6
S32_JM-mt2_S-ba6	NAFCAC -2	62.7	Nodular	Bt-2b	64.8	23.5
S32_JM-mt2_S-ba29	NAFCAC -2	62.7	Nodular	Bt-2b	64.8	22.9
S32_JM-mt2_S-ba29	NAFCAC -2	62.7	Nodular	Bt-2b	64.8	
S32_JM-mt2_S-ba3	NAFCAC -2	62.7	Nodular	Bt-2b	64.9	22.5
S32_JM-mt2_S-ba8	NAFCAC -2	62.7	Nodular	Bt-2b	65.4	23.5
S32_JM-mt2_S-ba13	NAFCAC -2	62.7	Nodular	Bt-2b	65.6	23.3
S32_JM-mt2_S-ba9	NAFCAC -2	62.7	Nodular	Bt-2b	65.7	22.8
S32_JM-mt2_S-ba1	NAFCAC -2	62.7	Nodular	Bt-2b	65.9	22.8
S32_JM-mt2_S-ba22	NAFCAC -2	62.7	Nodular	Bt-2b	66	
S32_JM-mt2_S-ba22	NAFCAC -2	62.7	Nodular	Bt-2b	66	
S32_JM-mt2_S-ba10	NAFCAC -2	62.7	Nodular	Bt-2b	66.1	
S32_JM-mt2_S-ba25	NAFCAC -2	62.7	Nodular	Bt-2b	66.3	
S32_JM-mt2_S-ba25	NAFCAC -2	62.7	Nodular	Bt-2b	66.4	
S32_JM-mt2_S-ba2	NAFCAC -2	62.7	Nodular	Bt-2b	66.6	22.6
S32_JM-mt2_S-ba16	NAFCAC -2	62.7	Nodular	Bt-2b	67.9	23.5
S32_JM-mt2_S-ba16	NAFCAC -2	62.7	Nodular	Bt-2b	67.9	
S45_JM-mt2_S-ba5a	Wise	99	Disseminated	Bt-1.	42.9	19.5
S45_JM-mt2_S-ba3	Wise	99	Disseminated	Bt-1.	43.1	19.6
S45_JM-mt2_S-ba9	Wise	99	Disseminated	Bt-1.	43.2	19.5
S45_JM-mt2_S-ba6	Wise	99	Disseminated	Bt-1.	43.9	19.1
S45_JM-mt2_S-ba10	Wise	99	Disseminated	Bt-1.	45.4	19.9
S45_JM-mt2_S-ba2	Wise	99	Disseminated	Bt-1.	46.6	21.1
S45_JM-mt2_S-ba7	Wise	99	Disseminated	Bt-1.	47.2	20.1

S45_JM-mt2_S-ba8	Wise	99	Disseminated	Bt-1.	47.5	21.2
S45_JM-mt2_S-ba4	Wise	99	Disseminated	Bt-1.	47.5	20.3
S45_JM-mt2_S-ba5	Wise	99	Disseminated	Bt-1.	47.7	20.1
S45_JM-mt2_S-ba12	Wise	99	Disseminated	Bt-1.	47.9	21.6
S45_JM-mt2_S-ba1	Wise	99	Disseminated	Bt-1.	48.2	21
S45_JM-mt2_S-ba11	Wise	99	Disseminated	Bt-1.	52.7	22.3

Appendix B

This is a supplementary data for Chapter 3 and is published as open access data publication in the GFZ Data Repository with the title "Petrography, quantitative mineralogy, and U-Pb geochronology of the Boundary Zone Zn-Pb-Ag prospect, Yukon, Canada" by Grema, H. M., Wudarska, A., Wilke, F. D. H., Schleicher, A. M., Milton, J. E., Magnall, J. M., Gleeson, S. A., and Schulz, H.-M. GFZ Data Services. https://doi.org/10.5880/GFZ.3.1.2024.007.

Please access via (https://dataservices.gfz-potsdam.de/panmetaworks/review/4d977202cbc26dabe4526cfbbe177869faff51af98518d4411dadc5e14d71768/).

This data comprises results of analyses carried out on drill core samples from the Boundary Zone. The data originates from multiple-scale petrographic examination, quantitative X-ray diffraction (QXRD), electron probe microanalysis (EPMA), and secondary ion mass spectrometry (SIMS) U-Pb fluorapatite geochronology.

Appendix C

This supplementary data forms part of Chapter 4 and is published as open access data publication in the GFZ Data Repository with the title " Sphalerite chemistry and fluid inclusion microthermometry data from the Zn-Pb±Ag Boundary Zone deposit, Yukon, Canada" by Haruna M. Grema, Marta Sośnicka, Vitor R. Barrote, Franziska D.H. Wilke, Jack E. Milton, Joseph M. Magnall, Sarah A. Gleeson, and Hans-Martin Schulz. GFZ Data Services. https://doi.org/10.5880/GFZ.3.1.2024.008.

Please access via https://dataservices.gfz-potsdam.de/panmetaworks/review/66434e4a4731d6ada2a01378e4fbfa88375c14b81a0168c15b7140db3540ee3f/

The data consists of sphalerite and quartz fluid inclusion microthermometry data and LA-ICP-MS sphalerite chemistry. The sphalerite and quartz were analyzed *in-situ* in samples from the Boundary Zone.